



MONASH University

A continuum and atomistic simulation study of ion transport in multilayered graphene membranes

***GengPing* JIANG**

Doctor of Philosophy

A thesis submitted for the degree of Doctor of Philosophy at

Monash University in 2016

Department of Materials Science and Engineering

Copyright Notices

Notice 1

© The author 2016. Except as provided in the Copyright Act 1968, this thesis may not be reproduced in any form without the written permission of the author.

I certify that I have made all reasonable efforts to secure copyright permissions for third-party content included in this thesis and have not knowingly added copyright content to my work without the owner's permission.

Abstract

Graphene membrane as a staggered multilayer structure was demonstrated to be a promising filter membrane for the gas and liquid separation. The superior property of graphene membrane is owing to the exotic behaviour of fluid confined in the graphene nanochannel (< 10 nm), namely the booming nanofluidics field. Unlike the 1-D nanochannel in lab-on-a-chip devices, the graphene membrane has a unique cascading nano-slit system. Understanding of ion transport in graphene membranes is very limited. Thus this thesis is devoted to study the microstructures and novel physical phenomena and mechanism that govern the ion transport inside graphene membranes via continuum and atomistic simulations.

A quantitative and statistical representative microstructure model is obtained for graphene membranes by correlating diffusion permeation experimental results with continuum simulation results. This task is achieved by taking advantages of the tuneable graphene membrane platform recently developed in our group. The crucial role of the pin-hole defects in graphene sheets is revealed.

Based on this structure model, comprehensive continuum simulations were performed to study the electrokinetic properties of ion transport inside graphene membranes. Comparison with direct experimental measurements leads to an interesting scaling law that correlates the relative conductance with channel size. We find some novel electric double layer (EDL) structures, such as EDL caused by external electric field (coined as binary boundary layer (BBL) in this thesis) and EDLs at the pore aperture regions. Influences of these EDL structures and the channel surface charges on the driving force distribution and ion concentration inside the cascading nanoslit system are carefully studied. With the obtained information, ion transport in graphene membranes was analysed.

To understand the unusual ion transport behaviour observed by the experiments at molecular scale, atomistic simulations for ion electro-kinetic flow through the membranes with and without surface charge were performed. The EDL structures, ion concentrations, and ion transport properties were carefully studied and compared with continuum simulations. For graphene membranes with zero surface charge, our MD simulations showed a strong BBL caused by external electric field. As a result, a novel polarized electro-osmosis flow (EOF) phenomenon is observed. Unlike the conventional EOF, the polarized EOF has two flows in opposite directions next to the two opposite walls of a slit, respectively. The polarized EOF accelerates the ion transport inside the membrane and could be utilized as a novel nano-mixer. With surface charges, the ion transport is a combination of ion electrophoresis, conventional EOF, and the polarised EOF. In small slits, the conventional EOF is dominant for enhancing electrokinetic conductivity. Our MD simulations provide novel physical insights that are missed in continuum simulations, which should be considered in future continuum simulations and models.

Overall, in this thesis, the combination of continuum and atomistic simulations, complemented by experimental results provide us much needed knowledge of ion transport in graphene membranes. This study should provide a basis for further fundamental study and practical applications of graphene membranes.

Declaration

This thesis contains no material which has been accepted for the award of any other degree or diploma at any university or equivalent institution and that, to the best of my knowledge and belief, this thesis contains no material previously published or written by another person, except where due reference is made in the text of the thesis.

Signature of the Candidate:

A handwritten signature in black ink, appearing to be '蒋野' (Jiang Ye), written over a yellow rectangular background.

Date: 31 March., 2016

Publications during enrolment

You may wish to list your publications arising from your research degree enrolment using the standard citation format of your academic unit. If you have no publications, remove this section.

Thesis including published works General Declaration

If your thesis is a 'thesis including published works' you must detail all publications in the section below. If you have not completed a thesis including published works, remove this section.

I hereby declare that this thesis contains no material which has been accepted for the award of any other degree or diploma at any university or equivalent institution and that, to the best of my knowledge and belief, this thesis contains no material previously published or written by another person, except where due reference is made in the text of the thesis.

This thesis includes 2 original papers published in peer reviewed journals and 0 unpublished publications. The core theme of the thesis is **the modelling of CCG membrane and ion transport**. The ideas, development and writing up of all the papers in the thesis were the principal responsibility of myself, the candidate, working within the *Department of Materials Science and Engineering* under the supervision of Prof. Dan LI.

(The inclusion of co-authors reflects the fact that the work came from active collaboration between researchers and acknowledges input into team-based research.)

In the case of 3-5 my contribution to the work involved the following:

(If this is a laboratory-based discipline, a paragraph outlining the assistance given during the experiments, the nature of the experiments and an attribution to the contributors could follow.)

Thesis chapter	Publication title	Publication status*	Nature and extent (%) of students contribution
3	Molecular dynamics simulations of the electric double layer capacitance of graphene electrodes in mono-valent aqueous electrolytes	Published	100%
4&5	Ion transport in complex layered graphene-based membranes with tuneable interlayer spacing	Published	50%

I have not renumbered sections of submitted or published papers in order to generate a consistent presentation within the thesis.

Student signature:

Date: 31March2016

The undersigned hereby certify that the above declaration correctly reflects the nature and extent of the student and co-authors' contributions to this work.

Main Supervisor signature:

Date: 31March2016

Acknowledgement

First and foremost, I would like to show my deepest gratitude to my supervisors Dr. Zhe LIU and Prof. Dan LI, who have guided and supported me through my Ph.D education. Without their instruction, kindness and patience, I could not complete the present thesis.

Secondly I should acknowledge my *Alma mater*, the Central South University and Monash University for their 2+2 undergraduate study project. The four year undergraduate experience in different country and different education system is a valuable life experience. I would be also extremely grateful to the Ph.D. scholarship funding (Faculty International Postgraduate Research Scholarship and Monash Graduate Scholarship) from the Faculty of Engineering and Monash University respectively.

Thirdly, my sincere appreciation also goes to my colleagues, Dr. Chi CHEN for his useful suggestion and discussion for my thesis writing, and most importantly, the experiment results for graphene membranes by CHEN which is the major motivation for the present theoretic study. I am also deeply indebted to all colleagues in both groups for their help and support, both in academic and in real life. Finally I would like to dedicate the present thesis to my parents for their invaluable caring and raising for 28 years.

Abbreviations

BLs	Boundary Layers
BBLs	Binary Boundary Layers
CCG	Chemical Converted Graphene
CNT	Carbon nanotube
EDLs	Electric Double Layers
EOF	Electro-Osmosis Flow
GO	Graphene Oxide
HL	Helmholtz Layer
IHL	Inner Helmholtz Layer
MD simulation	Molecular Dynamics simulation
OHL	Outer Helmholtz Layer
rMC	reverse Monte Carlo

Nomenclature

d	Aperture size (pin-hole deminesion)
d_H	Size of the hydration shell
d_{HL}	Distance of electrode surface to Helmholtz layer
e	Elementary charge
h	Nanochannel height or interlayer distance
h_G	The thickness of the graphene membrane
k	Coulomb's constant
k_B	Boltzmann constant
n	Concentration of partical
$n_{i,0}$	Concentration of i th ion in the reservoir.
n_{res}	Reservoir concentration for KCl solution
$\bar{n}_{m,i}$	Mean concentration of i th type ion inside the membrane
q_i, q_j	Net charge on i th and j th atom
$r_{i,j}$	Distance between i th and j th atom
\vec{u}	Background laminar flow
v_i	Velocity of i th atom
\bar{v}_{slit}	Mean velocity of ions in nanoslit region
z_i	Valence number of i th ion
A_m	Area of membrane
A_{sys}	Cross-section area of simulation system
D	Diffusivity of partical
D_{K+}, D_{Cl-}	Diffusivity of K^+ and Cl^- respectively,
D_m	Diffusivity of KCl solution in membrane, membrane diffusivity
$D_{m,exp}(h_i)$	Experimental membrane diffusivity for i th sample with
$\tilde{D}_{m,sim}(L, d, h_i)$	Linear interpolation for certain configuration (L, d, h_i)
\bar{E}_{slit}	Mean electric field strength in nanoslit region along Y-direction
F	Faraday constant
G_m	The electro-kinetic conductance of the membrane
H_{slit}	Height of nanoslit region (in X-direction)
I_{sys}	Total electro-kinetic current through the system
J_{K+}, J_{Cl-}	Electro-kinetic fluxes of K^+ and Cl^- through the system
L	Lateral size of graphene, pin-hole distance
L_m	Thickness of the membrane

L_{res}	Reservoir length in continuum modelling
L_{slit}	Length of nanoslit region (in Y-direction)
L_{sys}	Total length of the system in X-direction
N	Number of atom in MD simulation system
N_{slit}	Number of atom in the nanoslit region
$Q(x)$	Total charge in at x from the graphene surface
$S(\infty)$	Stationary permeation flow rate
S_m	Scaling law of membrane, electrophoresis enhancement inside
T	Temperature
U_{ion}	Electric potential by ions
U_{water}	Electric potential by water
U_{tot}	Electric potential by ions and water (electrolyte)
$Void_m$	Volume of the void space inside the membrane
ϵ_0	Dielectric constant of vacuum
ϵ_r	Dielectric constant of electrolyte
ϵ_w	Dielectric constant of water
ϵ_G	Dielectric constant of Graphene
κ_0	Conductivity of the bulk KCl solution ($n = n_{res}$)
κ_m	Conductivity of the membrane
κ_{sys}	Conductivity of system
λ_D	Debye Length of the electrolyte
μ_i	Electrophoresis mobility of i th ions
$\bar{\mu}_{slit}$	Mean electrophoresis mobility inside the nanoslit region
ρ	Number density of partical
ρ^*	Relative number density of particle to 1M electrolyte
σ	Surface charge density
Γ	Volumetric force for EOF by extra counter-ions
Φ_E	Electric potential
Φ_N	Nernst potential
$\Delta\Phi_{slit,E}$	Electric potential drop across the nanoslit region.
Ψ_i	Electric potential energy of i th atom by all other atoms

Table of Content

Abbreviations	i
Nomenclature	ii
Table of Content	iv
List of Figures	viii
List of Tables	xxi
Chapter 1: Introduction	1
1.1 Motivation.....	1
1.2 Objectives	4
1.3 Methods.....	5
1.3.1 Continuum numerical modelling	5
1.3.2 Molecular Dynamics (MD) simulation	5
1.4 Structure of thesis	6
Chapter 2: Background & Methodology	7
2.1 Introduction.....	7
2.2 Electric Double Layers (EDLs)	7
2.2.1 Classic disciplines (Continuum modelling)	7
2.2.2 Atomic MD insight	12
2.3 Transport 1D nanoflow	14
2.3.1 Continuum modelling	14
2.3.2 MD simulation	19
2.4 Conclusion	23

Chapter 3: MD simulation of EDLs on CCG membrane	25
3.1 Introduction	25
3.2 Methods	26
3.2.1 MD simulation Setup	26
3.1.1 Post-processing	29
3.2 Results and Discussions	30
3.2.1 Results of electrical double layer	30
3.2.2 Results of electrical double layer	37
3.3 Conclusion	44
Chapter 4: Continuum modelling of Diffusion on CCG membrane	46
4.1 Introduction	46
4.2 Microstructures of CCG membrane in experiments	48
4.3 Representative microstructures of cascading nanoslit system embedded in CCG hydrogel membranes	52
4.3.1 A two-dimension CCG structure model	52
4.3.2 Continuum simulation models	53
4.3.3 Membrane diffusivity from continuum simulations	55
4.3.4 Determining the key structure parameter via fitting experimental results	58
4.3.5 Effective length and cross-section area	61
4.4 3D model & aperiodic pin-hole arrangement	66
4.5 Conclusion	67
Chapter 5: Continuum simulation of electrophoresis on CCG membrane	69
5.1 Introduction	69
5.2 Continuum models to simulate the electrophoresis process in CCG membrane	70

5.3	Results for CCG membrane with zero surface charge.....	74
5.3.1	Ionic concentration distribution in CCG membrane.....	74
5.3.2	Electric potential and Nernst potential.....	78
5.3.3	Electro-kinetic conductivity of graphene membrane.....	84
5.4	Results for electrophoresis process in CCG membranes with surface charge....	85
5.4.1	EDLs structure	85
5.4.2	Electric potential and Nernst potential.....	90
5.4.3	Scaling law in charged graphene membrane	93
5.5	Conclusion	97
Chapter 6: MD simulation study on electro-kinetic flow in neutral Graphene hydrogel membrane		100
6.1	Introduction.....	100
6.2	Methods.....	101
6.2.1	MD simulation setup.....	101
6.2.2	Post-processing	106
6.3	Results and Discussion for neutral graphene membrane	108
6.3.1	Binary Boundary Layer (BBL) structure	108
6.3.2	Electric potential profile	120
6.3.3	Mobility in bulk solution	125
6.3.4	Electro-kinetic flow in graphene hydrogel membrane.....	126
6.4	Conclusion	131
Chapter 7: MD simulation of electro-kinetic flow on CCG membrane.....		133
7.1	Introduction.....	133
7.2	Methods.....	133

7.2.1	MD simulation setup.....	133
7.2.2	Post analysis.....	135
7.3	Results and Discussion for the charged graphene membrane.....	137
7.3.1	Binary Boundary Layers (BBLs) structure	137
7.3.2	Electric potential and Nernst potential.....	146
7.3.3	Velocity profile and ion mobility.....	150
7.3.4	Nanoslit electro-kinetic flux and Scaling law	155
7.4	Conclusion	159
Chapter 8: Conclusion.....		161
Reference		165

List of Figures

FIGURE 1.1 CLASSICAL DISCIPLINES RELATED TO NANOFLUIDICS AND SOME OF THE RELEVANT SUBJECTS STUDIED[3].....	1
FIGURE 1.2 SCHEMATIC FOR NANOFLUIDICS: (A) CONVENTIONAL 1D NANOFLOW[9] (2) CASCADING NANOFLOW IN GRAPHENE MEMBRANE[10]	2
FIGURE 1.3 THE EXPERIMENTAL CONDUCTIVITY RATIO(ENHANCEMENT) IN (A) CCG HYDROGEL AND (B) 1-D SILICA NANOCHANNEL[9]. NOTE THAT A MAXIMUM CONDUCTIVITY RATIO EMERGED ON DIFFERENT CHANNEL HEIGHT OF CCG MEMBRANE COMPARED WITH THE MONOTONICALLY INCREASE IN 1-D SILICA NANOCHANNEL.	4
FIGURE 1.4 THE STRUCTURE OF THE PRESENT THESIS	6
FIGURE 2.1 THE CLASSIC EQUILIBRIUM EDL MODELS: (A)HELMHOLTZ MODEL; (B) GOUY-CHAPMAN MODEL; (C) GOUY-CHAPMAN-STERN MODEL[29].....	8
FIGURE 2.2 CONCENTRATION PROFILE FOR SYMMETRIC ELECTROLYTE ON THE CHARGED SURFACE: (A) $z_i\Phi E > kBT$; (B) $z_i\Phi E < kBT$. $n +$ AND $n -$ REPRESENT THE CONCENTRATION OF COUNTER-IONS AND CO-IONS RESPECTIVELY[40].....	10
FIGURE 2.3 SCHEMATIC OF THE ELECTRICAL POTENTIAL DISTRIBUTION IN THE OVERLAPPED EDL FIELD BETWEEN TWO FLAT PLATES[43].	11
FIGURE 2.4 THE COMPARISON OF ION CONCENTRATION PROFILE FOR MD SIMULATION AND PB EQUATION: THE SOLID CURVES IN RED AND CL- COLOR ARE THE CONCENTRATION IN MD SIMULATION WHILE, THE DASHED LINE WITH THE SAME COLOR ARE THE RESULT BY PB EQUATION. NOTE AT LEFT AND RIGHT END ($X = 0$ OR 3.5 NM) DIFFERENT SURFACE CHARGE ARE IMPOSED.[57].....	13
FIGURE 2.5 VARIOUS LENGTH SCALES AT PLAY IN NANOFLUIDICS[1].....	14
FIGURE 2.6 THE SCHEMATIC OF 1-D NANOFLUIDICS [18] (A) PROFILES IN THE EQUILIBRIUM STATE; (B) PROFILES UNDER THE ELECTRIC POTENTIAL DIFFERENCE ($\Delta\Phi E$). AT EQUILIBRIUM, THE OVERLAP OF EDLS IN THE SMALL NANOCHANNEL ($\lambda_D > H$) INCREASED THE CONCENTRATION OF COUNTER-IONS (RED) AND DECREASED THAT OF CO-IONS (BLUE). A MENISCUS ELECTRIC POTENTIAL (GREEN) IS OBTAINED INSIDE THE NANOCHANNEL. THE MAXIMUM ELECTRIC POTENTIAL IN THE CENTRE OF NANOCHANNEL WOULD BE STILL LOWER THAN THAT OF BULK SOLUTION. AT $\Delta\Phi E$, THE ELECTRIC POTENTIAL GRADIENT WAS ESTABLISHED ACROSS THE WHOLE NANOCHANNEL. AND THE IONIC CONCENTRATIONS OF COUNTER-ION WOULD BE STILL MUCH HIGHER THAT OF CO-IONS AND EVEN HIGHER THAN THAT IN THE TWO SIDE	

RESERVOIR (N_{RES}). THUS THE COUNTER-IONS MAKE THE PREDOMINANT CONTRIBUTION TO THE TOTAL ELECTRO-KINETIC CURRENT.....	16
FIGURE 2.7 THE CONDUCTANCE OF THE DIFFERENT NANO/MICRO-CHANNEL AS A FUNCTION OF N_{RES} . THE SEPARATED DOTS ARE THE EXPERIMENTAL RESULTS AND THE CURVES ARE THE CONTINUUM MODELLING RESULTS WITH THE FITTED SURFACE CHARGE DENSITY[8].	17
FIGURE 2.8 THE SCHEMATICS OF NANOFLUIDICS DIODE[100] AND THE POTENTIAL-CURRENT CURVE[18].	18
FIGURE 2.9 THE SCHEMATICS OF NANOFLUIDIC FIELD-EFFECT TRANSISTOR AND THE POTENTIAL-CURRENT CURVE [18].	19
FIGURE 2.10 THE CONCENTRATION PROFILE FOR ROUGHLY 1M NAI (A) AND NACL SOLUTION BETWEEN NEUTRAL HYDROPHOBIC SURFACES. THE BLUE AND RED LINES INDICATE THE CONCENTRATION OF IONS; WHILE THE DOTTED LINES SHOW THE DENSITY OF WATER MOLECULES. THE VELOCITY PROFILE IN THE HYDROPHOBIC CHANNEL FOR 1M NAI. (C) AND NACL (D) SOLUTION. THE OPEN SQUIRE, CIRCLE AND TRIANGLE SYMBOLS REPRESENT THE VELOCITY PROFILE WITH DIFFERENT SURFACE CHARGE ($\Sigma = -62, 0$ AND $+62$ MC/M ² , FROM BOTTOM TO TOP)[92].	21
FIGURE 2.11 (A) WATER VELOCITY PROFILE ACROSS THE CHANNEL OBTAINED FROM MD AND CONTINUUM SIMULATIONS. (B) DRIVING FORCE FOR THE FLOW ACROSS THE CHANNEL USING THE ION CONCENTRATIONS OBTAINED FROM MD SIMULATION. THE INSET WAS THE CORRESPONDING CONCENTRATION PROFILE OF EDLS[123].	22
FIGURE 3.1 MOLECULAR SIMULATION SYSTEM INCLUDING A SINGLE LAYER GRAPHENE IMMERSED IN AQUEOUS ELECTROLYTE WITH IONIC CONCENTRATION OF 1MOL/L. THE INTERLAYER DISTANCE BETWEEN THE GRAPHENE LAYERS IS 5NM.	27
FIGURE 3.2 RELATIVE NUMBER DENSITY ρ^* OF DIFFERENT SOLUTE IONS AND WATER MOLECULES AS A FUNCTION OF DISTANCE FROM THE GRAPHENE CATHODE SURFACE WITH A CHARGE OF 0, -0.015 AND -0.041 E/C-ATOM, RESPECTIVELY. FOR CLARITY, THE DENSITY DISTRIBUTIONS OF COUNTER-IONS ARE PLOTTED ON THE OPPOSITE SIDES OF THE ‘ZERO’ RELATIVE DENSITY AXIS AS THE DASHED LINE. THE SHADED REGIONS REPRESENT THE IHL AND OHL LAYERS.	31
FIGURE 3.3 RELATIVE NUMBER DENSITY ρ^* OF DIFFERENT SOLUTE IONS AND WATER MOLECULES AS A FUNCTION OF DISTANCE FROM A GRAPHENE ANODE SURFACE WITH A CHARGE OF 0, $+0.015$ AND $+0.041$ E/C-ATOM, RESPECTIVELY. FOR CLARITY, THE DENSITY DISTRIBUTIONS OF COUNTER IONS ARE PLOTTED ON THE OPPOSITE SIDES OF THE ‘ZERO’	

RELATIVE DENSITY AXIS. THE SHADED REGIONS REPRESENT THE IHL AND OHL LAYERS.	31
FIGURE 3.4 RELATIVE NUMBER DENSITY ρ^* OF WATER MOLECULES OF NACL SOLUTION AS A FUNCTION OF DISTANCE FROM A GRAPHENE ANODE SURFACE WITH A CHARGE OF +0.041, +0.015, 0, -0.015 AND -0.041E/C-ATOM, RESPECTIVELY. FOR CLARITY, THE DENSITY DISTRIBUTIONS OF HYDROGEN ATOMS ARE PLOTTED ON THE OPPOSITE SIDES OF THE ‘ZERO’ RELATIVE DENSITY AXIS. IT HAS BEEN FOUND THERE IS NO OBVIOUS CHANGE OF WATER DISTRIBUTION BETWEEN DIFFERENT SOLUTES, THUS ONLY THE WATER DISTRIBUTIONS OF NACL SOLUTION ARE PLOTTED.	32
FIGURE 3.5 DISTANCE OF THE IHL AND OHL IONIC DENSITY PEAKS TO THE GRAPHENE CATHODE SURFACE AND RELATIVE NUMBER DENSITY OF IHL AND OHL PEAKS, SUBJECT TO AN ELECTRODE SURFACE CHARGE OF -0.015E/C OR -0.041E/C.	35
FIGURE 3.6 DISTANCE OF THE IHL AND OHL IONIC DENSITY PEAKS TO THE GRAPHENE ANODE SURFACE AND RELATIVE NUMBER DENSITY OF IHL AND OHL PEAKS, SUBJECT TO AN ELECTRODE SURFACE CHARGE OF +0.015E/C OR +0.041E/C.	35
FIGURE 3.7 THE VARIATION OF ELECTRIC POTENTIAL AS A FUNCTION OF THE DISTANCE FROM THE GRAPHENE CATHODE SURFACE FOR THE NACL AND CSCL ELECTROLYTE UNDER TWO CHARGING CASES: -0.015E/C AND -0.041E/C. THE TOTAL ELECTRICAL POTENTIAL U_{TOT} IS DECOMPOSED INTO TWO COMPONENTS: U_{ION} CALCULATED FROM THE EDL INCLUDING CATHODE SURFACE CHARGE AND THE IONIC DENSITY $\rho(X)$, AND U_{WATER} CALCULATED FROM THE WATER MOLECULAR DIPOLE.	37
FIGURE 3.8 THE VARIATION OF ELECTRIC POTENTIAL AS A FUNCTION OF THE DISTANCE FROM THE GRAPHENE ANODE SURFACE FOR THE NAF AND NAI ELECTROLYTE UNDER TWO CHARGING CASES: +0.015E/C AND +0.041E/C. THE TOTAL ELECTRICAL POTENTIAL U_{TOT} IS DECOMPOSED INTO TWO COMPONENTS: U_{ION} CALCULATED FROM THE EDL INCLUDING CATHODE SURFACE CHARGE AND THE IONIC DENSITY $\rho(X)$, AND U_{WATER} CALCULATED FROM THE WATER MOLECULAR DIPOLE.	38
FIGURE 4.1 THE STRUCTURE OF CCG: (A) THE TYPICAL SIZE OF CCG FLAKE IN AFM IMAGE[189]; (B) THE STEM IMAGE CONFIRMED THE MODELLING HYPOTHESIS WITH DEFECTS (BLUE REGION) AND OXYGEN FUNCTIONAL GROUP (RED REGION)[190]; (C) THE MD SIMULATION RESULT[191] INDICATES THE LARGE AMOUNT OF DEFECT AND FUNCTIONAL GROUPS ON CCG SHE. NOTE THAT THE SIZE OF PORE (~2NM) IS MUCH SMALLER THAN THAT OF WHOLE GRAPHENE FLAKE (~1MM) AND THE EXISTENCE OF PIN-HOLE CANNOT BE IDENTIFIED BY THE CONVENTIONAL SEM/AFM IMAGE.	48

FIGURE 4.2 SCHEMATIC VIEW OF MASS TRANSPORT THROUGH (A) PRISTINE GRAPHENE MEMBRANE AND (B) NANOPOROUS GRAPHENE MEMBRANE [195].....	49
FIGURE 4.3 THE SEM IMAGE OF THE CROSS-SECTION OF THE FREEZE-DRIED CCG MEMBRANE[35].....	50
FIGURE 4.4 THE INDIRECT MEASUREMENTS OF CCG MEMBRANE: (A) XRD SPECTRUM[35], THE GREY AND BLACK CURVES INDICATES THE SPECTRUM OF THE FREEZE-DRIED CCG AND THE HYDRATED CCG MEMBRANE, RESPECTIVELY;[35] (B) NEUTRON SCATTERING SPECTRUM[177], THE CURVES IN DIFFERENT COLOURS REPRESENT THE RESULT OF CCG WITH DIFFERENT INTERLAYER SPACING.....	51
FIGURE 4.5 THE SCHEMATICS OF THE STAGGERED MODEL IN CONTINUUM MODELLING: THE LONG DASHED SHEETS INDICATE THE POSITION OF GRAPHENE SHEET. H_G IS THE THICKNESS OF INDIVIDUAL GRAPHENE FLAKE (0.335NM).....	52
FIGURE 4.6 THE 2D CONTINUUM MODELLING SYSTEM WITH 20 LAYERS OF GRAPHENE SHEETS WITH $L = 10\text{NM}$, $H = 2\text{NM}$ AND $D = 4\text{NM}$. (A) THE SHADOW REGION REPRESENTS THE CASCADING FLOW NETWORK WITHIN GRAPHENE HYDROGEL. THE LEFT AND RIGHT END IS FIXED WITH THE CONSTANT CONCENTRATION DIFFERENCE FOR ENTRANCE (BLUE) AND EXIT (RED) RESPECTIVELY. (B) THE MESH STRUCTURE IN THE COMSOL CONTINUUM MODELLING.....	53
FIGURE 4.7 THE CONCENTRATION PROFILE OF 2D COMSOL MODELLING IN STEADY STATE WHERE $L = 10\text{NM}$, $H = 2\text{NM}$ AND $D = 2\text{NM}$	55
FIGURE 4.8 D_0/D_M AS A FUNCTION OF LATERAL SIZE (L) WITH $D = 2\text{NM}$: THE DOTS WITH DIFFERENT COLORS REPRESENT THE VARIATION OF CHANNEL HEIGHT (H) FROM 0.5 TO 12NM. THE DASHED TRENDLINES WERE BASED ON THE ESTIMATION OF EQ(4.4). THE VERTICAL DOTTED LINE LOCATES AT $H = 50\text{NM}$. NOTE THAT THE RESULT OF D_0/D_M IS MAINLY DEPENDS ON THE SIZE OF GRAPHENE FLAKE AND. FOR SMALL LATERAL SIZE ($L < 50\text{NM}$), D_0/D_M RESULT VARIES NONLINEARLY WITH LATERAL SIZE, ESPECIALLY FOR LARGE CHANNEL HEIGHT.	56
FIGURE 4.9 D_0/D_M RESULTS AGAINST THE APERTURE SIZE: (A) DIFFERENT DOTS REPRESENT DIFFERENT CHANNEL HEIGHT, WHEN $L = 50\text{NM}$; (B) DIFFERENT DOTS REPRESENT DIFFERENT LATERAL SIZE WHEN $H = 12\text{NM}$. NOTE THAT FOR CLARITY THE RESULT D_0/D_M IS NORMALIZED WITH THE CASE OF $D = 20\text{NM}$	57
FIGURE 4.10 DETERMINATION OF THE GEOMETRICAL VARIABLES L AND D THROUGH A REVERSE MONTE CARLO METHOD. THE PARAMETERS L AND D WERE FOUND TO RAPIDLY CONVERGE AFTER 10 LOOPS AS SHOWN IN THE FIGURES.....	59

FIGURE 4.11 THE COMPARISON OF D_M BETWEEN EXPERIMENT AND COMSOL MODELLING RESULT AS A FUNCTION OF CHANNEL HEIGHT H : THE ORANGE SQUARES REPRESENT THE RATIO BETWEEN THE LINEAR INTERPOLATION (D_M) OF $L = 49.760$ NM AND $D = 1.586$ NM AND THE EXPERIMENT. THE GREEN CIRCLES INDICATE THE RATIO BETWEEN COMSOL MODELLING RESULT OF $L = 50$ NM AND $D = 1.6$ NM AND THE EXPERIMENT. NOTE THAT BOTH INTERPOLATION AND COMSOL MODELLING FIT RELATIVELY WELL WITH EXPERIMENTAL DATA EXCEPT FOR THE VERY SMALL CHANNEL HEIGHT.	61
FIGURE 4.12 THE TRANSPORT THROUGH POROUS MATERIALS: (A) COMPUTER MODELLING FOR WATER FLOW IN POROUS MATERIALS[198]; (2) THE EQUIVALENT 1D MODEL. NOTE THAT THE INTUITIVE 1D MODEL IS CONSISTED BY TWO COMPONENTS: THE EFFECTIVE LENGTH, L_{EFF} AND THE EFFECTIVE CROSS-SECTION AREA, A_{EFF} . THE TRANSPORT THROUGH THE COMPLEX POROUS MATERIALS COULD BE REGARDED AS THE MASS TRANSPORT THROUGH THAT EFFECTIVE 1D CHANNEL.	62
FIGURE 4.13 THE EXAMPLE OF TIME-LAG METHODS: THE ACCUMULATION OF MASS IN PERMEATE BATH. THE DOT LINE INDICATE THE POSITION OF $Q = 0$, THE BLUE DASHED LINE IS THE ASYMPTOTE OF STEADY STATE. THE INTERSECTION WITH ZERO LINE IS LAG TIME, L_T , AND THE GRADIENT OF THE DASHED LINE IS DENOTED AS S^∞	63
FIGURE 4.14 EFFECTIVE DIFFUSION LENGTH: (A) L_{EFF} AGAINST DIFFERENT LATERAL SIZE, L , WHERE $D = 2$ NM. THE DASHED LINE INDICATES THE EQUATION OF ASYMPTOTE, $L_{EFF} = 0.5 \cdot (N-1) \cdot L$; NOTE THAT THE RESULT L_{EFF} DEVIATED FROM THE ASYMPTOTE FOR LARGE H AND SMALL L ; (B) L_{EFF} AGAINST DIFFERENT D , WHERE $L = 50$ NM.	64
FIGURE 4.15 EFFECTIVE CROSS-SECTION AREA, A_{EFF} AGAINST LATERAL SIZE (L) AT $D = 8$ NM: THE VERTICAL DASHED LINE INDICATE THE POSITION OF $L = 300$ NM. NOTE THAT WHEN LATERAL SIZE IS MUCH LARGER ($L > 300$ NM), THE RESULTS APPROACHED A CONSTANT VALUE THAT IS DETERMINED BY THE CHANNEL HEIGHT. HOWEVER FOR VERY SMALL LATERAL SIZE, THE APERTURE AREA DOMINATES THE EFFECTIVE CROSS-SECTION AND IT APPROACHES ABOUT $1.5D$	65
FIGURE 4.16 THE COMPARISON BETWEEN EXPERIMENTAL DATA AND 2D MODELLING: (A) TORTUOSITY, L_{EFF}/N ; (B) POROSITY, THE RATIO BETWEEN MEMBRANE SIZE AND EFFECTIVE CROSS-SECTION AREA, A_{EFF}/A_M , THE BLUE SQUARE, ORANGE CIRCLE REPRESENTS THE RESULT FROM EXPERIMENT, 2D MODELLING RESPECTIVELY.	66
FIGURE 5.1 THE SCHEMATIC OF ELECTROPHORESIS STUDY[177] ON CCG MEMBRANE WITH CONSTANT CURRENT PASSING THROUGH THE SYSTEM AND VOLTMETER MONITORING THE POTENTIAL DROP CROSS THE MEMBRANE.	69

FIGURE 5.2 THE SETUP OF CONTINUUM ELECTROPHORESIS MODELLING. THE 40 LAYERS GRAPHENE MEMBRANE IS SANDWICHED BY TWO 100NM-THICKNESS RESERVOIR. THE ARROW INDICATES THE DIRECTION OF EXTERNAL E-FIELD IN THE SYSTEM. THE VERTICAL BLACK THIN SHEETS INDICATE THE POSITION OF INDIVIDUAL GRAPHENE SHEETS IN MEMBRANE. THE EQUATIONS AROUND ARE THE BOUNDARY CONDITION FOR MODELLING SYSTEM.	71
FIGURE 5.3 THE MODELLING RESULT FOR ELECTROPHORESIS THROUGH THE CCG MEMBRANE WITH $N_{RES} = 0.01$ M AND $H = 4.46$ NM AND $\Delta\Phi E = 0.01$ V: (A) THE CONCENTRATION PROFILE OF K^+ ; THE DASHED RECTANGLE IS THE “CENTRE” OF MEMBRANE WHERE THE RESULT WOULD BE MAGNIFIED AND PRESENTED IN THE FOLLOWING FIGURES.	74
FIGURE 5.4 THE STRUCTURE OF DUEL EDLS WITH DIFFERENT CHANNEL HEIGHT (H), WHEN $N_{RES} = 0.1$ M, $\lambda_D = 0.96$ NM: (A) THE CHANNEL HEIGHT (6.7NM) IS MUCH LARGE THEN THE DEBYE LENGTH; (B) THE CHANNEL HEIGHT (2.2NM) IS APPROXIMATE TO $2\lambda_D$; (C) THE CHANNEL HEIGHT (1.2NM) IS MUCH SMALLER THAN $2\lambda_D$. THE BOTTOM FIGURES WERE THE SCHEMATIC OF SIMULATION RESULTS. NOTE THAT THE DATA RANGE WAS ABOUT MAX. $\pm 0.2\%$. FOR CLARITY THE CONCENTRATION FIGURES(A) WERE SHRUNKEN IN Y-AXIS BY 40%.	76
FIGURE 5.5 THE PROFILE OF BBLs AT $H = 2.6$ NM WITH DIFFERENT N_{RES} : (A) 1M; (B) 0.1M; (C) 0.01M. FOR CLARITY, THE FIGURES WERE SHRUNKEN IN Y-AXIS BY 40%.	77
FIGURE 5.6 THE ELECTRIC POTENTIAL PROFILE WHEN $N_{RES} = 0.01$ M AND $H = 4.46$ NM AND $\Delta\Phi E = 0.01$ V: (A) OVERALL; (B) 1D AVERAGE ALONG X-AXIS; THE ORANGE DASHED CURVE WOULD BE THE INITIAL ELECTRIC POTENTIAL PROFILE BEFORE THE FORMATION OF BBLs.	79
FIGURE 5.7 THE SKETCH OF “TRANSPORT PATH” IN GRAPHENE HYDROGEL MEMBRANE: THE RED DOTS IN THE MIDDLE OF MEMBRANE MARK THE TRANSPORT PATH OF IONS IN THE CASCADING FLOW. IT IS COINED AS THE “TRANSPORT PATH”.	80
FIGURE 5.8 THE POTENTIAL DROP ALONG THE “TRANSPORT PATH” WHEN $N_{RES} = 0.1$ M AND $\Delta\Phi E = 0.01$ V . THE SOLID AND DASHED LINES INDICATED ΦE AND $\Phi E + \Phi N$ RESPECTIVELY. THE CURVES WITH DIFFERENT COLOURS INDICATE THE RESULT OF DIFFERENT H FROM 0.5 TO 10 NM. THE DASHED REGION MARKS THE POSITION OF THE NANOSLIT REGION. THE SHORT VERTICAL LINES INDICATE THE POSITION OF THE APERTURE OPENING AND THE DOTTED LINE IS THE “CORNER” OF TRANSPORT PATH.....	82
FIGURE 5.9 THE FRACTION OF THE POTENTIAL DROP IN THE NANOSLIT REGION FOR DIFFERENT CHANNEL HEIGHT. THE BLACK AND RED CURVES REPRESENTED THE RESULT OF ΦE AND $\Phi E + \Phi N$ RESPECTIVELY.	83

FIGURE 5.10 THE CONDUCTANCE OF MEMBRANE AS A FUNCTION OF H AT $N_{RES} = 0.1M$. NOTE THAT TO CALCULATE THE CROSS-SECTION AREA OF MEMBRANE (A_M), THE EXTENSION OF 2D MODEL IN Z-AXIS WAS ASSUMED TO BE 1 M	84
FIGURE 5.11 THE SCALING LAW (S_M) OF THE NEUTRAL GRAPHENE MEMBRANE AGAINST THE DIFFERENT CHANNEL HEIGHT: THE DIFFERENCE SYMBOLS REPRESENT THE RESULTS WITH DIFFERENT RESERVOIR CONCENTRATION FROM 0.001M TO 1M.	85
FIGURE 5.12 THE CONCENTRATION DISTRIBUTION OF KCL SOLUTION WHEN $N_{RES} = 0.01M$, $H = 4.5NM$, $\Sigma = -2.3MC/M^2$: (A) CONCENTRATION PROFILE FOR IONS; NOTE THAT THE DASHED RECTANGULAR IS THE “CENTER” OF THE MEMBRANE; (B) CONCENTRATION PROFILE FOR IONS IN THE “CENTER” OF MEMBRANE IN EQUILIBRIUM STATE; (C) 1D CONCENTRATION PROFILE ALONG THEE DASHED LINE IN (B); (D) THE CONCENTRATE SUBTRACTION PROFILE BETWEEN $\Delta\Phi E = 0$ OR 0.01 V IN THE IN THE “CENTER” OF MEMBRANE. (E) 1D CONCENTRATION PROFILE ALONG THEE DASHED LINE IN (D); FOR CLARITY THE IMAGES IN (B)&(D) WERE RESCALED BY 40% ALONG THE Y-AXIS.....	87
FIGURE 5.13 THE CONCENTRATION PROFILE FOR DIFFERENT CHANNEL HEIGHT WITH $N_{RES} = 0.1M$, $\Sigma = -2.3MC/M^2$: (A) $H = 6.7$ NM; (B) $H = 2.2$ NM; (C) $H = 1.2$ NM; THE FIRST AND SECOND ROWS WERE THE REALLY CONCENTRATION DISTRIBUTION FOR K^+ AND Cl^- RESPECTIVELY. WHILE THE LAST TERMS IS THE CONCENTRATION SUBTRACTION PROFILE FOR K^+ . FOR CLARITY, ALL THE IMAGES WERE RESCALED BY 40% ALONG THE Y-AXIS.....	89
FIGURE 5.14 THE POTENTIAL DISTRIBUTION OF KCL SOLUTION WHEN $N_{RES} = 0.01$ M, $H = 4.46$ NM, $\Sigma = -2.3$ MC/M ² FOR (A) $\Delta U = 0.0V$; (B) $\Delta U = 0.01V$; (C) THE ELECTRIC POTENTIAL ALONG X-DIRECTION.....	91
FIGURE 5.15 THE POTENTIAL DROP ALONG THE “TRANSPORT PATH” WHEN $N_{RES} = 0.1$ M, $\Delta\Phi E = 0.01$ V AND $\Sigma = -2.3$ MC/M ² : THE SOLID AND DASHED LINES INDICATED ΦE AND $\Phi E + \Phi N$ RESPECTIVELY. THE CURVES WITH DIFFERENT COLOURS INDICATE THE RESULT OF DIFFERENT H FROM 0.5 TO 10 NM. THE SHADOW REGION MARKS THE POSITION OF THE NANOSLIT REGION. THE SHORT VERTICAL LINES INDICATE THE POSITION OF THE APERTURE OPENING AND THE DOTTED LINE IS THE “CORNER” OF “TRANSPORT PATH”..	92
FIGURE 5.16 THE SCALING LAW FOR EXPERIMENT AND MODELLING RESULT UNDER THE DIFFERENT NRES: (A) 1M; (B) 0.1M; (C) 0.01M; (D) 0.001M. THE OPEN AND SOLID CURVES REPRESENTED THE EXPERIMENTAL DATA AND MODELLING RESULT ($\Sigma = -2.3MC/M^2$), RESPECTIVELY. THE DASHED LINES MARKED THE POSITION OF UNITY ($S_M = 1$).....	94

FIGURE 5.17 THE MEAN CONCENTRATION IN THE MEMBRANE AGAINST CHANNEL HEIGHT FOR DIFFERENT N_{RES} WITH $\Sigma = -2.3 \text{ MC/M}^2$: (A) 1M; (B) 0.1M; (C) 0.01M; (D) 0.001M. THE BLACK SQUARES AND RED CIRCLES WERE THE MEAN CONCENTRATION OF IONS, WHILE THE BLUE TRIANGLES WERE “SALT” CONCENTRATION $NK + +NCl - 2$. THE DASHED LINES INDICATED THE LEVEL OF N_{RES} 96

FIGURE 6.1 MD SIMULATION SETUP FOR ELECTROPHORESIS, WHEN THE CHANNEL HEIGHT IS 30.66\AA WITH 150\AA LENGTH RESERVOIR ON EACH SIDE: (A) THE FULL CONFIGURATION OF MD SIMULATION WHERE RED, WHITE, ORANGE AND GREEN DOTS REPRESENT THE OXYGEN AND HYDROGEN ATOM ON WATER, K^+ AND Cl^- IONS RESPECTIVELY; THE GREY DOTS REPRESENT THE FROZEN GRAPHENE WALL; (B) THE FINAL STATE OF MD SIMULATION AFTER 8NS WHERE THE WATER THE MOLECULE HAS BEEN NEGLECTED. . 103

FIGURE 6.2 MD SIMULATION OF 1M KCL SOLUTION: (A) IN CUBIC PBC BOX, (B) IN 1D NANO-CHANNEL, WHEN $H = 12.8\text{\AA}$; RED, WHITE, ORANGE AND GREEN DOTS REPRESENT THE OXYGEN AND HYDROGEN ATOM ON WATER, K^+ AND Cl^- IONS RESPECTIVELY. THE DIRECTION OF EXTERNAL FIELD HAS BEEN IMPOSED ALONG THE ORANGE ARROW. 105

FIGURE 6.3 THE CONCENTRATION PROFILE (1M) FOR K^+ CATION (A) AND Cl^- ANION (B) WHERE $H = 22.11\text{\AA}$ AND $E = 0.01\text{V/\AA}$. THE SOLID GREEN LINES REPRESENT THE POSITION OF GRAPHENE SHEET AND THE SOLID RED LINES ARE JUST GUIDELINE LINE. THUS THE RECTANGULAR REGIONS SURROUNDED BY DOUBLE RED AND THE GREEN LINES INDICATED THE NANOSLIT REGION IN DISCUSSION. NOTE THAT A CLEARLY IONS SEPARATION, BBLS EMERGED ON THIS ELECTROPHORESIS STUDY. 109

FIGURE 6.4 THE CONCENTRATION PROFILE (1M) FOR K^+ CATION (A) AND Cl^- ANION (B) WHERE $H = 22.11\text{\AA}$ AND NO EXTERNAL E-FIELD. THE SOLID GREEN LINES REPRESENTED THE POSITION OF GRAPHENE SHEET AND THE SOLID RED LINES ARE JUST GUIDELINE LINE. 109

FIGURE 6.5 THE RELATIVE DENSITY PROFILE (1G/CM^3) FOR WATER MOLECULE: (A) OXYGEN ATOM AND (B) HYDROGEN ATOM, WHERE $H = 22.11\text{\AA}$ AND $E = 0.01\text{V/\AA}$. NOTE THAT THE LAYERED STRUCTURES APPEARED ON GRAPHENE SHEET SURFACE DUE TO THE VAN DER WAALS INTERACTION BETWEEN WATER AND GRAPHENE AND THE BREAKDOWN OF CONTINUOUS HYDROGEN BOND NETWORK. 110

FIGURE 6.6 THE 1D-CONCENTRATION PROFILE FOR KCL SOLUTION IN GRAPHENE HYDROGEL MEMBRANE WITH $H = 22.11\text{\AA}$: (A) IONIC CONCENTRATION WITH EXTERNAL E-FIELD (0.01V/\AA) AND (B) IONIC CONCENTRATION WITHOUT EXTERNAL E-FIELD; THE SOLID ORANGE AND BLUE LINES REPRESENT THE CONCENTRATION OF K^+ AND Cl^- IN THE

UNITS OF MOL/L; THE HORIZONTAL DOT LINE REPRESENTS THE CONCENTRATION OF 1M AND TWO VERTICAL DASHED LINES REPRESENT THE POSITION OF GRAPHENE SHEET (C) RELATIVE WATER DENSITY WITH BULK SOLUTION (1G/CM ³) WITH (SOLID) AND WITHOUT EXTERNAL E-FIELD (GREY DOT). NOTE THAT ONLY THE NANOSLIT REGIONS IN FIGURE 6.1 WERE AVERAGED CROSS THE Y-Z PLANE TO OBTAIN THE CURVES IN THIS FIGURE, NAMELY EXCLUDING THE APERTURE REGION.	111
FIGURE 6.7 THE CONCENTRATION OF IONS WITHIN HELMHOLTZ LAYERS (<0.6 Å) AT DIFFERENT CHANNEL HEIGHT (A) 30.66 Å; (B) 17.50 Å; (C) 12.80 Å. NOTE THAT THE ORIGIN AND GREEN LINES REPRESENT THE RESULT OF K ⁺ AND CL ⁻ RESPECTIVELY AND THE SOLID AND DASHED ONE IS THE CONDITION WITH AND WITHOUT THE EXTERNAL E-FIELD.	114
FIGURE 6.8 THE 1D CONCENTRATION PROFILE FOR KCL SOLUTION IN NANOSLIT REGION WITH DIFFERENT CHANNEL HEIGHT FROM 30.66 Å TO 6.99 Å. THE CORRESPONDING CONCENTRATION DISTRIBUTION WITHOUT THE EXTERNAL E-FIELD WAS PLOTTED AS THE BOTTOM PART. THE SOLID ORANGE AND GREEN LINES REPRESENT THE CONCENTRATION DISTRIBUTION OF K ⁺ AND CL ⁻ IN GRAPHENE HYDROGEL MEMBRANE. WHILE THE RED AND BLACK LINE INDICATED THE DENSITY OF OXYGEN AND HYDROGEN ATOMS VS 1G/CM ³ WATER. FOR COMPARISON, THE IONIC CONCENTRATION PROFILE OF 1M KCL SOLUTION IN 1D NANOCHANNEL WITH THE SAME SLIT HEIGHT IS PLOTTED AS THE DASHED CURVE. THE GREEN DOT CIRCLE INDICATED THE SIZE OF IONS AND THE DASHED BLACK CIRCLE INDICATED THE DIMENSION OF SURROUNDING HYDRATION SHELL.	114
FIGURE 6.9 THE CONCENTRATION PROFILE OF K ⁺ IN APERTURE REGION FOR GRAPHENE HYDROGEL UNDER THE EXTERNAL E-FIELD: (A) $H = 17.50\text{\AA}$; (B) $H = 12.80\text{\AA}$; (C) $H = 8.12\text{\AA}$; (D&E) SCHEMATIC FOR TRANSPORT PROCESS IN NANOCHANNEL, WHERE $H \approx D_H$ IN (D) AND $H < D_H$ IN (E). D_H IS THE DIAMETER OF IONS' HYDRATION SHELL. THE DASHED GREEN LINE INDICATES THE POSITION OF IONIC PLANE (CONCENTRATION PEAKS IN (A~C)). NOTE THAT THE MISMATCH OF THE IONIC PLANE IN (E) BY DEHYDRATION PROCESS. (F) THE CALCULATION HYDRATION NUMBER OF K ⁺ WITHIN THE APERTURE AND THE NANOSLIT REGION. NOTE THAT THE SHADOWED REGION IS MARKED AS THE APERTURE REGION. AND THE HORIZONTAL GREEN LINE PRESENTS THE HYDRATION NUMBER IN THE BULK SOLUTION.	118
FIGURE 6.10 THE ELECTRIC POTENTIAL OF OXYGEN ATOM WHERE $H = 22.11\text{\AA}$ AND $E = 0.01\text{V/\AA}$: (A) THE CONTOUR PLOT OF NET ELECTRIC POTENTIAL AFTER SMOOTH; (C) THE INNER	

ELECTRIC POTENTIAL BY ELECTROLYTE ITSELF. THE GREEN LINE REPRESENTS THE POSITION OF GRAPHENE WALL AND THE CYCLE DASHED LINES INDICATE THE “DIFFUSION” PATH TO EVALUATE THE POTENTIAL DROP IN THE CASCADING ELECTRO-KINETIC FLOW.	121
FIGURE 6.11 THE AVERAGE ELECTRIC POTENTIALS OF DIFFERENT KIND ALONG THE X-DIRECTION WITH $H = 20.11\text{\AA}$ AND $E = 0.01\text{V/\AA}$: THE DASHED YELLOW LINE INDICATES THE DISTRIBUTION OF INNER ELECTROLYTE POTENTIAL BY SOLUTION ITSELF WITH ZERO POTENTIAL ON EACH SIDE; THE DOT BLUE LINE INDICATES THE POTENTIAL BY EXTERNAL ELECTRIC FIELD; THE SOLID GREEN LINES WITH DIFFERENT COLOUR ARE NET ELECTRIC POTENTIAL ON DIFFERENT TYPE OF ATOMS. THE VERTICAL DASHED BLUE LINES SHOW POSITION OF GRAPHENE WALL. NOTE THAT THE BOUNDARY LAYERS ON GRAPHENE SHEET SURFACE INDUCES THE SIGNIFICANTLY VIBRATION OF ELECTRIC POTENTIAL.	123
FIGURE 6.12 THE POTENTIAL DISTRIBUTION ALONG THE “TRANSPORT PATH” IN FIGURE 6.11. THE LABELS ON THE RIGHT MARK THE CORRESPONDING SLIT HEIGHT AND THE POSITION OF TWO VERTICAL DOT LINES INDICATE THE ENTRANCE AND EXIT OF NANOSLIT REGION IN THAT PATH. THE SHORT VERTICAL LINES ON EACH CURVE INDICATE THE POSITION OF ENTRANCE AND EXIT APERTURE. BOTH THE POSITION AND POTENTIAL IN EACH CASE HAS BEEN SHIFTED FOR CLARITY. NOTE THAT THE POTENTIAL DROP IN THE NANOSLIT REGION IS ALMOST LINEARLY, WHILE ON THE TWO SIDE APERTURE REGION, A SIGNIFICANT POTENTIAL DROP OCCURS WITH THE CONSIDERABLE LARGE OR SMALL SLIT HEIGHT.	124
FIGURE 6.13 THE MEAN VELOCITY OF IONS IN 1M BULK KCL SOLUTION UNDER THE DIFFERENT E-FIELD STRENGTH. THE ORANGE AND GREEN CURVE REPRESENTS THE RESULT OF K^+ AND CL^- RESPECTIVELY. AND THE DASHED LINE WITH THE SAME COLOUR INDICATED THE SLOPE FITTING OF LINEARLY REGION, NAMELY THE MOBILITY.	126
FIGURE 6.14 THE VELOCITY (MOBILITY) OF IONS ALONG THE Y-DIRECTION IN THE NANOSLIT REGION OR 1-D NANOCHANNEL (TOP) AND THE VELOCITY OF WATER IN NANOSLIT REGION OR 1-D NANOCHANNEL (BOTTOM). THE SOLID ORANGE AND GREEN LINES REPRESENT THE MEAN VELOCITY PROFILE OF K^+ AND CL^- IN SLIT REGION. WHILE THE DASHED LINE WITH THE SAME COLOUR INDICATED THE VELOCITY PROFILE OF IONS IN 1-D NANOCHANNEL. THE RED AND DASHED BLACK LINES INDICATE THE VELOCITY PROFILE OF WATER MOLECULE (OXYGEN ATOM) IN NANOSLIT REGION AND IN 1-D NANOCHANNEL, RESPECTIVELY. NOTE THAT THE VELOCITY PROFILES WAS DIVIDED BY	

THE DRIVING FORCE OF E-FIELD: E_{slit} IN NANOSLIT REGION OR $E = 0.01V/\text{\AA}$ IN 1-D NANOCANNEL.....	127
FIGURE 6.15 THE MEAN MOBILITY VS DIFFERENT GRAPHENE CHANNEL HEIGHT: (A) FOR K^+ AND (B) Cl^- IN NANOSLIT REGION (SOLID LINE) AND 1-D NANOCANNEL (DASHED LINE). AND THE DOTTED HORIZONTAL LINE MARKS THE MOBILITY OF IONS IN BULK SOLUTION. NOTE THAT THE MOBILITY OF IONS DROPS WITH CHANNEL HEIGHT; HOWEVER AT LARGER CHANNEL HEIGHT THE RESULT IS EVEN HIGHER THAN THAT OF BULK SOLUTION.	130
FIGURE 7.1 MD SIMULATION SETUP FOR ELECTROPHORESIS, WHERE $H = 30.66\text{\AA}$ WITH 150\AA THICKNESS RESERVOIR ON EACH SIDE AND $\Sigma = -60.33 \text{ MC/M}^2$. THE FINAL STATE OF MD SIMULATION AFTER 12NS WHERE ORANGE AND GREEN DOTS REPRESENT THE K^+ AND Cl^- IONS RESPECTIVELY, THE WATER MOLECULE WAS NEGLECTED FOR CLARIFY. NOTE THAT DUE TO THE HIGH SURFACE CHARGE DENSITY ON GRAPHENE SHEET, THE NUMBER OF CATION IS MUCH LARGER THAN THAT OF THE ANION, HOWEVER THE STRONG EXTERNAL E-FIELD (ORANGE ARROW) STILL INDUCE A CONSIDERABLE SEPARATION OF CATION AND ANION IN THE NANOSLIT REGION.	134
FIGURE 7.2 IS THE SCHEMATIC OF EXTRA COMSOL MODELLING SETUP FOR DIFFUSIVITY DROP.	136
FIGURE 7.3 THE CONCENTRATION PROFILE (1M) FOR K^+ CATION (A) AND Cl^- ANION (B) WHERE $H = 22.11\text{\AA}$, $E = 0.01V/\text{\AA}$, $\Sigma = -60.33\text{MC/M}^2$. THE SOLID GREEN LINES REPRESENTED THE POSITION OF GRAPHENE SHEET AND THE SOLID RED LINES ARE JUST GUIDELINE LINE. THUS THE RECTANGULAR REGIONS SURROUNDED BY RED AND THE GREEN LINES INDICATE THE NANOSLIT REGIONS IN THE DISCUSSION. NOTE THAT THE HIGH SURFACE CHARGE DENSITY ON GRAPHENE HAS REPELLED THE CO-IONS FROM THE NANOSLIT REGION.	138
FIGURE 7.4 THE CONCENTRATION PROFILE (1M) FOR K^+ CATION (A) AND Cl^- ANION (B) WHERE $H = 22.11\text{\AA}$, $E = 0.0V/\text{\AA}$, $\Sigma = -60.33\text{MC/M}^2$. NOTE THAT THE EDLS FORMED ON THE GRAPHENE SURFACE.	138
FIGURE 7.5 THE RELATIVE DENSITY PROFILE FOR WATER MOLECULE VS BULK WATER ($1G/CM^3$): (A) OXYGEN ATOM AND (B) HYDROGEN ATOM, WHERE $H = 22.11\text{\AA}$, $E = 0.0V/\text{\AA}$ AND $\Sigma = -60.33\text{MC/M}^2$. NOTE THAT THE POINT CHARGE HYDROGEN ATOMS HAVE BEEN SIGNIFICANTLY ABSORBED ONTO THE GRAPHENE SURFACE THAT SHIFT THE ORIENTATION OF WATER MOLECULE IN THE FIRST WATER LAYER AND CONSIDERABLY INCREASE THE CONCENTRATION ON GRAPHENE SURFACE.....	139

FIGURE 7.6 THE 1D CONCENTRATION PROFILE FOR KCL SOLUTION IN NANOSLIT REGION WITH DIFFERENT CHANNEL HEIGHT FROM 30.66 Å TO 6.99 Å WITH (TOP) AND WITHOUT (BOTTOM) THE EXTERNAL E-FIELD. THE ORANGE AND GREEN LINES REPRESENT THE CONCENTRATION DISTRIBUTION OF K⁺ AND CL⁻, WHILE RED AND BLACK LINES REPRESENTED THE RELATIVE DENSITY (1M BULK SOLUTION) OF OXYGEN AND HYDROGEN ATOMS. NOTE THAT THE CONCENTRATION PROFILE OF ION AT $H = 6.99\text{Å}$ WAS RESCALED BY 0.5 TO PRESENT THE RESULT CLEARLY..... 141

FIGURE 7.7 THE K⁺ CONCENTRATION PROFILE IN APERTURE REGION FOR DIFFERENT CHANNEL HEIGHT (H) WITH (BOTTOM) AND WITHOUT (TOP) THE EXTERNAL E-FIELD: (A) $H = 17.50\text{Å}$; (B) $H = 12.80\text{Å}$; (C) $H = 8.12\text{Å}$. NOTE THAT OWING TO THE HIGH SURFACE CHARGE DENSITY ON GRAPHENE SHEET, THE CO-IONS (CL⁻) HAS BEEN CONSIDERABLY EXCLUDED FROM THE MEMBRANE AT SMALL CHANNEL HEIGHT. THUS ONLY THE CONCENTRATION OF K⁺ WAS PLOTTED..... 144

FIGURE 7.8 THE ELECTRIC POTENTIAL OF OXYGEN ATOM WHERE $H = 22.11\text{Å}$, $E = 0.01\text{V/Å}$ AND $\Sigma = -60.33\text{MC/M}^2$: (A) THE CONTOUR PLOT OF NET ELECTRIC POTENTIAL AFTER SMOOTH; (B) THE INNER ELECTRIC POTENTIAL BY ELECTROLYTE ITSELF. THE GREEN LINE REPRESENTS THE POSITION OF GRAPHENE WALL AND THE CYCLE DASHED LINES INDICATE THE “TRANSPORT PATH” TO EVALUATE THE POTENTIAL DROP IN THE CASCADING ELECTRO-KINETIC FLOW..... 147

FIGURE 7.9 THE AVERAGE ELECTRIC POTENTIAL OF DIFFERENT IONS ALONG THE X-DIRECTION WITH $H = 20.11\text{Å}$ AND $E = 0.01\text{V/Å}$ AND $\Sigma = -60.33\text{MC/M}^2$. THE DASHED ORANGE LINE INDICATED THE DISTRIBUTION OF INNER ELECTRIC POTENTIAL BY SOLUTION ITSELF WITH ZERO POTENTIAL ON EACH END. THE BLUE DOT LINE INDICATES THE POTENTIAL BY EXTERNAL ELECTRIC FIELD AND THE SOLID GREEN CURVES WITH DIFFERENT COLOUR WERE NET ELECTRIC POTENTIAL ON DIFFERENT TYPE OF ATOMS. THE VERTICAL DASHED BLUE LINES MARKED THE POSITION OF GRAPHENE WALL..... 148

FIGURE 7.10 THE POTENTIAL DISTRIBUTION ALONG THE “TRANSPORT PATH”: THE SOLID CURVES WITH DIFFERENT COLOUR WERE ΦE FOR DIFFERENT H , WHILE THE OVERLAPPED BLACK DOTTED CURVES WERE THE POTENTIAL OF $\Phi E + \Phi N$ FOR THE SAME H . THE LABELS ON THE RIGHT SHOWN THE CORRESPONDING H FOR EACH CURVED. THE SHADOWED REGION MARKED THE POSITIONS OF THE NANOSLIT REGION. THE SHORT VERTICAL LINES IN EACH CURVES INDICATED THE LOCATION OF THE APERTURE OPENING..... 150

FIGURE 7.11 THE MOBILITY PROFILE OF ELECTROLYTE ALONG THE GRAPHENE SHEET IN THE NANOSLIT REGION. THE SOLID ORANGE, GREEN AND RED LINES REPRESENT THE DISTRIBUTION OF MEAN VELOCITY FOR K^+ , Cl^- AND WATER RESPECTIVELY. THE HORIZONTAL ORANGE AND BLUE DOTTED LINES REPRESENT THE MOBILITY OF K^+ AND Cl^- IN BULK SOLUTION.	152
FIGURE 7.12 THE MEAN MOBILITY NANOSLIT REGION AS A FUNCTION OF DIFFERENT CHANNEL HEIGHT: THE CYCLE ORANGE AND SQUARE GREEN LINES INDICATED THE CALCULATED MOBILITY OF K^+ AND Cl^- RESPECTIVELY. THE DASHED LINES WITH THE SAME COLOURS WERE THE RESULTS FOR K^+ AND Cl^- IN THE NEUTRAL GRAPHENE MEMBRANE.	153
FIGURE 7.13 THE MEAN “MOBILITY” OF WATER MOLECULE BY EOF IN THE NANOSLIT REGION IN THE CHARGED GRAPHENE MEMBRANE.	155
FIGURE 7.14 THE ELECTRO-KINETIC FLUX OF IONS IN NANOSLIT REGION FOR DIFFERENT CHANNEL HEIGHT: (TOP) IN CHARGE GRAPHENE HYDROGEL MEMBRANE; (BOTTOM) IN NEUTRAL GRAPHENE HYDROGEL MEMBRANE AND 1-D NANOCHANNEL (DASHED LINE). THE RESULTS OF K^+ AND Cl^- WERE COLOURED AS ORANGE AND GREEN LINES RESPECTIVELY. NOTE THAT THE RESULT IN THE CHARGE MEMBRANE WITH $H = 6.99\text{\AA}$ HAVE BEEN SCALED BY 0.5 TO PRESENT THE RESULT CLEARLY.....	156
FIGURE 7.15 THE SCALING LAW FOR THE CASCADING ELECTRO-KINETIC FLOW IN THE NEUTRAL (RED) AND CHARGED (BLACK) MEMBRANE. THE INSET: THE EXPERIMENT S_M FOR $N_{RES} = 1E-3\text{ M}$	158

List of Tables

TABLE 3.1 PARTICLE NUMBERS OF THE M+X- AQUEOUS SOLUTION IN THE SIMULATION BOX FOR DIFFERENT CHARGES IN THE GRAPHENE ELECTRODES	28
TABLE 3.2 FORCE FIELD PARAMETERS FOR THE ELECTROLYTE IONS AND THE TIP3P WATER MODEL	29
TABLE 3.3 SPECIFIC CAPACITANCE OF A GRAPHENE CATHODE IMMERSSED IN DIFFERENT ELECTROLYTES, WITH A SURFACE CHARGE OF $-0.015\text{E}/\text{CARBON}$ OR $-0.041\text{E}/\text{CARBON}$	39
TABLE 3.4 SPECIFIC CAPACITANCE OF A GRAPHENE ANODE IMMERSSED IN DIFFERENT ELECTROLYTE, WITH A SURFACE CHARGE OF $0.015\text{E}/\text{CARBON}$ AND $0.041\text{E}/\text{CARBON}$	39
TABLE 3.5 THE ELECTRIC POTENTIAL DROP (IN UNIT OF V) IN INNER HELMHOLTZ LAYER, OUTER HELMHOLTZ LAYER AND THE DIFFUSION LAYER NEXT TO A GRAPHENE CATHODE WITH A CHARGE OF $\pm 0.015\text{E}/\text{C-ATOM}$ OR $\pm 0.041\text{E}/\text{C-ATOM}$	41
TABLE 3.6 THE ELECTRIC POTENTIAL DROP (IN UNIT OF V) IN INNER HELMHOLTZ LAYER, OUTER HELMHOLTZ LAYER AND THE DIFFUSION LAYER NEXT TO A GRAPHENE ANODE WITH A CHARGE OF $\pm 0.015\text{E}/\text{C-ATOM}$ OR $\pm 0.041\text{E}/\text{C-ATOM}$	42
TABLE 6.1 PARTICLE NUMBER OF KCL SOLUTION IN SIMULATION BOX FOR DIFFERENT CHANNEL HEIGHT.....	102
TABLE 6.2 THE MD SIMULATION SETUP OF 1-D NANOCHANNEL WITH DIFFERENT CHANNEL HEIGHT	105
TABLE 7.1 PARTICLE NUMBER OF KCL SOLUTION IN SIMULATION BOX FOR DIFFERENT CHANNEL HEIGHT.....	135

Chapter 1: Introduction

1.1 Motivation

The emergent nanofluidics is defined as the investigation of behavior and manipulation the fluid transport under the nanoscale confinement of the channel geometry ($< 10^2$ nm)[1]. Owing to the increasingly sophisticated nano-machining and probe technology, the mysterious and splendid phenomena behind this unfamiliar territory is gradually revealed. It has been found that under the nanoconfinement, the property of fluid would be influence by a broad spectrum of nanometric forces (e.g. van der Waals force, capillary force, Debye length), giving the unattainable phenomena for the microfluidics (10^2 nm $< h < 1$ mm) or millifluidics ($h > 1$ mm)[2].

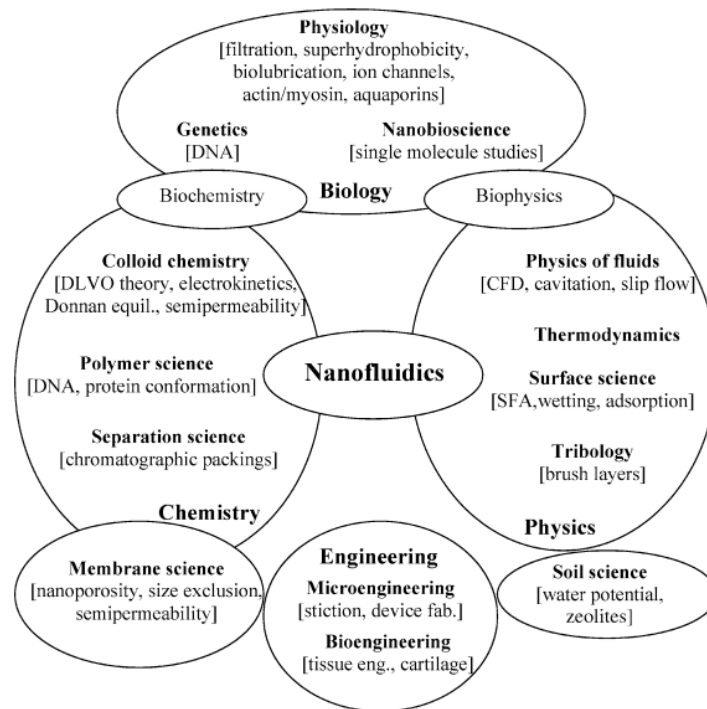


Figure 1.1 Classical disciplines related to nanofluidics and some of the relevant subjects studied[3]

The study of the nanofluidics is undoubtedly closely related to the classic principles (Figure 1.1) [3, 4]. Some of the phenomena in nanofluidics were stimulated studies for many years. Especially for the discovery in the physiology domain, the biological activities involving the transport of nanoscale pore in the protein (i.e. aquaporin's, ionic pump and

kidney osmotic filtering) has been ultimately optimized through the evolution, showing the exotic behaviors of transport[5-7]. The nanofluidics study could not only provide a fundamental understanding of mass transport, but also be beneficial to the applications of the relative subjects such as, high performance supercapacitor, nano-pipette, water desalination, smart biosensor and drug delivery[1-3].

Generally, the nanofluidics study was based on a nano-machined lab-on-a-chip device[8, 9]: the reservoirs are connected via a specially designed nanochannel and the mass transport through the nanochannel under the different driving force (Figure 1.2a[9]). By tuning the interaction between the channel wall and the fluid, the various novel phenomena and the applications have been demonstrated.

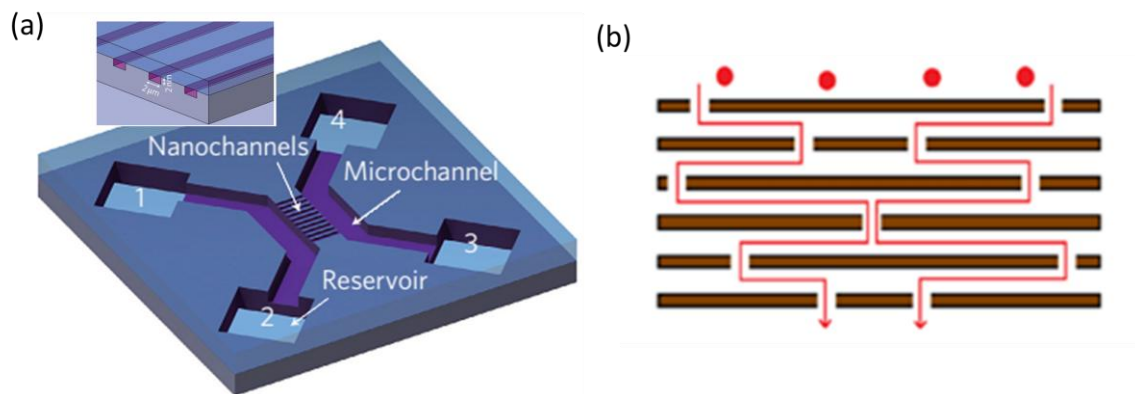


Figure 1.2 schematic for nanofluidics: (a) conventional 1D nanoflow[9] (2) cascading nanoflow in graphene membrane[10]

Although the understanding of the nanofluidics has been boosted with the development of nano-machining technology, the application of the novel discovery in nanoscale is still hindered by the sophisticated and expensive manufacture process[11]. Thus, the novel nanomaterials (e.g. graphene or CNT) are proposed as the promising candidature for the massive application among the community[2].

In experiment, the Graphene Oxide (GO) membrane has been demonstrated to be a promising membrane for liquid and gas separation with a high permeability and selectivity[12-16]. Owing to the single atom thickness of graphene or GO sheet, the ultrathin GO or Graphene membranes could be synthesized together with the ease of the controlling

interlayer slit sizes for precise molecular sieving. Thus, it attracted much effort to explore the applications of GO or graphene membrane.

With the boost of graphene membrane study, numerous novel phenomena have been reported. However, the underlying physical mechanisms remain elusive. There is still a lack of an in-depth understanding of the mass transport through the membrane. It may attribute to the two reasons: Firstly, the complex 3D microstructure of graphene membrane is still unknown, which cannot be directly determined using the conventional methods. Secondly, a novel cascading mass transport arises inside the membrane that has not been accounted in the previous 1-D nanochannel study.

As shown in Figure 1.2b[10], the graphene membranes are assembled from the individual single-atom-thickness Chemical Converted Graphene (CCG) or GO sheets, forming a staggered laminar layer-by-layer microstructure. The fluid is confined within the nanoslit regions between the adjacent layers of graphene sheets and passes through the impermeable graphene sheets via the edges of nanogaps or the in-plane defects of pin holes (i.e., cascading mass transport)

For the conventional 1-D nanofluidics, the driving force is tangent along the channel wall. Thus the mass transport can be largely understood by studying the velocity profile and molecular distributions at its cross-sections. However, the driving force of the cascading nanoflow inside the membrane is normal to the sheet wall. The molecular transport will follow a tortuous pathway and repeatedly encounter the nanoslit and aperture regions. Such complexity cannot be handled by conventional methodology. More important, such a drastic difference must implicate unique phenomena and manipulate mechanisms in graphene membrane that cannot be realized in the conventional 1-D nanofluidics.

Our group, as a world leading group in the graphene membrane field, focuses on the experiment study of ions transport driven by concentration difference (i.e., diffusion) and an external electric field (i.e., electro-kinetics) through the CCG membranes. Interesting phenomena have been discovered but are not understood yet.

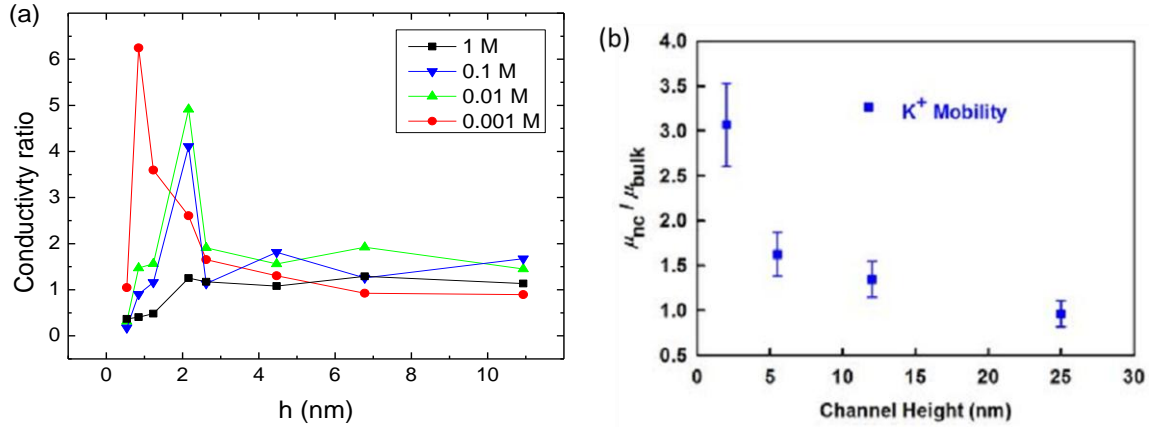


Figure 1.3 The experimental conductivity ratio(enhancement) in (a) CCG hydrogel and (b) 1-D silica nanochannel[9]. Note that a maximum conductivity ratio emerged on different channel height of CCG membrane compared with the monotonically increase in 1-D silica nanochannel.

Thus, my Ph.D. project is proposed to reveal the nanoscale molecular transport phenomena inside the CCG membranes by combining theoretical works (simulations) with my colleagues' experimental results. Our theoretical works should share the same fundamental physical principles to the previous nanofluidics studies for 1-D nanochannels. But the insights for the emergent cascading nanoflow are still a virgin territory to conquer. We will use two types of simulation methods that are widely adopted in the nanofluidics field, i.e., continuum modelling and Molecular Dynamics (MD) simulation. In this thesis, the comprehensive knowledge to understand the novel phenomena in our experiments will be obtained.

1.2 Objectives

Inspired by our experiment results, two objectives are proposed in this Ph.D. research:

1) To statistically and quantitatively represent the microstructure of graphene hydrogel membrane by combining the experimental and the simulation results. This will lay the ground to reveal the influence of the microstructure to the diffusion process.

2) To provide a general insight into the unique cascading electro-kinetic nanoflow inside the membrane; to investigate the effects of several important physical factors (e.g. channel height, ionic concentration and surface charge density) on the performance of electro-kinetic nanoflow, especially for the very small nanochannel ($h < 1$ nm)

1.3 Methods

Two types of the simulation methods are proposed for the cascading nanofluidics study: 1) continuum numeric modelling and 2) atomistic MD simulation. Both of them have been extensively employed for the conventional 1D nanofluidics study from the different aspects. Thus in the present thesis, both the continuum modelling and the MD simulation are taken to obtain a compressive understanding for different channel height ($h = 0.5\sim 10\text{nm}$)

1.3.1 Continuum numerical modelling

In the continuum modelling, the behavior of materials is modeled as a continuous field rather than the individual particles. The continuum modelling used for mass transport is set up within the classic thermodynamics framework. Using the governing equations together with the appropriate (reasonable) boundary conditions, the continuum modelling is able to accurately reproduce the property of fluids and ions at macroscale and microscale. [17].

The continuum modelling is favourable for its high accuracy and low computational cost. It could provide a large amount of result for different microstructure of the graphene membrane. Although the continuum modelling has been successfully employed in the microfluidics study (confinement $> 1\ \mu\text{m}$), the limitation of the continuum modelling is still in debated. The validation of continuum modelling in nanoscale ($< 2\ \text{nm}$) is still yet to be answered[1, 2, 18].

1.3.2 Molecular Dynamics (MD) simulation

Conversely, the atomistic Molecular Dynamics (MD) simulation deals with the individual atoms. The interactions among the atoms, e.g., bonded interactions (covalent bond, coordination bond, etc.) and the non-bonded interactions (van der Waals, Columbic interactions, etc), are described by using some empirical math functions (so called force field model). The parameters in the force field models should be empirically fitted from experimental results or ab initio calculations.

The MD simulations can provide much detailed information at the atomistic scale. It is particularly crucial for nanofluidics study considering that the channel/site size is comparable

with the size of molecules and atoms. But the computational cost of MD simulation is relatively high. In practice, statistical ensemble of the information at atomic scale should be performed to obtain physical quantities that can be measured or detected in experiments. It will take relatively long simulation time to provide a good statistical average. It is much more time demanding than continuum modelling[17, 19].

1.4 Structure of thesis

Figure 1.4 summarizes the structure of this thesis. In Chapter 1&2, we provide an introduction and literature review on the prior theoretical studies on the nanofluidics. In Chapter 3, we present our studies of the electrical double layers (EDLs) on graphene sheet surface, which is a fundamental topic of the nanofluidics study. In Chapter 4 we study the ion diffusion through the staggered graphene membrane using continuum simulation/modelling. Combining experimental results and simulation results, for the first time, we provide a quantitative representative microstructure of the graphene membranes. In Chapter 5, we use continuum simulations to study the electro-kinetic nanoflow through the graphene membrane. Chapter 6&7 will present our MD simulations for the electro-kinetic ion transport in graphene membranes. Through a comprehensive comparison, some critical physical factors that are missed in continuum modelling are revealed. In the end, we will use our simulation results to explain the observed abnormal phenomena in experiments.

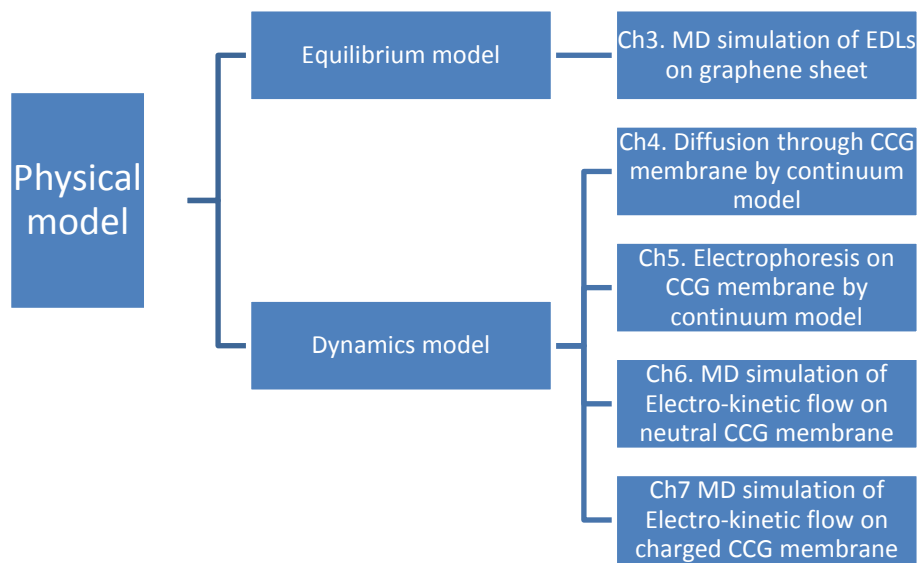


Figure 1.4 The structure of the present thesis

Chapter 2: Background & Methodology

2.1 Introduction

In the past decades, the anomalous phenomena of nanofluidics in the experiment have been investigated in the theoretical field[2, 17, 20-22]. Although the basic principle of the nanofluidics has been established, the prior study for the conventional 1-D nanochannel cannot provide a straight-forward understanding for the emergent cascading nanoflow in the graphene membrane. Hence, in the present chapter, we will review the basic principle and the discovery for the 1-D nanofluidics field which would be great reference for the development of the cascading nanofluidics.

The content of the present Chapter is consisted by two terms: The equilibrium Electric Double Layers (EDLs) and the Dynamic nanoflow. As mentioned before, the properties of the fluid confined within the nanochannel would be significantly different from that of the bulk solution. The anomalous properties originate from the abnormal mass distribution on the liquid/solid interface, referred as EDLs[1, 2]. Only with the formation of EDLs, the fluid prompted by the various driving force (e.g. chemical potential[23], electric potential[9, 24] concentration[25, 26] or even gravity[27]) would behavior the anomalous performance. Thus, this presented Chapter will firstly review the EDLs (Sec.2.1) then followed by the response of EDLs under the driving force (1-D Nanoflow in Sec.2.2). Moreover, the theoretical work under the classis continuum framework and the atomic MD simulation would be presented separately in both sections.

2.2 Electric Double Layers (EDLs)

2.2.1 Classic disciplines (Continuum modelling)

Since the proposal of nanofluidics, it is indebted to the development of the classic disciplines. The anomalous electrolyte/solid interface, also the essential of nanofluidics has been recognized for hundreds of years. Helmholtz firstly proposed the counter-ions would be absorbed onto the solid surface by surface charge that formed a dense electrolyte layer on the solid wall surface[28].

The concept of “electric double layers” (Figure 2.1a[29]) was introduced to describe the double layers of electric charge: one for the charge on the solid surface and another for the dense layer of counter-ions (Helmholtz Layer, HL). Actually it formed a parallel plate’s capacitor with separation distance of d and the linearly electric potential drop ($\Delta\Phi_E$). The areal capacitance (F/cm^2) would be calculated as[29-31]:

$$C = \frac{\varepsilon_0 \varepsilon_r}{d_{HL}} \quad (2.1)$$

Where ε_0 and ε_r is the permittivity of vacuum and the relative permittivity of the electrolyte respectively. Obviously, the areal capacitance of the EDLs would be significantly high owing to the extremely close of the two layers (small d_{HL}).

Thus the novel supercapacitor study was prompted by the higher areal EDLs capacitance and surface area. The porous conductive materials (e.g. amorphous carbon or activated carbon) are employed as the electrode materials with ultrahigh surface area (1000~3500 m^2/g)[29]. Owing to the higher specific surface area and good conductivity, the CCG hydrogel membrane has been demonstrated to be an excellent electrode material in the supercapacitor[32-34] with the comparable energy density to the Li-battery ($\sim 150 \text{ Wh/kg}$)[35] and the superior volumetric density ($\sim 60 \text{ Wh/L}$) among the porous carbonaceous electrode[36].

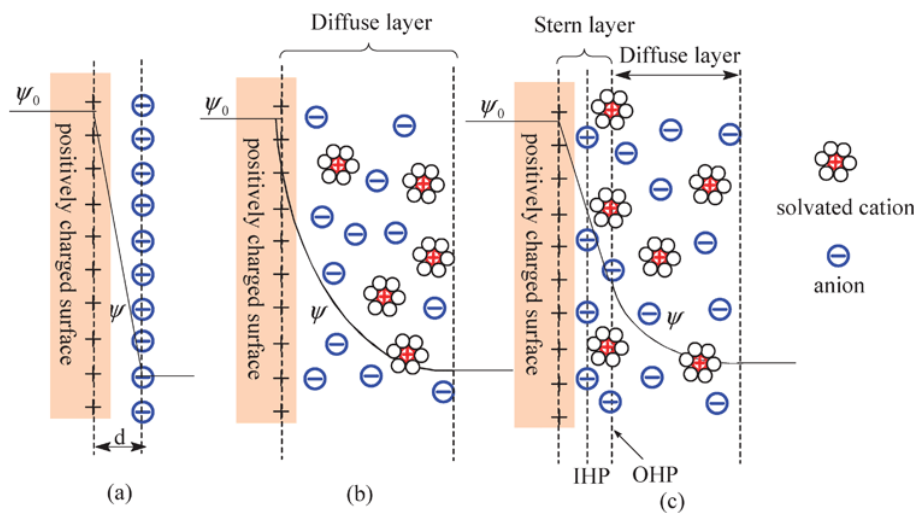


Figure 2.1 The classic equilibrium EDL models: (a)Helmholtz Model; (b) Gouy-Chapman Model; (c) Gouy-Chapman-Stern Model[29].

With the development of the electrochemistry, the Gouy and Chapman modify the EDLs model with the account of the thermal fluctuation (entropy) of ions [37]. Based on the deviation of the Poisson-Boltzmann (PB) equation, there would be a continuous concentration profile of ions from the solid surface with the accumulation of counter-ions and the repelling of the co-ions[38]. At the distance far-away from the solid wall, the concentration of ions would be the same as that in the bulk reservoirs ($n_{i,0}$)[38]:

$$\nabla^2 \Phi_E = \frac{\partial^2 \Phi_E}{\partial x^2} = -\frac{e}{\varepsilon_0 \varepsilon_r} \sum z_i n_{i,0} \exp\left[\frac{-z_i e \Phi_E(x)}{k_B T}\right] \quad (2.2)$$

Where z_i is the valence number of the i th ions, and $n_{i,0}$ is the concentration of i th ions in the far-away bulk reservoirs; e is the elementary charge; k_B is the Boltzmann constant and T is the absolute temperature;

The above second order partial differential equation, Eq.(2.2) could be approximated for a small surface potential which is considerably lower than the thermal voltage ($z_i \Phi_E < k_B T$), giving the Debye-Hückel approximation[39]:

$$\nabla^2 \Phi_E = \frac{\partial^2 \Phi_E}{\partial x^2} = \left(\frac{1}{\lambda_D}\right)^2 \Phi_E(x) \quad (2.3)$$

Where λ_D is the Debye-length for the EDLs and it is defined as

$$\lambda_D = \sqrt{\frac{\varepsilon_0 \varepsilon_r k_B T}{e^2 \sum z_i^2 n_{i,0}}} \quad (2.4)$$

The Debye length is usually used to evaluate the extension of EDLs and it increased with the drop of the reservoir concentration. Thus at relative low concentration, the characteristic size of the nanochannel is comparable to that of the EDLs, giving the anomalous property of fluid under the confinement.

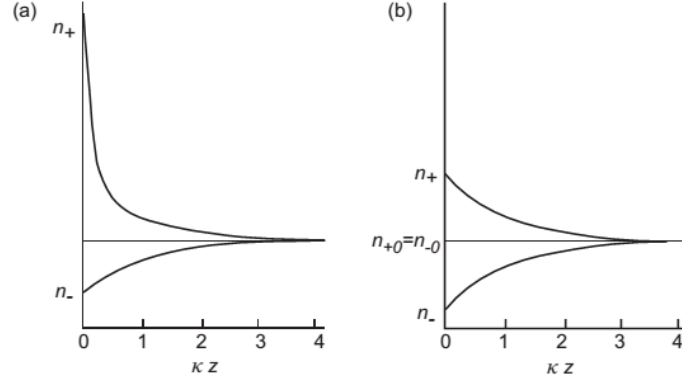


Figure 2.2 concentration profile for symmetric electrolyte on the charged surface: (a) $z_i \Phi_E > k_B T$; (b) $z_i \Phi_E < k_B T$. n_+ and n_- represent the concentration of counter-ions and co-ions respectively[40].

Obviously the expansions of EDLs in both cases are similar which is determined by λ_D namely the reservoir concentration. At low surface potential, the exclusion of co-ion is balanced by the same amount of the counter-ions enrichment, giving the constant charge carrier density ($n_+ + n_-$). However the high surface charge would significantly increase the concentration of counter-ions, namely the increase of the charge carrier density[38]. The changes of the charge carrier density on the solid surface would also modify the behavior of fluids on EDLs.

By combining the initial Helmholtz model and the following Gouy-Chapman model, the Gouy-Chapman-Stern (GCS) model[37, 41, 42] was proposed (Figure 2.1c[29]). In the GCS model, the EDLs is consisted by as the Stern layers (a dense ion absorption) and the diffusion layers (an exponential decay of concentration). Grahame has further divided the stern layers into two parts: the extra Inner and Outer Helmholtz Layer (IHL or OHL) are added. For IHL, the solvent and the small anions would be specifically absorbed onto the solid surface. Beyond the IHL, the cations (counter-ions) would be adsorbed by the Columbic attraction, forming the OHL. The left diffusion layer is the same as that in Gouy-Chapman model due to the thermal fluctuation (entropy) of ions.

Due to the simplicity of analysis, all the above models are targeted on the single wall plate with infinity length of reservoir. However for the nanofluidics study, the channel height is usually comparable or even lower than that of the Debye Length ($h < \lambda_D$). Thus, the EDLs

from the opposite walls would start to overlap with each other, giving a different structure from the single plate case. The several pioneer theoretical works for nanochannel EDLs, based on the PB equation have also been taken for different geometry of nanochannel (nanoslit[43, 44], or nanotube[45]).

It has been found that once the EDLs was overlapped ($h < \lambda_D$), the electric potential in the middle of nanochannel would be considerably elevated and the concentration of ions varied with the electric potential in Figure 2.3[43]. The overlapped EDLs have attracted much attention owing to the discovery of the anomalous increase of the areal capacitance in nanochannel ($d \sim 1\text{nm}$)[46, 47]. The analytic models deviated from PB equation have also been proposed to explain that[48].

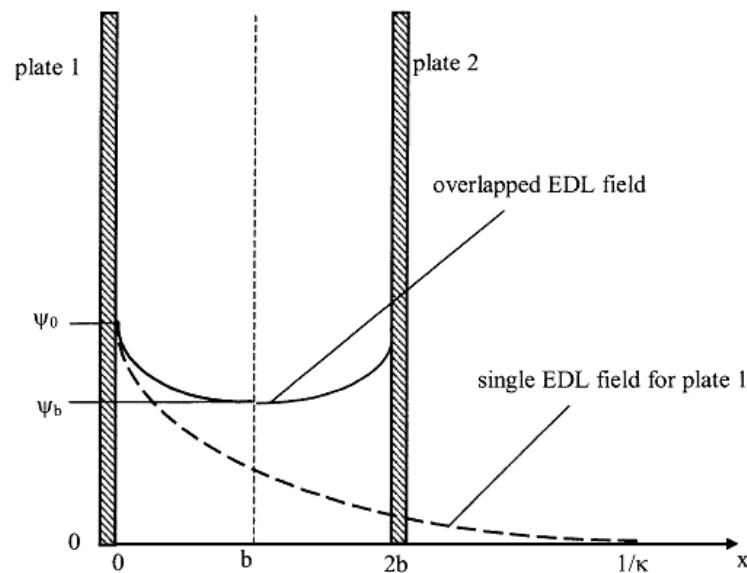


Figure 2.3 Schematic of the electrical potential distribution in the overlapped EDL field between two flat plates[43].

Although the attempt of continuum modelling for EDLs confined in nanochannel have devoted, the limitation of the continuum models based on the continuum model (PB equation) cannot be eliminated[49]. The concentration of the electrolyte ions, rather than the activity of ions are employed in PB equation. The steric effect of ions and the interaction between the solute even with the solid wall are usually ignored. Thus the PB equation description would be only valid for low concentration result without the strong nanoconfinement.

Besides, The PB equation also treated the solvent as a homogenously background with constant permittivity. However it has been known that the orientation and the density of the water on the solid surface would be changed. In small nanochannel, there was found to be a laminar structure of water[31]. Thus we cannot simplify the water molecules as a continuous structureless medium with uniform physical constant[17].

Hence, the analytics (continuum) models for EDLs developed from the colloid or membrane science cannot provide a quantitatively description for the electrolyte confined inside the small nanochannels. But the prior theoretical study still provides a general understanding about the EDLs, which is the starting point for the following nanofluidics study

2.2.2 Atomic MD insight

To address the limitation of the continuum model in small nanochannels, MD simulation is employed to provide an atomistic insight into the EDLs structure, especially for the very small nanochannel ($< 2\text{nm}$). Initially, the single plate EDLs for the aqueous electrolyte on different electrode surfaces (e.g. metal[50, 51], silica[52] or image plane[53-56]) were studied. The oscillated concentration profile (laminar ion distribution) is demonstrated by the steric effect of ions and solvent which cannot be reproduced in the continuum modelling. Figure 2.4[57] is the typical example of the MD simulation result for EDLs and the comparison with the PB prediction. Note the mean field approximation in the continuum model eliminate the laminar structure of EDLs.

With the awareness of the superior of MD simulation, the aqueous EDLs was firstly extensively studied for different issues, i.e., temperature ion size, dielectric constant, ion polarizability, Dispersion interaction, surface roughness, residual functional group, electrode topology, nanochannel geometry[58-63] The potential dependent EDLs structure with bell or U shape differential capacitance were reported[64, 65].

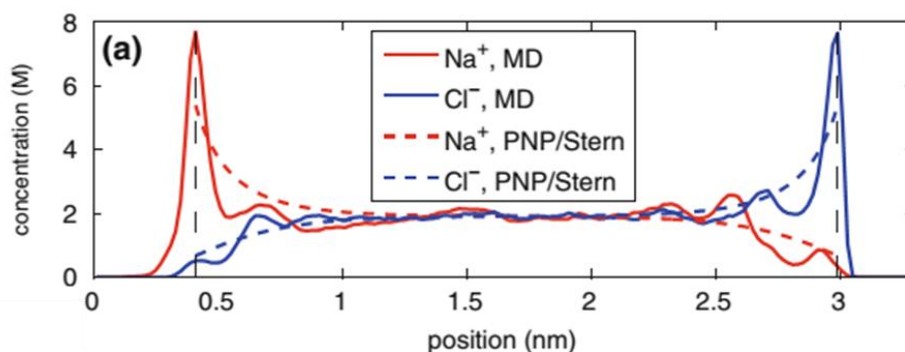


Figure 2.4 The comparison of ion concentration profile for MD simulation and PB equation: The solid curves in red and Cl- color are the concentration in MD simulation while, the dashed line with the same color are the result by PB equation. Note at left and right end ($x = 0$ or 3.5 nm) different surface charge are imposed.[57]

Moreover, the range of MD study has also been extended from the aqua ions into the Ionic Liquids (ILs)[62-64, 66, 67], from the water solvent into the organic one (e.g. acetonitrile, ACN)[68, 69]. The specific absorption of the solute or solvent into the electrode surface has been discovery especially for the ILs[62, 63, 65, 66, 68], which was not quantitatively accounted in the classic continuum modelling.

Following the MD study on the single plate, the EDLs in the different geometry of nanochannel were also investigated from the nanoslit[70-72] to nanotube[69, 73, 74], from the carbon onion[75-77] to the amorphous carbon derivative[78, 79]. The geometry, voltage or temperature dependent differential capacitance of EDLs was demonstrated[63, 80, 81]. It seems that the onion shaped of electrode could avoid the capacitance drop at large electric potential[59].

After that, the discovery of the anomalous increase of the capacitance inside the nanochannel (1~2 nm) inspired the investigation of EDLs into the nanochannel. The superionic state of ions has founded in the small nanochannel[60, 61]. It is accompanied with an oscillated scaling of the capacitance over the channel height. Because, the overlap of the oscillated EDLs structure in the nanochannel was found to be interference for different channel height. At the construction of EDLs structure, the increase of counter-ions also increases the capacitance, and vice versa [59, 82-84]. It provides a better fundamental understanding for the anomalous increase of the capacitance inside the membrane.

Taken together, the MD simulation is a further development of the continuum modelling. The trivial detail of EDLs annihilated by the mean field approximation of the continuum modelling has been reconstructed from the MD simulation. Although the EDLs study cannot directly present the transport behavior of nanoflow, the investigation of EDLs on the equilibrium state would be a good prior knowledge for the following nanofluidics study. And we found there is still no comprehensive comparative study for different ionic types. Thus in the Chapter 3, the EDLs for different electrolytes were investigated. The result would be a good starting point for the following MD simulation on the cascading nanoflow.

2.3 Transport 1D nanoflow

2.3.1 Continuum modelling

Since the extensions of the fluidic study into the nanoscale, the continuum modelling with wonderful successes in microfluidic field ($h > 1\mu\text{m}$) is “inherited” by the nanofluidics-community[18, 85]. However the reasonable interaction in nanofluidics would be much more complex than that of the microfluidics. Figure 2.5[1] summarized the characteristic size of the nanochannel becomes comparable with many microscopic scales (e.g. molecular size, Debye length, “Dukhin” length). Thus the validation of the continuum model should be review firstly.

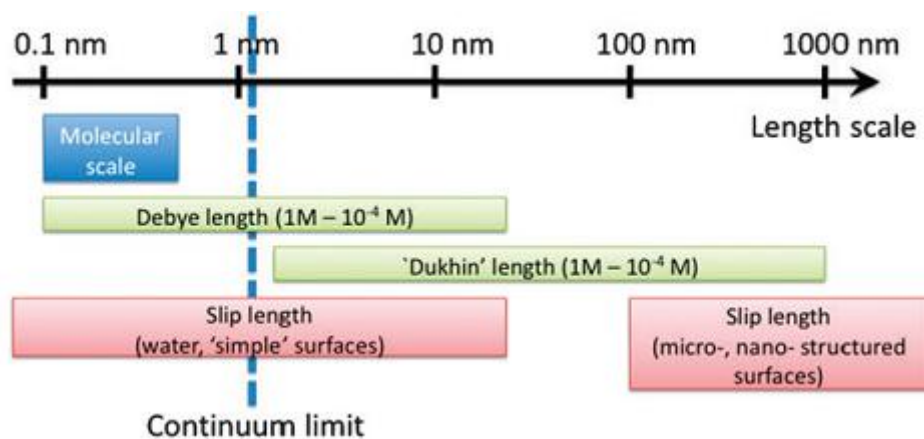


Figure 2.5 Various length scales at play in nanofluidics[1].

Through the comparison with MD simulation, the validation of homogeneous description of background water molecules was confirmed for the channel size larger than 1~1.5nm. At

$h > 1\sim 1.5\text{nm}$, the water molecules could be treated as a continuum incompressible medium with the constant viscosity as the bulk solution [1, 86, 87]. However, ionic profile would be different. It was found to provide the same result in the continuum modelling; the characteristics length of nanochannel should be 10 time larger than that of molecular size. Otherwise, the steric effect of the laminar ions profile cannot be ignored. For the aqueous electrolyte, the result of continuum modelling at $h < 3\text{nm}$ should be further investigated via the MD simulation[87, 88].

For the continuum modelling of the nanoflow, the various driving force has been investigated for different application, such as pressure, temperature, electric potential, concentration, chemical potential or gravity and so on[2, 4]. The electric potential driving nanoflow is superior to the other method owing to the fast and precise control and manipulation of the mass transport in nanochannel.

For the electrophoresis modelling, the Poisson-Nernst-Planck equation (PNP equation)[1] was usually employed as the governing equation:

$$\nabla^2 \Phi_E = \frac{F}{-\varepsilon_0 \varepsilon_w} \sum z_i n_i \quad (2.5)$$

$$\frac{\partial n_i}{\partial t} = D_i \nabla^2 n_i + \mu_i z_i e n_i \nabla \Phi_E + n_i \vec{u} \quad (2.6)$$

Where F is the Faraday constant and μ_i is the electrophoresis mobility of i th ion, \vec{u} is the background laminar flow. The first, second and third terms in Eq.(2.6) represented the contribution of ionic flow via diffusion, electrophoresis and convection respectively. However, the contribution of the water flow is usually neglected in the conventional electrophoresis study[89-91]. Because, the water flow, precisely speaking the Electro-Osmosis Flow (EOF) is attributed to external electric potential difference or the strength of the E-field, which is defined as Eq.(2.7).

$$\Gamma = \nabla \Phi_E F \sum z_i n_i \quad (2.7)$$

Where Γ is the volumetric force for EOF; $\nabla\Phi_E$ is the local electric field (E-field) strength; $F \sum z_i n_i$ would be the volumetric net charge in the electrolyte. Thus the background water is dragged by the unbalanced extra ions (volumetric charge) and the strength of the volumetric force would be proportional to the local E-field.

To be consistent with the experimental setup[9, 92], the breakdown voltage of water (~ 1 V) limits the strength of the E-field in the continuum modelling ($< 0.01\text{V/nm}$) [89, 91]. And the magnitude EOF is proportional to the local E-field strength. Thus it has been founded that the result with the dynamics EOF has no obvious difference [89, 91] with that of stationary water ($\vec{u} = 0$) for the low external E-field strength (conventional experimental setup). And the EOF study was focused on the microfluidic devices ($1\sim 10\mu\text{m}$) under a strong E-field ($\sim 0.1\sim 1\text{V/nm}$) as an efficiency water pump[93-95]. Hence, the last term of Eq.(2.6) is usually removed in the conventional nanofluidics modelling.

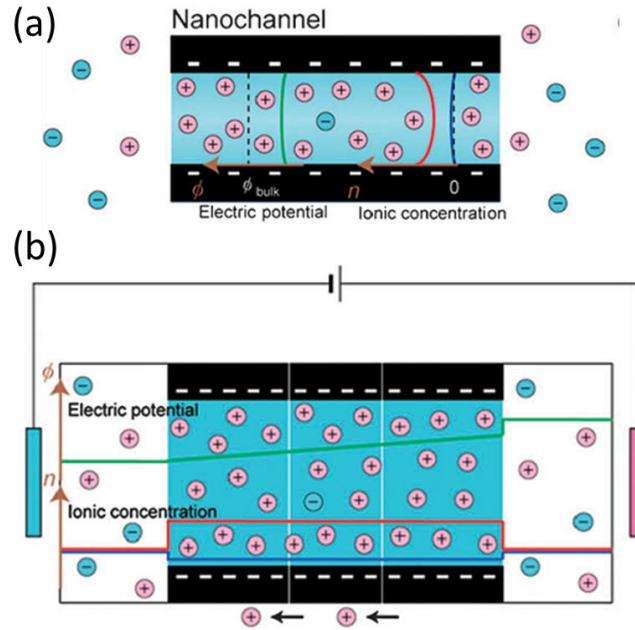


Figure 2.6 The schematic of 1-D nanofluidics [18] (a) profiles in the equilibrium state; (b) profiles under the electric potential difference ($\Delta\Phi_E$). At equilibrium, the overlap of EDLs in the small nanochannel ($\lambda_D > h$) increased the concentration of counter-ions (red) and decreased that of co-ions (blue). A meniscus electric potential (green) is obtained inside the nanochannel. The maximum electric potential in the centre of nanochannel would be still lower than that of bulk solution. At $\Delta\Phi_E$, the electric potential gradient was established across the whole nanochannel. And the ionic concentrations of counter-ion would be still much higher than that of co-ions and even higher than that in the two side reservoir (n_{res}). Thus the counter-ions make the predominant contribution to the total electro-kinetic current.

Figure 2.6[18], is the typical schematic for the continuum modelling of the conventional 1-D nanoflow. Figure 2.6a shown typical concentration profile of EDLs overlap ($\lambda_D > h$) in equilibrium where the concentration of counter-ion increase with the exclusion of co-ion. It is worth noting that if the surface charge density is high enough ($\frac{\sigma}{Fh} \gg n_{res}$), the co-ions would be completely excluded from the nanochannel. And the electric potential inside the nanochannel would be always lower than that in the bulk solution.

The influence of surface charge could be defined as σ/h . At low reservoir concentration ($n_{res} \ll \frac{\sigma}{Fh}$), the anions is completely repelled from the nanochannel and the concentration of cation was determined by surface charge and channel height ($\frac{\sigma}{Fh}$). Thus the charge carrier density in the 1-D nanochannel is fixed by the surface charges that giving a constant conductance at different low n_{res} . Both the experiment[8, 9, 96] and the continuum modelling[44, 97] demonstrated the constant conductance of nanochannel at lower reservoir concentration ($n_{res} \ll \frac{\sigma}{Fh}$), shown in Figure 2.7[8].

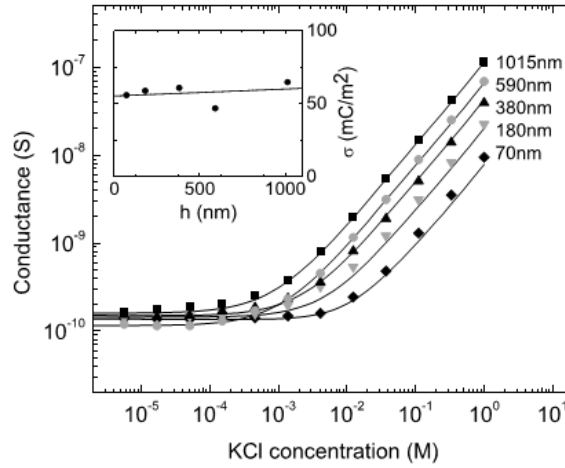


Figure 2.7 The conductance of the different nano/micro-channel as a function of n_{res} . The separated dots are the experimental results and the curves are the continuum modelling results with the fitted surface charge density[8].

Besides the study with the uniform distribution of surface charge, the 1D nanochannel with the asymmetric surface charge distribution has also been proposed and calculated via the continuum modelling. It has been found that the property of the confined solution was modified by the surface charge on the adjacent channel wall. Similar to the strategy in semi-

conductor devices, the heterojunction of different property of solution was employed inside the nanochannel. The novel nanofluidics diode has been demonstrated in both theory and experiment[98-101]. Figure 2.8a[18, 100], are the schematics of the nanofluidics diode with the asymmetric current potential curve. The functional groups on the channel wall surface were modified to cause the positive and neutral (or negative) region. Then, the asymmetric surface charge distribution in nanochannels induced the single direction of ion current. Because On the internal electric potential different between the positive and the neutral region blocked the reverse current. Moreover, the asymmetric reservoir concentration[102, 103] or asymmetric channel geometry[104-106] were also demonstrated the rectification ability of the ionic current.

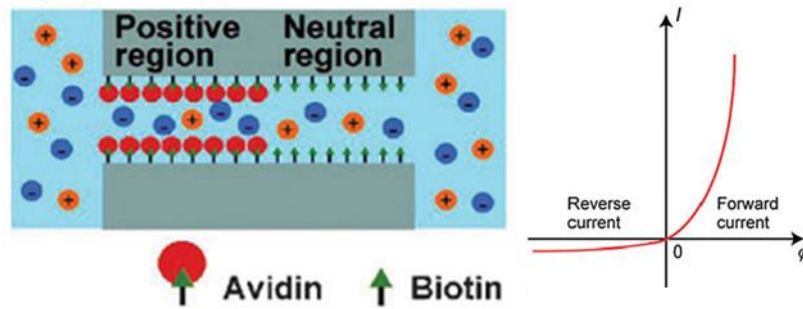


Figure 2.8 The schematics of nanofluidics diode[100] and the potential-current curve[18].

Based on the invention of the nanofluidics diode, the nanofluidics field-effect transistor was also reported in theory[89] and experiment[107]. Unlike the fixed surface charge in the nanofluidics diode, the electric potential (surface charge) on the gate region was control externally. As shown in Figure 2.9[18], the positive charged gate would completely repelled the counter-ions (cation) in the gate region. Thus, the ionic current through the nanochannel was blocked. While, the negative charged gate allowed the passing of cation.

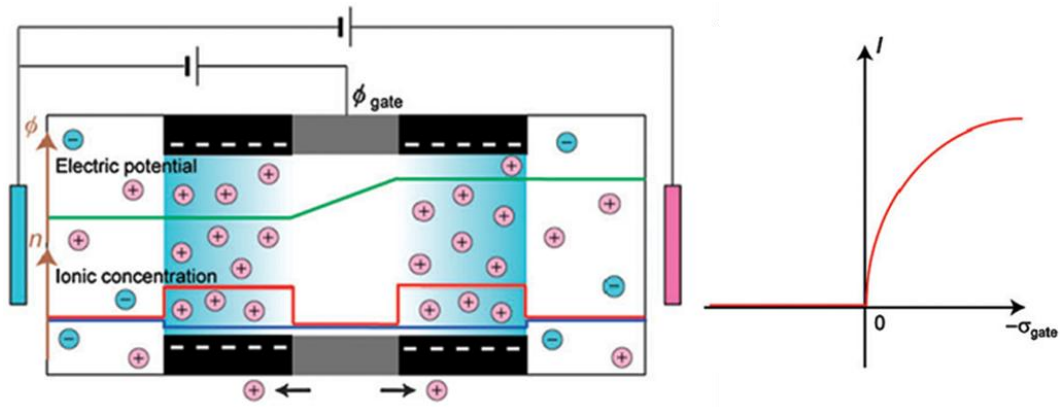


Figure 2.9 The schematics of nanofluidic field-effect transistor and the potential-current curve [18]

With the assist of continuum modelling, the phenomena behind the novel nanofluidics devices were identified. And it provides a feasible access to quantitatively control the performance of the nanofluidic device. However the prior continuum modelling was focused on the conventional 1-D nanochannel rather than the staggered graphene structure. The present section still reviewed the basic principle and the recent advance for the continuum modelling. That would be a great starting-point to exploit the undermined potential of the graphene membrane.

2.3.2 MD simulation

Although the MD simulation is favorable for the accurate description in nanoscale, the temporal and spatial range of MD simulation ($t < 100$ ns & $d < 100$ nm) is still significantly limited by its poor computational efficiency. To overcome the thermal fluctuation in the small MD simulation system (total atom number is smaller than 10^5), the driving force in MD simulation is usually thousands or ten thousand times higher than that in experiment[18], to obtain a markedly higher mean flow rate than the thermal noise

Hence, all the prior MD works of nanofluidics is considerably deviated from the experimental setup, but they could still provide some qualitatively or semi-quantitatively insight into nanoscale. Especially for the 1-D nanochannel, the driving force is tangent along the channel wall. Thus the influence of the driving force is regarded to be proportional to the flow rate[108].

Taken the electric potential driving for example, a large amount of MD simulation has been taken to study the transport property of electrolyte under the different nanochannel in hydrophobic[109] and hydrophilic surface[92, 110], realistic membrane proteins[111], smooth graphene sheet[108] and polar silica surface[110], nanoslite[112] or nanotube[113, 114]. The E-field is applied parallel along the channel wall with a range of strength ($E=0.1\sim1\text{V/nm}$) [110, 115]. And result (electrophoresis current) obtained in 1-D nanochannel still seems to be linearly with E-field strength range. Compared with the continuum modelling, the unavoidable high external E-field usually induced the EOF in MD simulation which considerably modify the ion transport property and should be significantly noted.

As discussed in the present Chapter, it is well known that the extra counter-ions by surface charge will induce the EOF in micro- or nanochannel. Hence, the neutral channel without extra counter-ions is considered to be not able to induce the EOF in the classic thermodynamics framework. However through the MD simulation some “exotic” EOF has been discovered in neutral nanochannel

It has been widely known that EDLs structure will be significantly influenced by the wall property. In the other prior study, the large anions such as Br^- and I^- is demonstrated to be special attraction to the hydrophobic surface that forms the high concentration peaks on the wall surface. Based on the exotic EDLs, the electro-osmosis flow (EOF) has been found in neutral nanochannel, (open circle in Figure 2.10c[92]). The middle circle curve in Figure 2.10c&d is the water velocity profile for NaI and NaCl solution without surface charge.

It has been mentioned before the transport of extra counter-ions by surface charge will drag the surround water molecules that induce the EOF in nanochannel and the direction of EOF is consistency with the direction of counter-ions. Thus the water velocity profile of NaCl (Figure 2.10d) is a typical result for EOF in nanochannel with different surface charge. However the velocity profile of NaI (Figure 2.10d) is considerably different from that of NaCl solution. Especially for neutral wall (middle curve), the exotic EOF is driven by the boundary layer of Na^+ cation at $z = -17\text{\AA}$ rather that of I^- anion at $z = -20\text{\AA}$. Thus at $\sigma = 0\text{mC/m}^2$, the water in the middle of channel flows along the direction of cation transport.

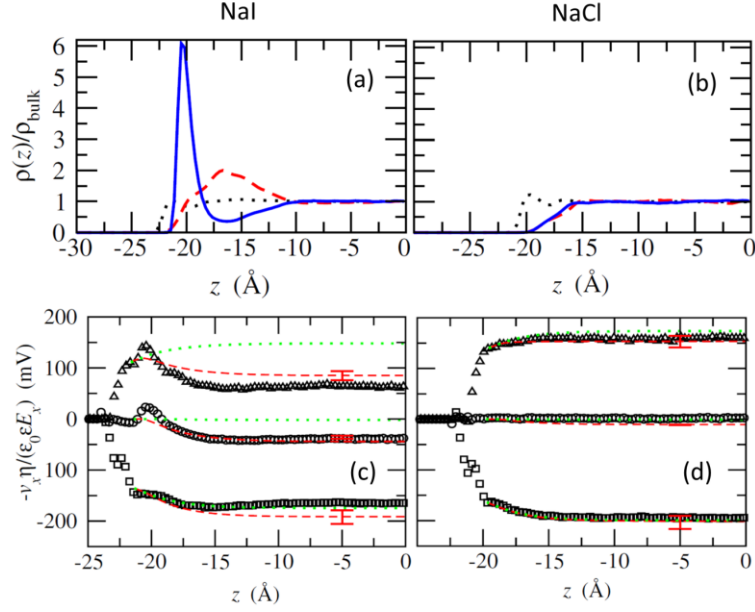


Figure 2.10 The concentration profile for roughly 1M NaI (a) and NaCl solution between neutral hydrophobic surfaces. The blue and red lines indicate the concentration of ions; while the dotted lines show the density of water molecules. The velocity profile in the hydrophobic channel for 1M NaI. (c) and NaCl (d) solution. The open squire, circle and triangle symbols represent the velocity profile with different surface charge ($\sigma = -62, 0$ and $+62$ mC/m², from bottom to top)[92].

Based on the EDLs dependent EOF in nanochannel, the studies has been extended to different channel. It has been found that the magnitude of EOF at neutral wall depends on the ratio between channel height and Debye length[115, 116]. And the superhydrophobic surface will not enhance the EOF further[116].

Another discovery was based on different drag coefficient of ions in nanochannel[117]. It has been found the transport of ions in nanochannel could drag the surround particle of solution[118]. However the cation and anion under the nanoconfinement has the different drag ability for water molecules. Thus, under the external E-field, the transport of cation and anions in opposite direction will induces a EOF in in small nanotube (< 1 nm). But the different drag coefficient between ions is only valid at small nanochannel, and that disappears in the large channel[117].

Besides the neutral wall, the ions transport through the charged nanochannel was also been studied via the MD simulation. On one hand, some MD simulations for charge nanochannel were proposed to verify the discovery in the continuum modelling[119]; on the

other hand, some unique phenomena for the atomistic description of MD simulation were reported[92, 120, 121].

It was found that the EDLs would be considerably modified by the charge density, ion arrangement, the ion type and the wall topology (i.e. smooth or rough, hydrophobic or hydrophilic)[122]. Thus, the velocity profile inside the nanochannel also deviated from the continuum predictions with the different ion distribution.

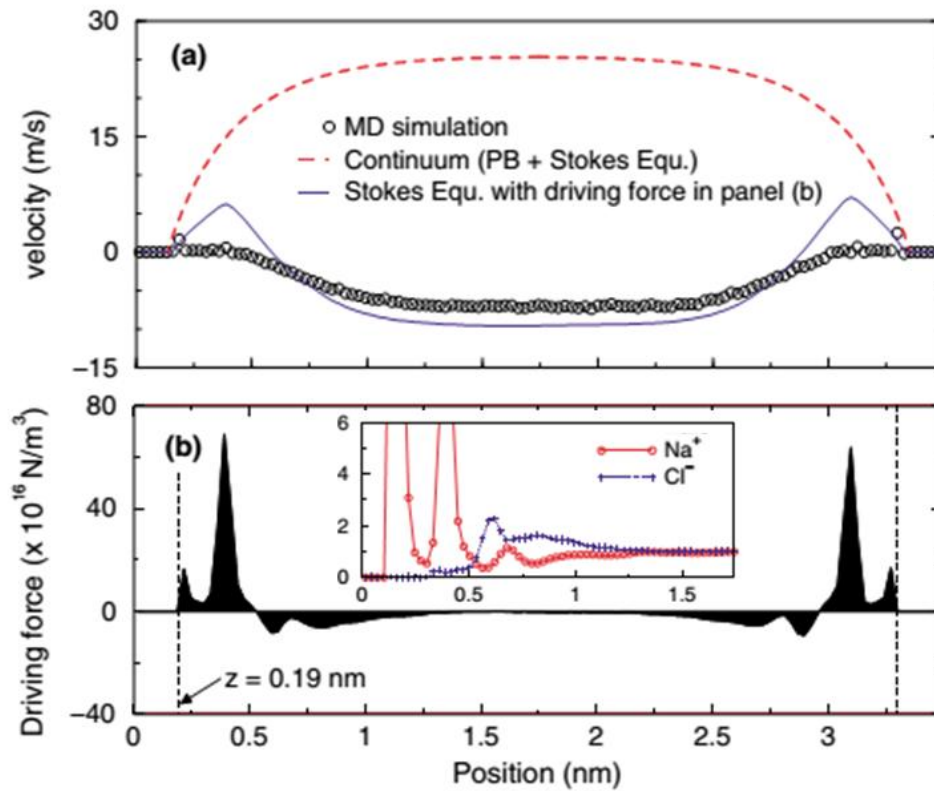


Figure 2.11 (a) Water velocity profile across the channel obtained from MD and continuum simulations. (b) Driving force for the flow across the channel using the ion concentrations obtained from MD simulation. The inset was the corresponding concentration profile of EDLs[123].

Figure 2.11[123] plotted the abnormal EOF inside the negatively charged nanochannel. As shown in the inset of Figure 2.11b, the counter-ions (K⁺) was absorbed onto the graphene surface, leaving the co-ions (Cl⁻) behind the Helmholtz Layers, which was defined as the charge inversion. Thus negative driving force (drifted by the co-ions) inside the nanochannel would induced a negative EOF (circle in Figure 2.11a), which is obviously different from that of the continuum prediction in the previous section (dashed red line in Figure 2.11a). And it

was found the charge inversion would be considerably enhanced in the solution with the multivalent ions ion[124].

Beside the deviation of EDLs, the viscosity of solution near the channel wall was also found to be markedly increased [120]. Thus, even with the similar EDLs structure, the EOF in continuum modelling was reported to be stronger than that in MD simulation[124, 125]. It may attribute to the strong E-field inside the EDLs structure or the hydrogen bonding with the channel wall[40, 125].

Generally speaking, the novel phenomena revealed by the MD simulation could be attributed to the nanoscale interaction (e.g. van der Waals wall absorption, steric effect, ion hydration shell) which is not or really difficulty to be accounted into the continuum modelling. Thus the expensive MD simulation was still employed to provide a good understanding of fluid inside the small nanochannel.

Similar to the continuum modelling, the basic principle of MD simulation has been well established and demonstrated, but the study of cascading electro-kinetic flow in the staggered structure is still a virgin territory for nanofluidic community. Thus, the novel cascading electro-kinetic flow will be studied in Chapter 6&7, especially for the small nanochannel.

2.4 Conclusion

The present chapter first introduced the terms of equilibrium EDLs and the dynamic nanoflow where the understanding of the former would be the fundamental of the latter. Thus the introduction of EDLs would be a current state of knowledge from the view of continuum modelling and MD simulation. For the dynamics nanofluidics, the basic principles of the continuum model were firstly reviewed and the novel nanofluidics device for 1-D nanochannel were presented and discussed.

For the following MD simulation of electro-kinetic flow, the unavoidable higher driving force usually induced a high EOF which deviated from the classic continuum modelling. It is worth noting that the considerable EOF could be generated in the neutral nanochannel for the different EDLs and the drag ability. Besides the neutral channel wall, the nanochannel with

the surface charge was also been investigated via the MD simulation. Some results on one hand verified the proposal in the continuum modelling but also reveal the novel property in the nanoscale.

Although the reviewed literature in this Chapter cannot provide a direct insight into the cascading nanoflow, the prior study has established the basic principle and the methodology in the nanofluidics field. The setup of the continuum modelling is similar to that of the experiment, but some nanoscale interactions are ignored. However, the MD simulation provided a more accurate atomistic description with the at the expense of computational efficiency and the extremely high driving force. Thus a good cascading nanofluidics study would be a combination of two terms which will be presented in the following Chapters.

Based on the literature reviewed in the present Chapter, the abnormal electrolyte/solid interface (boundary layer) would also be the essential term in the cascading nanofluidics. Especially, the boundary layers are under a normal driving force (E-field) rather than a tangent one. Thus, the different concentration and electric potential distribution would emerge with the completely different transport behavior. The articles mentioned before provide a good suggestive insight for the novel mechanism in the graphene membrane. Moreover, the present thesis is still a preliminary study for the cascading nanoflow inside the graphene membrane which cannot provide the various nanofluidics devices as the literature.

Chapter 3: MD simulation of EDLs on CCG membrane

3.1 Introduction

With increased public awareness of the climate change and dwindling fossil fuel supply problems, there has been a growing demand for clean and low-emission renewable energy sources. Electricity-based energy generated from renewable sources, such as solar or wind, offers enormous potential for meeting future energy demands[126-128]. However, the use of these intermittent, renewable sources requires efficient electrical energy storage. Electrochemical super-capacitors (ECSC) are considered as promising candidates for alternative energy storage devices, because they have a range of advantageous features such as high power density, fast charging, long cycle life and low maintenance, high Columbic efficiency and environmental friendliness[129-131].

The electric double layer (EDL) plays an essential role in the performance of ECSC[31, 35, 132, 133]. For a charged ECSC electrode immersed in an electrolyte, the oppositely charged counter-ions will be accumulated near the electrode surface to maintain the electro-neutrality. Such a screening region is denoted as the EDL. Since the electrical energy is stored in the EDL, enhancement of the electrode surface area is a widely adopted strategy to improve the energy density stored in the ECSC[30, 130, 131, 134]. Graphene, a single layer of graphite with extraordinary electrical properties and a high specific surface area ($\sim 2630\text{m}^2/\text{g}$), is considered as the ideal electrode materials in the ECSC[135]. In the past few years, there have been intensive and exciting researches on the graphene based supercapacitors[35], demonstrating the superior power density (776.8 kW/kg) and an energy density (150.9 Wh/kg) close to that of Li-ion batteries. Despite recent advances, the energy densities of most of the graphene supercapacitors are still one order of magnitude lower than the Li-ion batteries[135, 136]. Developing high performance graphene supercapacitor requires in-depth knowledge of the physics of EDL structures at the graphene electrode surface, and, therefrom, how to best optimize its performance.

Aqueous electrolyte has several advantages in comparison with two other currently widely used electrolytes in graphene ECSC: organic and ionic liquid electrolytes[131]. Graphene supercapacitors with aqueous electrolyte often have excellent power density, higher specific capacitance (130~200F/g), High volumetric energy density (200~250F/cm³) and fabrication feasibility[35, 36, 134, 135]. Thus detailed understanding of the structures of EDL, which are determined by the interactions of electrolyte ions, graphene, and the water molecules on a molecular scale, is essential for a full understanding of the operation of EDL capacitor and the capacitance values. However, such highly desirable knowledge is still not adequate[130].

As mentioned in the Chapter 1&2, the EDLs is a crucial background for the nanofluidics study and the atomistic EDLs would be considerably different from that of PB equation. Thus it is necessary to take the MD simulation for the EDLs on the graphene sheet, which would be beneficial to the following MD simulation of the electro-kinetic flow in the Chapter 6&7. Although the influence of ionic type on aqueous EDLs has been mentioned in the prior study[54, 56], there is still no comprehensive comparative study for different ions. Thus in the present Chapter, the influence of the ion type on the EDLs would be compared and discussed.

3.2 Methods

3.2.1 MD simulation Setup

Figure 3.1 shows the molecular system in our MD simulations, in which the graphene layers are separated by the aqueous electrolyte solution with a 5nm interlayer distance. The in-plane dimension of our graphene layer is about 10.2 nm ×10.0 nm. Periodic boundary conditions (PBC) were employed in all three dimensions. Symmetric monovalent electrolyte ions (M^+X^-) were investigated. The electrolyte ion concentration was 1mol/L. This molecular model resembles the typical graphene supercapacitors in our experiments [35, 36].

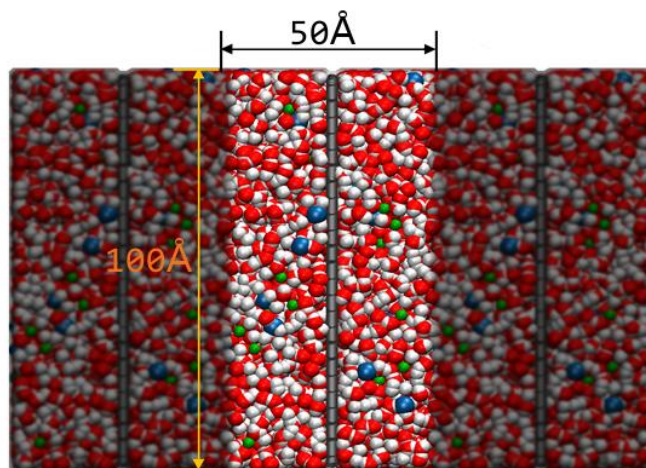


Figure 3.1 Molecular simulation system including a single layer graphene immersed in aqueous electrolyte with ionic concentration of 1mol/L. The interlayer distance between the graphene layers is 5nm.

Using $21 \mu\text{F}/\text{cm}$ or $550\text{F}/\text{g}$ as the intrinsic capacitance of a graphene ECSC[137] and 1V electrical potential window for the aqueous electrolyte, we estimated the maximum charge per carbon atom would be $0.0685 \text{ e}/\text{C}$, which is equivalent to a total charge of 270 e for one graphene layer with 3936 carbon atoms in our simulation box. We thus selected a total charge of 0, ± 60 , or ± 160 electrons imposed on the graphene layer (Figure 3.1), which corresponds to 0, 0.015e or 0.041e per carbon atom. The constant partial charge has been imposed on graphene sheet like most of the other electrochemical simulation [75, 138-142].

Although the MD simulation with the constant electrode potential[143] has been proposed as the conventional electrochemistry experiment, the computational times is expensive comparing to the constant surface charge[144]. The difference of EDLs structure in both methods is negligible at low potential difference ($<2\text{V}$)[145, 146]. The dynamics constant electrode potential study is favourable for transient charging process and complex nanoporous structure[78, 79, 144, 145]. However the object of current MD simulation is a comparative study of equilibrium EDLs among different electrolyte. The simple and efficient constant charge methods could provide the reasonable result.

The number of the electrolyte solute ions was determined using two conditions: (1) overall ion concentration is 1M; (2) the whole system is charge neutral (including charges on

the graphene layer). Table 3.1 summarizes the number of solute ions in our MD simulation systems.

Table 3.1 Particle numbers of the M+X- aqueous solution in the simulation box for different charges in the graphene electrodes

Charge on one graphene layer (3936 carbon atoms)	M ⁺	X ⁻	Water
0e	310	310	48884
+60e	280	340	48884
+100e	260	360	48884
+160e	230	390	48884
-60e	340	280	48884
-100e	360	260	48884
-160e	390	230	48884

Motion of carbon atoms in the graphene layer was frozen in our MD simulations, because (1) the typical corrugation amplitude of the graphene layer[147] is negligible in comparison with the channel size[35, 36] and (2) our previous MD studies showed that the corrugation of graphene layer has a negligible effect on the molecular structure of the first water layer next to it[108, 148, 149] and the frozen graphene sheet has been widely adopted among the supercapacitor simulation [58, 59, 79, 144]. The TIP/3P model was used for water with the SHAKE algorithm[150, 151]. The TIP/3P model was demonstrated to provide the better property[152] and the most LJ parameters from the Charmm27 force field were optimized with the TIP/3P model to reproduce the experimental result [153]. In addition to the electrostatic forces, the interactions among the ions, carbon atoms, and the water molecules were described by using the modified Lenard-Jones potential with an additional switching function that tunes the force and energy smoothly into zero between inner (8Å) and outer cutoff (10Å)[154]. Unlike the simplest hard sphere simulation, the soft van der Waals shell by LJ potential could more precisely describe the interaction between the electrode and electrolyte[155]. The parameters of LJ potentials of the most ions were taken from CHARMM27 force field[153], except that the parameters for Γ^- and F^- anions were taken from references[156, 157]. Table 3.2 summarizes the parameters and the charges of each type

of ions. The Lorentz-Berthelot Mixing rules were adopted for the LJ force field models between different types of ion.

Table 3.2 Force field parameters for the electrolyte ions and the TIP3P water model

Ions	ϵ (eV)	σ (Å)	Molar Mass	Valence (e)
Na ⁺	0.00203	2.430	22.990	-1
K ⁺	0.00377	3.143	39.102	+1
Cs ⁺	0.00824	3.742	132.90	+1
F ⁻ [157]	0.00781	3.118	18.998	-1
Cl ⁻	0.00650	4.045	35.450	-1
I ⁻ [156]	0.00434	5.167	126.90	-1
O (TIP3P)	0.00660	3.151	15.999	-0.834
H (TIP3P)	0.00000	0.000	1.0080	0.417

Our MD simulations were carried out using the LAMMPS code. Time step was set as 1.5 fs. The van der Waals forces were truncated at 1.0 nm with long-range Columbic interactions computed using the particle-particle particle- mesh (PPPM) algorithm. In our MD simulations, first, the temperature was gradually increased from 298K up to 373K with the Berendsen thermostat for 10ps. Then the system was kept at 373K for an additional 10ps. After that our molecular systems were gradually cooling down from 373K down to 298K. At last, the NVE ensemble simulations at 298K were carried out for about 1.2 ns. Although the result in the Berendsen thermostat was regarded to be deviated from a canonical ensemble, the Berendsen thermostat was still favourable for its fast convergence of the temperature control. Moreover for the large system with thousands or ten thousands of atoms, the Berendsen thermostat provide a little deviation of the calculated property [158], Thus, it is widely applied among the different application [159, 160].

The resultant trajectory of the last 150ps was analysed to obtain the EDL structures. Longer MD simulations up to 2 ns were also tried for some selected cases and we found negligible differences in term of the structures of EDL.

3.1.1 Post-processing

Density distribution of the electrolyte solute ions in the direction perpendicular to the graphene electrode surface is adopted as a key representation of the EDL structures. We split the channels into a set of bins (of 0.05 Å in width) along the direction perpendicular to the

graphene surface. The averaged number density of each kind of particles (e.g., water, electrolyte ions) within a bin during the last 150ps of our MD simulations was calculated to represent the number densities ρ of the corresponding particles in a plane that ran across the centre of the bin and parallel to the graphene electrode surface. Since the distribution of particles within each plane should be statistically uniform, the resultant electric potential only depends on the distance to graphene surface (i.e., x -axis), which can be computed by integrating a one dimensional Poisson equation:

$$\frac{\partial^2 \Phi_E(x)}{\partial x^2} = -\frac{Q(x)}{2A_{sys}\epsilon_0} \quad (3.1)$$

where A_{sys} represents the surface area of graphene electrode (102 nm^2), factor of 2 counts for the double side surfaces, ϵ_0 is the vacuum dielectric constant, and x is the distance to the graphene surface. $\Phi_E(x)$ is the electric potential with the electrical potential at the graphene electrode surface taking as a reference. Note that $Q(x)$ includes the electrode charge, electrolyte ion charge, and charges of hydrogen and oxygen atoms of water molecules. The term $2A_{sys}$ in Eq.(3.1) is due to double accounting of electrolyte charges from both sides of graphene surface.

We used a numerical integration of Eq.(3.1) to obtain $\Phi_E(x)$. The $\Phi_E(x)$ in the middle of the channel ($x = \pm L/2$) was used as a reference ($\Phi_E = 0$). Since the channel is symmetrical, the $d\Phi_E(x)/dx$ value at $x = L/2$ should be equal to zero. The integral of Eq.(3.1) yields the potential $\Phi_E(x)$.

$$\Phi_E(x) = -\iint_{L/2}^x \frac{Q(x)}{2A_{sys}\epsilon_0} dx^2 \quad (3.2)$$

3.2 Results and Discussions

3.2.1 Results of electrical double layer

We normalized the number densities ρ of ions and water molecules within each bin with respect to their number densities in the bulk aqueous solution to obtain the relative number

densities ρ^* . Figure 3.2 summarizes the relative number density ρ^* of the electrolyte ions, Na^+ , K^+ , Rb^+ , Cs^+ cation and co-ion Cl^- , in different aqueous electrolyte close to the negatively charged graphene cathode surfaces. Figure 3.3 shows the results of ρ^* for the F^- , Cl^- , I^- anions and co-ion Na^+ in different aqueous electrolyte close to the positively charged graphene anode surfaces.

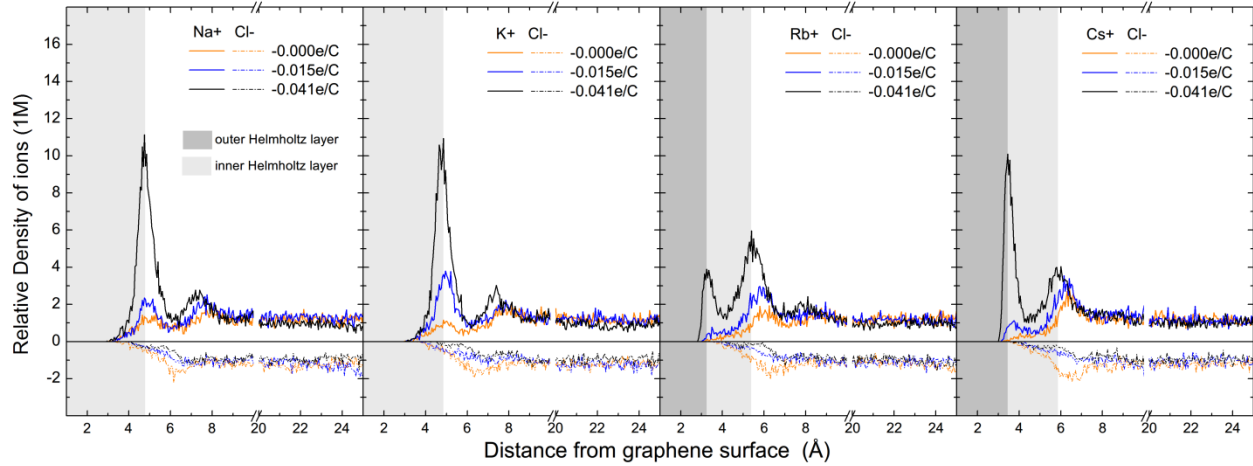


Figure 3.2 Relative number density ρ^* of different solute ions and water molecules as a function of distance from the graphene cathode surface with a charge of 0, -0.015 and -0.041 e/C-atom, respectively. For clarity, the density distributions of counter-ions are plotted on the opposite sides of the 'zero' relative density axis as the dashed line. The shaded regions represent the IHL and OHL layers.

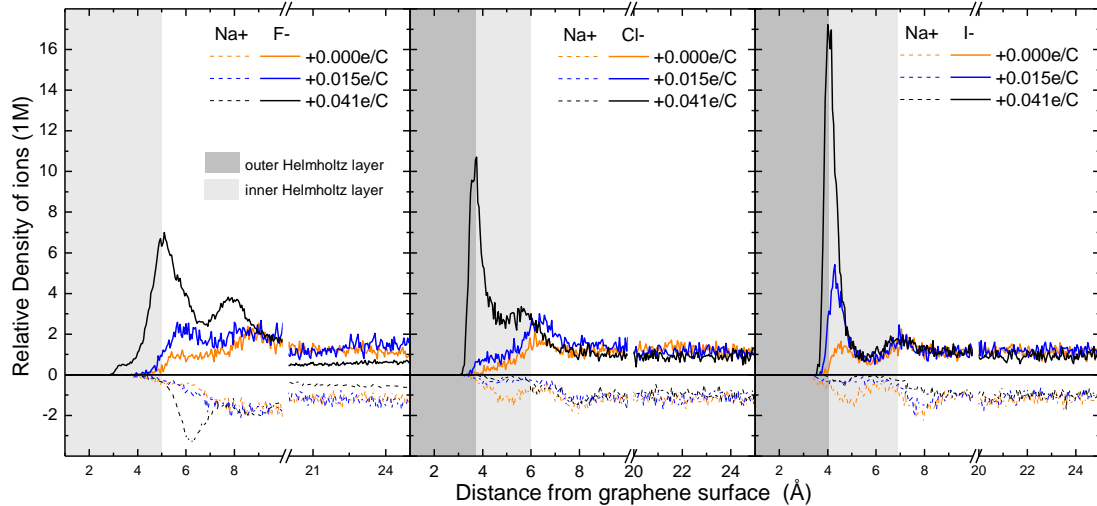


Figure 3.3 Relative number density ρ^* of different solute ions and water molecules as a function of distance from a graphene anode surface with a charge of 0, +0.015 and +0.041 e/C-atom, respectively. For clarity, the density distributions of counter ions are plotted on the opposite sides of the 'zero' relative density axis. The shaded regions represent the IHL and OHL layers.

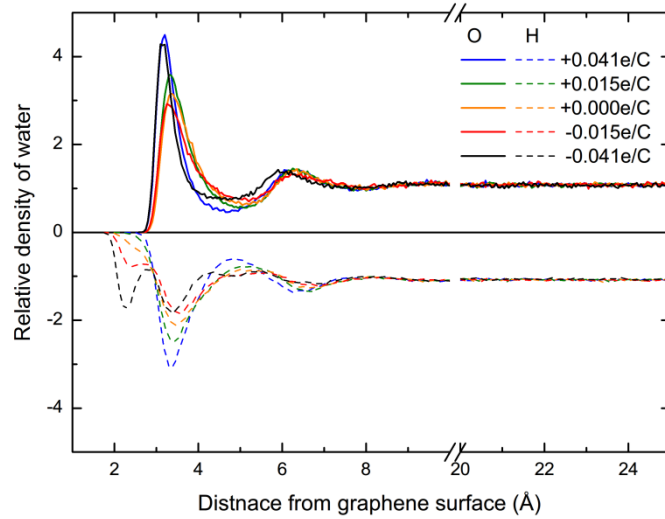


Figure 3.4 Relative number density ρ^* of water molecules of NaCl solution as a function of distance from a graphene anode surface with a charge of +0.041, +0.015, 0, -0.015 and -0.041e/C-atom, respectively. For clarity, the density distributions of Hydrogen atoms are plotted on the opposite sides of the 'zero' relative density axis. It has been found there is no obvious change of water distribution between different solutes, thus only the water distributions of NaCl solution are plotted.

The sharp density peaks of the solute ions in Figure 3.2&3.3 depict the accumulation of electrolyte ions subject to the electrical interactions from the charges on the electrode surfaces. The regions between the peaks and the electrode surface represent the impact Helmholtz layers (HLs) in the GCS model. Beyond the HLs, the ionic density gradually converges to the nominal density in the solution bulk — the so-called as diffusion layer. For our electrolyte with a relatively high concentration (e.g., 1M), the EDL substantially localized to a thickness of only 0.7-1.0 nm. This is close to the predictions of the GCS model[31, 161]. But different from the GCS model that predicts an exponential decay of concentration ρ to the bulk solution starting from the electrode surface, in Figs. 2 and 3, a multi-layered oscillated structure of ρ with declining magnitudes was observe instead: a cation density peak often followed by an anion density peak[55, 140-142, 162, 163] (Figure 3.2) and vice versa (Figure 3.3). This is because the first electrolyte ion layer next to the graphene electrode often contains more opposite charges than the electrode surface charges. A following ion layer with opposite charges is thus needed for compensation. Such an over-screening effect has been identified to be unfavourable in a sense that it effectively increases the distance between electrode and counter-ions and thus decreases the capacitance[78, 164-166].

In Figure 3.4, there is a clear water layer adsorbed on the graphene surface. The relative number density ρ^* of O atom is about 3 to 4 depending on the strength of electric field (caused by the charged electrode). It has been called as “the first water layer”[108, 167, 168]. It is worth noting that we did not see noticeable influences of the different electrolyte ions on the number density of the first water layer. For clarity, we only show the ρ^* of water in electrolyte with Na^+ and Cl^- solute ions in Figure 3.4.

The formation of the first water layer can be attributed to the interruption of continuous hydrogen-bonded network by the graphene electrode and the hydrophobic nature of graphene layer. For the case of zero electrode charge, the relative number density is about 3 and the distance to the electrode surface is about 3.2 Å in Figure 3.4, which agree with other MD results very well[140-142, 169]. We also found that the density profiles of hydrogen atoms are slightly closer to the electrode surface than those of oxygen atoms in the charge neutral case. It indicates that the water molecules next to the graphene having one of its OH bond pointing toward the surface. And the hydrogen peak beyond the first water layer responded with the surface charge density with growth of magnitude in the negative charge surface, and verse vice. It represented the titling of water molecule on the first water layer.

In Figure 3.2, cation Na^+ and K^+ have their first density peaks behind the first water layer. This is because that they have a strong hydration shell and the interaction with the water layer will hinder the movement of hydrated cation towards the charged graphene surface[52, 57]. This concentrated cation layer is often called as the outer Helmholtz layer (OHL)[37, 90, 170]. The EDL structures of Rb^+ and Cs^+ cations in Figure 3.2, in contrast, are very different. For the graphene cathode with a surface charge of -0.015e/C , a new ionic density peak appears next to the electrode surface, overlapping with the first water layer. Note that at -0.015e/C , the IHL ionic density peak for Rb^+ is more like a shoulder (different from Cs^+). Careful inspections on the molecular structures of this layer concluded the formation of partially dehydrated cations. It is well know that large ions often have a weak hydration shell so that when being subject to external electrical field or nanoconfinement dehydration would

occur[139, 171-174]. Such a partially dehydrated ion layer is often called as inner-Helmholtz layer (IHL)[170, 175]. We then call the cation density peak behind IHL as OHL.

Figure 3.3 shows the EDL molecular structures for the electrolyte anions being subject to the electrical field from the positively charged graphene anode. It is interested to notice that the three types of anions exhibit distinctive behaviours. The F^- anion only forms OHL, which is similar to Na^+ and K^+ but with a much larger distance from electrode surface. For the Cl^- anion, only an OHL formed under a low surface charge of $+0.015e/C$. The result is contrast with the previous report of specific absorption of Cl^- on metal surface[176]. Whereas an IHL emerged under a relatively high surface charge of $+0.041e/C$. But for I^- anion, even under a zero electrode surface charge, a clear IHL ionic density peak can be seen in Figure 3.3. This is because that I^- anion has a strong affinity to graphene owing to its pronounced lone-pair electron donicities. The similar particular ions/electrode affinity has been discovered in the interaction between IL/graphene sheets with particular ion structure and orientation. The special absorption of Ionic Liquids (IL) into graphene or graphite surface has proven to increase the mobility and the capacitance of EDLs[66-68]. Generally, the EDLs structure in anode is more vulnerable under the electric field than that in cathode. Because the asymmetry of charge distribution in water molecule lowers the hydration energy of anion[176].

The EDL structures, such as the thickness of the impact Helmholtz layer (i.e., the position of the ionic density peaks) and the values of relative number density ρ^* , exhibit a clear dependence on the size of solute cation/anion. The results are shown in Figure 3.5. Overall, the thickness of the IHL/OHL increases with the increase of cation/anion size that can be attributed to the steric effects. The IHL, which only formed for the relative large ions such as Rb^+ , Cs^+ , Cl^- , has a smaller thickness than those of the OHLs, due to the fact that the partial dehydrated ions can penetrate through the first water layer. But for the magnitude of ρ^* of the OHLs, there is no clear trend on the ionic size under an electrical field caused by the electrode surface charge of $0.015 \pm e/C$. It appears that the K^+ ion has the largest ρ^* value of OHL than other cations and the Cl^- has the largest ρ^* value of OHL than other anions. But with increasing the graphene surface charge to $0.041 \pm e/C$, the ρ^* of OHL shows a clear trend:

decreasing with the ionic size. Note that the ρ^* of the IHL shows an opposite trend: increasing with the increase of the ion size. This could also be understood in terms of dehydration: it is relative easier for larger ions to dehydrate subject to an electrical field and consequently a more profound accumulation near the charged electrode surface (i.e., IHL) and subsequently the OHLs become depleted.

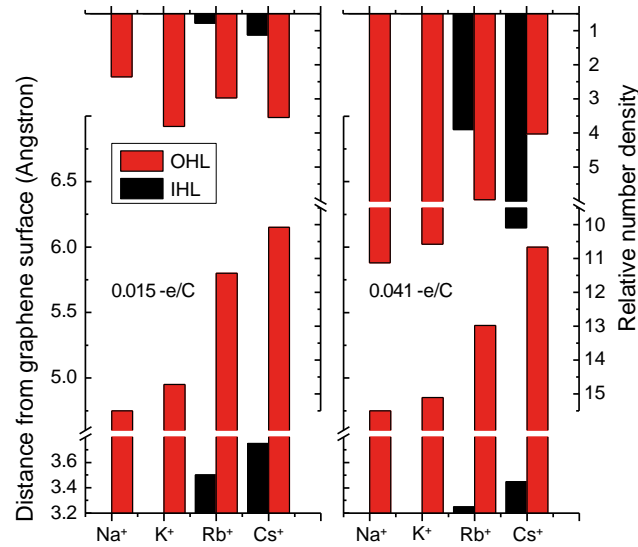


Figure 3.5 Distance of the IHL and OHL ionic density peaks to the graphene cathode surface and relative number density of IHL and OHL peaks, subject to an electrode surface charge of -0.015 e/C or -0.041 e/C .

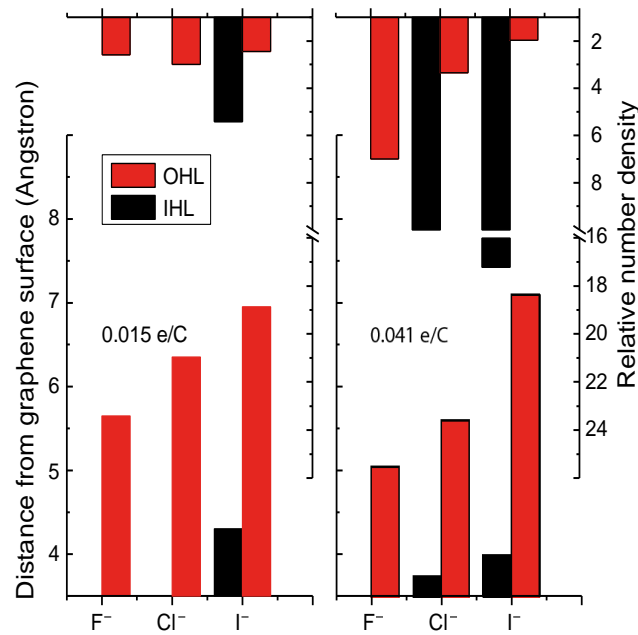


Figure 3.6 Distance of the IHL and OHL ionic density peaks to the graphene anode surface and relative number density of IHL and OHL peaks, subject to an electrode surface charge of $+0.015 \text{ e/C}$ or $+0.041 \text{ e/C}$.

The electrical field from the graphene surface charges can significantly change the structures of the IHL/OHLs and the first water layers. In most cases, an increase of the electrical field leads to a reduction of the IHL/OHL thickness (*i.e.*, ions moving toward the charged graphene surface) and an enhancement of the relative number density of the IHL/OHL layers (Figure 3.5&3.6). Generally, the enhancement of the ρ^* is not proportional to the increase of charges on electrode, *e.g.*, 5 times increase of ρ^* of the Na⁺ OHL subject to a 2.67 times increase of electrode surface charges. The reduction of the IHL/OHL thickness of the F⁻ and Cl⁻ anion is more significant than that of the cations. In addition to the ionic size effect, the different charges of ions could make some contributions as well. For example, F⁻ has a similar size to K⁺, *i.e.*, 1.36Å vs. 1.33Å, but the OHL thickness reduction is much more significant. It could be attributed to the weaker hydration shell formed around an anion, owing to the polarity and structure of water molecules[172]. An enhanced electric field thus could lead to a more significant motion of the hydrated anions.

But in Figure 3.5, we observed two exception cases. First, strength of the electrical field has a negligible effect on the thickness of OHL of Na⁺ and K⁺ cations. Second, for I⁻, increasing the electrical field results in an increase of the thickness of the OHL and the reduction of the ionic ρ^* . We believe that the interaction between the strong hydration shell of the small ion, like Na⁺ and K⁺, and the first water layer has prevented the motions of the ionic layers being subject to an increased electrical field. Thus no clear reduction in the IHL/OHL thickness is observed (Figure 3.5). For the I⁻ anion, the significantly increased ρ^* IHL could generate a repelling force overwhelming the attraction force from the graphene surface charges. It prevents the accumulation of counter-ion on OHL, thus induces the increased thickness of OHL and decreased ρ^* of OHL.

The electrode surface charge also alters the molecular structure of the first water layer, via the partial re-orientation of the water molecular dipoles. The negative charge on the graphene cathode lead to the water dipole pointing toward the graphene surface, which is manifested by the more profound hydrogen atom density peak in front of the oxygen atom density peak in Figure 3.2. For a graphene anode (Figure 3.3), the positive charges result in

an opposite effect. The tendency of water molecule dipole pointing toward surface at zero charge is cancelled out, resulting in a retraction of hydrogen density peak with reference to that of oxygen atom in Figure 3. The changes in the water molecular network are expect to alter the dielectric of aqueous solution and hence the capacitance values. This effect will be discussed in next section.

3.2.2 Results of electrical double layer

In this section, the capacitance values of the graphene ECSCs with different aqueous electrolyte and under different electrode surface charges are calculated, based on our MD simulation results using Eq.(3.1)&(3.2). A comparison is made with our experimental results. The influences of EDL structures and dielectrics of H₂O solvent on the values of capacitance are examined.

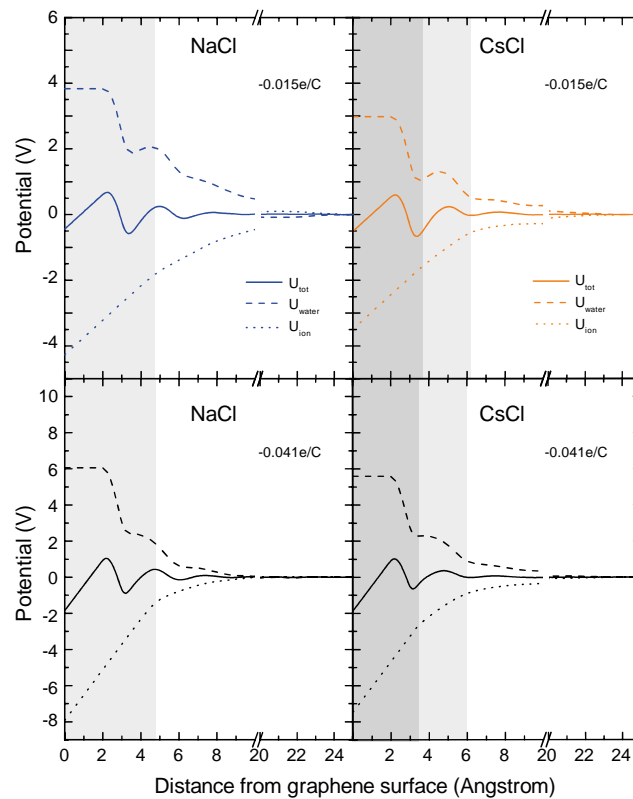


Figure 3.7 The variation of electric potential as a function of the distance from the graphene cathode surface for the NaCl and CsCl electrolyte under two charging cases: $-0.015e/C$ and $-0.041e/C$. The total electrical potential U_{tot} is decomposed into two components: U_{ion} calculated from the EDL including cathode surface charge and the ionic density $\rho(x)$, and U_{water} calculated from the water molecular dipole.

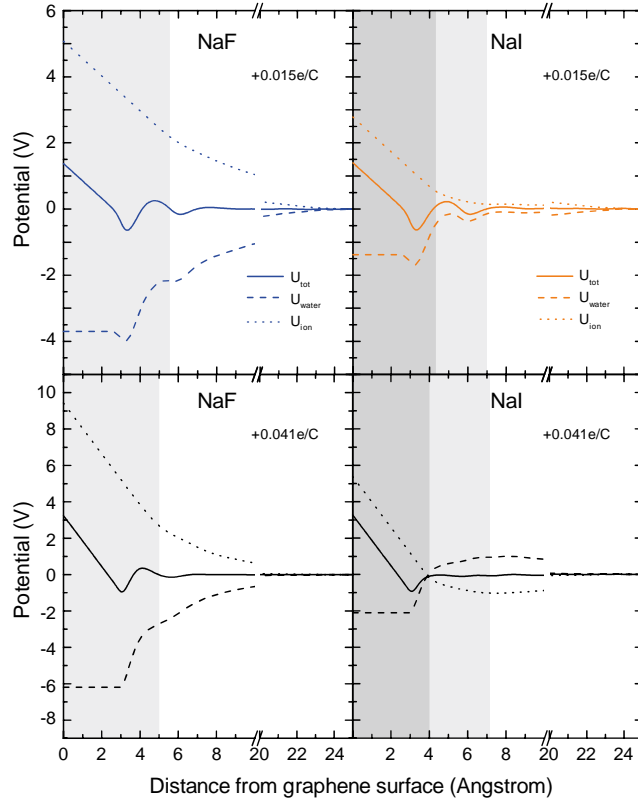


Figure 3.8 The variation of electric potential as a function of the distance from the graphene anode surface for the NaF and NaI electrolyte under two charging cases: $+0.015e/C$ and $+0.041e/C$. The total electrical potential U_{tot} is decomposed into two components: U_{ion} calculated from the EDL including cathode surface charge and the ionic density $\rho(x)$, and U_{water} calculated from the water molecular dipole.

Figure 3.7 shows the calculated electric potentials for the NaCl and CsCl electrolyte as a function of the distance from a graphene cathode with a surface charge of $-0.015e/C$ or $-0.041e/C$. Figure 3.8 summarizes the results for NaF and NaI electrolytes next to a positively charged graphene with a surface charge of $+0.015e/C$ or $+0.041e/C$. The electric potential in the bulk solution was taken as a reference. To clearly reveal the roles of the EDL structures and the water solvent to the supercapacitor capacitance, the electric potentials U_{tot} were decomposed into the contributions from the ionic EDL (U_{ion}) and water solvent (U_{water}) separately. The U_{ion} is computed based both the charges on graphene electrode and ion density $\rho(x)$. The U_{water} is computed by only considering the polar moments of water molecules.

With the obtained U_{tot} , we can calculate the capacitance value of the graphene ECSCs and the results are summarized in Table 3 and 4. First, it is a surprise to notice that the specific

capacitance values of the cathodes and anodes have a small dependence on the electrolytes types, despite the significantly different EDL structures observed in Figs. 2 and 3. The calculated capacitance in simulation (100~280 F/g) is really close to the experiment report (130~200F/g) [35, 134, 135]. And my group colleague has demonstrated that the capacitance of cathode would be 100F/g higher than that of anode in three electrode setup. Second, increasing the cathode surface charge density leads to significantly reduced specific capacitance values (Table 3)[59], which is also consistent with capacitance reduction in three electrode setup. Third, the specific capacitance values of graphene anodes are only about 1/3 of those of the cathodes. In experiment the similar capacitance different (about 100F/g) has been found between cathode and anode[177]. In the following, we will provide an in-depth analysis to understand these phenomena.

Table 3.3 Specific capacitance of a graphene cathode immersed in different electrolytes, with a surface charge of $-0.015\text{e}/\text{carbon}$ or $-0.041\text{e}/\text{carbon}$.

(F/g)	$-0.015\text{e}/\text{C}$	$-0.041\text{e}/\text{C}$
NaCl	279.8	176.4
KCl	282.7	175.5
RbCl	254.9	178.2
CsCl	237.9	174.5

Table 3.4 Specific capacitance of a graphene anode immersed in different electrolyte, with a surface charge of $0.015\text{e}/\text{carbon}$ and $0.041\text{e}/\text{carbon}$.

(F/g)	$+0.015\text{e}/\text{C}$	$+0.041\text{e}/\text{C}$
NaF	89.14	99.47
NaCl	90.53	100.9
NaI	87.70	99.66

To gain deep understandings, we summarize the electric potential results in Table 3.5 for the graphene cathodes. Despite the distinct EDL structures of NaCl and CsCl aqueous electrolytes shown in Figure 3.2 and discussed in the previous section, their electric potential profiles almost overlap with each other (Figure 3.5), indicating a similar capacitance value (Table 3). For the U_{ion} , a linear relation is observed up to 4–6 Å from graphene surface. This region corresponds to the OHL/IHL in Figure 3.2. Since it is equivalent to a parallel plate capacitor composed of the Helmholtz layer and the charged electrode, the electric potential

exhibit a nearly linear relation. Beyond that in the diffusive layer, U_{ion} gradually approaches the reference state (i.e., zero in bulk electrolyte). The overall drops of U_{ion} for NaCl and CsCl solution in this case are 4.267V and 3.496V (Table 3.5), respectively. This is as expected because the Cs^+ is closer to graphene electrode than the Na^+ cation as shown in the EDL structure (Figure 3.2), leading to a lower potential drop. As expected, the U_{water} has an opposite sign against the ionic potential drop due to its dielectric nature. The U_{water} exhibits a significant oscillation. A flat electric potential is observed in the water depletion region (between the graphene and the first water layer). The dipoles caused by the reorientation of water molecules being subject to external electric field (Figure 3.2) results in the sharp potential drop in U_{water} from 2 to 3 Å. The small recovery of the potential corresponds to the drop of water density after the first water layer in Figure 3.3. In the diffusion layer, the U_{water} gradually reduces to the reference potential level. The total water potential drop is on the order of +3 to +4V. After the compensation of water dielectric, the overall electric potential change is almost the same for Cs^+ and Na^+ , despite their significantly different U_{ion} as results of the different EDL. The electric potential of other electrolyte: Rb^+ or K^+ in the cathode side is quite similar as that of Na^+ or Cs^+ . Over here, the dielectric water molecule plays a critical role in determining the overall potential drop in EDLs[178], which is equally important in the anomalous capacitance enhancement in sub-nm channel[179].

Table 3.5 The electric potential drop (in unit of V) in inner Helmholtz layer, outer Helmholtz layer and the diffusion layer next to a graphene cathode with a charge of $\pm 0.015\text{e/C-atom}$ or $\pm 0.041\text{e/C-atom}$.

		NaCl		KCl		RbCl		CsCl	
Surface charge (e/C)		+0.015	+0.041	+0.015	+0.041	+0.015	+0.041	+0.015	+0.041
IHL	U_{ion}					1.837	4.539	1.960	4.795
	U_{water}	—		—		-1.954	-3.440	-1.884	-3.319
	$U_{\text{ion}}+U_{\text{water}}$					-0.117	1.099	0.07608	1.477
OHL	U_{ion}	2.454	6.485	2.501	6.571	1.004	2.198	0.9704	1.777
	U_{water}	-1.796	-4.195	-1.798	-4.284	-0.3477	-1.188	-0.5556	-1.388
	$U_{\text{ion}}+U_{\text{water}}$	0.6580	2.290	0.7034	2.287	0.6559	1.009	0.4148	0.3889
ε_{HL}		3.739	2.832	3.556	2.873	5.272	3.196	5.970	3.522
Diffusion layer	U_{ion}	1.813	1.433	-0.1605	0.9625	0.6514	0.8837	0.5653	0.8972
	U_{water}	-2.033	-1.871	-0.1094	-1.387	-0.7097	-1.159	-0.5412	-0.8905
	$U_{\text{ion}}+U_{\text{water}}$	-0.2220	-0.4382	-0.2700	-0.4249	-0.0583	-0.2748	0.02412	0.006682
EDL	U_{ion}	4.267	7.918	2.341	7.533	3.492	7.621	3.496	7.469
	U_{water}	-3.829	-6.066	-1.907	-5.671	-3.011	-5.787	-2.981	-5.598
	U_{tot}	0.4379	1.852	0.4334	1.862	0.4806	1.834	0.5150	1.872
ε_{EDL}		9.744	4.275	5.401	4.046	7.266	4.155	6.788	3.990

Figure 3.8 and Table 3.6 show the electric potential at the anode surface for F^- , Cl^- , and I^- electrolyte anions. A much smaller ionic potential drop U_{ion} is observed for I^- anion, e.g., 2.780V in comparison with the 5.074V for NaF, under an electrode surface charge of $+0.015\text{e/C-atom}$. This can be understood in terms of the much closer IHL/OHL of I^- to the electrode surface than those of F^- (Figs. 3 and 5). But after the compensation of water dielectrics, the overall potential drops are almost the same, which is similar to the observations in Figure 3.7. It should be noted that that a significant drop in U_{water} occurs between 3 and 4 Å (after the first water layer) in Figure 3.8, which is different from the case in Figure 3.6, *i.e.*, 2-3 Å (in front of water layer). This can be attributed to the different water

molecules re-orientation subject to the different charges from electrodes. The U_{ion} , U_{water} , and U_{tot} for all types of anions are summarized in Table 3.6.

Table 3.6 The electric potential drop (in unit of V) in inner Helmholtz layer, outer Helmholtz layer and the diffusion layer next to a graphene anode with a charge of $\pm 0.015\text{e/C-atom}$ or $\pm 0.041\text{e/C-atom}$.

		NaF		NaCl		NaI	
Electrode Surface charge(e)		+0.015	+0.041	+0.015	+0.041	+0.015	+0.041
IHL	U_{ion}				-5.163		-5.553
	U_{water}	—		—	1.771	—	2.175
	$U_{\text{ion}}+U_{\text{water}}$				-3.393		-3.378
OHL	U_{ion}	-2.931	-6.817	-3.070	-1.038	-2.235	-0.8537
	U_{water}	1.520	3.498	1.503	1.090	0.9040	0.8829
	$U_{\text{ion}}+U_{\text{water}}$	-1.412	-3.319	-1.567	0.05220	-1.331	0.02921
ϵ_{HL}		2.076	2.053	1.959	1.856	1.679	1.913
Diffusion layer	U_{ion}	-2.1428	-2.709	0.1602	-0.2605	-0.5459	1.022
	U_{water}	2.1801	2.743	0.05339	0.3619	0.4794	-0.9515
	$U_{\text{ion}}+U_{\text{water}}$	0.03727	0.03405	0.2136	0.1014	-0.06644	0.07056
EDL	U_{ion}	-5.074	-9.526	-2.910	-6.462	-2.781	-5.385
	U_{water}	3.700	6.241	1.556	3.223	1.383	2.106
	U_{tot}	-1.374	-3.285	-1.353	-3.239	-1.397	-3.278
ϵ_{EDL}		3.693	2.900	2.151	1.995	1.991	1.643

The previous discussions indicate that in addition to EDL structure, the water solvent also play a crucial role in determining the capacitance values, which can be understood in terms of the dielectric constants in the EDL (ϵ_{EDL}). Table 3.5 and Table 3.6 list the calculated results. We found a general trend that a larger ion tends to have a lower ϵ_{EDL} : $9.744 (\text{Na}^+) > 7.266 (\text{Rb}^+) > 6.788 (\text{Cs}^+)$ and $3.693 (\text{F}^-) > 2.151 (\text{Cl}^-) > 1.991 (\text{I}^-)$. It agrees with the trend in bulk salty water[180]. It is such a reduction in dielectric constant that cancels out the beneficial of a thinner EDL (thus a small U_{ion}) for those large ions Rb^+ , Cs^+ , Cl^- , and I^- , leading to the small differences in the calculated capacitance values.

We also calculated the dielectric constant in the Helmholtz layer ϵ_{HL} and found that in most cases the obtained values were much smaller than the ϵ_{EDL} : 3.739 vs. 9.744 for Na^+ , 2.075 vs. 3.293 for F^- and so on. This can be understood by the well-known effect of “dielectric decrement”, *i.e.*, dielectric of salt water decreasing with the increase of ion concentration[181]. It is also found that for the large ions, such as Rb^+ , Cs^+ , Cl^- , and I^- , the difference between the ϵ_{EDL} and ϵ_{HL} is relatively small. It indicates that the IHL/OHL indeed dominates EDL for these types of ions, which is consistent to the molecular structures of EDLs discussed in previous section. The largest ion considered in this paper I^- is an exception case: the value of ϵ_{HL} slightly larger than the ϵ_{EDL} , *i.e.*, 1.91 vs. 1.64. It is inconsistent with the “dielectric decrement” phenomena in the bulk salty water. It may suggest some other factors that could also influence the dielectric in such a thin EDL layer ($< 7\text{--}10 \text{ \AA}$).

In Table 3.2&3.3, the calculated capacitance of graphene anodes is only one half to one third of cathodes. These results agree with our experimental observation quite well. However, graphene anode with NaCl or NaI solute has a smaller U_{ion} than that of the most of graphene cathodes (Table 3.5 and 3.6). The low capacitance value must be attributed to the water solvent. Indeed, after compensation of U_{water} , the total potential drop U_{tot} of the anode becomes much larger than the U_{tot} of the cathodes, as seen in Table 3.6. The calculated ϵ_{EDL} and ϵ_{HL} of the aqueous electrolyte in graphene anode side (Table 3.6) are significantly lower than the results for that in cathode (Table 3.5). This might be understood in terms of the re-orientation of the water molecules in the first water layer under different electrical fields. As shown in Figure 3.4, the water molecules in the first water layer naturally intend to have one of its O-H bonds pointing toward the graphene surface (with zero charge). At the anode surface, the positive charge has to overcome such a tendency to re-orientate the OH bond pointing away from the anode surface. In other words, the water molecules near the anode surface are relatively more difficult to be polarized and thus the dielectric constant is smaller.

The effects of electric field on the values of capacitance have been manifested in two aspects. First, a higher density of electrode surface charges will enhance the attraction of

counter-ions towards graphene electrode and thus reduce the thickness of EDLs (Figure 3.5&3.6). The increase of U_{ion} is less proportional to increase of the surface charges, suggesting a tendency of capacitance enhancement. But subject to a high electric field, the water molecules are highly orientated (or ordered) thus has less capability to re-orientated further, the dielectric constants are smaller than those in the weak electric field (the so-called “dielectric saturation”)[31, 81, 182], which can be seen in our calculated results in Table 3.5 and 6. Overall, for graphene cathode, the dielectric saturation effect dominates. We, therefore, obtain significantly reduced capacitances, i.e., about 30-40% reduction (Table 3.3). But for anodes, these two contributions almost cancel out each other. There is, therefore, a negligible change in capacitance (Table 3.4).

3.3 Conclusion

In summary, MD simulations have been carried out to systematically study the EDL molecular structures at the graphene cathodes with some typical monovalent electrolyte ions and the resultant capacitance under different electrode surface charges. We found that the larger ions, such as Rb^+ , Cs^+ , Cl^- and I^- , will be dehydrated subject to the external electric field and penetrate the first water layer to form the impact Helmholtz layer (IHL). In contrast, the small ions, such as Na^+ , K^+ , and F^- , no IHL will be formed. Generally, thickness of the IHL and OHL layer increases with the size of ions, while the ionic number density of the IHL shows an opposite trend with respect to the ionic size. The formation of IHL will effectively reduce the thickness of the whole EDL. Thus the electric potential drop U_{ion} from the electrode surface to electrolyte bulk is smaller for the large ions. However, because of the low dielectric constants for the electrolyte with large size ions, the overall potential drop U_{tot} is almost the same, rendering a similar capacitance, which is consistent to our experimental results. It is worth noting in the Helmholtz layer there is a lower dielectric constant than the average value of whole EDL. This can be partly understood in terms of high density in HL. Our results also suggest the size confinement could also make a non-negligible contribution. Our simulation results also show that graphene anode has $\frac{1}{2}$ to $\frac{1}{3}$ capacitance of the counterpart cathode, which also agree with our experimental results very well. It is primarily

due to the different dielectric constants. We believe that the water re-orientation in the first water layer could play an important role here.

Our results also show that the electrical field from the electrode (or the surface charges) also plays crucial role in EDL molecular structure and the capacitance values. Subject to higher electrical field, the ionic density peaks tend to get closer to the electrode surface, leading to a reduced IHL/OHL layers thickness. Thus U_{ion} is less proportional to the increase of the surface charges, suggesting an increasing trend of capacitance. However, due to the observed dielectric saturation effect (i.e., reduced dielectric constant under a high electric field), the calculated capacitance of cathode is reduced and the capacitance of anodes almost remains unchanged. This provides clear explanations to our experimental results.

Chapter 4: Continuum modelling of Diffusion on CCG membrane

4.1 Introduction

Since the synthesis of CCG hydrogel membrane, it has been demonstrated to be an excellent candidate for gas/solution separation. The pioneer studies have revealed the promising selectivity and diffusivity enhancement of GO or graphene membrane [12-16]. Benefiting to the feasible synthesis methods, the microstructure of the CCG membrane (i.e. the graphene flake size and shapes, interlayer spacing, corrugation size, nanopore size and distribution, and so on) could be varied by changing the synthesis methods[183-186] or some external treatment (*e.g.*, KOH solution activation[34, 187]). Our group has developed the novel capillary compression method[36] to control the interlayer spacing of the CCG hydrogel membrane, which is crucial to control the property of mass transport in nanoscale.

Till now, there are numerous efforts to improve the performance of CCG membrane via changing its microstructure in experiments. But all available experimental efforts are still at the qualitative or semi-quantitative level. There is almost no understanding of the microstructure and ion transport progress in the CCG membranes. Such information is crucial to interpret and understand the ion transport properties across the CCG membranes in experiments. There are two primary difficulties.

The first difficulty is the collapse of the hydrated microstructure during the characterisation. The nanochannels embedded in graphene membrane has a characteristic length scale $< 10\text{nm}$. To directly detect such small structures requires high resolution electron microscopes. However, using such techniques usually destroys the microstructure in the hydrated state. For the complicated porous materials, the gas molecule is usually taken as the probe to indirectly investigate the inner microstructure. Although the complicated theoretical model has been successfully established to reproduce the microstructures of the porous carbonaceous materials (*e.g.* the amorphous carbon or activated carbon),[188] the microstructure of CCG hydrogel membrane is different from the conventional carbonaceous materials. Moreover, the conventional investigation methods (*i.e.* Brunauer–Emmett–Teller method) also required a dehydration process that usually breaks the hydrated microstructure.

The second difficulty is the lack of a good representative microstructure model to statistically describe the complex CCG membranes. There are several different types of nanometer sized structures that play the significant roles in the mass transport, such as the channel height among adjacent graphene layers, the gaps between graphene flakes in the same layer, the pin holes in graphene layers. How to develop a simple yet robust representative microstructure model to statistically character the microstructure of CCG membranes in experiments is a topic of great important but not explored yet.

In the present chapter, we will attempt to combine the experiment study via the capillary compression technique with continuum simulations to investigate the microstructures of the CCG membranes. In section 4.2, a brief literature review on the CCG membrane microstructure in experiments will be provided. In section 4.3, we proposed a representative microstructure model for the cascading nanoslit system embedded in CCG membrane, which include three key representative structure parameters, i.e., interlayer distance (h), trans-layer pore size (d), and distance between neighboring trans-layer holes (L). Continuum modelling based on Fick's law was carried out for this representative model with the key parameters varying in a wide range.

Owing to the development of the capillary compression technique by our group, we could roughly control the interlayer distance of the CCG membrane varied from 0.5 nm to 10 nm. Thus only the interlayer distance (h) in the representative microstructure model could be regarded as the shrinkage of CCG membrane. The membrane diffusivity D_m will be determined as a function of the key parameters. By comparing with the experimental membrane diffusivity for the KCl aqueous electrolyte through the CCG membrane sample with interlayer distances, the other two key structure parameters (L and d) are determined. It is worth noting that optimal values of these two structure parameters can reproduce 6 independent diffusion experimental results very well, indicating the success of our attempt on this crucial task.

Furthermore, in section 4.4, for the ease of usage in describing/understanding the diffusion of ions, we also tried to equate the two-dimensional representative structures to an

effective 1-D nanoslit channel with two key structure parameters, such as effective diffusion length (L_{eff}) and effective cross-section area (A_{eff}). The relationship among the key structure parameters in these two microstructure models was established.

4.2 Microstructures of CCG membrane in experiments

Before the discussion of the microstructure of CCG membrane, the structure of building blocks (CCG flakes) should be mentioned before. Firstly, the arbitrary shapes of the CCG flakes with the dimensions of $1\mu\text{m}$ was reported from the AFM image (Figure 4.1a[189]). However the nanoscale characteristics on the CCG flakes cannot be determined by the conventional SEM/AFM image, which could be only revealed by the sophisticated STEM image. Figure 4.1b[190] is the magnification of CCG flakes in the STEM image. Thus we could recognize: 1) the region of the pristine graphene (sp^2 backbone) in green; 2) the region with the oxygen residual functional group in red 3) the formation of the pin-holes ($1\sim 2\text{ nm}$) on the CCG flake with the removing of carbon atoms in blue.

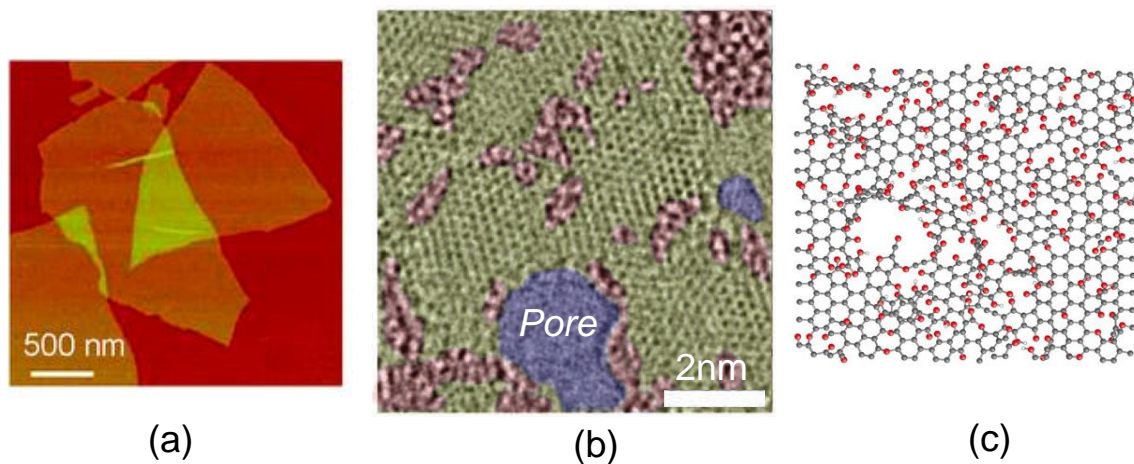


Figure 4.1 The structure of CCG: (a) The typical size of CCG flake in AFM image[189]; (b) The STEM image confirmed the modelling hypothesis with defects (blue region) and oxygen functional group (red region)[190]; (c) The MD simulation result[191] indicates the large amount of defect and functional groups on CCG she. Note that the size of pore ($\sim 2\text{nm}$) is much smaller than that of whole graphene flake ($\sim 1\mu\text{m}$) and the existence of pin-hole cannot be identified by the conventional SEM/AFM image.

Besides, the MD simulation in Figure 4.1c[191] has not only confirmed the formation of pin-hole and the residual functional group via the reduction process, but also the introducing of the corrugation on the CCG flakes with the magnitude of $\sim 1\text{ nm}$ [192]. Thus, four issues (e.g. sp^2 backbone, residual functional group, pin-hole and corrugations) would be accounted

for the CCG flakes structure. However, the conventional electron microscope instrument could only provide a qualitative understanding and there is no statistic average for the individual CCG flakes.

With the qualitative understanding of CCG flakes, we could propose a staggered layer-by-layer microstructure of CCG membrane. The formation of the free-standing CCG membrane would be a competition of two terms [36, 193, 194]: 1) The collapsed of the π - π interactions and 2) the repelling of the residual functional group (via the hydrogen bond with water). As the representative of the soft materials, the structure of the flexible CCG flakes could be easily deformed by these two terms. Thus, even the structure of the every graphene flake is known, the assembly of CCG membrane is still puzzling.

It is worth noting that the pin-hole was found to play a crucial role in the performance of the CCG membrane[195], which would be unavoidable via the chemical process. Figure 4.2a[195] is the schematic of the pristine graphene (perfect) membrane where the mass transport has to bypass the whole graphene flakes and permeate through the edge nanogap with the adjacent graphene layers. However, with the presence of the pin-hole (Figure 4.2b[195]), the length of the transport path would be significantly reduced in the nanoporous graphene membrane and the amount of transport channel would also be considerably increased. Thus the tiny pin-holes in 1~2nm was regarded to significantly enhance the performance (diffusivity) of GO membrane, which has also been demonstrated for the supercapacitor with KOH activated CCG membrane [34, 187].

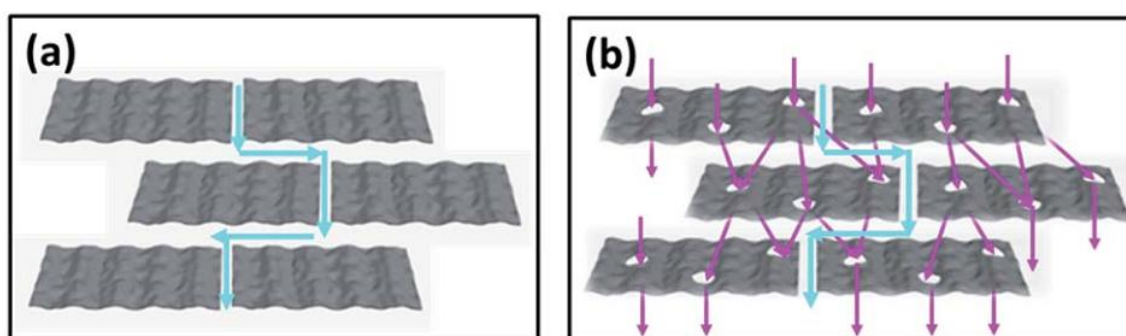


Figure 4.2 Schematic view of mass transport through (a) pristine graphene membrane and (b) nanoporous graphene membrane [195].

With the awareness of the staggered graphene structure, the various attempts have been taken to characterize the microstructure of the graphene membrane. The discoveries and difficulties in each method would be discussed separately in the following section.

For the conventional electron (SEM/TEM) microscopes, the removing of the hydrated water between the CCG flakes is necessary. However this water in CCG membrane was found to be the critical issues for the gelation of the CCG membrane. With the dehydration of CCG membrane, the interlayer distance would also be considerably decreased into 0.5 nm[35]. Namely, the microstructure of the hydrated CCG membrane would be destroyed via the dehydration process. Although the freeze-dried methods with the water crystallization in advance was employed to remain the large interlayer distance of CCG membrane, the formation of the ice within the CCG membrane still modified the microstructure with the changes of the membrane thickness [35].

Even employing the good dehydration process with the minimum damage of microstructure, the SEM/TEM images could only reveal the surface or the cross-section image (Figure 4.3 [35]). From the SEM image, we only confirmed the staggered layer-by-layer structure of membrane but there was no further understanding of the inside detailed.

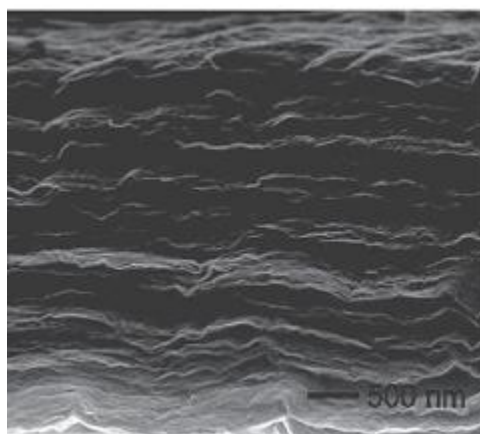


Figure 4.3 The SEM image of the cross-section of the freeze-dried CCG membrane[35].

Beyond the electron microscopy, the indirect XRD or neutral scattering has been proposed, which are favourable to probe the material in the hydrated state. Unfortunately, the spectrum of XRD or neutral scattering cannot provide the nanoscale details of the

microstructure, only giving the statistic average result for the microstructure. Figure 4.4a[35]&b[177] are the XRD spectrum and the neutron scattering spectrum respectively. Only the average interlayer distance (h) and its broadness distribution could be determined from the XRD spectrum. However, there is no further understanding of the microstructure has been drawn from the neutron scattering spectrum.

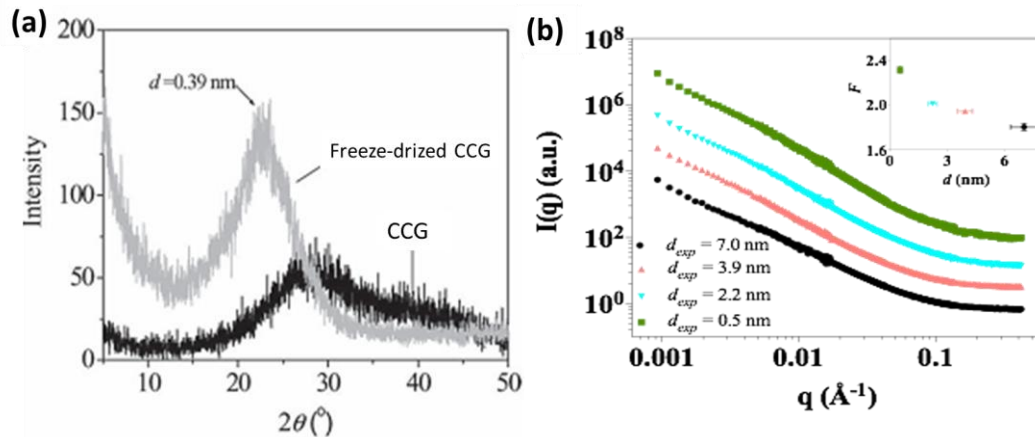


Figure 4.4 The indirect measurements of CCG membrane: (a) XRD spectrum[35], the grey and black curves indicates the spectrum of the Freeze-dried CCG and the hydrated CCG membrane, respectively;[35] (b) neutron scattering spectrum[177], the curves in different colours represent the result of CCG with different interlayer spacing.

Beyond the aforementioned methods, the gas probe methods (*e.g.*, Brunauer-Emmett-Teller (BET)) have been proposed to determine the microstructure of the CCG membrane. Although the specific surface area of the freeze-dried CCG membrane could be provided via the BET methods [196], the detail understanding of microstructure (the confinement condition of the solution) was still beyond the capability of gas adsorption process.

Taken together, the microstructure of the flexible CCG membrane could be easily modified during the dehydration process and the current measurement methods could only provide the general idea of the CCG flakes or the interlayer distance of CCG membrane. For the detail microstructure, other novel experimental method is required to probe the hydrated CCG membrane. Thus, the diffusion of KCl solution through the CCG membrane, employed by my colleagues would be a non-destructive method to study the microstructure of CCG membrane.

4.3 Representative microstructures of cascading nanoslit system embedded in CCG hydrogel membranes

4.3.1 A two-dimension CCG structure model

As mentioned before, the complex 3D network of the CCG membrane is still obscured beyond the conventional measurement instrument and there is no reasonable model which could provide the quantitative understanding of mass transport inside the CCG membrane. Hence, we proposed a very preliminary model with only three key geometrical parameters: the lateral size (L), aperture size (d) and channel height (h).

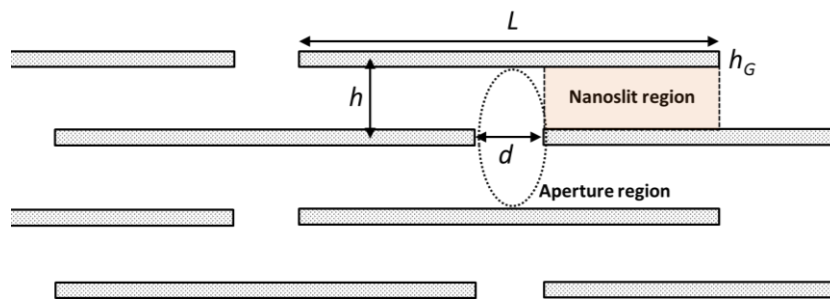


Figure 4.5 The schematics of the staggered model in continuum modelling: the long dashed sheets indicate the position of graphene sheet. h_G is the thickness of individual graphene flake (0.335nm)

The lateral size of the graphene flake (L) would be about transport path of mass in each layer. Thus for pristine graphene membrane, L would be about the size of the individual graphene flake ($\sim 1\mu\text{m}$). For CCG membrane, the nanopore would significantly reduce L . d would be the diameter of nanopore or edge nanogap with the adjacent sheet, h is defined as the mean interlayer spacing measured in experiment (0.5~10nm). h_G would be the thickness of graphene sheet. Due to the large channel height ($h = 10\text{nm}$), we could proposed all the graphene sheets are separated giving $h_G = 0.335\text{nm}$.

As marked the dashed rectangular region in Figure 4.5, the region between the two parallel graphene sheets is defined as the nanoslit region where the mass transport in nanoslit region could be regarded as that in a 1-D nanochannel. The length of transport path in nanoslit region is determined by L and the transport channel size is determined by h . However the region surrounded by the dotted line is named as the aperture region, where the transport process is rather complicated. Obviously, the novelty of the mass transport through

the staggered CCG membrane originated from the presence of the aperture region. Otherwise, the mass transport could be regarded as the transport in the conventional 1D nanochannel with L and h .

4.3.2 Continuum simulation models

Once the 2D CCG structure model has been proposed, we could calculate the mass transport property of membrane under the different configuration. The continuum simulation of diffusion process was carried out by using the COMSOL Multiphysics software. The COMSOL software is a powerful commercial continuum modelling tool which has been widely adopted in academia and engineering field for mechanical design, electromagnetics modelling, fluidic study, electro-chemical modelling and so on.

The complex staggered graphene hydrogel microstructure could be simplified as a combination of repeated 2D CCG structure model with 3 key parameters, graphene lateral size, L , aperture opening size, d and channel height, h , the dimension of microstructure in experiment are still unknown. Hence a series of study will be done for all reasonable ranges of configuration where $8 \leq L \leq 1000$ nm, $1 \leq d \leq 20$ nm and $0.5 \leq h \leq 12$ nm. We performed a series of the modelling with varied L , d and h to create a 3D data space (19x6x6).

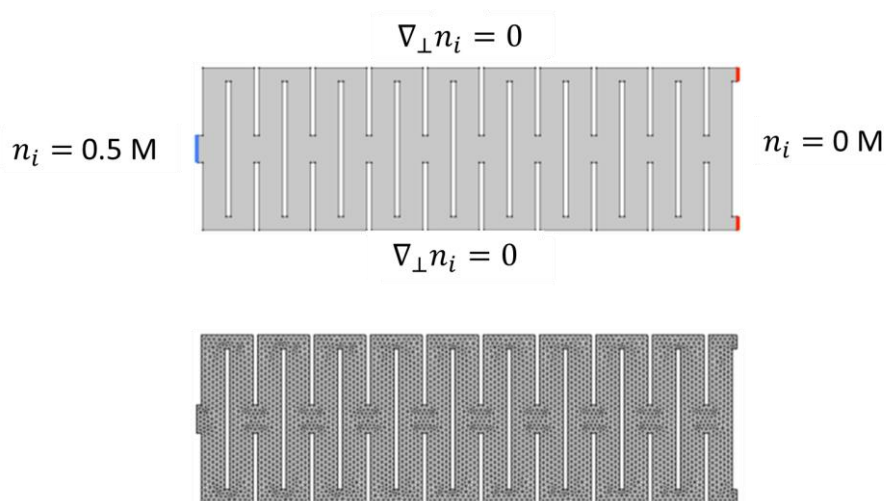


Figure 4.6 The 2D continuum modelling system with 20 layers of graphene sheets with $L = 10$ nm, $h = 2$ nm and $d = 4$ nm. (a) The shadow region represents the cascading flow network within graphene hydrogel. The left and right end is fixed with the constant concentration difference for entrance (blue) and exit (red) respectively. (b) The mesh structure in the COMSOL continuum modelling.

Figure 4.6 was an example of my continuum diffusion study with $L = 10\text{nm}$, $h = 2\text{nm}$ and $d = 4\text{nm}$. The grey region in Figure 4.6a represented the flow voids within the porous graphene hydrogel and the thin white plates represent the impermeable graphene sheets. The system was consisted by 20 layers of graphene flake with the thickness (h_G) of 0.335nm

The KCl solution is one of the most widely used aqueous electrolyte solution in nanofluidic community. There are two clear advantages, (1) the hydrated K^+ and Cl^- ions have the similar size and (2) their diffusion coefficients are very close ($D_{\text{K}^+} = 1.84\text{E-}5 \text{ cm}^2/\text{s}$ and $D_{\text{Cl}^-} = 1.91\text{E-}5 \text{ cm}^2/\text{s}$) [9]. Due to the Columbic attraction, the K^+ cation and Cl^- anion should diffuse together in pairs. Hence the continuum modelling of KCl solution could be simplified as a diffusion of neutral particle through the graphene membrane. The diffusivity of the neutral particle was set as $1.85\text{E-}5 \text{ cm}^2/\text{s}$, similar as the experiment data of 0.5M KCl solution[197].

The bottom part of Figure 4.6 was the corresponding mesh structure of COMSOL modelling. The mesh was built automatically by COMSOL software and it has been refined dense enough to ensure the convergence of the result. In the inner domain, the governing equation was merely the Fick's first law, Eq.(4.1):

$$\frac{\partial n_i}{\partial t} = D_i \nabla^2 n_i \quad (4.1)$$

Where n_i and D_i is the local concentration and diffusivity of particle type i .

By employing mirror boundary condition, the top and bottom layer could be set to be the same as the inner impermeable electrolyte/graphene interface, Eq.(4.2).

$$\nabla_{\perp} n_i = 0 \quad (4.2)$$

Besides, the constant concentration difference ($\Delta n = 0.5 \text{ M}$) was applied on the entrance and exit of membrane, as marked in Figure 4.6a.

Once the governing equations and the boundary conditions were established in the COMSOL software, the time-dependent modelling was performed for the varied geometric parameters, giving the 19x6x6 3D data space. During time-dependent modelling, the permeate flow rate, $S(t)$ was recorded over time until the system reach the stationary state ($\Delta S(t)/S(t) < 10^{-6}$). Then, the diffusivity of membrane could be calculated as:

$$D_m = \frac{S(\infty)}{\Delta n} \frac{L_m}{A_m} \quad (4.3)$$

Where L_m and A_m is the thickness and the cross-section area of CCG membrane; $S(\infty)$ is the stationary permeation flow rate and Δn is concentration differernt cross the membrane (0.5 M)

4.3.3 Membrane diffusivity from continuum simulations

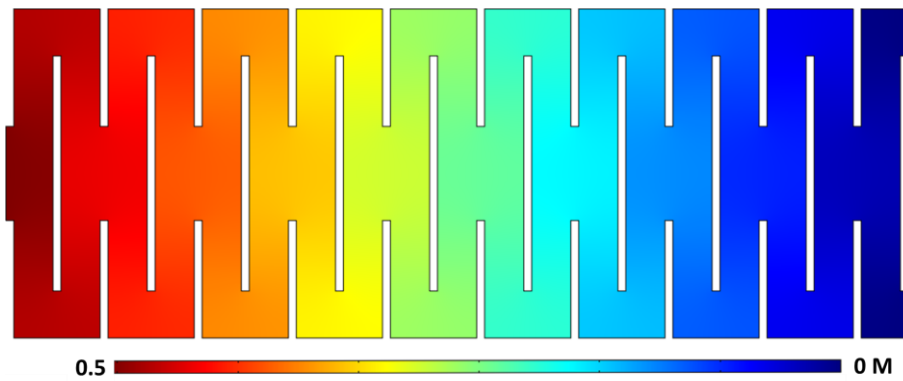


Figure 4.7 The concentration profile of 2D COMSOL modelling in steady state where $L = 10\text{nm}$, $h = 2\text{nm}$ and $d = 2\text{nm}$.

Once we established the continuum model in COMSOL software, we could calculate the diffusivity of the membrane for the arbitrary microstructure. Figure 4.7 was the typical example of concentration profile in steady state with $L = 10\text{nm}$, $h = 2\text{nm}$ and $d = 2\text{nm}$. Obviously, there was a continuous concentration gradient from left (0.5M) to right (0M) in the steady state. For the steady state, we could calculate the drop of ion diffusivity inside the membrane, defined as $D_0/D_{m,sim}$.

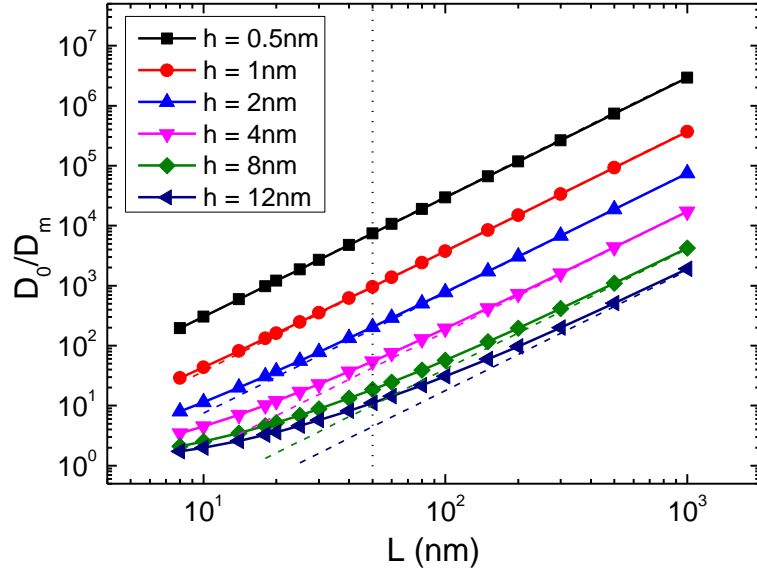


Figure 4.8 D_0/D_m as a function of lateral size (L) with $d = 2\text{nm}$: The dots with different colors represent the variation of channel height (h) from 0.5 to 12nm. The dashed trendlines were based on the estimation of Eq(4.4). The vertical dotted line locates at $h = 50\text{ nm}$. Note that the result of D_0/D_m is mainly depends on the size of graphene flake and. For small lateral size ($L < 50\text{nm}$), D_0/D_m result varies nonlinearly with lateral size, especially for large channel height.

Figure 4.8 was the result of D_0/D_m for different lateral size and channel height with $d = 2\text{nm}$. The dashed trandlines in Figure 4.8 are defined as:

$$\frac{D_0}{D_m} \approx \frac{h}{4(h - h_G)} * \frac{L^2}{h_G^2} \quad (4.4)$$

Namely the major mass transport was determined by the nanoslit region (h and L) with the negligible influence of the aperture region.

Intuitively, the D_0/D_m increased with the size of graphene sheet. Because, the transport path was increased to bypass the larger graphene sheet. And the D_0/D_m also increased with the reduction of the channel height. Because, the amount of transport channel was reduced with the compression of the CCG hydrogel membrane.

Although L and h is the dominant factors, determining the transport process in graphene membrane, it didn't mean the result D_0/D_m always varied linearly with L and h . Only for the large lateral size ($L > 50\text{nm}$) or very small channel height ($h < 1\text{ nm}$), we could observe that the experimental D_0/D_m located on the linear trendlines (dashed lines in Figure 4.8). In these cases, the long and parallel nanochannel (nanoslit region) dominates the transport process,

namely the parallel diffusion model. However for small lateral size, the D_0/D_m varies nonlinearly with L , indicating the influence of the aperture region. Especially for large channel height ($h > 10$ nm), the bottlenecking of the aperture opening ($d = 2$ nm $\ll h$) enhanced the nonlinear relationship.

Beside the dominant parameters of L and h , the influence of aperture size (d) to D_0/D_M for the different L and h was plotted in Figure 4.9. For clarity, all data in the same curve was rescaled with the case of $d = 20$ nm. Namely the normalized D_0/D_M in each curve was the result compared that at $d = 20$ nm. For the same L and h (Figure 4.9a), the D_0/D_M increased with the reduction of d that decreased the amount of transport channel. But at constant L but larger h , the decrease of d gave a higher enhancement of D_0/D_M .

For constant $L = 50$ nm (Figure 4.9b), the magnitude of D_0/D_M expanded with the reduction of d . At $h = 12$ nm, there was an almost 2 times increase of D_0/D_M . However at $h = 0.5$ nm, the magnitudes of increase was just 1.2 times. It indicated that at small channel height, the result D_0/D_M was less sensitive to the size of the aperture opening. For the constant channel height $h = 12$ nm (Figure 4.9), the magnitudes of D_0/D_M expansion also increased with the reduction of L .

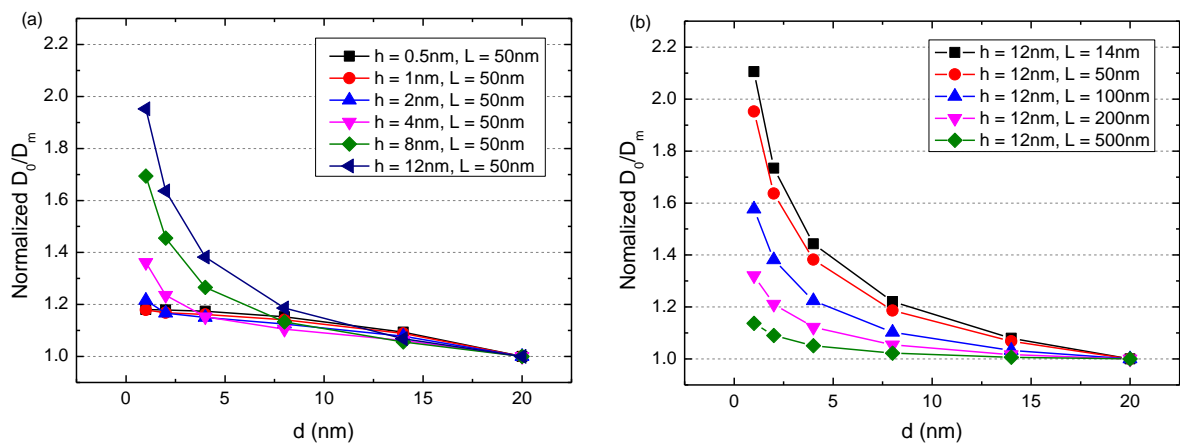


Figure 4.9 D_0/D_M results against the aperture size: (a) different dots represent different channel height, when $L = 50$ nm; (b) different dots represent different lateral size when $h = 12$ nm. Note that for clarity the result D_0/D_M is normalized with the case of $d = 20$ nm.

Figure 4.9 indicated the influence of d would be enhanced at large channel height and small lateral size which was similar to the region of the nonlinear scaling in Figure 4.8. At this region ($L < 50$ nm and $h > 4$ nm), the influence of aperture region (bottleneck of mass

transport), namely the size of d would be enhanced, which could be removed by chemical/electro-chemical etch in the experiment.

4.3.4 Determining the key structure parameter via fitting experimental results

After we finished the modelling for all reasonable geometry configurations, a 3D data space (19x6x6) for D_m is obtained for different L , h and d . The transport property in any arbitrary configuration of 2D model could be predicted from the 3D data space (linear interpolation). Thus, a reverse Monte Carlo (rMC) calculation was taken to locate the optimized geometry parameters that provide the minimum difference ($\min\{\Delta\}$) between the modelling and experimental result:

$$\min\{\Delta\} = \min \sum_{i=1} \left[\frac{\tilde{D}_{m,\text{sim}}(L, d, h_i)}{D_0} - \frac{D_{m,\text{exp}}(h_i)}{D_0} \right]^2 \quad (4.5)$$

where h_i is the known interlayer spacing of the i th CCG membrane measured in the experiment, $D_{m,\text{exp}}(h_i)$ is the experimentally measured diffusivity of the CCG membrane with the interlayer spacing of h_i . $\tilde{D}_{m,\text{sim}}(L, d, h_i)$ is the linear interpolation of $D_{m,\text{sim}}$ calculated from the 3D data space with a set of L , d and h .

Note that the direct minimization of the difference for diffusivity drop (D_0/D_m) gave a good fitting at very small channel height ($h < 1\text{nm}$), but large deviation at large channel height. Reversely, the minimization of D_m/D_0 enhances the weight of difference at large channel and provide a good fitting of diffusivity at large channel height except for very small one ($h < 1\text{nm}$). Thus by accounting the limitation of continuum model in small channel ($< 2\text{nm}$) and the influence of the corrugation of CCG flake ($\sim 1\text{nm}$), the geometrical parameters predicted by D_m/D_0 minimization could better describe the microstructure of CCG hydrogel membrane.

During the rMC calculation, 100 loops were performed. And the result (linear interpolation) with a million pairs of varied L and d were compared in each loop. The range of parameters in the first loop was $8 \leq L \leq 1000 \text{ nm}$ and $1 \leq d \leq 20 \text{ nm}$ with known h_i as

measured in the experiments. The range of parameters was gradually reduced for each loop. The values of L and d at the top 20% fitting in the previous loop were taken as the parameter ranges for the next loop. The ranges of L and d were found rapidly convergent after 10 loops (Figure 4.10), and the values of L and d were able to be determined after 100 loops, giving $L = 49.760$ nm and $d = 1.586$ nm. Based on the prediction by the reverse Monte Carlo calculation, the extra 2D modelling was taken with $L = 50$ nm and $d = 1.6$ nm to verify the prediction of the reverse Monte Carlo calculation.

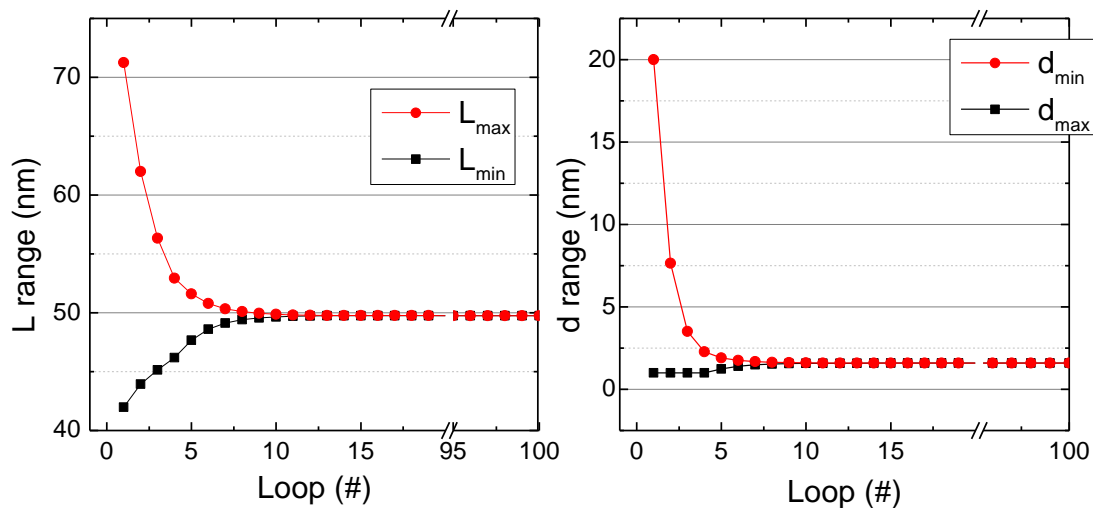


Figure 4.10 Determination of the geometrical variables L and d through a reverse Monte Carlo method. The parameters L and d were found to rapidly converge after 10 loops as shown in the figures.

Once finishing the aforementioned calculation and modelling, we could compare the result with the experimental data. Figure 4.11 plotted the comparison of membrane diffusivity (D_m) between theory study and the experiment as a function of h . The unity dashed line indicates the perfect fitting between theory and the experiment.

It clearly showed the prediction by the reverse Monte Carlo calculation fitted relatively well with the experimental data except for the very small channel height ($h < 1$ nm). The deviation may attribute to the corrugation of graphene flake (~ 1 nm) and the special solution/wall interaction in the nanochannel, which is not accounted into the classic thermodynamics framework. Thus in order to minimize the deviation between the theory and experiment, the extra effort and hypothesis should be taken to improve the classic

thermodynamics framework in nanochannel and optimize the modelling structure that complicated the modelling system.

Compared with the other graphene membrane microstructure study with constant h , the development of the capillary compression method could provide a continuous change of interlayer distance. At large h (10 nm), the classic thermodynamics framework was assumed to be valid for ion diffusion. Then with the shrinkage of membrane, ion transport would gradually deviate from the classic thermodynamics framework. Thus, the orange curve in Figure 4.11 was similar to the mentioned trend and the large deviation is located at aforementioned limitation of continuum modelling ($< 2\text{nm}$).

Owing to the result of multi-channel-height, the single and converged solution for certain L and d could be derived from the rMC calculation. Moreover, the CCG membrane samples with large h weighted heavier during the rMC calculation. Thus, we could conclude that, the microstructure of the arbitrary CCG membrane could be determined by combining the capillary compression methods in experiment and the rMC calculation of the 3D data space ($19\times6\times6$).

To verify the prediction by the rMC, the extra 2D modelling has (green curve in Figure 4.11) been taken and compared with the experimental data. The curve of the extra 2D modelling owned the similar tendency as that of linear interpolation except for $h < 1\text{ nm}$. It seems that the obtained 3D data space was dense enough to provide the good prediction of the modelling result for $h > 1\text{ nm}$. For $h < 1\text{ nm}$, the significantly changed of D_m at small interlayer distance required a denser data space. However with the account of the limitation of continuum modelling and less weight of the small nanochannel in rMC calculation, the deviation between the linear interpolation and modelling at $h < 1\text{ nm}$ would be acceptable.

After the verification of the rMC calculation, the result lateral size (L) was found to be significantly lower than the dimension of the individual CCG flakes ($\sim 1\text{ }\mu\text{m}$). Because, the nanoscale pin-hole ($1\sim 2\text{ nm}$) on CCG flakes has significantly reduced the transport path in the CCG membrane. However, the invisible nanoscale pin-holes in the conventional SEM/TEM image were usually ignored among the community. Thus the distance between the

pin-holes (L) rather than the dimension of the CCG flakes should be taken to evaluate the mass transport process inside the CCG membrane. As to the aperture size (d), the modelling result was consistence with the STEM image and the MD simulation. The nanoscale pin-hole played a crucial role on the ions transport inside the CCG membrane.

In summary, the classic thermodynamic framework was accurate enough to describe the ion transport inside the CCG membrane, at least for $h > 1\text{nm}$. By combining the continuous changes of the graphene thickness and the 3D data space prediction, we could propose the abstract 2D model for the arbitrary CCG membrane microstructure. And there was no significantly difference between the linear interpolation and the modelling calculation. The work in the present section provided a novel method to identify the microstructure of the CCG membrane which cannot be achieved before.

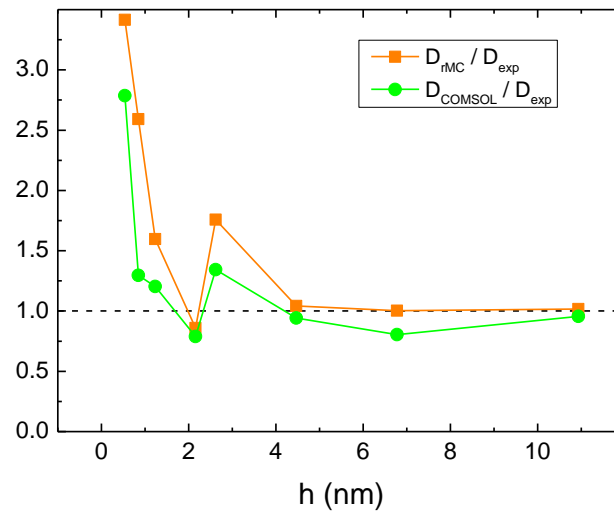


Figure 4.11 the comparison of D_m between experiment and COMSOL modelling result as a function of channel height h : The orange squares represent the ratio between the linear interpolation (D_m) of $L = 49.760\text{ nm}$ and $d = 1.586\text{ nm}$ and the experiment. The green circles indicate the ratio between COMSOL modelling result of $L = 50\text{ nm}$ and $d = 1.6\text{ nm}$ and the experiment. Note that both interpolation and COMSOL modelling fit relatively well with experimental data except for the very small channel height.

4.3.5 Effective length and cross-section area

Although the simplified 2D staggered CCG model has been proposed and verified in the previous section, the result of three key parameters still cannot directly reflect the performance of the mass transport process inside the membrane. Thus the time-lag methods were employed in this section, which were widely employed to characterize the

microstructure of the complex porous materials. It could simplify the complex 3D network into a straightforward effective 1D channel. Figure 4.12[198] illustrates the transfer from the complex network into the simple effective 1D channel

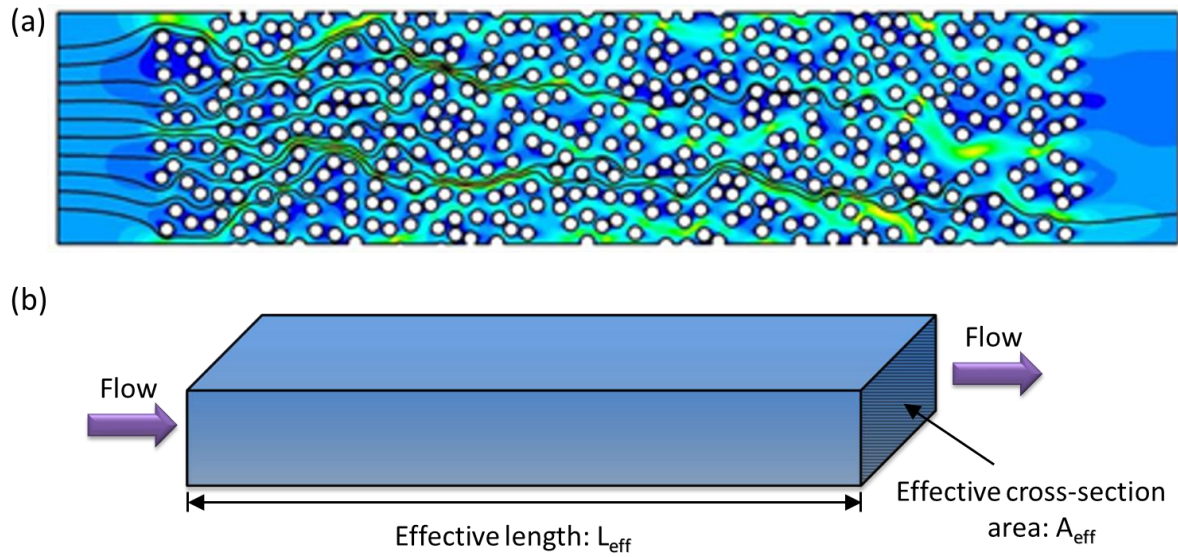


Figure 4.12 The transport through porous materials: (a) computer modelling for water flow in porous materials[198]; (2) The equivalent 1D model. Note that the intuitive 1D model is consisted by two components: the effective length, L_{eff} and the effective cross-section area, A_{eff} . The transport through the complex porous materials could be regarded as the mass transport through that effective 1D channel.

Two geometrical parameters are included in the effective 1D channel: 1) effective length, L_{eff} and 2) effective cross-section area, A_{eff} . Thus, the permeability/diffusivity drops of membrane could be derived as:

$$\frac{D_0}{D_m} = \frac{\tau}{\varepsilon_t} = \frac{L_{eff}}{L_m} \bigg/ \frac{A_{eff}}{A_m} \quad (4.6)$$

Where D_0 is the diffusivity of mass in bulk state; D_m is the measured diffusivity of membrane; τ , defined as L_{eff}/L_m is the tortuosity and ε_t , defined as A_{eff}/A_m is the porosity of membrane; L_m and A_m and is the thickness and cross-section area of membrane.

In the time-lag methods, two reservoir bathes are separated by the porous membrane where both the concentration of membrane and permeate bath is zero and the concentration in the feed bath is Δn (inset of Figure 4.13). Under the concentration difference, the mass

diffuse through the membrane into the permeate bath. The accumulation of the mass, $Q(t)$ in the permeate bath is recorded over time, as plotted in Figure 4.13.

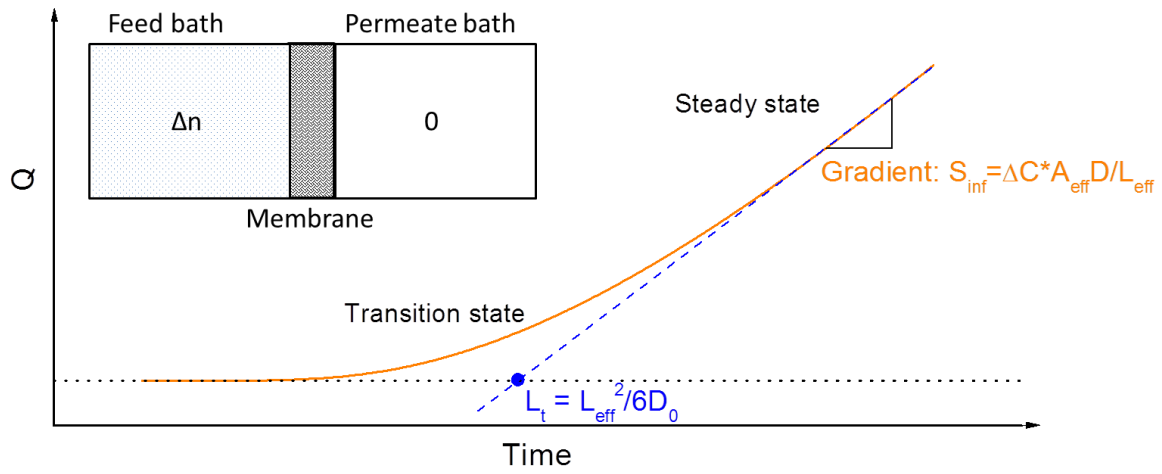


Figure 4.13 The example of time-lag methods: The accumulation of mass in permeate bath. The dot line indicate the position of $Q = 0$, the blue dashed line is the asymptote of steady state. The intersection with zero line is lag time, L_t , and the gradient of the dashed line is denoted as S_∞ .

Initially, there is a transition state with the gradually increase the accumulation of mass in the permeate bath. Then it transfer into a steady state with the constant gradient (i.e. permeate flow rate). If time is longer enough, $Q(t)$ curve would be found to be overlapped with the asymptote. And the intersection of the asymptote with the X-axis ($Q = 0$) is coined as the Lag time (L_t).

Thus the effective Length and effective cross-section area of membrane could be derived from Eq.(4.7) and Eq. (4.8):

$$L_t = \frac{L_{\text{eff}}^2}{6D_0} \quad (4.7)$$

$$\frac{S_\infty}{\Delta C} = D_0 \frac{A_{\text{eff}}}{L_{\text{eff}}} \quad (4.8)$$

Where D_0 is the diffusivity of mass in bulk solution; L_t is the lag time of diffusion; S_∞ is the gradient of $Q(t)$ in in steady state; Δn is the concentration difference cross the membrane.

Figure 4.14a plotted the variation of L_{eff} over L for different channel height with $d = 2$ nm. Intuitively, L_{eff} was dependent on the lateral size L . At large L (>200 nm), the L_{eff} curves located on the dashed asymptote, $L_{eff} = 0.5*(N-1)*L$, where the transport path was almost dependent on the lateral size. However with the decrease of the lateral size, the result L_{eff} deviated from the asymptote, especially for the large h . The increase of channel height also increased the magnitudes of deviation. As shown the inset of Figure 4.14a, with the increase of h , the mass transport transferred from the parallel diffusion model into the diagonal diffusion model (inset of Figure 4.14)

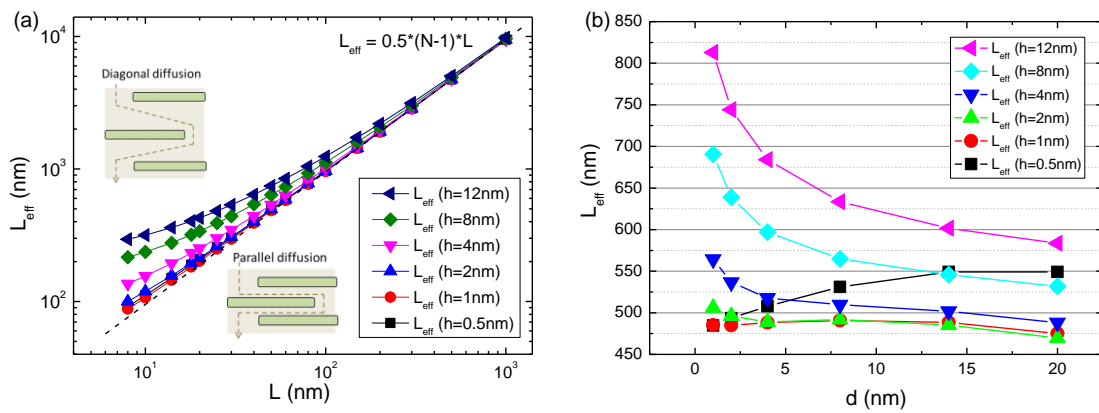


Figure 4.14 Effective diffusion length: (a) L_{eff} against different lateral size, L , where $d = 2$ nm. The dashed line indicates the equation of asymptote, $L_{eff} = 0.5*(N-1)*L$; Note that the result L_{eff} deviated from the asymptote for large h and small L ; (b) L_{eff} against different d , where $L = 50$ nm.

Figure 4.14b plotted influence of d on the variation of L_{eff} over different h at $L = 50$ nm. We found the different scaling law for large and small channel height:

- 1) At $h \geq 2$ nm, the decrease of aperture size would significantly increase L_{eff} . The sensitive of the scaling law increased with the channel height. Compared with the large channel height, the small aperture opening ($d \ll 2*h$) became the bottleneck of mass transport process. It elongated the lag-time, namely L_{eff} . For the same d , the larger the channel height the more serious the bottleneck would be.
- 2) Reversely, for very small channel height ($h = 0.5$ nm), L_{eff} decreased with d . This counterintuitive variation was attributed to the “double channel height” of the aperture region. In this case, the volume of aperture is much larger than that of the nanoslit. For the diffusion of the Time-lag methods, L_{eff} , namely the lag-time L_t

would be roughly the time to establish a constant concentration gradient inside the porous membrane. Thus with the reduction of d , the void of the aperture region would be shrunk, giving a short periods of L_t , namely lowering L_{eff} .

Beyond L_{eff} , the amount of transport channel (A_{eff}) also determined the diffusivity of the membrane. Figure 4.15 plotted the variation of A_{eff} over L for different channel height at $h = 8$ nm. For large L (≥ 300 nm), the result A_{eff} approached a constant value, determined by the channel height. about $2 \cdot (h - h_G)$, where the parallel nanoslit region dominated the transport process. However with the decrease of lateral size ($L < 300$ nm), the result A_{eff} gradually converged to about $1.5d$. It seemed that at smaller lateral size, the influence of aperture region would be increased that modify the result A_{eff} .

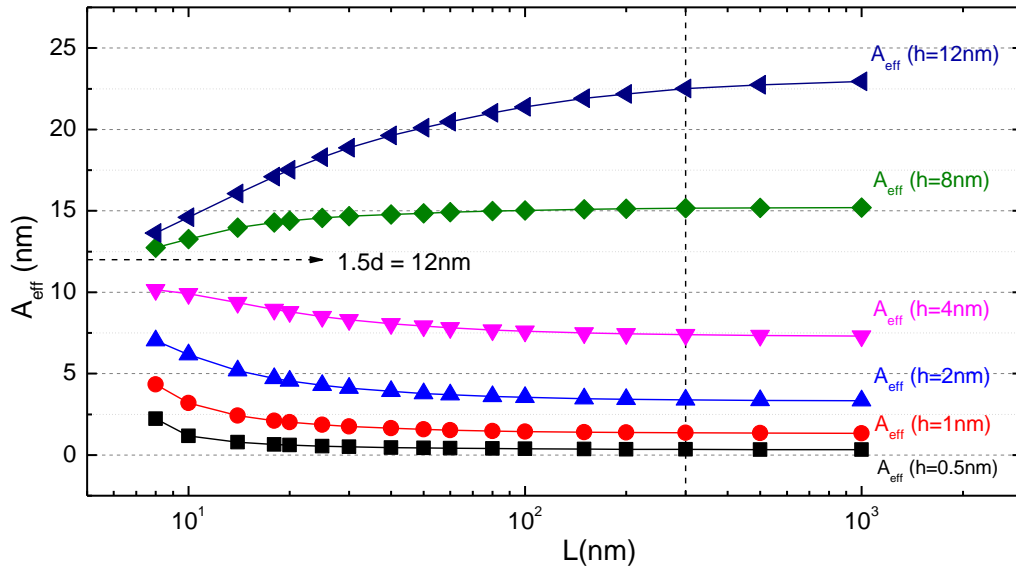


Figure 4.15 Effective cross-section area, A_{eff} against lateral size (L) at $d = 8$ nm: the vertical dashed line indicate the position of $L = 300$ nm. Note that when lateral size is much larger ($L > 300$ nm), the results approached a constant value that is determined by the channel height. However for very small lateral size, the aperture area dominates the effective cross-section and it approaches about $1.5d$.

Taken together, the influence of the aperture region would be enhanced at small lateral size ($L < 50$ nm) and large channel height ($h > 5$ nm). In these cases, the transport behaviour inside the graphene membrane cannot be simply determined from the linear equation.

As the definition of Time-lag methods, the effect 1-D nanochannel for the experimental CCG membrane samples could also been calculated. Figure 4.16 plotted the L_{eff} and A_{eff} for the COMSOL simulation ($L = 50$ nm and $d = 1.6$ nm) and experimental result. The result in

Figure 4.16a&b could be defined as the tortuosity (L_{eff}/N) and the porosity (A_{eff}/A_m) of membrane, respectively.

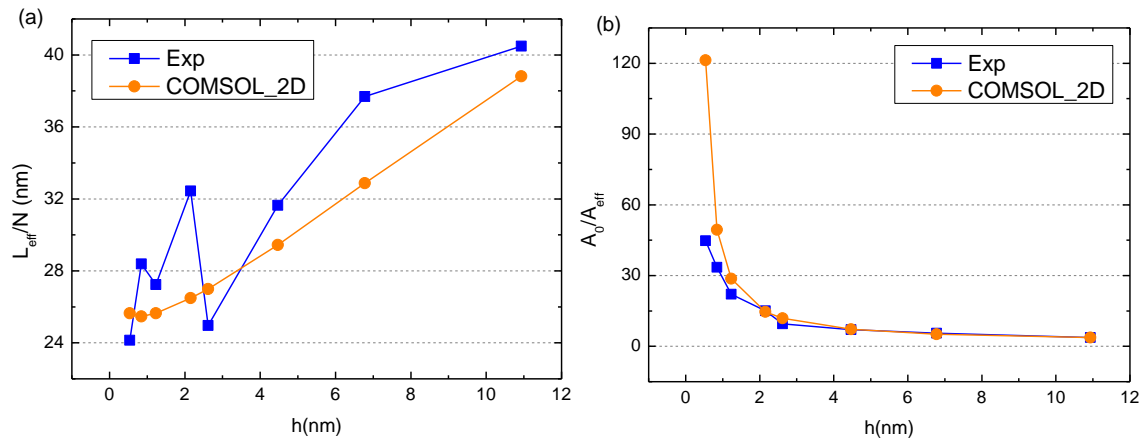


Figure 4.16 The comparison between experimental data and 2D modelling: (a) tortuosity, L_{eff}/N ; (b) porosity, the ratio between membrane size and effective cross-section area, A_{eff}/A_m . The blue square, orange circle represents the result from experiment, 2D modelling respectively.

Obviously, tortuosity in the 2D modelling was similar to that in the experiment. The experimental curve just vibrated around the modelling curve. It may attribute to the difference among the CCG membrane samples. In average, the tortuosity of membrane in modelling could be regarded to be the same as the experiment one.

However, the porosity also fitted well except for the very small channel height. The large deviation in the porosity fitting would induce the large deviation in D_0/D_m . It seems that we underestimated the transport channel in the CCG membrane at very small channel height. It may attribute to the corrugation of the CCG flakes and the strong solution-wall interaction in nanochannel.

4.4 3D model & aperiodic pin-hole arrangement

Apparently, as a preliminary study of the cascading nanoflow in the CCG membrane, the simplest 2D periodic microstructure was studied in the present Chapter. However, the ion transport in the practice CCG membrane was a 3D aperiodic network. Thus the difference between the abstract 2D model and the experimental complex 3D network should be discussed in the present section.

In 3D models, the transport path would be different from that in 2D model. Obviously the variable “transport cross-section area” would be accounted in the 3D model, with the minimum in the aperture region and the maximum in the middle of nanoslit region. The uneven distributed cross-section area would also induce the inhomogeneous distribution of driving force (“concentration or electric potential”). Thus the most vital discover in the present thesis, (the novel Binary Boundary Layers, BBLs), also the major motivation of the nanofluidics study would be consistent between 2D and 3D model. The result in 2D model would be regarded as a “projection” of the transport in 3D model. Although, some extra information in 3D model has been annihilated via the “projection”, the essential feature of the novel graphene/electrolyte interface still remained.

For the aperiodic pin-hole arrangement, the interlayer space was “cut” by the pin-hole into the different “dimension” of nanoslit regions. Obviously, the driving force (concentration and electric potential) distribution in nanoslit depends on its and neighbours “dimension”. However the feature of the novel boundary layers was still the same as that in the periodic arrangement. Thus the whole distribution in nanochannel could be regarded as an assembly of result in the periodic counterpart with different L . Intuitively, the result in the aperiodic arrangement would better represent the phenomena inside the CCG membrane (e.g. better graphene dimension “ L ”). The result in the present periodic arrangement could be accounted as a mean-field result in the practice aperiodic one. However a significant large system should be established to obtain the convergent result. Thus the aperiodic model was planned in the following study.

4.5 Conclusion

In this chapter, we performed a series of continuum modelling of mass diffusion through the staggered grapheme membrane and successfully demonstrated the classic thermodynamics theory was accurate enough to describe the diffusion in complex CCG membrane and the complicated 3D nanoporous network could be simplified as an order 2D staggered CG model.

Through the reverse Monte Carlo calculation, the geometrical parameters of 2D model could be determined, giving the similar result D_0/D_m as the experimental membrane. The prediction (linear interpolation) with $L = 50\text{nm}$ and $d = 1.6\text{nm}$ has been verified via the extra 2D modelling. There is a little deviation between two methods, except for the very small channel height ($h < 1\text{ nm}$) where the corrugation of CCG flakes and the strong solution/wall interactions were not accounted into the classic thermodynamics framework. However, the present chapter still demonstrated that the classic thermodynamic framework was accurate enough to describe the ion transport inside the CCG membrane, at least for $h > 1\text{nm}$. By combining the continuous changes of the graphene thickness and the 3D data space prediction, we could propose the abstract 2D model for the arbitrary CCG membrane microstructure, which cannot be achieved by the other methods.

Besides the experimental fitting, we also investigated the influence of geometrical parameter to the diffusion process. We found at small L and large h , the influence of the aperture area would be enhanced. For the CCG membrane, the real “lateral size” of individual graphene flake should be much less than that in the SEM/AFM images ($L = 50\text{ nm} < 1\text{ }\mu\text{m}$). Thus transport property of CCG membrane cannot be simply determined from the SEM/AFM images.

We also further simplified the 2D staggered model into an effective 1-D nanochannel with L_{eff} and A_{eff} , which could provide an intuitive insight about the mass transport through the complex membrane structure. The relationship between the key geometric parameters and the effective 1-D nanochannel were presented and discussed. And the deviation of effective 1-D nanochannel between the modelling and experiment was also studies. Due to the corrugation of graphene sheets and the strong solution-wall interaction, A_{eff} in the modelling study at $h < 1\text{ nm}$ was found to be considerably underestimated.

Chapter 5: Continuum simulation of electrophoresis on CCG membrane

5.1 Introduction

With the reveal of the microstructure of CCG membrane in the previous Chapter, the nanoscale mass transport in the CCG membrane could be quantitatively understood and manipulated. Unlike the other driving force (e.g. concentration, pressure or gravity gradient) in nanofluidics, the electric potential gradient could easily and precisely control the mass transport in nanoscale. And the electro-kinetic flow through the protein nanochannel was demonstrated to be is vital in many biological activities. Thus, the electro-kinetic nanofluidics study has been boosted among the community and many exquisite lab-on-a-chip designs have been demonstrated such as nanofluidic diode [98-101] or nanofluidic field-effect transistor [89, 107].

As the latest materials of graphene, the cascading electro-kinetic flow in graphene membrane is still a virgin territory. Our group studied the ion transport (KCl solution) through the CCG hydrogel membrane with the different interlayer spacing (h). Figure 5.1 [177] is the schematic of electrophoresis study setup in experiment. The constant electro-kinetic current was maintained and the electric potential difference through the membrane was monitored.

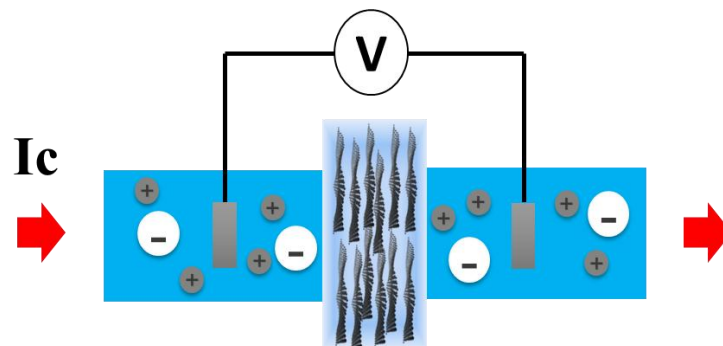


Figure 5.1 The schematic of electrophoresis study[177] on CCG membrane with constant current passing through the system and voltmeter monitoring the potential drop cross the membrane.

Compared with the conventional nanofluidics study where the channel wall is tangent to the driving force, the impermeable graphene sheet was normal to external driving force (electric potential gradient) that induced the novel cascading nanoflow. It required a distinctive description for cascading ion transport in the CCG membrane.

Hence the continuum modelling was taken in this Chapter to explain the cascading electro-kinetic flow in the CCG membrane. The similar continuum modelling has been taken to explain the ion transport in the conventional 1D nanochannel. The mechanism of cascading flow and origin of exotic scaling law would be identified through the continuum modelling.

We firstly presented the results for the neutral graphene membrane ($\sigma = 0$) in this section, then followed by the result for the charged grapheme membrane in the next one. The surface charge density ($\sigma = -2.3\text{mC/m}^2$) in the membrane was consistent with that of CCG flakes dispersion in the aqueous solution [199]. Through the comparison, we could obtain the better insight about the role of surface charge in the novel cascading electrophoresis flow.

5.2 Continuum models to simulate the electrophoresis process in CCG membrane

The continuum modelling in this Chapter was also performed via the COMSOL Multiphysics software as the Chapter 4. Owing to the discovery of 2D model in the previous Chapter, The geometry of membrane was set as the prediction with $L = 50\text{ nm}$ and $d = 1.6\text{ nm}$ but the different channel height from 0.5 to 10.9 nm , which was the same as that of the experimental CCG membrane samples

However to deal with edge effect of membrane in the electrophoresis, the different 2D model was built. Figure 5.2 is the example of the continuum electrophoresis modelling setup ($h = \text{nm}$): The membrane with 40 graphene layers (the vertical black sheet), was sandwiched by two extra reservoirs ($L_{res} = 100\text{nm}$). The numbers of layers in membrane was doubled ($N = 40$) to remove the edge effect. Thus the result in the modelling would be comparable to that of experiment ($N \approx 1000$).

Furthermore, the surface charge (σ) has been regarded to play a crucial role in the nanofluidic study. Thus the different amounts of the surface charge density were applied into the graphene sheet surface from 0 (pristine graphene) to -2.3mC/m^2 (CCG sheet).

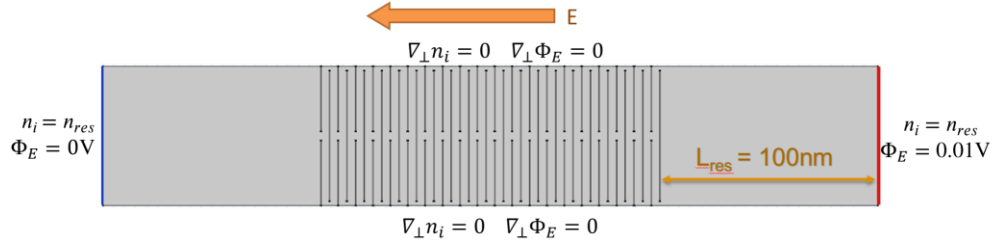


Figure 5.2 The setup of continuum electrophoresis modelling. The 40 layers graphene membrane is sandwiched by two 100nm-thickness reservoir. The arrow indicates the direction of external E-field in the system. The vertical black thin sheets indicate the position of individual graphene sheets in membrane. The equations around are the boundary condition for modelling system.

Unlike the straightforward Fick's' law for neutral mass diffusion, electrophoresis modelling is rather complicated, the Poisson-Nernst-Planck (PNP) equations was employed as the governing equation for the evolution of concentration and electric potential :

$$\nabla^2 \Phi_E = \frac{F}{-\varepsilon_0 \varepsilon_w} \sum z_i n_i \quad (5.1)$$

Where ε_0 and ε_w is the vacuum and relative permittivity of water (80 in the modelling); Φ_E is the local electric potential; z_i and n_i is the valence number and concentration of i th ions; F is the Faraday constant.

$$\frac{\partial n_i}{\partial t} = D_i \nabla^2 n_i + \mu_i z_i e n_i \nabla \Phi_E \quad (5.2)$$

where KCl solution was taken as the electrolyte for modelling, thus μ_i is electrophoresis mobility of ions ($\mu_{K^+} = 7.62 \times 10^{-8}$ and $\mu_{Cl^-} = 7.91 \times 10^{-8} \text{ m}^2 \text{ V}^{-1} \text{ s}^{-1}$)[9]; e is the elementary charge. D_i is the diffusivity of ions according to Einstein–Smoluchowski relation:

$$D_i = \mu_i k_B T \quad (5.3)$$

where T is the temperature set as 300K in modelling, k_B is the Boltzmann constant.

As marked in Figure 5.2, the boundary conditions for modelling system were set as:

1) at the CCG/electrolyte interface,

$$\begin{aligned}\nabla_{\perp} n_i &= 0 \\ (\varepsilon_w - \varepsilon_G) \nabla_{\perp} \Phi_E &= -\frac{\sigma}{\varepsilon_0}\end{aligned}\tag{5.4}$$

Where σ is the surface charge on the CCG sheet and ε_G is the dielectric constant of graphene sheet (4 in modelling). Note that the different boundary conditions were set for the electric potential and concentration field. The finite dielectric constant of graphene provided a permeable electric potential field. However, the dielectric constant of pristine graphene was still in debate (2~15) [200-202]. Fortunately, we found the variance of ε_G (2~15) had a negligible effects on the simulation result.

2) the upper and bottom periodic boundary conditions,

$$\nabla_{\perp} n_i = 0 \quad \nabla_{\perp} \Phi_E = 0\tag{5.5}$$

3) concentration and electric potential at the entrance (left end coloured in blue),

$$n_i = n_{res} \quad \Phi_E = 0 \text{ V}\tag{5.6}$$

4) concentration and electric potential at the exit (right end coloured in red),

$$n_i = n_{res} \quad \Phi_E = 0.01 \text{ V}\tag{5.7}$$

Where n_{res} was concentrations of the reservoirs varied from 0.001 to 1 M. The electric potential difference ($\Delta\Phi_E$) externally applied was 0.01 V. Thus, the strength of the electric field passing through the membrane would be comparable with that in the experiment ($7.7 \times 10^{-8} \sim 3.5 \times 10^{-5} \text{ V/nm}$) [177].

After automatically building the meshes in modelling system, we could calculate the stationary state of the electrophoresis through the graphene membrane. Once the convergence of model reached the preset (10^{-6}), the concentration, electric potential and ions flux profile could be obtained. To elucidate the influence of the external E-field, both the conditions with and without the external E-field (Equilibrium and Dynamics state) were calculated.

Once we finish the continuum modelling, the resistance of the whole system including two reservoirs and the graphene membrane could be calculated as:

$$R = \frac{\Delta\Phi}{F(J_{K+} - J_{Cl-})A_m} = \frac{1}{G_m} + \frac{2 \times L_{res}}{\kappa_0 A_m} \quad (5.8)$$

where κ_0 is the conductivity of the reservoir (bulk solution) given by $\kappa_0 = F(\mu_{K+}C_0 + \mu_{Cl-}C_0)$, J_{K+} and J_{Cl-} are the electro-kinetic fluxes of K^+ and Cl^- through the system respectively and G_m is the conductance of graphene membrane; A_m are the cross-section of the graphene membranes.

Then it is derived from the Eq.(5.9) as:

$$G_m = \left[\frac{\Delta\Phi}{F(J_{K+} - J_{Cl-})A_m} - \frac{2 \times L_{res}}{\kappa_0 A_m} \right]^{-1} \quad (5.9)$$

Then the conductivity of membrane could be calculated as:

$$\kappa_m = \frac{t_m}{A_m} G_m \quad (5.10)$$

where t_m is the thickness of the graphene membrane.

Thus, we could compare the drops of conductivity and diffusivity of the same membrane, which was defined as the scaling law of the membrane:

$$S_m = \frac{\kappa_m}{\kappa_0} / \frac{D_m}{D_0} \quad (5.11)$$

where κ_0 is the conductivity of the bulk solution (n_{res}), D_m is the diffusivity of ions inside the membrane and D_0 is the diffusivity of the bulk solution.

The discovery of the anomalous scaling law in experiment was the major motivation for the present Chapter, and the result S_m could be regarded as how much enhancement (hindrance) of ion electro-kinetic transport inside the membrane compared with the diffusion process.

5.3 Results for CCG membrane with zero surface charge

In this section, we firstly present the stationary ionic concentration, i.e., electric double layer, in the cascading nanoslit system, followed by the driving force profile (Nernst potential and electrical potential) for the ion flow. In the end, we will show the overall membrane conductivity or resistance. The relation between the membrane conductance with the ion concentration and potential profile will be discussed in the end.

5.3.1 Ionic concentration distribution in CCG membrane

Figure 5.3 shows a typical ion concentration distribution in CCG membrane being subject to an external electric field under the stationary state. Here the ion concentration is $n_{res} = 0.01$ M and the channel height $h = 4.446$ nm. There is an interesting feature. The cation and ion accumulate at the opposite sides of the nanoslit. Note that there is no obvious change of concentration in the reservoirs.

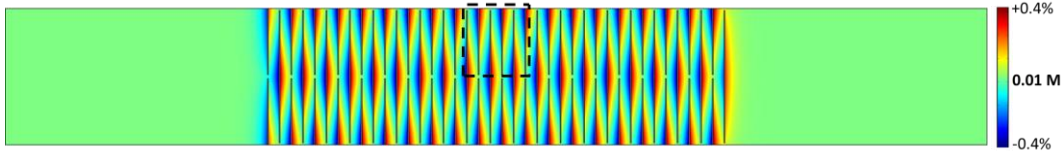


Figure 5.3 The modelling result for electrophoresis through the CCG membrane with $n_{res} = 0.01$ M and $h = 4.46$ nm and $\Delta\Phi_E = 0.01$ V: (a) The concentration profile of K^+ ; The dashed rectangle is the “centre” of membrane where the result would be magnified and presented in the following figures.

As the experimental setup, the impermeable graphene sheets were normal to the external E-field (X-axis). Thus, the electrophoresis flow along the external E-field was hindered by the graphene sheets that induced the accumulation of ions on graphene sheet surface. Note that there are two distinctive regions with the different ion accumulations: The red region is the K^+ enriched one with the positive charge. However the blue region is the K^+ depleted but Cl^- enriched one with the negative charge.

The accumulations of ions on the solid/liquids interface are usually referred as EDLs, but the novel ion accumulations in the modelling was induced by the external E-field rather than the conventional surface charge. Thus we decided to take the different terminology --

“Boundary Layers” (BLs) to describe the ion accumulation in by the external E-field. And the distinctive accumulations of cations and anions on the different side of nanoslit were coined as the “Binary Boundary Layers” (BBLs).

To better investigate structures of the BBLs, we only taken a center region of the membrane for analysis (the dashed rectangle in Figure 5.3). Figure 5.4 shows the concentration distribution in the “center” of the membrane for the different channel height ($h = 1.2\sim 6.7$ nm) with $n_{res} = 0.1$ M. The top row of Figure 5.4 shows the BBLs structure obtained in our COMSOL simulations and the bottom part of Figure 5.4 shows the corresponding sketches. For easy visualization, the scales along x and y direction are different, i.e., the images in y axis was squeezed (to 40%). To help understanding BBL structures, we break the cascading nanoslit into two parts: slit region and aperture region (show in Figure 5.4).

For a relatively large channel height ($h = 6.7$ or 2.2 nm at Figure 5.4), we could clearly observe that the BBLs formed next to the graphene surface. But the extension of BBLs along the channel axial direction was not uniform. The maximum ion accumulation occurred in the aperture region. Overall, in Figure 5.4, a triangular shapes of BBLs was presented and the cation-enriched region was named as the cationic BLs or +BLs, whereas, the anion-enriched one would be the anionic BLs or –BLs. Actually, the formation of BBLs is similar to the hypothesis of “Binary EDLs” in the zwitterionic porous membrane[203, 204]. But the binary EDLs are maintained by the surface charge, while the presence of BBLs was caused by the external E-field.

Similar to the conventional EDLs, the Debye length λ_D quantify the extension of BBLs. At $n_{res} = 0.1$ M, $\lambda_D \approx 0.96$ nm. For $h = 6.7$ nm $\gg 2\lambda_D$ (Figure 5.4a), in the channel, the BBLs just formed on the opposite graphene wall surfaces, while in the middle of the channel the concentration of cation and anion is similar to the bulk solution n_{res} . With reducing the slit height (Figure 5.4b at $h = 2.2$ nm), the BBLs from one graphene wall get closer to the opposite wall. Near the aperture region, one BBL would almost fill the entire nanoslit region ($h \approx 2\lambda_D$). The region with bulk ion solution n_{res} was significantly reduced. Inside the slit, the

triangular shape of BBLs still remained. Note that in the aperture region, the ion concentration is almost a constant, in contrast to the $h = 6.7$ nm case.

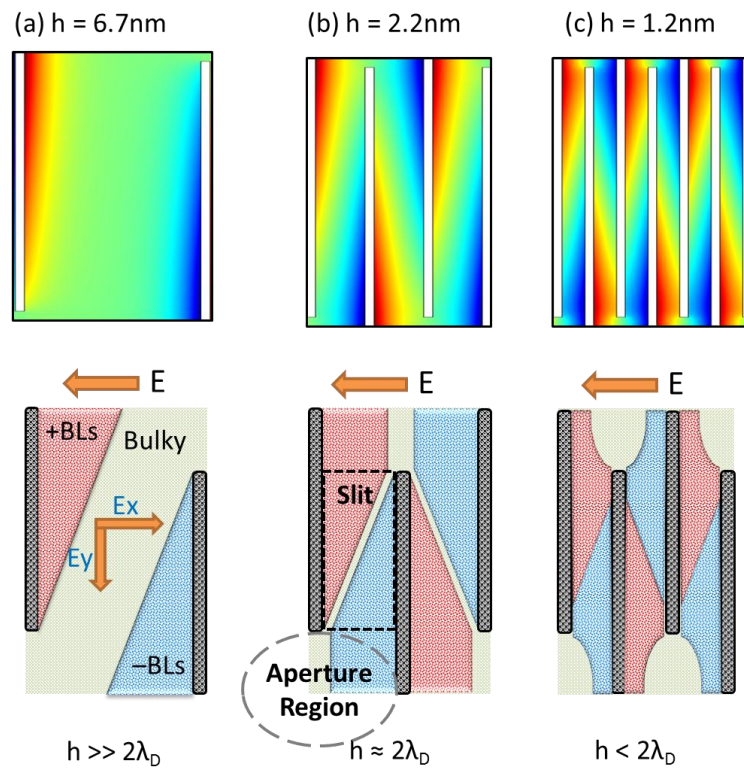


Figure 5.4 The structure of dual EDLs with different channel height (h), when $n_{res} = 0.1M$, $\lambda_D = 0.96$ nm: (a) the channel height (6.7nm) is much large then the Debye length; (b) the channel height (2.2nm) is approximate to $2\lambda_D$; (c) The channel height (1.2nm) is much smaller than $2\lambda_D$. The bottom figures were the schematic of simulation results. Note that the data range was about Max. $\pm 0.2\%$. For clarity the concentration figures(a) were shrunken in Y-axis by 40%.

At a very small channel height ($h = 1.2$ nm), the BBLs was considerably overlapped with each other ($h < 2\lambda_D$). The triangular shape still remains. However on the two ends of the nanoslit region, i.e., near the aperture, one BL completely occupied the nanoslit. Beyond the nanoslit region, the BBLs structure in the aperture region was also significantly changed. Due to the symmetric of BBLs structure, the annihilation of +BLs and -BLs occurred on the aperture opening. Thus a meniscus shape of bulk-like solution region formed in the aperture region.

We find in COMSOL modelling, the ion concentration in the center of the aperture region is n_{res} . This is reasonable to understand. Under the external E-field, the ions accumulated on the one side of the graphene surface ($n > n_{res}$) with the exclusion on the other side ($n < n_{res}$).

Thus we could always find the position with the concentration is n_{res} between two sides. Namely the BBLs from the opposite graphene sheets annihilated with each other in the aperture region. However this hypothesis may not suitable for very small channel height ($h < 1$ nm), where the steric effect of ions should be taken into account.

The influence of the reservoir concentration n_{res} on the BBLs structure has also been investigated. Figure 5.5 plotted the concentration profile for the different $n_{res} = 1, 0.1, 0.01$ M at $h = 2.6$ nm. As we known, λ_D depends on the concentration of the reservoir (n_{res}). The corresponding λ_D would be 0.30, 0.96, 3.0 nm respectively. Thus, at $n_{res} = 1$ M, the extension of BBLs was extremely short due to the higher ionic strength of n_{res} . And there is a large amount of the bulk-like solution in the middle of nanoslit region.

With the reduction of n_{res} to 0.1M, both the magnitude and the extension of BBLs would be enhanced. And the channel height ($h = 2.6$ nm) was slightly larger than the $2\lambda_D$. However at very low concentration, $n_{res} = 0.01$ M, the magnitude and extension of BBLs was significantly increased. The result concentration profile is similar to that in Figure 5.4c ($h < 2\lambda_D$). The overlap of BBLs modified the BBLs structure on the two ends of the nanoslit and the meniscus Bulk-like solution region still remained.

All of discovery for different concentration are similar to the previous Figure 5.4 for constant n_{res} but different h . actually the BBLs structure is determined by both the nano confinement effect and ionic strength of the reservoir.

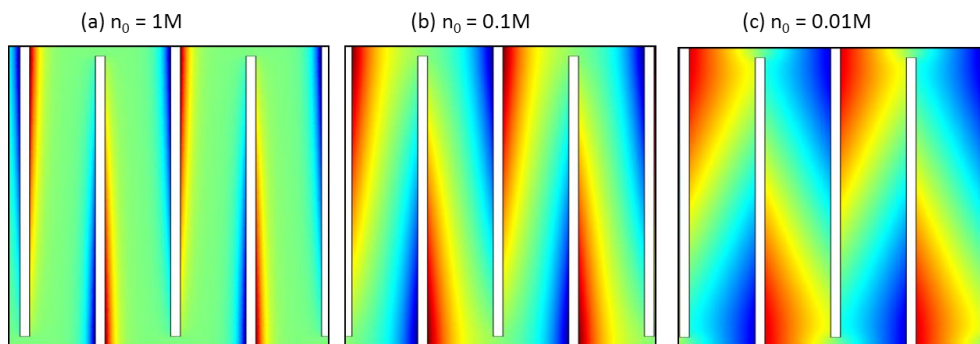


Figure 5.5 The profile of BBLs at $h = 2.6$ nm with different n_{res} : (a) 1M; (b) 0.1M; (c) 0.01M. For clarity, the figures were shrunken in Y-axis by 40%.

In general, a novel BBL structure was observed in the cascading nanoslit system under an external E-field applied perpendicular to graphene surface. The structure of BBLs depends on the microstructure of the cascading nanoslit and the reservoir ion concentration n_{res} . The unique BBLs structure could play a critical role to induce a tortious electric potential drop to drive the electrophoresis flow where the ions drift along a tortious pathway (to bypass the graphene sheets).

5.3.2 Electric potential and Nernst potential

It is easily to understand that the BBLs also modified the E-field inside the membrane. It induced two extra E-fields (Figure 5.4a): 1) E_{slitX} and 2) E_{slitY} . In the nanoslit region, the influence of the external E-field (in the X-axis) would be cancelled by E_{slitX} and the electrophoresis flow normal to the graphene sheet would be eliminated. While, E_{slitY} is generated to turn the direction of electrophoresis flow tangent to the graphene sheet (Y-axis). Thus with the formation of BBLs, a tortious electrophoresis flow, namely, electric potential drop emerged into the membrane to drive the ions to bypass the staggered graphene sheets.

The novel BBLs structure and tortious electric potential drop would be the major difference between the cascading flow in the graphene membrane and the conventional 1D flow. The different transport behaviour could provide the different tuning methods and strategy in the applications.

Figure 5.6a shows the overall electric potential profiled with $n_{res} = 0.01$ M and $h = 4.46$ nm under a total electric potential drop across the membrane of $\Delta\Phi_E = 0.01$ V. Figure 5.6b was the corresponding 1D average of electric potential, by Eq. (5.12)

$$\Phi_E(x) = \int_{-L_y/2}^{L_y/2} \Phi_E(x, y) dy \quad (5.12)$$

Obviously, there is a linear drop of the potential in the two side reservoirs, indicating a constant E-field. However the most of the electric potential drop was inside the graphene membrane rather than the reservoirs. It was attributed to the significant conductivity drop of the staggered graphene membrane.

Inside the membrane, a ladder potential curve formed in Figure 5.6b. It is due to the periodic BBLs structure. For a comparison, the potential profile in the absence of graphene membrane (orange curve) is also shown in Figure 5.6b. And the major potential drop occurred on the surface of the graphene sheet rather than the two side reservoirs to maintain the BBLs structure.

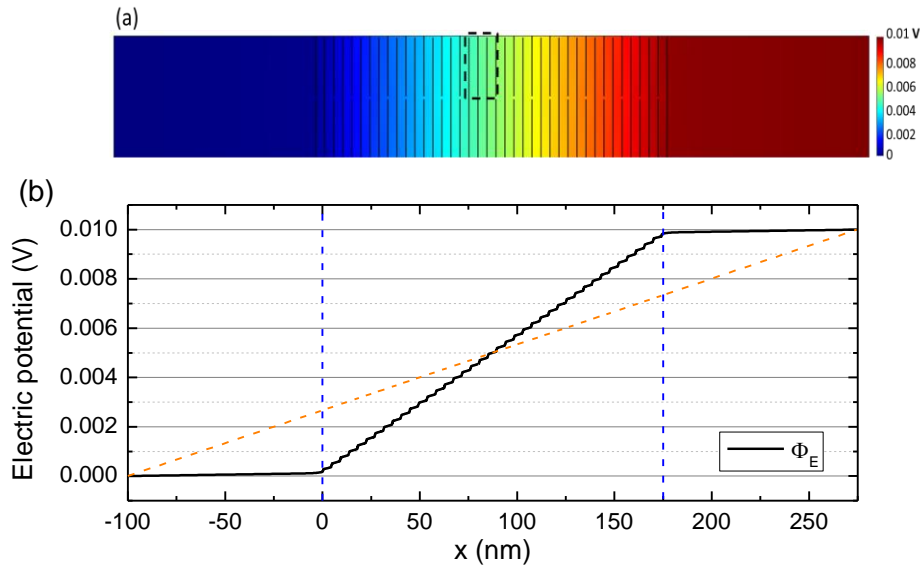


Figure 5.6 The electric potential profile when $n_{res} = 0.01$ M and $h = 4.46$ nm and $\Delta\Phi_E = 0.01$ V: (a) overall; (b) 1D average along X-axis; the orange dashed curve would be the initial electric potential profile before the formation of BBLs.

To better understand the electric potential drop within the membrane, a virtual “transport path” has been proposed which is defined as in Figure 5.7. All the red dots located at the center of the nanochannel structure. By analyzing the result along the “transport path”, an intuitive insight into the ion transport was obtained and the result would be comparable with that in the different channel height.

The potential drops (solid curves) along the “transport path” were plotted in Figure 5.8 for different channel height with $n_{res} = 0.1$ M. The dashed region indicated the position of the nanoslit region. While, the short solid vertical line in each curve indicated the position of the aperture opening.

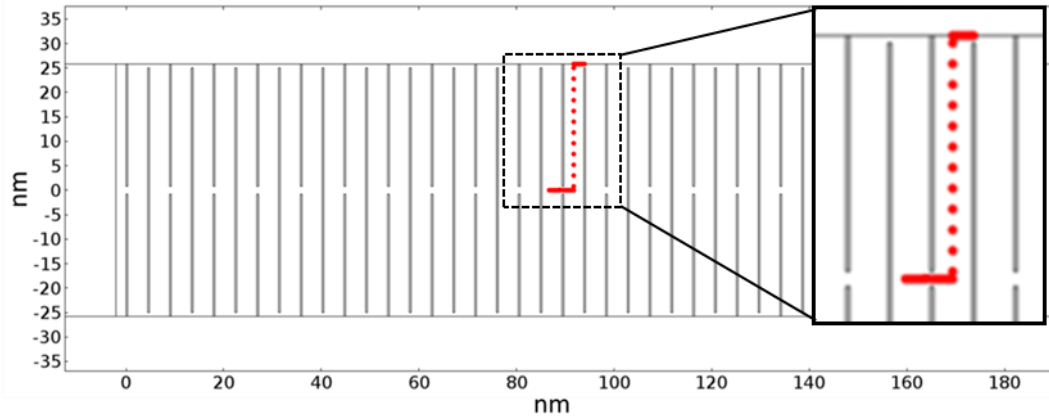


Figure 5.7 The sketch of “transport path” in graphene hydrogel membrane: The red dots in the middle of membrane mark the transport path of ions in the cascading flow. It is coined as the “transport path”.

We could found that the electric potential drops (Φ_E) in the nanoslit region were almost linear indication the constant electrophoresis flow moving tangent to the graphene sheet. However abrupt electric potential drop occurs in the aperture opening or the ends of the nanoslit region. At $h = 10.9\text{nm}$, there is an abrupt electric potential drop in the aperture opening. Because, the dimension of aperture opening ($d = 1.6\text{ nm}$) is much smaller than the size of electrophoresis channel ($2h = 21.8\text{ nm}$), which is similar to the discovery in the diffusion modelling. Thus the bottleneck of aperture opening required a larger potential drop. With the reducing of the channel height, the extent of bottleneck was gradually alleviated that decrease the potential drop in the aperture region.

At very small channel height ($h < 1\text{ nm}$), the potential drops in the aperture regions were considerably reduced. However the abrupt potential drops emerged again at the two ends of the nanoslit regions. As described in Figure 5.4c, the BBLs structure would be significantly modified at very small channel height where one end of the nanoslit region was completely occupied by one types of the BL structure.

In order to explain the abrupt electric potential drop inside the nanoslit region, the Nernst potential (Φ_N) [205] along the “transport path” which was defined as Eq. (5.13)

$$\Phi_N = \frac{RT}{F} \ln\left(\frac{n_{K^+} + n_{res}}{n_{res} + n_{Cl^-}}\right) \quad (5.13)$$

Where R is the gas constant and F is the faraday constant and n_{K^+} and n_{Cl^-} is the concentration of K^+ and Cl^- respectively. Both the Nernst potential and the electric potential could be used to evaluate the ions transport but for different terms: One for the diffusion flow under the concentration polarization (Δn), another for the electrophoresis flow under the electric potential difference.

We noticed that there is not concentration different on two ends of reservoirs ($\Delta n_{res} = 0$), namely no net Nernst potential difference ($\Delta \Phi_N = 0$). The overall driving force of ion transport originates from the external electric potential difference ($\Delta \Phi_N = 0.01$ V). And the Nernst potential was defined to provide a comparable evaluation between the electrophoresis flow by electric potential gradient and the diffusion flow by the concentration gradient.

The dash-dot lines in Figure 5.8 represent the $\Phi_E + \Phi_N$ along the “transport path”. We note that the beginning and ending of both types of curves coincided with each other. It appears that Φ_N only locally modified the shapes of potential curves.

For larger channel heights ($h > 4.466$ nm), the two curves overlap over each other, indicating the negligible influence of Φ_N . Because, the BBLs only develop on the surface of graphene sheet, leaving the bulk-like solution in the centre of nanoslit region (Figure 5.4a). However with the decrease of the channel height, a large deviation between two curves emerged. As discussed before, the bulk-like solution in the center of nanoslit region was gradually reduced with the decrease of the channel height. Thus the fraction of concentration polarization (BBLs structure) in the nanoslit region was increased. Hence, the influence of Φ_N emerges for the case of small h . At $h < 1.5$ nm, the nanoslit region was fully occupied by BBLs, giving rise to the maximum influence of Φ_N .

Another interesting result is that with the decrease of the channel height, the $\Phi_E + \Phi_N$ curves became more and more smooth. At $h < 1.5$ nm, abrupt electric potential drop at the entrance of the nanoslit region disappears. It indicates that the formation of BBLs could

smooth the driving force distribution inside the membrane, which drove a smooth continuous electrophoresis flow.

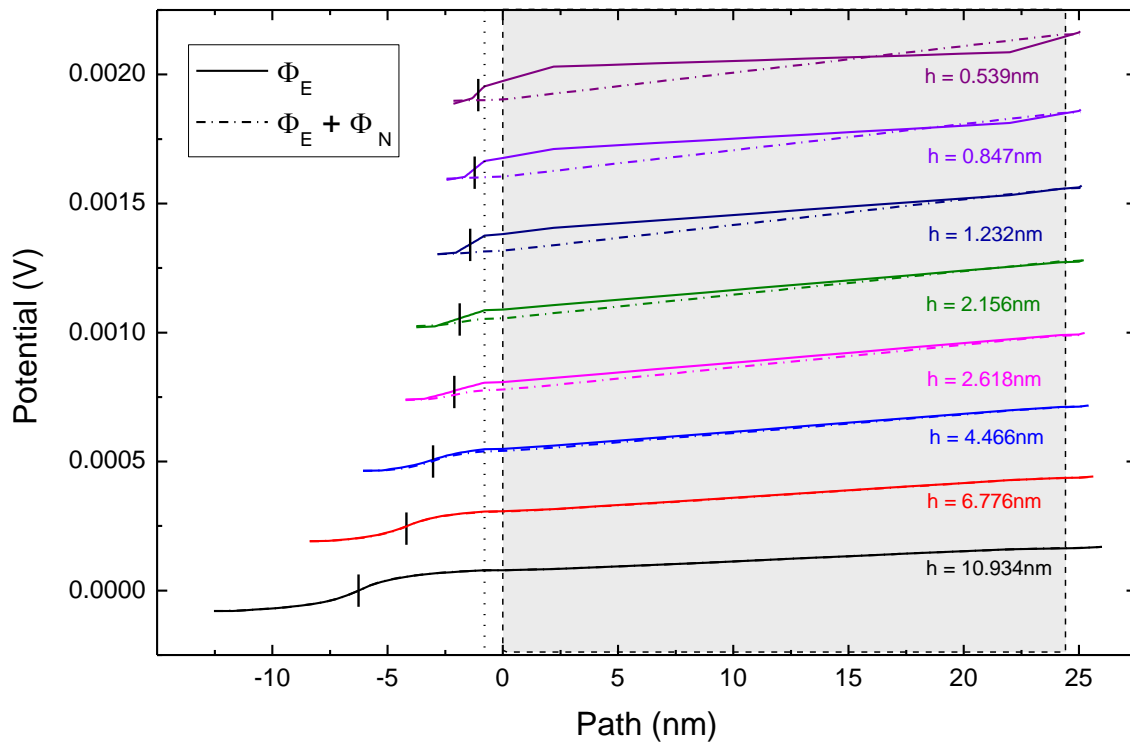


Figure 5.8 The potential drop along the “transport path” when $n_{res} = 0.1$ M and $\Delta\Phi_E = 0.01$ V. The solid and dashed lines indicated Φ_E and $\Phi_E + \Phi_N$ respectively. The curves with different colours indicate the result of different h from 0.5 to 10 nm. The dashed region marks the position of the nanoslit region. The short vertical lines indicate the position of the aperture opening and the dotted line is the “corner” of transport path.

To better investigate the influence of Φ_N , the fractions of potential drops in the nanoslit region to the whole potential drops ($\frac{\Delta\Phi_E}{N} = \frac{0.01 \text{ V}}{40}$) along the “transport path” were plotted in Figure 5.9. The potential drops in the nanoslit region was based the slope of the linear potential drop in the middle of the nanoslit region, $\frac{\partial\Phi}{\partial y} * L_{slit}$.

With the decrease of the channel height, the fraction of $\Phi_E + \Phi_N$ was gradually increased. At very small channel height, the fraction was almost to be 1, indicating most of the potential drop takes place in the nanoslit region. This is because with the reducing the channel height, the cross-section area of nanoslit region became the bottleneck of the ion transport that increased the fraction of $\Phi_E + \Phi_N$.

For Φ_E , the decrease of channel height also increased the fraction of Φ_E . However at $h < 2.6\text{nm}$, the decreased of channel height also decreased the fraction of Φ_E . As mentioned before, at $h = 2.6\text{nm}$, the BBLs structure would almost fully occupy the entrance/exit of the nanoslit region ($h \approx 2\lambda_D$). With further reducing the channel height, the overlap of BBLs structure induces the ion concentration polarization and thus the influence of Φ_N is becoming dominant. The magnitude of Φ_E or Φ_N results is proportional to the ion drift or diffusion flux. Thus, at $h = 0.5\text{ nm}$, we should find that the diffusion flow flux ($\sim 75\%$) would be about three times higher than that of ion electrophoresis flux ($\sim 25\%$) in the nanoslit region.

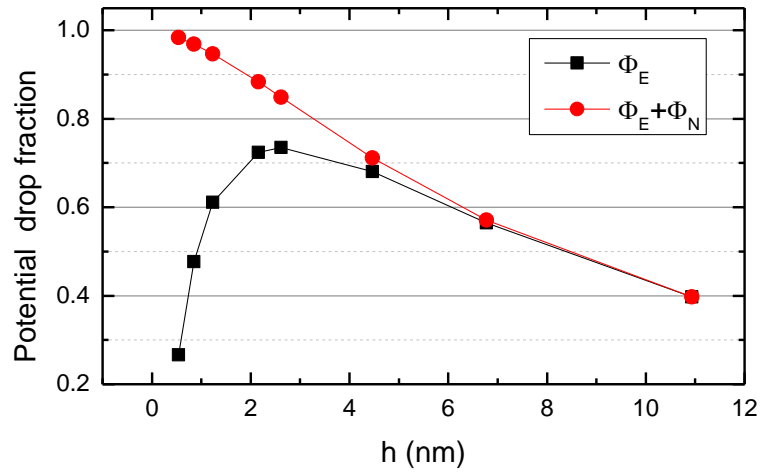


Figure 5.9 The fraction of the potential drop in the nanoslit region for different channel height. The black and red curves represented the result of Φ_E and $\Phi_E + \Phi_N$ respectively.

The influence of Φ_N should be attributed to the novel BBLs structure in the cascading nanoslit system in graphene membrane. In the conventional 1D nanofluidic study, the significance of the diffusion flow (Nernst potential difference) is not available. With the reducing the channel height, the influence of BBLs structure in the nanoslit region was enhanced with the influence of Φ_N . At very small channel height ($h < 1.5\text{nm}$), the nanoslit region is the bottleneck of the ions transport and the amount of diffusion flow is higher than that of electrophoresis flow. On the contrast, at large channel height, the small aperture opening is the bottleneck of the ions transport and Φ_N has the negligible influence.

In the end, for graphene membranes with large slit height h , it is acceptable to only taken the dominant Φ_E into account. However for small channel height, both Φ_E and Φ_N should be considered.

5.3.3 Electro-kinetic conductivity of graphene membrane

Besides the stationary concentration and potential profile, the dynamic electrophoresis flow on the ends of the modelling system could be obtained. Thus the conductance of membrane (G_m) could be calculated as Eq.(5.9). Figure 5.10 plotted G_m for different h at $n_{res} = 0.1 \text{ M}$, where the extension of 2D model in z-axis was assumed to be 1 m.

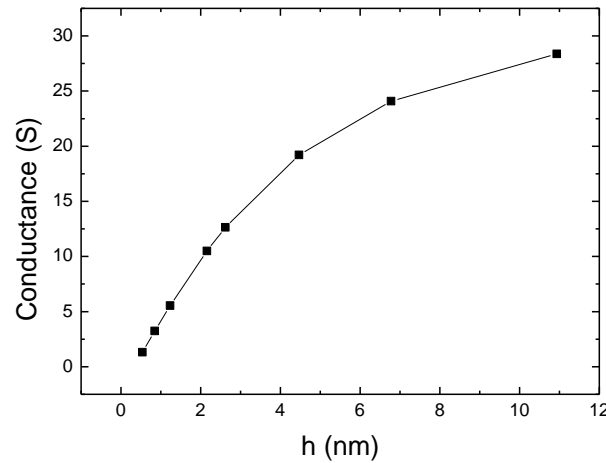


Figure 5.10 The conductance of membrane as a function of h at $n_{res} = 0.1\text{M}$. Note that to calculate the cross-section area of membrane (A_m), the extension of 2D model in z-axis was assumed to be 1 m

Similar to the discovery in the diffusion process, the conductance of membrane dropped with the reduction of channel height. It was attributed to the decrease of the transport channel. Based on the conductance of membrane, we could calculate the conductivity of each membrane and compared it with the diffusion process.

The result scale law (S_m) defined in Eq.(5.11) was plotted in Figure 5.11. However, unlike the reported varied S_m in experiment, the result in the modelling was shown to be unity for all different concentration and channel height. It seems that in the neutral graphene membrane, the behavior of the electrophoresis flow is similar to that of the diffusion flow. The unity scaling law would be attributed to the weak BBLs that owned the negligible influence on the electrophoresis flow.

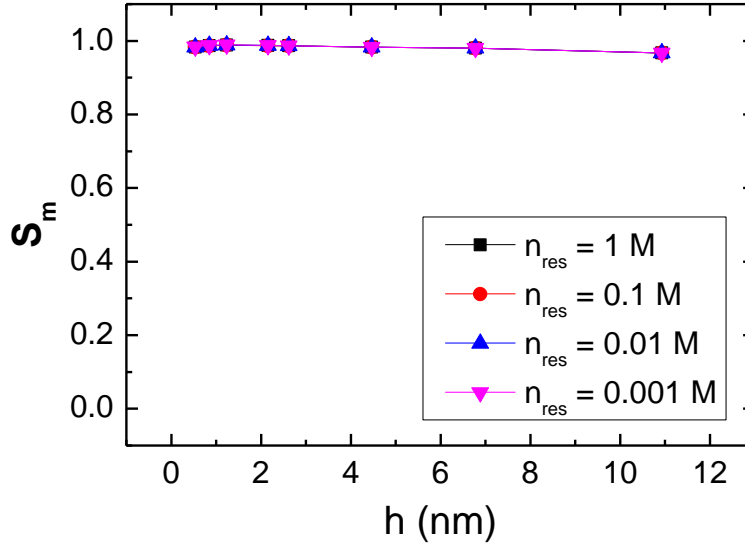


Figure 5.11 The scaling law (S_m) of the neutral graphene membrane against the different channel height: The difference symbols represent the results with different reservoir concentration from 0.001M to 1M.

Although the novel BBLs structure was discovered from the continuum modelling for the neutral graphene membrane was taken, the result S_m was not consistent with the varied experimental result. Thus, the left surface charge may play an important role in the ion transport process which would be discussed in the following section.

5.4 Results for electrophoresis process in CCG membranes with surface charge

After the modelling with the neutral graphene membrane, we established the basic idea about the cascading nanoflow in graphene membrane. Then the influence of the surface charge by the residual functional group will be discussed in this section.

5.4.1 EDLs structure

Once the surface charge is introduced into the graphene sheet, the EDLs would forms on the surface and the magnitude of EDLs depended on the surface charge density. Figure 5.12a was an example of the overall concentration distribution with $n_{res} = 0.01\text{M}$, $h = 4.46\text{nm}$, $\sigma = -2.3\text{mC/m}^2$. The negative charged graphene sheet increased the concentration of cation with the exclusion of anion.

Figure 5.12b was the magnification of the concentration profile in the “center” of membrane (dashed rectangular). The EDLs formed on the surface of the graphene sheet. Unlike the triangular structure of BBLs, the extensions of EDLs were uniform except for the edges of sheet.

Furthermore, the low ionic strength of the reservoir concentration extended the EDLs ($\lambda_D = 3.0$ nm). At $h = 4.5$ nm, the EDLs from the opposite wall overlapped with each other. It increased the concentration of cation in the center of the nanoslit region. Thus we cannot observe the bulk-like solution inside the membrane, compared with the concentrations in the reservoirs (Figure 5.11c).

With the introducing of the electric potential difference ($\Delta\Phi_E = 0.01$ V), the EDLs would response with the external E-field and the dynamic concentration distribution would be different from the equilibrium state. Unfortunately, the influence of the external $\Delta\Phi_E$ was significantly lower than that of the surface charge. Thus, we cannot find the observable difference between the equilibrium ($\Delta\Phi_E = 0$ V) and dynamics ($\Delta\Phi_E = 0.01$ V) states.

However by subtracting the concentration profile between two states, the weak BBLs structure could be observed inside the membrane. Figure 5.12d is the magnification of the concentration subtraction in the “center” of membrane. We also found the shape of BBLs structure emerged on graphene sheet surface which was similar to the previous modelling of the neutral membrane.

Figure 5.12e is that concentration profile along the dashed line in Figure 5.12d. Clearly, the BBLs structure formed on each side of the graphene sheet but the magnitudes of BBLs is much lower than that of EDLs (Figure 5.12c).

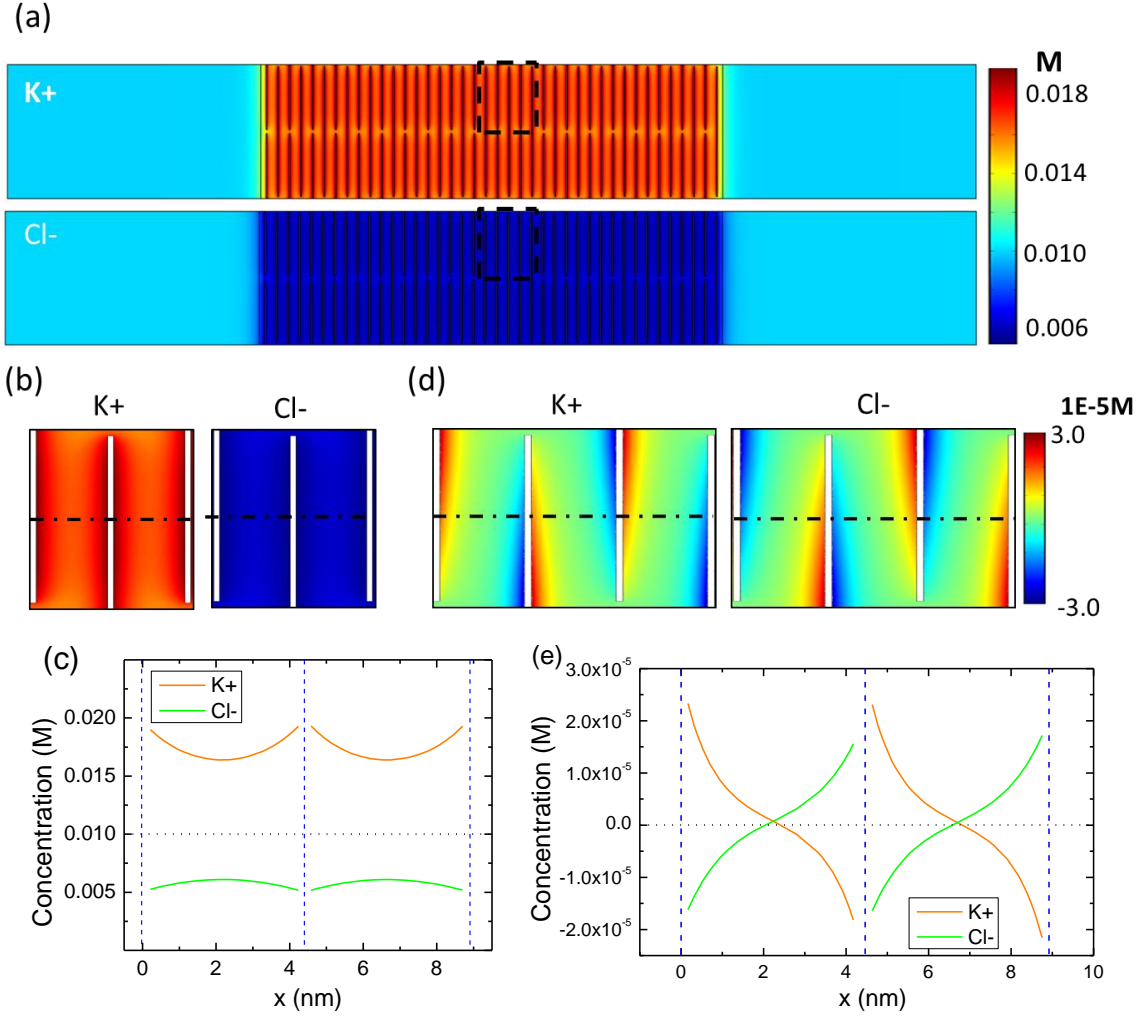


Figure 5.12 The concentration distribution of KCl solution when $n_{res} = 0.01\text{M}$, $h = 4.5\text{nm}$, $\sigma = -2.3\text{mC/m}^2$: (a) concentration profile for ions; Note that the dashed rectangular is the “center” of the membrane; (b) concentration profile for ions in the “center” of membrane in equilibrium state; (c) 1D concentration profile along the dashed line in (b); (d) The concentration subtraction profile between $\Delta\Phi_E = 0$ or 0.01 V in the “center” of membrane. (e) 1D concentration profile along the dashed line in (d); For clarity the images in (b)&(d) were rescaled by 40% along the Y-axis.

Actually for the charged graphene membrane, the concentration profile in the dynamic state would be a combination of two terms: 1) EDLs by the surface charge, 2) BBLs by the external E-field. For our modelling setup (low electric field strength), the magnitude of BBLs would be always much lower than that of EDLs but still existed in the system.

In the following discussion of the concentration profile, we would discuss both the EDLs structure and the BBLs induced by the external E-field. Figure 5.12 presented the concentration profile in the “center” of membrane for different channel height. At $h = 6.7\text{ nm}$, the EDLs only occurred on the surface of the graphene sheet, leaving the bulk-like solution in

the center of the nanoslit region ($h > \lambda_D$). However with the reduction of the channel height ($h = 2.2$ nm), the EDLs fully occupied the nanoslit region that even increase the concentration in the center of the nanoslit region. Only the concentration in the aperture region was similar to n_{res} .

However with the further decrease of the channel height ($h = 1.2$ nm), the EDLs was significantly overlapped with each other, Thus the concentration of cation in the nanoslit region was 30% higher than the outside reservoir. Even in that case, the concentration in the aperture was still lower than that in the nanoslit region but higher than that in the reservoirs.

It seems that the “channel height” of the aperture region was double higher than that in the nanoslit region. And the surface charge was assumed to be distributed uniformly along the graphene sheet. Thus the influence of the surface charge (σ/h) in the aperture region was weaker than that in the nanoslit region, indicating the different property of solution in two regions.

Like the strategy in the semiconductor technology, the heterojunction of solution region with different property was widely employed in the nanofluidic field to manipulate and control the transport of fluids [89, 101, 119]. Thus the rise of aperture region actually provided a novel access to the nanofluidics control.

The last row of Figure 5.12 was the BBLs (concentration subtraction profile) for different h . The variation of BBLs was similar to the discovery in the neutral membrane. At $h = 6.7$ nm, the BBLs only occurred on the surface of the graphene sheet. With the decrease of the channel height, the region of bulk-like solution was greatly reduced. Finally at $h = 1.2$ nm, the one type of BLs structure fully occupied the one end of nanoslit region and BBLs structure in the aperture region was distorted.

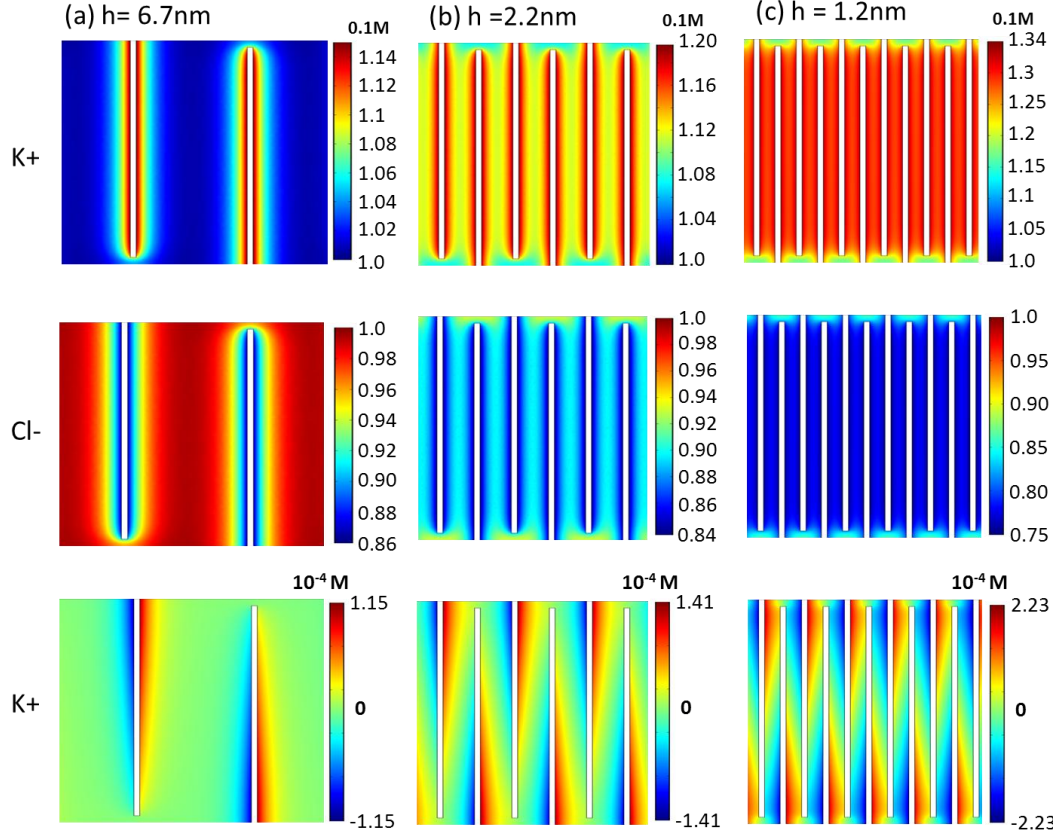


Figure 5.13 The concentration profile for different channel height with $n_{res} = 0.1M$, $\sigma = -2.3mC/m^2$: (a) $h = 6.7$ nm; (b) $h = 2.2$ nm; (c) $h = 1.2$ nm; The first and second rows were the really concentration distribution for K^+ and Cl^- respectively. While the last terms is the concentration subtraction profile for K^+ . For clarity, all the images were rescaled by 40% along the Y-axis.

Furthermore, the influence of the reservoir concentration (n_{res}) was also investigated. With the decrease of n_{res} , the EDLs expanded with the increase of λ_D . The changes of BBLs structure for n_{res} were similar to the neutral graphene membrane. The n_{res} decreased with the increase of the length and magnitudes of BBLs.

Taken together, with the introducing of the surface charge, both the EDLs and BBLs would emerge on the graphene sheet surface under the external E-field. The property of EDLs was determined by the surface charge. With the reducing the channel height or reservoir concentration the overlap of EDLs would increase the concentration in the membrane. But it was found the property (concentration) of solution in the aperture region was different from that in the nanoslit region. The difference influence of surface charge in

the aperture region may provide a new access to manipulate the cascading flow in the membrane.

However the property of BBLs revealed by the concentration subtraction was similar to the discovery in the previous neutral membrane. Although, the magnitude of BBLs by the external E-field ($\Delta\Phi_E$) is significantly lower than that of EDLs, the weak BBLs still played a critical role in the cascading nanoflow. Thus the total concentration distribution of ions under $\Delta\Phi_E$, would be a combination of two terms: 1) EDLs and 2) BBLs. The behaviour of both could be regarded to be independent to each other.

5.4.2 Electric potential and Nernst potential

As discussed in the neutral membrane, the Nernst Potential may play a unique role in the cascading electrophoresis flow. Thus, both Φ_E and $\Phi_E + \Phi_N$ profiles should be analysed. Figure 5.14 was an example for potential profile in the modelling system with $n_{res} = 0.1$ M, $h = 4.46$ nm, $\sigma = -2.3$ mC/m² respectively. Figure 5.14a was Φ_E profile with/without the external E-field. While Figure 5.14b was the profile of $\Phi_E + \Phi_N$.

As expected, the negatively charged graphene sheet produced a negative electric potential in the membrane (Figure 5.14a). However the absorption of counter-ions increased the Nernst potential on the graphene sheets surface. In the equilibrium state ($\Delta\Phi_E = 0$), the decrease of Φ_E would be annihilated with the increase of Φ_N , giving a nearly constant potential profile $\Delta\Phi_E + \Delta\Phi_N = 0$ (Figure 5.14b). In the equilibrium state, it established a balance between the absorption of counter-ions by the electrophoresis flow with dissipation of counter-ions by the diffusion flow.

With the introducing of electric potential difference ($\Delta\Phi_E = 0.01$ V), the different electric potential distributions were presented in Figure 5.14a. To better present the result of driving force, the 1D average potential profiles for Figure 5.14a&b were plotted as Figure 5.14c. It clearly showed the cancellations of Φ_E and Φ_N in the equilibrium state.

With the imposing of external $\Delta\Phi_E$, the electric potential curve (solid orange) was elevated. However the result Φ_E curve cannot be regarded as a reasonable driving force for cascading nanoflow, especially for the left exit of membrane. If combing Φ_E and Φ_N together, the $\Phi_E + \Phi_N$ curve was similar to the previous Φ_E curve in the neutral membrane in Figure 5.6. The potential of both curves were gradually decrease from right to left.

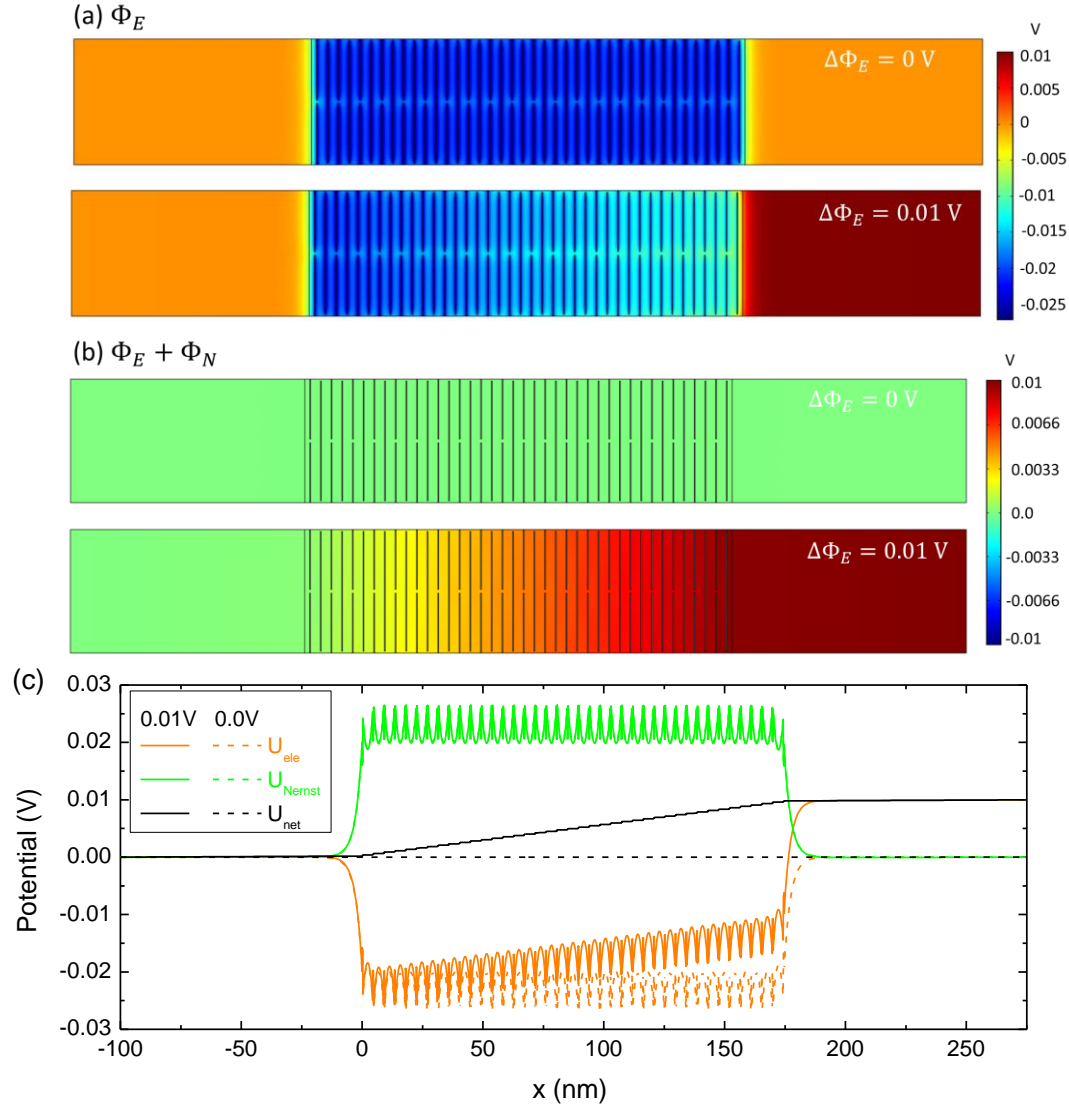


Figure 5.14 The potential distribution of KCl solution when $n_{res} = 0.01$ M, $h = 4.46$ nm, $\sigma = -2.3$ mC/m² for (a) $\Delta U = 0.0$ V; (b) $\Delta U = 0.01$ V; (c) The electric potential along X-direction.

It seemed that both Φ_E and Φ_N played a crucial role in the cascading flow in the charge membrane. However, for the neutral membrane, the influence of Φ_N is negligible at small channel height.

To further investigate the driving force distribution in the charged membrane, the potential ($\Phi_E + \Phi_N$) along the “transport path” was drawn in Figure 5.15 with $n_{res} = 0.1$ M and $\Delta\Phi_E = 0.01$ V. The marks in Figure 5.15 were the same as that in the previous “transport path” profile of the neutral membrane (Figure 5.8). For comparison, the electric potential (Φ_E) profile was also added into as the dashed line in Figure 5.15.

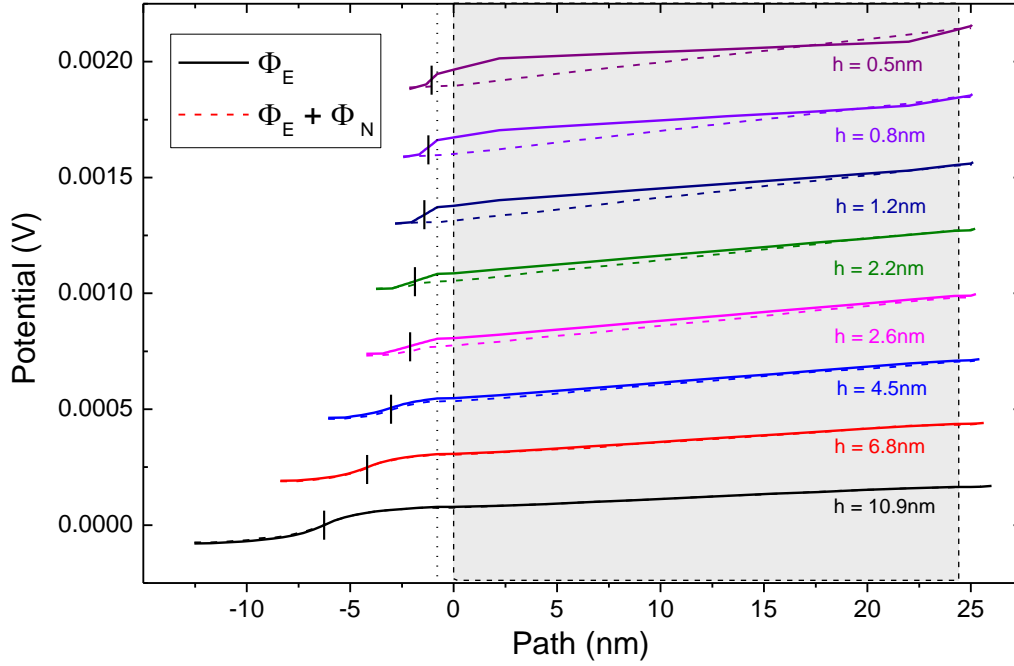


Figure 5.15 The potential drop along the “transport path” when $n_{res} = 0.1$ M, $\Delta\Phi_E = 0.01$ V and $\sigma = -2.3$ mC/m²: The solid and dashed lines indicated Φ_E and $\Phi_E + \Phi_N$ respectively. The curves with different colours indicate the result of different h from 0.5 to 10 nm. The shadow region marks the position of the nanoslit region. The short vertical lines indicate the position of the aperture opening and the dotted line is the “corner” of “transport path”.

To removing the non-zero background of Φ_E and Φ_N , the results in Figure 5.15 were the difference between the equilibrium and dynamic state. Namely, the extra electrophoresis flow and diffusion flow by Φ_E and Φ_N respectively, which contributed the net ions transport through the membrane.

For both Φ_E and $\Phi_E + \Phi_N$ curves, the results were similar to the description for the neutral graphene membrane. For Φ_E , the abrupt potential drops occurred at very large or small channel height. While at small channel height, there is large deviation between Φ_E and $\Phi_E + \Phi_N$. And the abrupt potential drops of Φ_E on the two ends of the nanoslit region were removed in the $\Phi_E + \Phi_N$ curves.

Actually the similarity of the potential curved between the neutral and charged graphene membrane would be attributed to the similar BBLs structure by the external E-fields. With the reduction of the channel height, the significantly weak BBLs structure still increased, giving a large deviation between Φ_E and $\Phi_E + \Phi_N$ curves.

And the potential fractions in the charged membrane were also found to be similar to that in the neutral graphene membrane. At very small channel height ($h = 0.5$ nm), the extra ion diffusion was the predominant ion transport method in nanoslit region, while at large channel height, the extra electrophoresis flow by the external E-field was the dominant terms.

In summary, owing to the formation of similar BBLs in the charged membrane, there was negligible difference for driving force distribution ($\Phi_E + \Phi_N$) in the neutral and charged graphene membrane. To deal with the charged graphene membrane, the background potential distribution (equilibrium state) by the EDLs should be accounted. However for the neutral graphene membrane, the background potentials were zero for both Φ_E and Φ_N .

5.4.3 Scaling law in charged graphene membrane

Although the BBLs structure and the driving force distribution in the charged graphene membrane were similar to that in neutral one, the electrophoresis flow was found to be different. Figure 5.16 plotted the scaling law (S_m) of charged graphene membrane for all the different n_{res} . And the experimental S_m was also added into the Figure 5.16 for comparison.

We found that the modelling S_m was a monotonically increasing function with the decrease of h . With the decrease of the reservoir concentration, there was an elevation of S_m curves. The deviation of result from $S_m = 1$ indicated the increase of the local conductivity inside the graphene membrane.

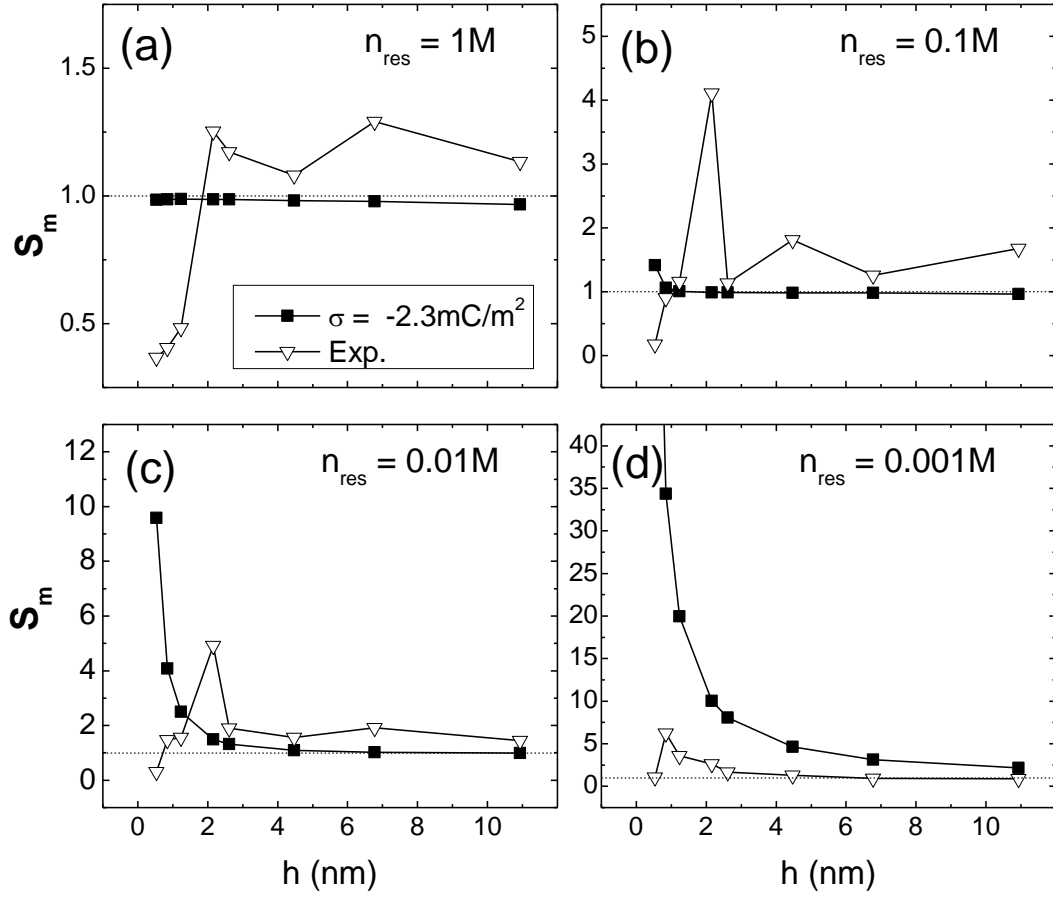


Figure 5.16 The scaling law for experiment and modelling result under the different n_{res} : (a) 1M; (b) 0.1M; (c) 0.01M; (d) 0.001M. The open and solid curves represented the experimental data and modelling result ($\sigma = -2.3 \text{ mC/m}^2$), respectively. The dashed lines marked the position of unity ($S_m = 1$).

It was reported that the increase of the conductivity in nanochannel could be ascribed to the increase of ions' concentration (charge carrier density) in the nanochannel. Thus, Figure 5.17 summarized the mean concentration of ions ($\bar{n}_{m,i}$) inside the membrane for the different n_{res} , defined as:

$$\bar{n}_{m,i} = \frac{N_i - (2L_m * A_{res} * n_{res})}{Void_m} \quad (5.14)$$

Where N_i is the total amount of i type ions; $A_m * L_{res}$ is the volume of the reservoirs; $Void_m$ is the volume of the void space inside the nanoporous graphene membrane:

Namely, the concentration in the two sides reservoirs was assumed to be the same as n_{res} . The major concentration difference of the modelling system would be attributed to the formation of EDLs inside the graphene membrane.

As mentioned before, the concentration of cation would be increase by the surface charge absorption with the repelling of the anion. At large channel height, the concentrations of cations and anions were similar to that in the reservoir (n_{res}). With the decrease of h , the influence of the surface charge (σ/h) would be enhanced, giving the large deviation of concentration curves from n_{res} (dashed line).

The EDLs and the overlap under the nanoconfinement have been intensively studied in the classic thermodynamic framework. It has been founded that at low electrode electric potential case ($e\Phi_E < kT$), the increase of counter-ions would be approximate to the decrease of co-ions, giving an unchanged charge carrier density ($\Delta n_{K^+} + \Delta n_{Cl^-} \approx 0$). The blue triangles in Figure 5.17 was the “salt” concentration in the membrane, defined as $\frac{n_{K^+} + n_{Cl^-}}{2}$. Due to the similar electrophoresis mobility of K^+ and Cl^- , the conductivity inside the membrane could be accounted to be proportional to the “salt” concentration.

Thus for large $h > 5$ nm and high $n_{res} > 0.01$ M, the result of “salt” concentration was almost equal to n_{res} , giving the S_m approximate to be 1. However with the decrease h and n_{res} , the “salt” concentration would be larger than n_{res} . Because, the reduction of channel height increased the density of surface charge (σ/h), namely increase the electric potential on graphene surface ($e\Phi_E > kT$). It provided an unequal change of the ionic concentration. The increase of the charge carrier density would be the major contribution to the increase of S_m .

Similar to the conventional 1D nanofluidics study, at large (σ/h), the anions was almost repulsed from the nanoporous membrane and the concentration of the counter-ions was determined by σ/h [89]. Thus, K^+ curve with $n_{res} = 0.01$ M was approximately the same as that in $n_{res} = 0.001$ M.

With the investigation of the concentration changes inside the membrane, the origins of S_m variations in the modelling would be identified. For $n_{res} = 1$ M, the variation of S_m was negligible, owing to the negligible change of “salt” concentration. With the decrease of n_{res} to 0.1 M, only for sub-nanometer channel height ($h < 1$ nm), the result would be considerably deviated from the unity. Only in that region, the “salt” concentration would higher than n_{res} .

With the further decrease of n_{res} to 0.01M and 0.001M, they owned the similar cation concentration curved with the essential zero concentration of anion. Namely, the current (ion transport flow) was predominantly attributed to the transport of K⁺. However the different S_m curves were obtained. As the definition of S_m , the conductivity of membrane and bulk reservoir was compared (κ_m/κ_0), namely the comparison between the concentration in the membrane and reservoirs (n_{res}) Thus the lower n_{res} , would elevated the S_m curves in Figure 5.16.

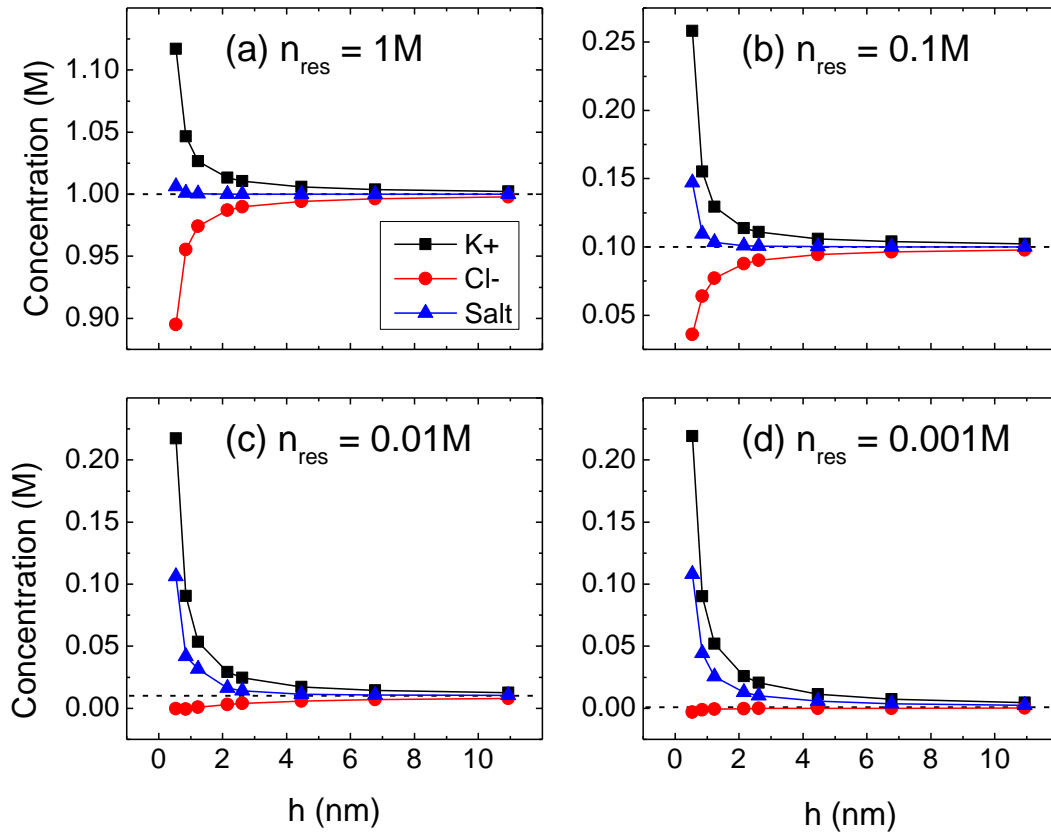


Figure 5.17 The mean concentration in the membrane against channel height for different n_{res} with $\sigma = -2.3 \text{ mC/m}^2$: (a) 1M; (b) 0.1M; (c) 0.01M; (d) 0.001M. The black squares and red circles were the mean concentration of ions, while the blue triangles were “salt” concentration $\frac{n_{K^+} + n_{Cl^-}}{2}$. The dashed lines indicated the level of n_{res} .

Although the changes of S_m in the modelling were identified, the result still cannot conclusively explain the experimental data. Both of them owned the tendency of the S_m increase with the different magnitudes. For $n_{res} \geq 0.1 \text{ M}$, the result seemed to be completely lower than that in the experimental data. For $n_{res} = 0.001 \text{ M}$, the result was much higher than that in experiment data.

Similar to the other nanofluidic discovery, the increase of the S_m in experiment may originate from the surface charge by the residual functional group. Our model only qualitatively reproduced the increase of S_m in experiment. If we change the surface charge density on the graphene sheet, the monotonic shape of S_m in modelling would be maintained with the shift of the location.

However the deviation from the experiment seemed that the result cannot be fitted for all n_{res} , by simply modifying the surface charge density. It seemed that some other issues (e.g. corrugation of graphene sheet, functional group distribution, and aperture opening confinement) should be taken into account to provide a reproductive result.

Besides the increase of S_m , there was a decrease of S_m at small h in the experimental curves, which cannot be predicted by the modelling result. The decrease of S_m at small h may be attributed to the mobility drops of ions under the strong nanoconfinement. The influence of nanoconfinement was not accounted in the classic thermodynamics framework. And the validation of the continuum modelling for small nanochannel ($h < 2$ nm) is still ambiguous. Thus we cannot reproduce the S_m drops in the small channel height in the continuum modelling. And the MD simulation was proposed in the next 2 Chapters to study the ions transport through the small nanochannel ($h < 3$ nm)

Taken together, the changes of concentration by the surface charge induced the increase of S_m , namely the increase of the conductivity of solution inside the membrane. The modelling result only provided a qualitative explain for the increase of S_m and some other issues were not accounted into the modelling. For the decrease of S_m at very small channel height ($h < 2$ nm), it cannot be explained by the continuum modelling, which would be discussed in the following MD simulation.

5.5 Conclusion

Through the continuum modelling, we investigated the ion transport through the graphene membrane with the different channel height ($h = 0.5\sim 10$ nm), reservoir concentration ($n_{res} = 0.001\sim 1$ M) and surface charge ($\sigma = 0, -2.3$ mC/m²). The results revealed the novel BBLs

structure in the neutral staggered graphene membrane. And the magnitudes and shapes of BBLs structure depended on the strength of the external E-field, Debye length and nanochannel size.

The formations of BBLs structure in the neutral membrane would modify the potential distribution in the membrane, giving torturous electric potential drop that drives the ions to bypass the graphene sheet. We also found not only the electrophoresis flow, but also the diffusion flow contributed the total ion transport. However for the neutral membrane, the unity scaling law was obtained, which was different from the experiment discovery.

With the introducing the surface charge, the EDLs formed on the surface of the graphene sheet. The shapes of EDLs depended on the surface charge density, Debye length and the size of nanoconfinement. The solution in the aperture region was found to be different from that in the nanoslit region indicating a heterojunction in the nanoporous graphene membrane. The novel behavior of ion transport could be achieved by utilize the heterojunction between the aperture and nanoslit.

Even for the charged graphene membrane, the BBLs structure was still induced by the external E-field. But the magnitude of BBLs structure was really weak which was covered by the strong EDLs. The behavior of BBLs structure was similar to the discovery in the neutral membrane and the weak BBLs structure played a crucial role in generating the tortuous electrophoresis flow.

The electric (Φ_E) and Nernst (Φ_N) potential profile in the charged membrane was similar as that in the neutral membrane. But the surface charge induced a “background” distribution of Φ_E and Φ_N with $\Phi_E + \Phi_N = 0$. To discuss the influence of the external electric potential different ($\Delta\Phi_E = 0.01$ V), the background should be removed.

Even for the similar BBLs structure and the potential profile, the different EDLs structure in the charge membrane provided a different scaling law. Similar to the experiment result, the increase of S_m with the decrease of h was found. It was attributed to the increase of ion concentration (charge carrier density) by the EDLs. But there was still a large deviation

between the modelling and the experiment. Moreover the result cannot reproduce the decrease of S_m by the nanoconfinement effect. Thus the MD simulation was proposed to study the ion transport through the graphene membrane with small channel height.

Chapter 6: MD simulation study on electro-kinetic flow in neutral Graphene hydrogel membrane

6.1 Introduction

With the boost of nanofluidics, much attention has been drawn on this virgin territory to reveal the new phenomena and behaviors in nanoscale ($<100\text{nm}$)[1, 2, 18]. Although much progress has been made in fabricating nanoscale fluidic system, the vision of fluid inside the nanoscale is still obscured by the inferior probe technology. Thus, the nanofluidics community turns to the simulation technology for help to reveal the underground mysteries in nanofluidics.

Although the widely employment of classic continuum modelling in microfluidics field has been extended into the nanofluidics field, the validation of continuum modelling in nanochannel is still a controversy in the academia. It has been discovered that the viscosity of water still hold until the confinement is larger than $\sim 1\text{ nm}$ [1]. It seems that the exotic discipline is required to describe the hydrodynamics of water in sub-nanometer channels. Beyond the background water solvent, the property of electro-kinetic flow is closely related to the liquid/solid interface (boundary structure). It has been shown in Chapter 3 and other prior study that the classic continuum model cannot describe the oscillated laminar boundary layers structure[123]. Especially for the small nanochannel ($<10\text{nm}$), the high-surface to volume ratio and the overlap of boundary layers will significantly modify the structure of fluidics in nanoscale. Furthermore, the nanofluidics is not only dominated by the Navier-Stoke equation and the geometry of microchannel like microfluidics, but also the subtle interaction between solid and fluidics, such as the van der Waals interaction, surface charge, molecular scale, Debye length and so on[1]. These subtle but crucial effects may not be included in the classic continuum model. Hence, atomistic MD simulation has been proposed to develop nanofluidics.

Although the computational efficiency of MD simulation is considerably inferior to that of continuum modelling, the MD simulation could provide a more realistic description of

insight into the nanoscale. The great success has been taken in the field of biological study to reveal the nanoscale water and ionic channel in protein[111]. Hence, the MD simulation has been extensively adopted to study the fluidic behavior in nanochannel. And a great number of exotic phenomena and genius design has been proposed such as conductivity enhancement, nanofluidics diodes, nanofiltration membrane.

Based on the previous discovery in the continuum modelling of electrophoresis, an atomistic MD simulation is employed to study the transport of 1M KCl solution through two-layer graphene hydrogel membrane under the external E-field ($0.01\text{V}/\text{\AA}$). Inspired by the anomalous water transport in CNT[206, 207], the Electro-Osmosis Flow (EOF) in nanochannel is a promising candidate in many fields such as water desalination, biomimetic devices, biosensor and so on. In our MD simulation, a novel EOF similar to the prior study of “electro-osmosis of second kind” [208-210] has been discovered in neutral graphene hydrogel with large channel height. Due to the unique staggered structure, the structure of the EOF in graphene hydrogel is neither different from “electro-osmosis of second kind” in ion exchange membrane nor the conventional EOF in 1-D nanochannel.

Although the surface charge has been demonstrate to play a crucial role in nanofluidics field, the study and discussion in this Chapter will be focused on the neutral channel wall. It provides a fundamental understanding of the novel cascading electrokinetic flow in neutral nanochannel. The result of corresponding graphene hydrogel membrane with surface charge will be discussed in Chapter 7.

6.2 Methods

6.2.1 MD simulation setup

Figure 6.1 is an example of initial configuration of MD simulation where 2-Layers graphene hydrogel membrane was sandwiched by two 10-nm length 1M KCl solution reservoirs. The red and white dots indicate the position of oxygen and hydrogen atoms on water molecule, while the orange and green dots represent the cation K^+ and anion Cl^- respectively. The length of the graphene sheet was $14 \times 5\text{nm}$, the aperture size was about 2nm

and the slit height varies from 7 to 30Å. In the initial state, the 10nm-reservoir was filled by 1M KCl solution, while pure water was filled within the graphene hydrogel. During the simulation, the ions moved into the graphene hydrogel membrane.

The details of each simulation case were listed in Table 6.1, where h is the channel height (interlayer distance between two sheets of graphene). The reservoirs in 30.66Å-spacing graphene hydrogel have been enlarged by 1.5 times to maintain the similar mean concentration (water/ion ratios) in simulation box.

Table 6.1 Particle number of KCl solution in simulation box for different channel height

h (Å)	Reservoir Length (Å)	K+, Cl- pairs	Water #	Water/ion	Graphene #
6.99	100	880	50726	57.64	5280
8.12	100	880	51126	58.10	5280
12.8	100	880	53526	60.83	5280
17.50	100	880	55926	63.55	5280
22.11	100	880	58326	66.28	5280
30.66	150	1448	87180	60.21	5280

An external E-field (orange arrow in Figure 6.1) was imposed through the simulation box that driven the cation and anion moving towards opposite directions and the strength of E-field is 0.01V/Å. As discussed before, the strength of E-field in MD simulation was ten thousand times higher than that in previous continuum modelling and experiment setup, the MD simulation results still could provide some qualitative or even semi-quantitative result.

Under the external E-field, an obvious separation of cation and anion was expected to be shown in the final state of Figure 6.1b. The shadow region in Figure 6.1b was marked as slit regions which was the most attractive region with unique phenomena unrevealed. Hence, my post-analysis will focus on this nanoslit region to reveal the unique boundary layer structure and dynamic transport behavior. For the convenience of post-analysis, the electric potential between two black circles in same YxZ plane was defined as the potential drop across the slit region, denoted as $\Delta\Phi_{slit,E}$.

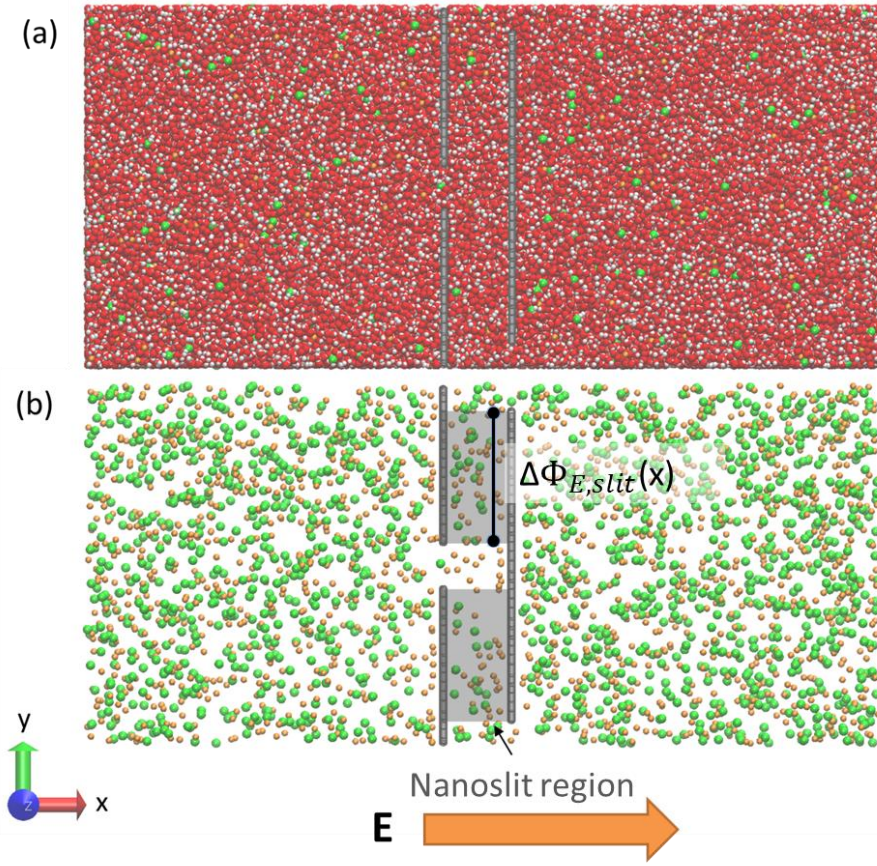


Figure 6.1 MD simulation setup for electrophoresis, when the channel height is 30.66\AA with 150\AA length reservoir on each side: (a) The full configuration of MD simulation where red, white, orange and green dots represent the oxygen and hydrogen atom on water, K^+ and Cl^- ions respectively; The grey dots represent the frozen graphene wall; (b) The final state of MD simulation after 8ns where the water the molecule has been neglected.

The bonded and non-bonded interaction in the simulation box was the same as that in Chapter 3, and simulation was carried out using the LAMMPS code. All the boundaries were periodic boundary conditions. The time step was set as 1 fs. The van der Waals forces were truncated at 1.0 nm with long-range Columbic interactions computed using the particle-particle particle-mesh (PPPM) algorithm. As discussed in Section 3.3.1, the atoms on graphene are frozen during the simulation.

In our MD simulations, the temperature was gradually increased from 298K up to 1000K with the Berendsen thermostat for 10ps. Then the system was kept at 1000K for an additional 10ps. After that our molecular systems were gradually cooling down from 1000K down to 298K. After that the size of our molecular box along the X-direction was tuned to approach

the zero pressure in three directions. The pressure in the following 298K equilibrium stage has been monitored to ensure the approach to zero pressure in X-direction.

After that the box was firstly equilibrated at 298K for another 2ns using Berendsen thermostat. Finally, the external E-field was imposed into the system and the temperature was controlled by Berendsen thermostat at 298K for about 8ns. The resultant trajectory of the last 4ns was taken for post-analysed. In order to obtain the equilibrium boundary layer structure, another 4ns Berendsen thermostat at 298K was followed by the previous equilibrium thermostat, where the last 2ns was employed for post-analysis.

In order to obtain a comprehensive understanding of electro-kinetic flow in graphene nanochannel, two extra MD simulations were employed. First is the electrophoresis of 1M KCl solution in a PBC cubic simulation box with the size of 55.68Å, as shown in Figure 6.2a. The orange arrow indicates the direction of external E-field on system.

All the non-bonded and bonded interaction is set as the previous setup. And the size of simulation box has been tuned to approach the zero pressure in all directions at 298K for 10ps. Then, the simulation system is taken the same simulation annealing process as the previous graphene hydrogel membrane simulation. Similarly, an extra 4ns equilibrium using Berendsen thermostat is employed at 298K. And the pressure of equilibrium state has been monitored to ensure the approach the zero pressure. After that, the simulation box is driven under the external E-field with different strength (0.005~0.5V/Å) for 4ns and the temperature of solution is controlled by Berendsen thermostat at 298K. The trajectory file of last 2ns has been used for post-analysis. Thus the electrophoresis mobility of ions has been obtained.

The second extra MD simulation is to study the 1M KCl solution under the nanoconfinement. As shown the example of Figure 6.2b, 1M KCl solution was confined within two parallel neutral graphene sheets, the slit height of 1D nanochannel was about 12.8Å. All the boundaries in simulation box were periodic. The electric field was imposed along the X-direction. A series of simulation with different channel height from 7Å to 31Å was calculated. However the height of simulation box should be larger than that the double

size of pairwise truncated cutoff ($2 \times 10 \text{ \AA}$). Thus the height of simulation box was increased by repeating the nanochannel. The simulation box in Figure 6.2b is consisted by three 12.8 \AA -height nanochannels, giving a total height of $L_y = 38.4 \text{ \AA}$.

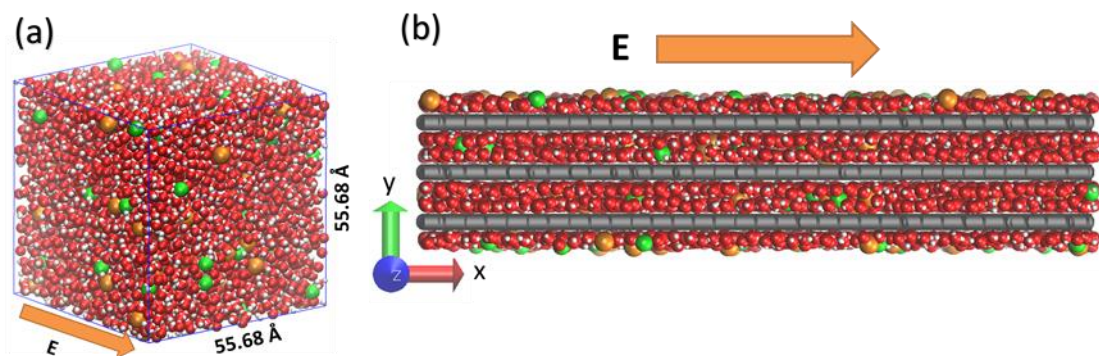


Figure 6.2 MD simulation of 1M KCl solution: (a) in cubic PBC box, (b) in 1D nano-channel, when $h = 12.8 \text{ \AA}$; red, white, orange and green dots represent the oxygen and hydrogen atom on water, K^+ and Cl^- ions respectively. The direction of external field has been imposed along the orange arrow.

The MD simulation setup for 1D nanochannel was summarized in Table 6.2. The constant concentration (water/ions ratio) was maintained in all case. For $h < 10 \text{ \AA}$, the size of system was enlarged to improve the statistic average. Although the channel heights of 1-D nanochannel were not exactly the same as these in the corresponding graphene hydrogel, the maximum 2% variance is negligible. Thus the results in 1D nanochannel were still comparable with that in the corresponding graphene hydrogel membrane.

Table 6.2 The MD simulation setup of 1-D nanochannel with different channel height

$h \text{ (\AA)}$	$L_y \text{ (\AA)}$	$L_z \text{ (\AA)}$	$L_x \text{ (\AA)}$	$K^+, Cl^- \text{ pairs}$	Water #	Water/ion	Graphene #
7.09	42.54	98.2419	140.382	168	9312	55.43	31680
8.21	32.84	73.68	140.382	96	5316	55.38	15840
12.8	38.4	49.121	140.382	105	5820	55.43	7920
17.41	34.825	49.121	140.382	108	5984	55.41	5280
21.89	43.7778	49.121	140.382	144	7976	55.39	5280
31	31	49.121	140.382	108	5984	55.41	2640

The 1D nanochannel simulation also performed the same simulation annealing process, and the channel height was optimized to approach the zero pressure in solution. Then it is first equilibrated at 298K for 4ns using Berendsen thermostat, then the system is accelerated by 0.01 V/\AA E-field for another 12ns along X-direction and the temperature is controlled by

Berendsen thermostat at 298K, and the last 8ns was used for post analysis. Similarly the pressure in equilibrium state was monitored to ensure the approach to zero pressure. Thus both the boundary layer structure and dynamics transport property of KCl solution under the nanoconfinement were obtained.

6.2.2 Post-processing

To reduce the disk usage, two kinds of trajectory files were dumped for post-analysis: firstly, the ionic trajectory file that only the position of ions were saved for every 100fs; Secondly, the full ionic trajectory file that the position and velocity of all atoms were saved for every 10ps. Namely one trajectory file contains few atoms (<1k) but large number of frames (~10k), another contains lots of atoms (>150k) but few frames (~100).

Hence the distribution of ions could be obtained directly from the ionic trajectory files. And the velocity of ions could be drawn from the displacement of ions between the frames. The division between displacement and time span (100fs) was the mean velocity of ions in certain frames. Then according to the position of ions and the mean velocity, the average velocity distribution over the all frame could be calculated. Once the displacement of ions in certain dimension was larger than the corresponding half size, the ions must pass through the periodic boundary and the corresponding displacement could be corrected.

The concentration and velocity of water was drawn from the full trajectory file. Although the number of frames in the trajectory file was relatively small, a large amount of water molecule (>50k) ensures the good statistical average for water property.

In order to understand the electrophoresis in graphene hydrogel membrane, the driving force of electric potential profile was necessary. Then, the full trajectory file has been “rerun” by LAMMPS code with the same simulation setup without LJ interaction. The same statistic averages, such as the short & long electric potential energy, the kinetic energy and so on, could be reproduced during the “rerun” process and the net energy, namely the electric potential energy of each atoms in each frame (every 10ps) was saved. Then electric potential of each atom could be derived from Eq.(6.1).

$$\Psi_i = \frac{1}{2} \sum_{i,j,j \neq i}^N k \frac{q_j q_i}{r_{i,j}} = \frac{1}{2} \Phi_i q_i \quad (6.1)$$

Where Ψ_i is the dumped electric potential energy of atom i , q_i is the net charge on atoms i , $r_{i,j}$ is the distance between atom i,j ; k is the Coulomb's constant and Φ_i is the electric potential of atom i . Once the electric potential and position of each atom was known, the potential profile could be derived.

Once we obtained the concentration and electric potential profile in 2D, we could just even out the concentration or potential cross the x-direction. Actually there are two kinds of average methods: (1) nanoslit region average and (2) electrolyte average.

In nanoslit region average, only the particle in nanoslit region (between the red lines in Figure 6.3) was taken for average calculation. Figure 6.8 shows boundary layers structure in graphene hydrogel membrane with a bin size of 0.2\AA . It gives a zero result in the graphene surface. However, for electrolyte average, the particles in electrolyte except graphene atoms have been taken for average calculation. Thus a continuous curve is obtained along the X-direction with the description of aperture region.

In order to numerically compare the dynamic transportation property in nanoslit region, the mean velocity of ions v_{slit} , and the mean E-field strength E_{slit} , were required to calculate the mean mobility in slits, μ_{slit} .

$$\bar{v}_{slit} = \frac{1}{N_{slit}} \sum_i^{N_{slit}} v_i \quad (6.2)$$

The mean velocity was defined by Eq.(6.2) as the average velocity (v_i) of all cation or anion in slit (N_{slit}). However the mean E-field strength was defined by Eq.(6.3):

$$\bar{E}_{slit} = \frac{1}{L_{slit} H_{slit}} \int_0^{H_{slit}} \Delta\Phi_{E,slit}(x) dx \quad (6.3)$$

Where L_{slit} and W_{slit} are the length and height of slit region, $\Delta\Phi_{E,slit}(x)$ is the potential drop cross the nanoslit region at position of x . Then the mean mobility is derived from Eq.(6.4):

$$\bar{\mu}_{slit} = \frac{\bar{v}_{slit}}{\bar{E}_{slit}} \quad (6.4)$$

6.3 Results and Discussion for neutral graphene membrane

6.3.1 Binary Boundary Layer (BBL) structure

As discussed in Chapter 5, the transport of ions in opposite direction induced the accumulation of ions on graphene sheet, which was coined as the BBLs. The similar BBLs also arisen in the MD simulation of electrophoresis in graphene hydrogel membrane. Figure 6.3 is a typical example of concentration profile of MD simulation with $h = 22.11 \text{ \AA}$. Obviously, the cation K^+ accumulated on the left side of graphene sheet and anion Cl^- on the right side, and the boundary layers of K^+ was a laminar structure due to the steric effect of ions. The formation of BBLs steered the direction of E-field and driven the ions moving across the hydrogel membrane. Beyond the graphene surface, the concentration in the reservoir was almost homogeneous (about 0.9M). The green line indicated the position of graphene sheet and the rectangular region surrounded by red and green line was defined as nanoslit region where it was the focus of the present chapter.

In order to better understanding the effect of E-field, the concentration profiles of ions without external E-field were plotted in Figure 6.4. We could find the similar boundary layers formed on both side of graphene sheet which was induced by the LJ interaction between ion and graphene wall. Compared with the E-field case, there was no obvious polarization of boundary layers with the similar magnitude on both sides. In the reservoir, the similar homogeneous distribution of ions as bulk solution was found.

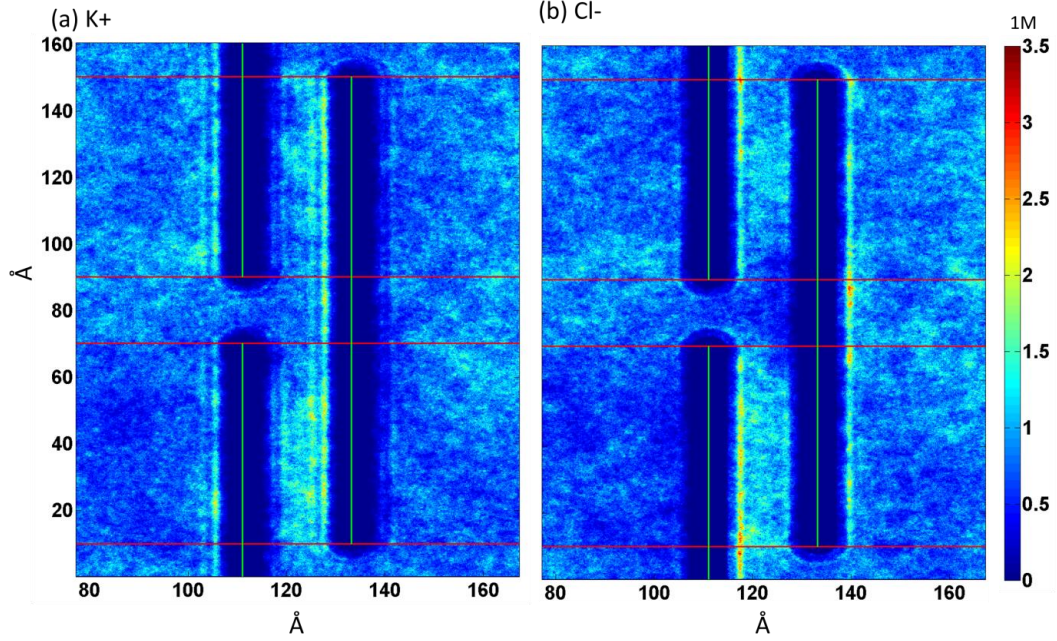


Figure 6.3 The concentration profile (1M) for K⁺ cation (a) and Cl⁻ anion (b) where $h = 22.11\text{\AA}$ and $E = 0.01\text{V/\AA}$. The solid green lines represent the position of graphene sheet and the solid red lines are just guideline line. Thus the rectangular regions surrounded by double red and the green lines indicated the nanoslit region in discussion. Note that a clearly ions separation, BBLs emerged on this electrophoresis study.

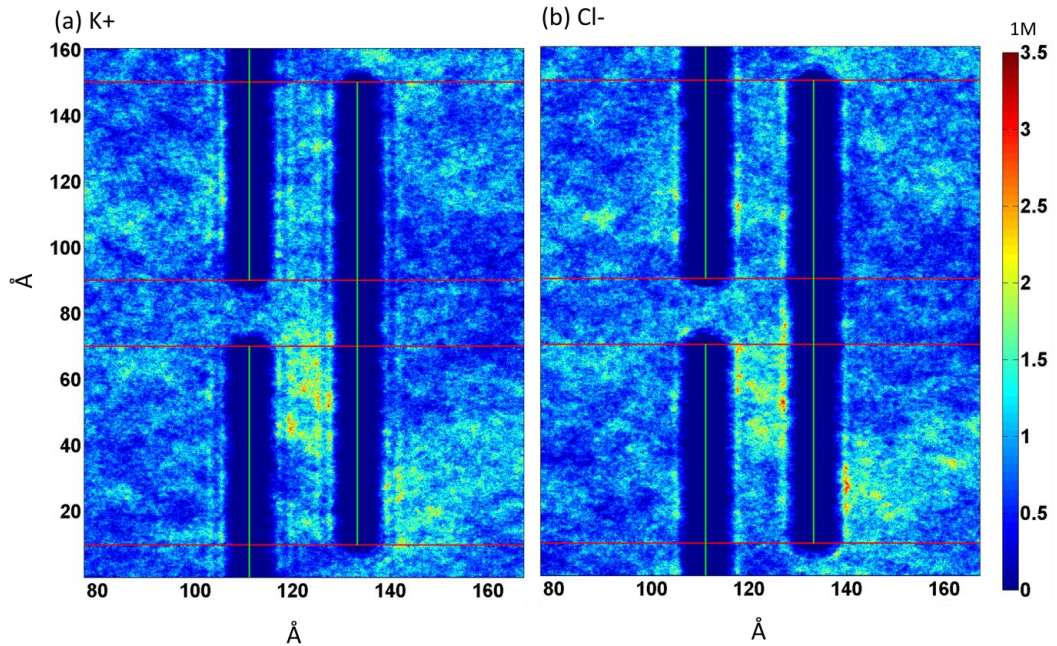


Figure 6.4 The concentration profile (1M) for K⁺ cation (a) and Cl⁻ anion (b) where $h = 22.11\text{\AA}$ and no external E-field. The solid green lines represented the position of graphene sheet and the solid red lines are just guideline line.

Besides the electrolyte ions, the position of water molecule, namely oxygen and hydrogen atom distributions under the same E-field were plotted in Figure 6.5. Obviously, the laminar

boundary layer of water molecule formed on graphene sheet surface. The solid graphene walls break down the continuous hydrogen bond network that induced the accumulation of water in the liquid/solid interface. However, the external E-field only slightly deflected the orientation of water molecule on liquid/solid interface without the noticeable change of concentration distribution. Thus, the concentration profile of water molecule in equilibrium state was neglected.

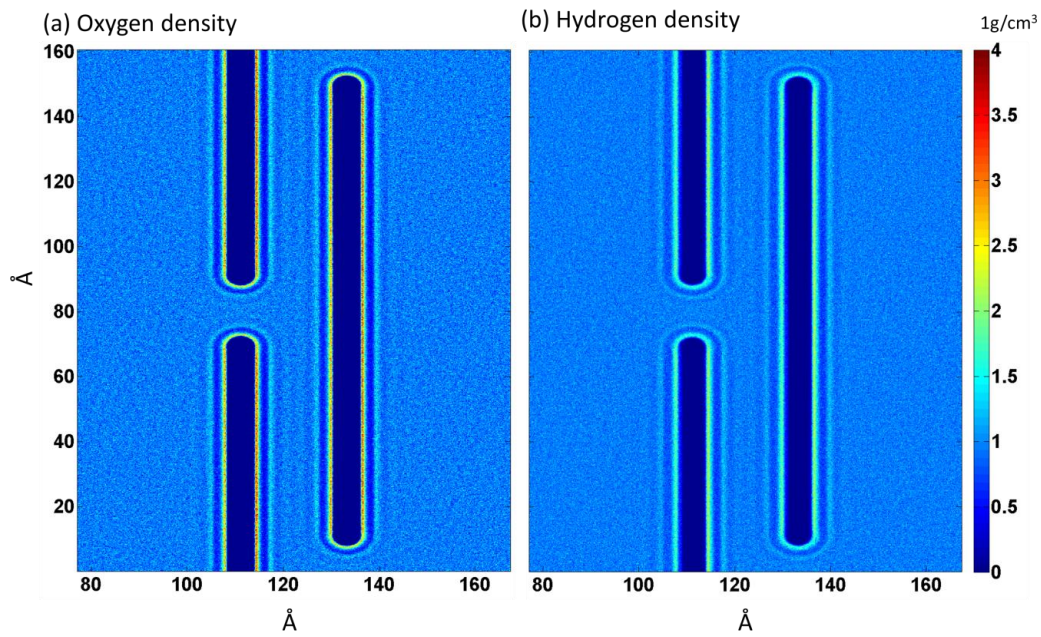


Figure 6.5 The relative density profile ($1\text{g}/\text{cm}^3$) for water molecule: (a) Oxygen atom and (b) Hydrogen atom, where $h = 22.11\text{\AA}$ and $E = 0.01\text{V}/\text{\AA}$. Note that the layered structures appeared on graphene sheet surface due to the van der Waals interaction between water and graphene and the breakdown of continuous hydrogen bond network.

With a precise view on the boundary layers structure, a concentration average profile along the X-direction was drawn in Figure 6.6. However only the nanoslit regions surrounded by the upper or bottom double red lines was taken for the average. Figure 6.6a was the result of graphene hydrogel membrane under the external E-field that the BBLs forms on each side of graphene sheet. The vertical dashed vertical lines indicate the position of graphene sheet. Thus the region between two vertical lines is the nanoslit region in Figure 6.1.

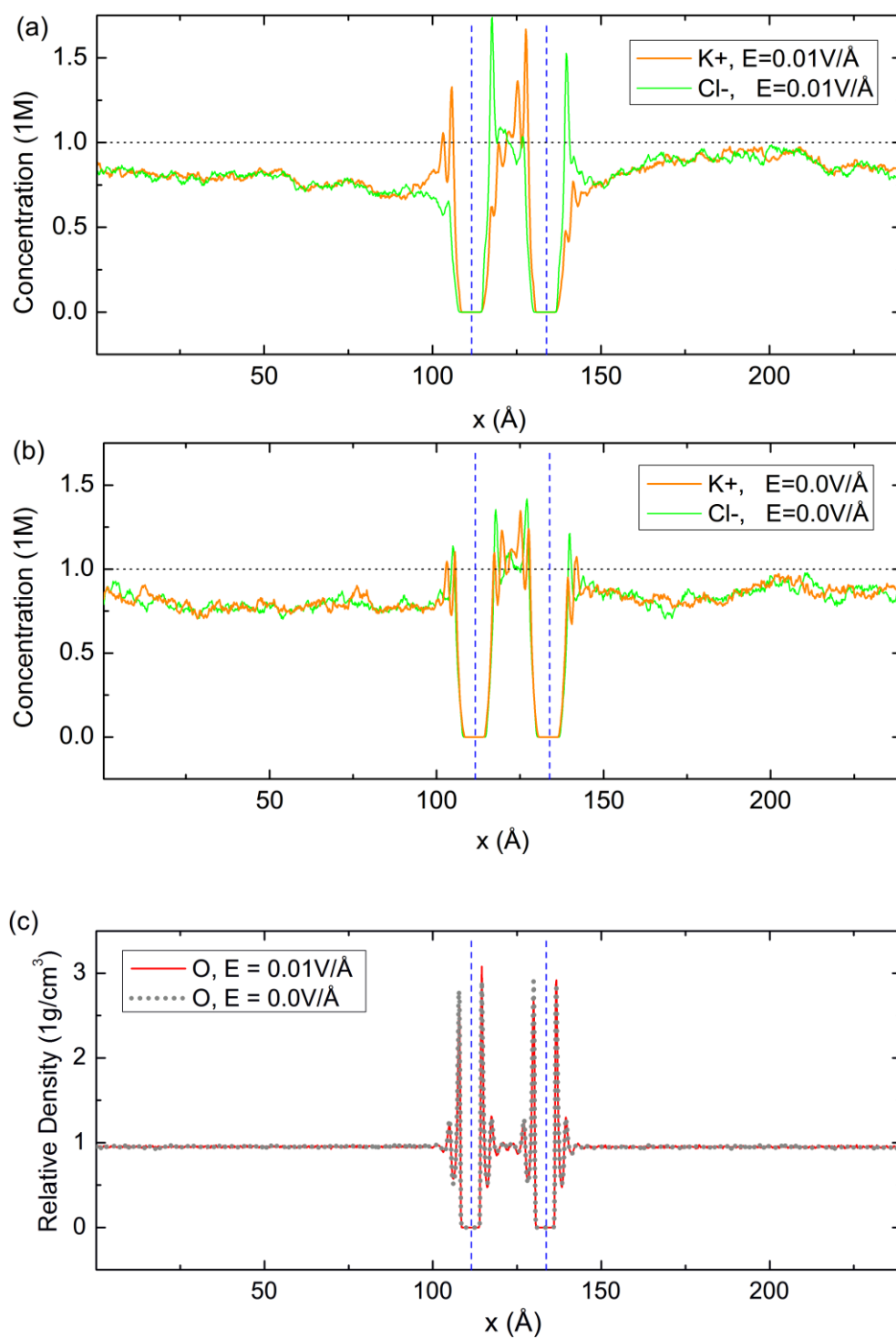


Figure 6.6 The 1D-concentration profile for KCl solution in graphene hydrogel membrane with $h = 22.11\text{\AA}$: (a) ionic concentration with external E-field (0.01V/\AA) and (b) ionic concentration without external E-field; the solid orange and blue lines represent the concentration of K⁺ and Cl⁻ in the units of mol/L; the horizontal dot line represents the concentration of 1M and two vertical dashed lines represent the position of graphene sheet (c) relative water density with bulk solution (1g/cm^3) with (solid) and without external E-field (grey dot). Note that only the nanoslit regions in Figure 6.1 were averaged cross the Y-Z plane to obtain the curves in this figure, namely excluding the aperture region.

Similar to the ordinary boundary layers by surface charge, a laminar structure with oscillation peaks occurs in BBLs. And there was a depletion zone of electrolyte on graphene sheet surface by the strong van der Waals repulsion. It was worth noting that not only the BBLs form inside the slit region, but also occurred on the outside of graphene hydrogel membrane. Because, the external E-field will push the electrolyte ions onto the graphene sheet that forms the BBLs. Obviously, the magnitude of inside BBLs is considerably stronger than that of outside one. Because, much electric potential would be consumed inside the hydrogel membrane that induced the strong BBLs.

Beyond the outside boundary layers, a bulk-like solution was obtained in reservoir. And the concentration in the reservoir was lower than that in 1M. Because the ions moved into the hydrogel membrane filled with pure water. It decreased the preset 1M concentration in reservoir. Unlike the result of equilibrium state in Chapter 3, a constant electrolyte current flows through the simulation system, giving a stationary state of concentration and potential profile.

For comparison the concentration average in nanoslit region on equilibrium state of the same graphene hydrogel without the external E-field has been plot in Figure 6.6b. Clearly, the general EDLs formed on graphene sheet surface by the wall/electrolyte chemical affinity. And the EDLs inside the graphene hydrogel membrane were also stronger than that of outside surface. Because the overlap of EDLs from opposite graphene sheet that will substantially increase the concentration of ions inside the nanochannel. By comparing Figure 6.6a&b, the polarization of boundary layers is introduced by the external E-field, and the magnitudes of counter-ions in one side increased further with consumption of counter-ions accumulation on the other side.

Lastly, the density profile of water molecule with and without the external E-field in nanoslit region was drawn in Figure 6.6c. Obviously, the oscillation EDLs of water molecules also formed on the surface of graphene sheet in both case. It was induced by the breakdown of continuum hydrogel network and water-wall interaction [50, 54]. It seems that the overlap of boundary layers has slightly increased the density of water inside the hydrogel.

However, even under the strong external E-field, there were no significantly changes of EDLs structure of water molecules. Compared with the concentration changes of ions, the density difference of water under the external E-field were negligible.

Although the emergence of the BLs on graphene surface has been identified, triangular concentration distribution discovery in the continuum model has not been demonstrated in the MD simulation. According to the finding in the Chapter 3 and Debye length Eq.(2.4), the most of the counter-ions would locate within the HLs. Thus the densities of counter-ions within the distance of 6 Å from the graphene surface were plotted in Figure 6.7. Note that the binary concentration distribution under the external E-field has been confirmed in Figure 6.6a. Thus the result of K⁺ and Cl⁻ were from the opposite side of the nanoslit region. For comparison, the equilibrium states were also plotted in the dotted lines.

Obviously, at $h > 12.80$ Å, there was a declined tendency of density distribution with maximum on one side and minimum on the other. And the sign of the decline slope varied with the charges of the ions. Nevertheless, such declined distribution was eliminated with the cancel of the external E-field. Both features are consistent with the definition of BBLs in continuum model, but it was unveiled by the narrow extension of BBLs with low λ_d (0.3nm). At $h = 12.80$ Å, the BBLs structure collapsed in the single layer model where the triangle structure breakdown with the maximum density in the middle of the nanochannel and the minimum on exist of the aperture region. The breakdown of BBLs was induced by the overlapped of BBLs from the opposite side and the strong ion/wall interaction in nanoscale enhanced the absorption of ions in the middle nanochannel.

Obviously with the introducing of E-field, the ionic density within HLs would be considerable increased for all cases in Figure 6.7. It could be explained by the forward movement of counter-ion in Chapter 3. However the increase of ionic density would be different among the cases (especially, for the significant increase K⁺ at $h = 17.50$ Å). The divergence of the increase would be attributed to the different local E-field and ionic hydration shell and the overlap of BBLs (nanoconfinement effects).

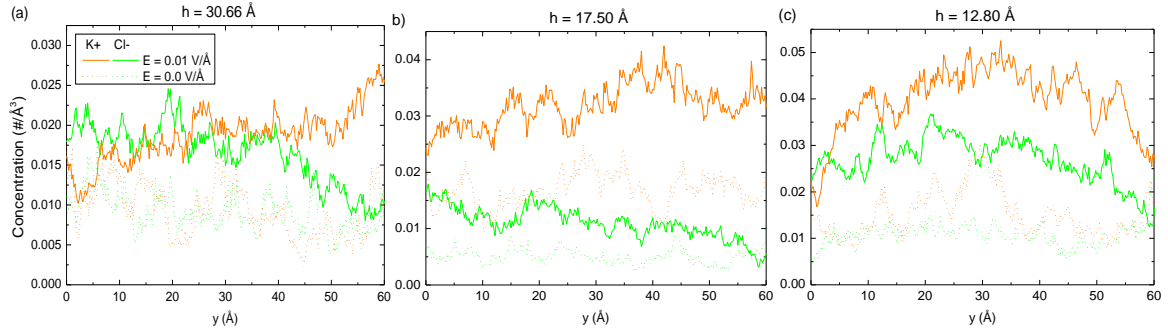


Figure 6.7 The concentration of ions within Helmholtz Layers ($<0.6 \text{ \AA}$) at different channel height (a) 30.66 \AA ; (b) 17.50 \AA ; (c) 12.80 \AA . Note that the origin and green lines represent the result of K^+ and Cl^- respectively and the solid and dashed one is the condition with and without the external E-field.

Figure 6.8 plotted the concentration profile for graphene hydrogel membrane in nanoslit region and the corresponding 1-D nanochannel. The vertical solid lines indicated the position of graphene wall. The concentration profiles with and without external E-field are plotted in upper and bottom part respectively. And the density profile of water compared with 1g/cm^3 bulk water was been plotted as red (O) and black (H) curve.

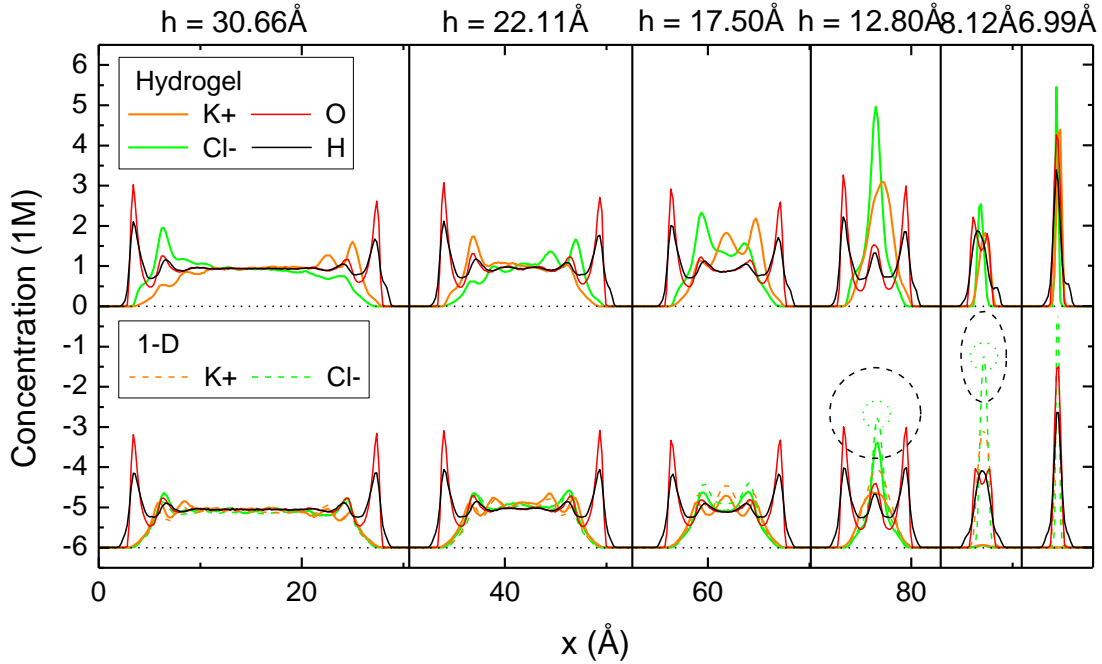


Figure 6.8 The 1D concentration profile for KCl solution in nanoslit region with different channel height from 30.66 \AA to 6.99 \AA . The corresponding concentration distribution without the external E-field was plotted as the bottom part. The solid orange and green lines represent the concentration distribution of K^+ and Cl^- in graphene hydrogel membrane. While the red and black line indicated the density of oxygen and hydrogen atoms vs 1g/cm^3 water. For comparison, the ionic concentration profile of 1M KCl solution in 1D nanochannel with the same slit height is plotted as the dashed curve. The green dot circle indicated the size of ions and the dashed black circle indicated the dimension of surrounding hydration shell.

Although the simulation configuration of graphene hydrogel membrane and 1-D nanochannel was different, the concentration profile of ions in nanoslit region was similar to that of 1-D nanochannel in equilibrium state (dashed line), except for slightly different magnitudes. Because, the nanoslit region could be regarded as the 1-D parallel nanochannel with the same wall/electrolyte interaction.

For the large slit height ($h = 30.66\text{\AA}$), the boundary layers emerges on the surface of graphene sheet ($\sim 9\text{\AA}$) in equilibrium state. In the middle of nanochannel, the oscillation of concentration has been annihilated giving a “bulk” solution with constant concentration (about 0.9M). As described in Chapter 3, both ions is behind the first water layer indicate a strong hydration shell between water and electrolyte ions.

Then with the decrease of slit height, the boundary layers from the opposite sheets started to overlap with each other. It increased the average concentration in nanochannel and extinguishes the middle “bulk” solution. But the ions still sandwiched by the two first water layers on each end in equilibrium state.

If we further decreased the channel height into 12.8\AA , the multi-peaks of overlapped boundary layers transferred into a single layer structure. At that stage ($h = 12.8\text{\AA}$), the nanochannel could merely contain the single layer of ions (dot circle) in the centre with its first hydration shell (dashed circle). Thus we obtained the structure that the three layers of water molecule sandwiched the single layer of ions in the centre[179].

With the further reducing the channel height ($h < 10\text{\AA}$), the first hydration shell (dash circle at $h = 8.12\text{\AA}$) will be significantly distorted under the strong nanofinement[179]. At $h = 8.12\text{\AA}$, the two first water layers in two side merged together significantly with slight decrease of density of water in the center. However at $h = 6.99\text{\AA}$, the single peaks structure was obtain for both water and ions.

Usually a dehydration process occurs in the entrance of small nanochannel and extra thermodynamics energy is required. Moreover, the van der Waals repulsion between ions and walls would be considerably strong at small channel that further block the entrance of ions.

Thus, the concentration in graphene hydrogel membrane will be significantly reduced for the smaller channel height ($h < 10\text{\AA}$). In equilibrium state, the concentration inside hydrogel membrane is almost zero compared with about 1M solution in the electrolyte.

However, the concentration of KCl solution in 1-D nanochannel is set as constant (1M), namely a constant water/ion number ratio (~ 55.4). The decrease of slit height will induce an increase of the magnitudes of boundary layers, giving a high but sharp peak. Thus 6 times higher concentration peaks was obtained in the 1-D nanochannel at $h = 6.99\text{\AA}$ rather than nearly zero in the graphene hydrogel. In practically, it just represents the shapes of boundary layers in open nanochannel rather than the magnitude.

Intuitively, all boundary layers structures for ions and water in equilibrium state were symmetric. However with the introducing of external E-field, the polarization of boundary layers was imposed into the system which is named as the BBLs in Chapter 5. For large channel height ($h = 30.66\text{\AA}$), the BBLs developed with the accumulation of counter-ions and the repulsion of co-ions. Thus it formed a continuous decrease of concentration profile from one side to the other side. Even for BBLs, the laminar oscillated structure also still preserved on the graphene sheet surface and a “bulk” solution was still obtained in the middle of channel.

As discussed in Chapter 3, the dipole nature of water molecule ensured the negligible influence of density distribution under the strong E-field. The external E-field marginally increased the density of oxygen in the left boundary layers, but considerably shifts the orientation of water on the right graphene surface. Similar to the description of boundary layers on negative charged graphene surface, the hydrogen density beyond the first water layer has been considerably increased by the external E-field.

With regard to the nano-confinement effect, the decrease of channel height would produce the overlap of BBLs. But the polarized boundary layers structure still reserved. It is worth noting that for $h = 17.50\text{\AA}$, the position and number of boundary layers peaks under the external E-field was the same as there in the equilibrium state. It seemed that the external E-

field only modifies the magnitudes of oscillation peaks of boundary layers without the changes of the initial laminar structure. Because the positions of first peak (OHLs) and the wavelength of the concentration oscillation was determined by the hydration shell size of ions. Thus the external E-field could only modify the magnitudes of boundary layers rather the position of peaks (Helmholtz layers).

As discussed in Chapter 4, the BBLs on two sides with positive or negative net charge are induced by the external E-field. The similar binary structure has been reported in the nanochannel with the opposite surface charge on top and bottom walls[139]. And, the surface charge density on walls could be equivalent as the strength of external E-fields. Thus, the magnitude of BBLs dominantly depended on the strength of external E-field. The magnitude of BBLs increases with the decrease of the channel height, owing to a large electric potential drop.

Although the BBLs moved into the single peak profile with the further reduce of channel height ($h \leq 12.8\text{\AA}$), the separation of cation and anion still remained (different peak position). Even for the smallest channel height ($h = 6.99\text{\AA}$), the separation of ion concentration peaks was about 0.2\AA . It is induced by the strong external E-field. But the shapes of boundary layers in graphene hydrogel membrane under the external E-field was similar to that in 1-D nanochannel at equilibrium state.

Contrasty, the concentration of graphene hydrogel membrane in the very small channel ($h < 10\text{\AA}$) under the external E-field would be significantly higher than that in equilibrium state. Because the driving force by external E-field was strong enough to overcome the energy barrier of partial dehydration on the entrance of nanochannel[211]. Thus the concentration in nanoslit region was considerably increased by the external E-field.

As similar to the equilibrium state, the water profile also shows a strong deformation of hydration shell and the similar dehydration process occurs in very small channel ($h < 10\text{\AA}$). Thus the ions will firstly dehydrate at the aperture area and then flow through the nanoslit region under the E-field in Y-direction, finally rehydrate at the other aperture area.

Although the E-field was strong enough to induce the current flow, the energy barrier of partial dehydration will still hinder the entrance of ions. Thus under the external E-field, the concentration of ions for very small channel height ($h < 10\text{\AA}$) would be considerably lower than that at $h = 12.8\text{\AA}$. However the similar number of ions is obtained for both $h = 8.12\text{\AA}$ and 6.99\AA . It gives a higher but sharp concentration peak at $h = 6.99\text{\AA}$.

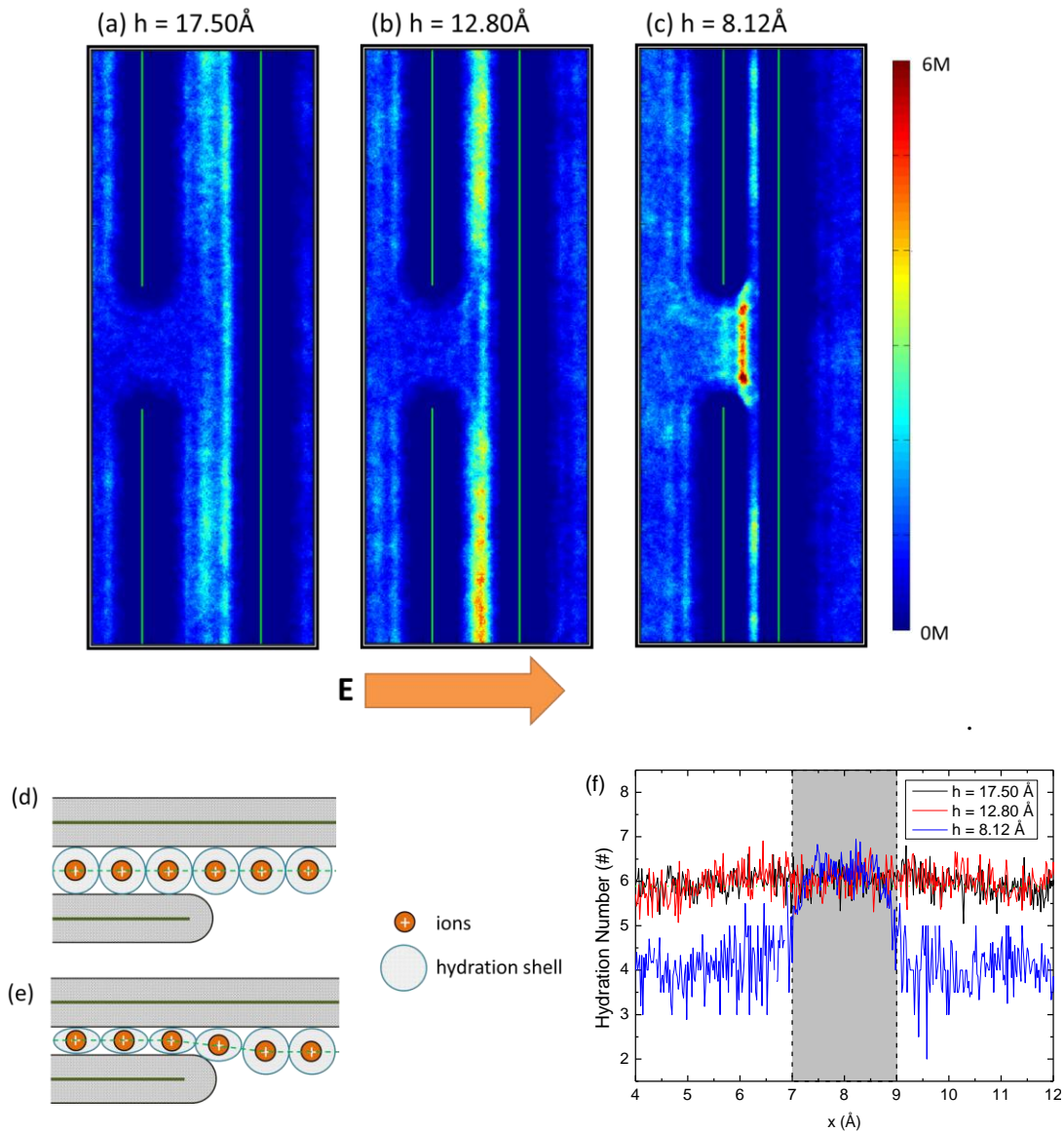


Figure 6.9 The concentration profile of K⁺ in aperture region for graphene hydrogel under the external E-field: (a) $h = 17.50\text{\AA}$; (b) $h = 12.80\text{\AA}$; (c) $h = 8.12\text{\AA}$; (d&e) schematic for transport process in nanochannel, where $h \approx d_H$ in (d) and $h < d_H$ in (e). d_H is the diameter of ions' hydration shell. The dashed green line indicates the position of ionic plane (concentration peaks in (a~c)). Note that the mismatch of the ionic plane in (e) by dehydration process. (f) The calculation hydration number of K⁺ within the aperture and the nanoslit region. Note that the shadowed region is marked as the aperture region. And the horizontal green line presents the hydration number in the bulk solution.

To verify the partial dehydration hypothesis in the very small channel, a concentration profile of K^+ in aperture region was drawn in Figure 6.9. With gradually decrease the channel height from (a) to (c), there was a significant accumulation of K^+ in apertures region at very small channel ($h < 10\text{\AA}$), owing to the hindrance of partially dehydration process.

Figure 6.9(d) is the schematic for transport process in large nanochannel. If the channel height (h) was larger than or similar to the size of hydration shell (d_H), the counter-ions forms a parallel ionic plane (dash green line) on graphene sheet surface. And the distance between the ionic plane and graphene sheet was determined by the hydration shell dimension.

Thus, for $h = 17.5\text{\AA}$ (Figure 6.9a), the oscillated boundary layers structure with multiple concentration peaks could be identified. For $h = 12.8\text{\AA}$ (Figure 6.9b), the overlap of BBLs fallen into a single peak profile that considerably increase the concentration in the slits. For both figures ($h > 10\text{\AA}$), a continuous parallel bright ribbon (concentration peak) could be found on the graphene sheet surface. And the interlayer distances between the ionic plane and graphene sheet were the same for both cases.

Once $h < d_H$, the nanoconfinement induced the partial dehydration phenomena. As described in (Figure 6.9e), the entrance of ions into the nanoslit region required a distortion of hydration shell and the ionic plate in the nanoslit region was located in the centre. However the free accumulation of counter-ions in aperture region remained its intrinsic hydration shell. Thus in Figure 6.9c, we could discovery a mismatch of the ionic planes in the nanoslit region and in the aperture region. And the transition from full to partially hydrated state occurs at the entrance of slit region. The similar mismatch of ionic plane and transition found be identified in (c) with $h = 8.12\text{\AA}$. Hence, the change of concentration peak between aperture and nanoslit region clearly demonstrates the partial dehydration process at $h < 10\text{\AA}$

To verify the hypothesis of partial dehydration, the hydration number of K^+ within the nanoslit and aperture region (between the X-Y planes of the two graphene sheets) was presented in Figure 6.9f. The horizontal dashed line is the bulk hydration number of K^+ (5.89) which is consistent with 6-coordinate in the literature [212, 213]. At $h < 10\text{\AA}$, the strong

nanoconfinement stripped the hydrated water and decreased the hydration number of K^+ . While in the aperture region, the hydration number was almost the same as that in the bulk solution. Nevertheless, At $h > 10 \text{ \AA}$, the hydration number remained the same in the both nanoslit and the aperture region. That present result in Figure 6.9f definitely demonstrated the partial dehydration of ions into the nanochannel.

Taken together, the BBLs emerged on the nanoslit region with the introduction of the external E-field. The structure of BBLs was different from that in equilibrium state. With the reduction of channel height, both boundary layers structure would overlap with each other and finally transfer into a single peak profile. Beyond the critical height ($h = 12.8 \text{ \AA}$), the very small channel will block the entrance of ions into slit region. However the strong E-field could overcome the energy barrier that significantly increases the concentration in nanoslit region and induce an ionic flow through the simulation system.

6.3.2 Electric potential profile

Besides the stationary concentration profile, the driving force of the electric potential profile would be the other critical issues in this cascading electro-kinetic flow. Hence the electric potential profile extracted from the electric potential energy of oxygen atom has been plotted in Figure 6.10.

Figure 6.10a was the counter plot of net electric potential in system with a gradually drop from left to right. For clarity, the data in the counter plot was smoothed via a Matlab code. The potential in counter plot is an average result with its 10×10 square neighbours (size of $2 \times 2 \text{ \AA}^2$). The vertical white region with solid green line inside indicates the position graphene sheet with the exclusion of electrolyte by the van der Waals repulsion.

In the reservoir, the potential drop would be almost uniform along the x-direction. With the approach to the graphene surface, a tunnel-like potential drop profile emerges on the aperture region that driven the electrolyte ions into the aperture region. Inside the graphene hydrogel, the potential drop developed along the graphene sheet in Y-direction. Finally, another tunnel-like potential drop occurs in the other aperture region, which moved ions out

of membrane. This continuous electric potential drop could prompt the ions bypassing the staggered graphene structure.

As the aforementioned superposition of electric potential in Chapter 3, the net electric potential was a linearly combination of electrolyte potential profile by electrolyte itself with the external one by the external E-field.

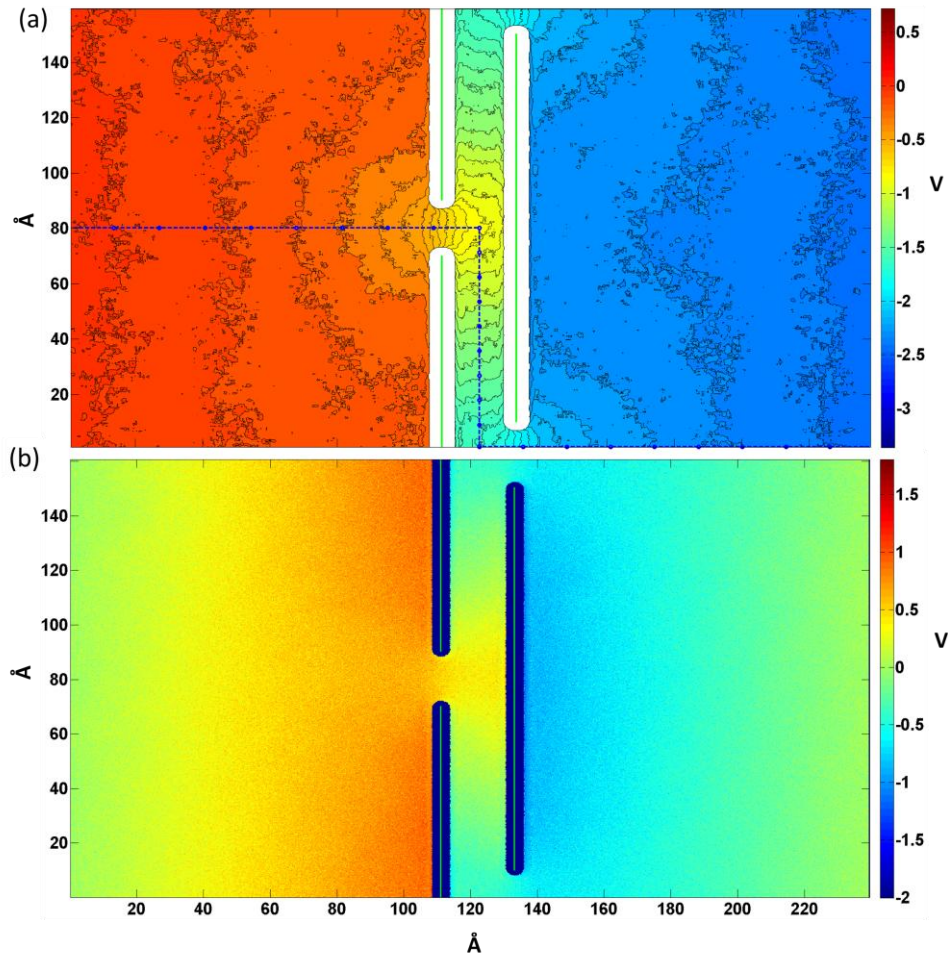


Figure 6.10 The electric potential of oxygen atom where $h = 22.11\text{\AA}$ and $E = 0.01\text{V}/\text{\AA}$: (a) the contour plot of net electric potential after smooth; (c) The inner electric potential by electrolyte itself. The green line represents the position of graphene wall and the cycle dashed lines indicate the “diffusion” path to evaluate the potential drop in the cascading electro-kinetic flow.

Due to the PBC of simulation box, the electric potential of electrolyte itself should be the same on both sides. Thus, Figure 6.10b is the electrolyte potential on oxygen atoms. As described in Chapter 5, the formation of the BBLs would induce a reverse E-field in reservoir

against the external E-field. Thus, the potential drop was decreased in reservoir but increased in the graphene hydrogel membrane.

In order to better compare the different kinds of electric potential, the average electric potential of electrolyte in system along the X-direction has been taken. Figure 6.11 is the example of result in graphene hydrogel membrane with $h = 22.11 \text{ \AA}$.

The dashed yellow lines was the inside electrolyte potential on oxygen atom. Thus there was a constant reverse E-field in the reservoir that decreased the net potential drop in reservoir, but increases the potential drop across the membrane owing to the different conductivity of ions in membrane. In middle of graphene hydrogel, there is another reverse E-field by the induced BBLs against the external E-field in X-direction. It prevented the electro-kinetic flow normal to the graphene sheet.

The dot line was the electric potential by the external E-field with constant potential gradient. The combination of two lines gives the net potential drop in system (solid lines in Figure 6.11). As discussed in post-analysis section, an electrolyte average gives a continuous curve with the description of the aperture region.

The solid line (net potential) was a linearly combination of the electrolyte and external potential., Electric potential on all kinds of electrolyte atoms (O, H, K⁺ and Cl⁻) has been plotted in Figure 6.11. All of them owned the similar electric potential distribution (the solid lines in different colour), except for the Helmholtz layer. However the number of ions in the system is much less than that of water molecules. And comparing to the point charge of hydrogen atom in TIP3P water model, the oxygen with the steric van der Waals shell was more applicable to describe the electric potential on the system. And a very good statistical average could be taken in Figure 6.10.

The solid green line is the overall electric potential on oxygen atoms. It clearly shows the potential drop in the reservoir would be significantly lower than that in graphene membrane. As described in Chapter 5, the mean conductivity of membrane would be several times lower

than that of bulk solution. Thus a large amount of electric potential drop was required to push the ions pass through the staggered graphene structure.

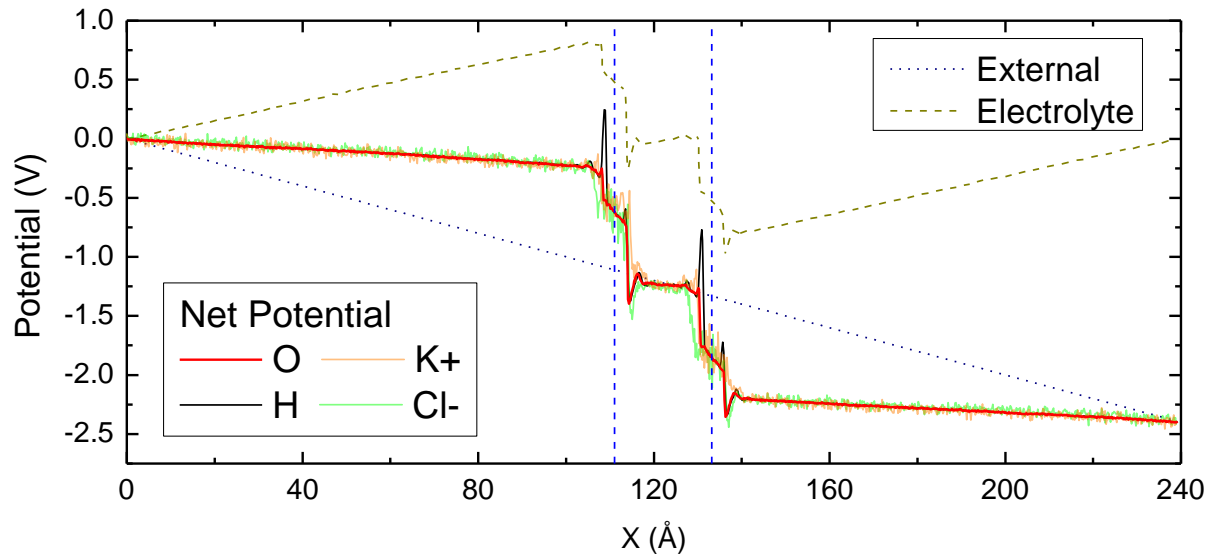


Figure 6.11 The average electric potentials of different kind along the X-direction with $h = 20.11\text{\AA}$ and $E = 0.01\text{V/\AA}$: The dashed yellow line indicates the distribution of inner electrolyte potential by solution itself with zero potential on each side; The dot blue line indicates the potential by external electric field; The solid green lines with different colour are net electric potential on different type of atoms. The vertical dashed blue lines show position of graphene wall. Note that the boundary layers on graphene sheet surface induces the significantly vibration of electric potential.

The above potential figures just provided an overall insight into the electric potential distribution. It cannot value the transport process straight forward. Hence, an intuitive “transport path” (the circle dashed line in Figure 6.10a) was proposed to evaluate transport property in simulation system, similar to Chapter 5.

Figure 6.12 indicated the potential drop along the “diffusion” path for different channel height and the position of nanoslit region in the “diffusion” path was marked by the vertical dotted line. While the short solid line at each curve indicated the position of aperture opening at “transport path”. With the reduction of channel height, the apertures opening get closer to slit region.

Evidently, the potential drop in slit regions was almost linearly in all cases. With regard to the high aspect ratio of slit region, especially for small channel, a linear potential drop occurs in slit region. Another linear potential drop was also found in the reservoir. But the

slope of the potential drop in reservoir is much lower than that in the slit region, owing to the different conductivity of membrane and reservoir.

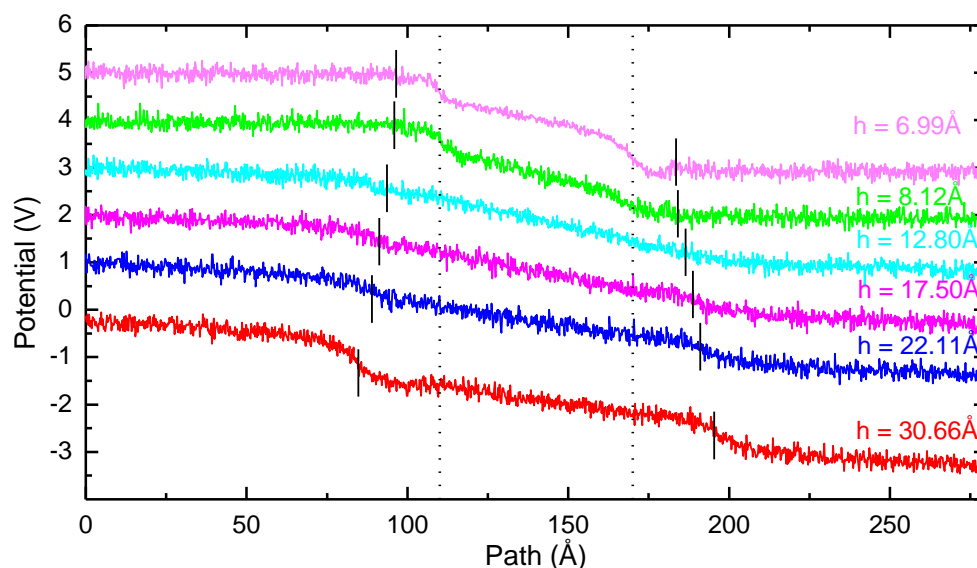


Figure 6.12 The potential distribution along the “transport path” in Figure 6.11. The labels on the right mark the corresponding slit height and the position of two vertical dot lines indicate the entrance and exit of nanoslit region in that path. The short vertical lines on each curve indicate the position of entrance and exit aperture. Both the position and potential in each case has been shifted for clarity. Note that the potential drop in the nanoslit region is almost linearly, while on the two side aperture region, a significant potential drop occurs with the considerable large or small slit height.

Similar to the previous discovery in classic thermodynamics framework, the potential drops in aperture region depended on the channel height. For large channel height ($h = 30.66\text{\AA}$), the potential drop considerably increased in the aperture opening (short vertical line). As discussed in Chapter 5, once the aperture size (20.0\AA) was much smaller than the double of the channel height ($h = 30.66\text{\AA}$), the bottleneck of aperture region required a large potential drop.

However for $h = 12.80\sim 17.50\text{\AA}$ with the similar aperture size and double channel height, the slope of potential drop in aperture region was similar to that in slit region, which is the same as the discovery in Chapter 5.

If the channel height is further decreased, the partial dehydration occurs on the entrance of nanoslit region (dotted lines) and extra potential drop was consumed to push the ions into the slit region. Clearly, a hasty potential drop emerges again in the entrance of nanoslit region

for $h < 10\text{\AA}$. It is similar to the reported the hasty potential of mean force (PMF) drop in the entrance of nanochannel[211].

Although similar phenomena were founded in previous COMSOL modelling, the hasty potential drop in MD simulation was owing to the partial dehydration process rather than the distortion of continuous BBLs structure. The atomistic partial dehydration phenomena cannot be described by the classic thermodynamics framework. The position of hasty potential drop (slit region entrance) at very small channel height was also different from that in large channel. It confirmed the aforementioned discovery that partially dehydration process will occurs in the entrance of slit region.

In summary, under the external E-field, the BBLs formed in nanoslit region that deflect the E-field along the graphene sheet. The BBLs are enhanced with the decrease of channel height. And the ions transport in nanoslit region under a torturous continuous E-field. Besides the slit region, the potential drop in the aperture regions also varied considerably with the channel height. For large channel, the bottleneck of apertures region limited the electrokinetic flow. For very small channel, the partial dehydration process considerably blocked the entrance of ions and increased the potential drop.

6.3.3 Mobility in bulk solution

Before studying the dynamic transport property of electrolyte in slit region, the dynamics property of KCl electrolyte in bulk solution should be studied firstly. Figure 6.13 summarized the mean velocity of electro-kinetic flow under the different E-field.

At the low strength of E-field ($E \leq 0.1\text{V}/\text{\AA}$), the mean velocity of both ions increase linearly with E-field. Conversely, the electrophoresis of ions will be significantly enhanced at high E-field ($E > 0.1\text{V}/\text{\AA}$). Thus the simulation setup of E-field ($0.01\text{V}/\text{\AA}$) within the linear region is still acceptable for the following discussion.

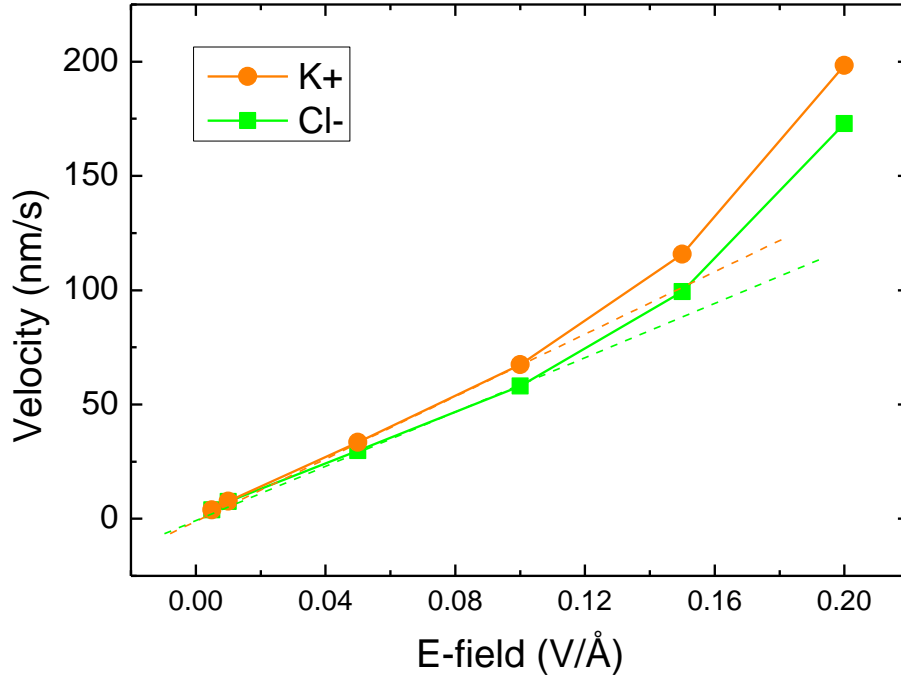


Figure 6.13 The mean velocity of ions in 1M bulk KCl solution under the different E-field strength. The orange and green curve represents the result of K⁺ and Cl⁻ respectively. And the dashed line with the same colour indicated the slope fitting of linearly region, namely the mobility.

Then the electrophoresis mobility of both ions is calculated by fitting the result in linear region, (the slope of dashed line), giving $\mu_{K^+} = 67.41 \text{ nm}^2/(\text{V}\cdot\text{ns})$ and $\mu_{Cl^-} = 58.10 \text{ nm}^2/(\text{V}\cdot\text{ns})$ respectively. Fortunately, the result of K⁺ in MD simulation is similar to that in experiment[9], $\mu_{K^+, \text{exp}} = 72.5 \text{ nm}^2/(\text{V}\cdot\text{ns})$. But the experiment result[9] of Cl⁻, $\mu_{Cl^-, \text{exp}} = 79.1 \text{ nm}^2/(\text{V}\cdot\text{ns})$ was still considerably higher than that in MD simulation.

The similar mismatch between the simulation and experiment has ever been reported in the other MD studies[214], owing to the lack of parameter optimization. However through the comparative study of electrophoresis in different nanochannel, our MD simulation could still provide a qualitatively or semi-quantitatively description of electro-kinetic flow of 1M KCl solution.

6.3.4 Electro-kinetic flow in graphene hydrogel membrane

In order to understand the electro-kinetic flow in slit region, the average velocity profiles along the graphene sheet in nanoslit region was plotted in Figure 6.14. For comparison, the

result in 1-D nanochannel was also added in in Figure 6.14. The horizontal dotted line indicated the mobility of ions in bulk solution

In the nanoslit region, the transport direction of cation was regarded as the positive direction. Thus the velocity of anion is the negative. All the velocity profiles in Figure 6.14 have been divided by the driving force of E-field along the channel. Namely, the mobility profile was obtained. For graphene hydrogel, the E-field was regarded to be a constant (\bar{E}_{slit}) and calculated as Eq.(6.3). For 1-D nanochannel, the driving force was just the external E-field ($0.01\text{V}/\text{\AA}$).

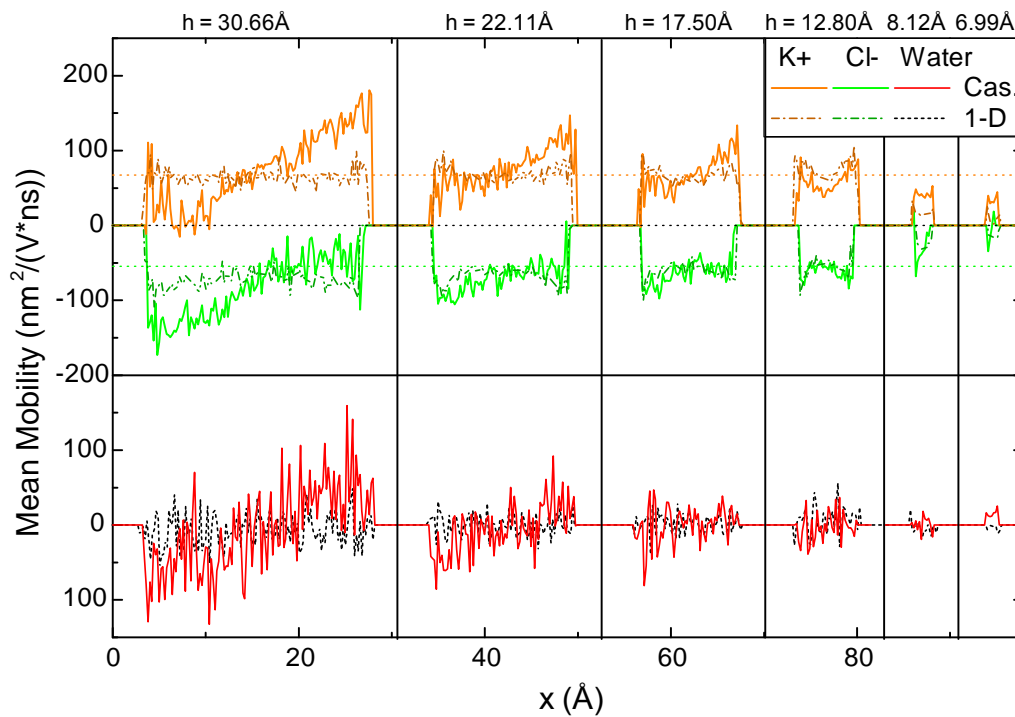


Figure 6.14 The velocity (mobility) of ions along the Y-direction in the nanoslit region or 1-D nanochannel (top) and the velocity of water in nanoslit region or 1-D nanochannel (bottom). The solid orange and green lines represent the mean velocity profile of K⁺ and Cl⁻ in slit region. While the dashed line with the same colour indicated the velocity profile of ions in 1-D nanochannel. The red and dashed black lines indicate the velocity profile of water molecule (Oxygen atom) in nanoslit region and in 1-D nanochannel, respectively. Note that the velocity profiles was divided by the driving force of E-field: \bar{E}_{slit} in nanoslit region or $E = 0.01\text{V}/\text{\AA}$ in 1-D nanochannel.

Under the external E-field, the polarized BBLs induced a polarized velocity profile in graphene hydrogel membrane. For large channel height ($h = 30.66\text{\AA}$), the maximum velocity of cation (K⁺) was obtained on the right side cationic boundary layers. Reversely, the maximum velocity of anion (Cl⁻) locates on the opposite side of anionic boundary layers. The

velocity (mobility) profile derives from the classic linearly electrophoresis process and the result is even higher than the bulk mobility of ions.

Actually, the separation of cation and anion by the BBLs induced two acceleration mechanisms:

- 1) Compared with bulk solution where the same amount of cation and anion traveled in the opposite direction, the number of counter-ions in the BBLs was much larger than that of co-ions. Thus the friction between the ions will be considerably reduced that accelerates the movement of counter-ions in BBLs.
- 2) The extra counter-ions in BBLs will drag the surrounding hydrated water molecule moves along the same direction, entitled as the EOF. Unlike the conventional EOF with a plug-like flow velocity[122] in the middle of microchannel, the EOF generated by the BBLs was polarized with maximum velocity on each side but in the opposite direction (red line in Figure 6.14). Hence the polarized EOF was a sheared laminar flow with zero velocity in the center of slit region. This polarized EOF was consistent with the transport direction of counter-ions in each BBLs that will further increase the velocity of counter-ions in each side.

With regards to the nano-confinement effect, the decrease of channel height will bring a decrease of velocity for ion even with the increase of \bar{E}_{slit} . It declined the mean velocity in two terms.

- 1) The overlap of BBLs will increase the number of co-ions that raise the friction between the ions in the BBLs.
- 2) The polarized EOF was a laminar flow sheared by the extra counter-ion in each side of BBLs. The overlap of boundary layers not only lowers the number of extra counter-ions (driving force) but also reduced the shear force distance. Thus the magnitudes of EOF will be considerably reduced by the channel confinement.

Hence, the polarization of velocity profile was weakened with the decrease of channel height.

At $h = 12.8\text{\AA}$, the BBLs overlapped into a single peak profile that introduced a symmetric velocity profile of ions and the corresponding EOF in nanoslit region was eliminated. With the further reduction of channel height, the heavy confinement of graphene wall (at $h < 10\text{\AA}$) will significantly increase the friction force between the ions and solid graphene wall. Thus the velocity of ions in the very small channel would be substantially shrunk.

The polarized EOF in graphene hydrogel membrane is similar to the prior study of the electro-osmosis of “second kind”[209, 215]. Both of EOF was stem from the peculiar boundary layers structure by the normal E-field. However, the peculiar boundary layers induced another tangent E-field along the boundary layers. It drives the electrophoresis/electro-osmosis flow to bypassing the impermeable or semipermeable particles with considerably increase of flow velocity.

Usually the electro-osmosis of “second kind” was studies in the granule particle with the maximum EOF velocity at 45° [208, 210]. However the polarized EOF in MD simulation is almost 90° to the external E-field and the concentration of MD simulation ($\sim 1\text{M}$) is significantly higher than that in the experiment of electro-osmosis of “second kind” ($10^{-3\sim 5}\text{M}$)[208-210, 215]. That would be the reason that the enhancement of the electro-kinetic flow in MD simulation was much lower than the result in electro-osmosis of “second kind”.

Beyond the similarity with the electro-osmosis of “second kind”, the polarized EOF with opposite flow direction was distinctively difference from the conventional 1-D nanochannel study with single flow direction. The novel polarized EOF in graphene hydrogel membrane has reveals two new applications for graphene staggered structure:

- 1) the nanomixer in the aperture region
- 2) The laminar shear flow to deform or appeal the particles in nanochannel.

Figure 6.14 also presented the symmetrical velocity profile of ions in 1-D nanochannel (dashed lines) with maximum velocity of ions on the surface of graphene sheet. It was reported that the frictionless graphene wall or carbon nanotube wall could significantly increase the transport velocity of water flow. Thus the partially dehydrated ion could also

travel faster on the smooth graphene wall surface that slight increased the velocity on the 1-D nanochannel. It gives a meniscus shape of velocity profile in 1-D nanochannel. However if we considerably decrease the channel height ($h < 10\text{\AA}$), the heavy confinement of graphene wall would reversely increase the friction force, namely decreased the velocity in 1-D nanochannel. The results were even lower than that of bulk solution.

From the velocity profile, we could concluded that the velocity of ions could be considerably enhanced by the unique BBLs structure at large channel height ($h = 30.66\text{\AA}$). And the mobility of ions would be higher than that in 1-D nanochannel. With the decrease of nanochannel, the polarization phenomena would be eliminated at $h = 12.8\text{\AA}$, giving the similar velocity profile in 1-D nanochannel. At very small channel ($h < 10\text{\AA}$), the mobility of ions will be considerably reduced by the strong nano-confinement of solid graphene wall.

In order to verify the above observation, the mean mobility of ions in nanoslit region and 1-D nanochannel was calculated by Eq.(6.4). The result is been plotted in Figure 6.15. The mobility of bulk solution was added as the horizontal dotted line for comparison.

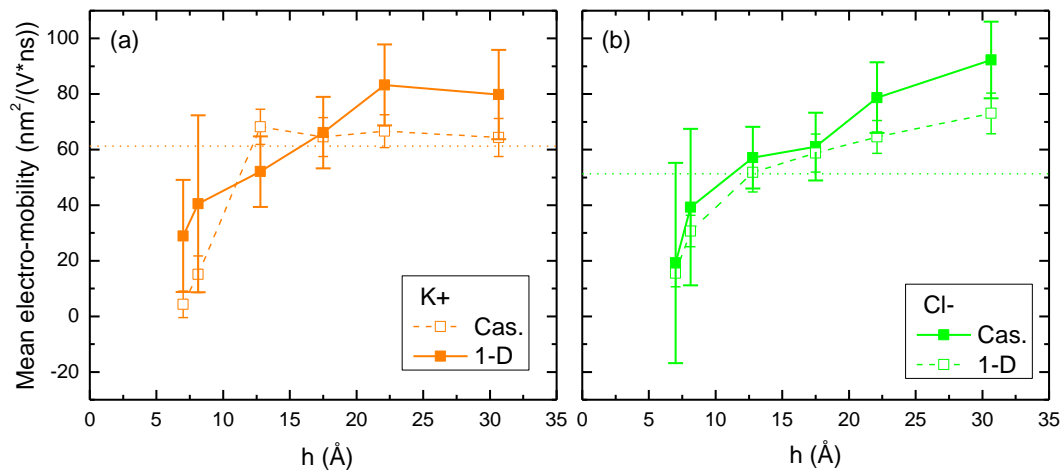


Figure 6.15 The mean mobility vs different graphene channel height: (a) For K⁺ and (b) Cl⁻ in nanoslit region (solid line) and 1-D nanochannel (dashed line). And the dotted horizontal line marks the mobility of ions in bulk solution. Note that the mobility of ions drops with channel height; however at larger channel height the result is even higher than that of bulk solution.

As described above, the mean mobility of both ions in nanoslit region with $h = 30.66\text{\AA}$ was higher than that in 1-D nanochannel and the result is even higher than that in bulk. It may originate from the BBLs and novel polarized EOF.

However, the mobility of ions in slit and 1-D nanochannel dropped with the decrease of channel height. It indicated that the confinement effect has hindered the transport of ions in nanochannel. Finally, the mobility in very small channel ($h < 10\text{\AA}$) was considerably lower than that in bulk solution.

The mobility of K^+ in nanoslit region is always higher than that in 1-D nanochannel except at $h = 12.8\text{\AA}$. For 1-D nanochannel, the mobility of K^+ is similar to that in bulk solution at large channel ($h > 10\text{\AA}$).

However the mobility of Cl^- in nanoslit region was always higher than that in 1-D nanochannel. At large nanochannel ($h > 15\text{\AA}$), the mobility of Cl^- was even larger than that in bulk solution. As discussed in Chapter 3, the anion with a weaker hydration shell would easily dehydrate in the liquid/solid interface. Thus, the mobility of anion on the interface would be higher than that in the middle of nanochannel. It increases the mobility of anion, but dropped with the confinement effect of solid graphene wall.

6.4 Conclusion

We studied the concentration and potential of boundary layers of KCl solution in staggered graphene hydrogel membrane and 1-D nanochannel using MD simulation. The similar BBLs, as predicted in the previous continuum modelling were induced by the strong external E-field. The reducing of channel height introduced the overlap of BBLs structure that diminishes the polarization of boundary layers structure. At $h = 12.8\text{\AA}$, the BBLs shrunk into a single peak profile with the single layer of ions sandwiched by its hydration water on two side. Moreover, the triangular ionic density with HLs was also confirmed at $h > 12.8\text{\AA}$. However at single layer model, the BBLs structure prediction by the continuum model was breakdown. With further reduction of channel height, the partial dehydration process has been confirmed by the mismatch of the ionic plane on graphene surface. It was a visual evidence for the partial dehydration process in very small nanochannel ($h < 10\text{\AA}$) and confirmed by the decrease of the hydration number.

For electric potential drop we found the E-field in nanoslit region was almost constant along the graphene sheet (in Y-direction). The potential drop normal to the graphene sheet was consumed to maintain the BBLs, rather than driving the ions in normal direction. Moreover, the partial dehydration process was also confirmed by the hasty potential drop in the entrance of nanoslit region ($h < 10\text{\AA}$)

Besides the stationary concentration and potential profile, the novel polarized EOF was discovered in nanoslit region with opposite direction on both sides. The separation of ions in large channel was benefit for the enhancement of the sheared laminar EOF. With the reduction of channel height, the diminishing of polarization would reduce the EOFs and at $h = 12.8\text{\AA}$, a nearly symmetric velocity profile in slit region. With the further reduction of channel height, the strong friction interaction between the wall and ions would significantly hinder the transport of ions in very small nanochannel.

The current MD study in the present Chapter reported a novel EOF phenomenon in the neutral nanochannel, which may be benefit for the development of nano-mixer or nanoparticle shearing. The novel EOF has been demonstrated to able to enhance the mobility of ions. Thus at large channel height, the mobility of ions is larger than that in 1-D nanochannel, or even higher than that in bulk solution. Although the enhancement of mobility by the novel EOF has been found at strong E-field, the magnitude of enhancement is considerably lower than that in experiment setup. And the E-field in experiment is significantly lower than that in MD simulation. Thus, there would be some another unforeseen issues that considerably increase the conductivity of membrane in experiment. The surface charge by the residual functional group on CCG sheet would plays a critical role in ion transport. The influence of surface charge would be discussed in the next Chapter.

Chapter 7: MD simulation of electro-kinetic flow on CCG membrane

7.1 Introduction

Since the development of nanofluidics field, the MD simulation is favorable for its atomistic description for fluid transport and the relative economic computational cost. Thus the various hypothesis and nano-devices have been “realized” by the MD simulation study [92, 108-112]. Inspired by the partial charge on the protein nanochannel wall for the various bio-activities, the MD simulations with the charged nanochannel wall have attracted much attention to investigate the fluid under the influence of both the strong nanoconfinement and the surface charge.

As mentioned in the previous Chapter, MD simulation would provide a more realistic description for the electro-kinetic flow. Thus, the MD simulation of electro-kinetic flow through the charged staggered graphene membrane was taken in the present Chapter. Although the novel atomic BBLs structure in the neutral graphene membrane has been revealed in the previous Chapter, the surface would significantly modify the structure of BBLs, similar to the discovery in the continuum model.

In the present Chapter, the uniform constant surface charge was imposed into the graphene sheet similar to the MD simulation of conventional 1D nanochannel but rather different nanochannel topology. Although the computational expensive equipotential simulation was proposed by varying the amount of partial charge on each atom, the constant charge simulation in this Chapter was still favor for the economic computational time and relative good descriptions for the order structure.

7.2 Methods

7.2.1 MD simulation setup

Figure 7.1 was an example of final state of MD simulation study on charged graphene hydrogel membrane. All the MD simulation setup in Chapter 7 was the same as the previous

MD simulation on neutral one, except for the negative surface charge on graphene sheet. The result clearly showed both the separation of cation and anion by external E-field and the accumulation of extra cation by surface charge.

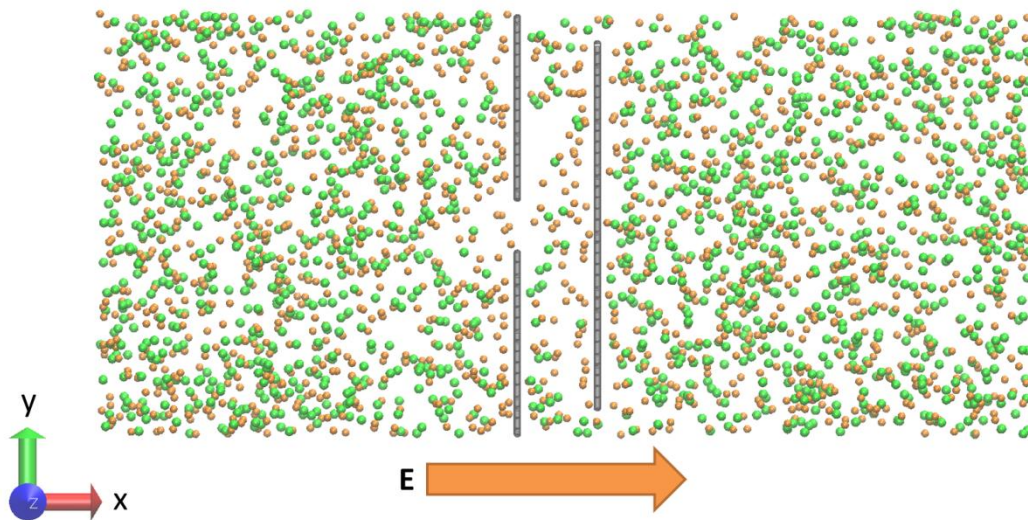


Figure 7.1 MD simulation setup for electrophoresis, where $h = 30.66\text{\AA}$ with 150\AA thickness reservoir on each side and $\sigma = -60.33\text{ mC/m}^2$. The final state of MD simulation after 12ns where orange and green dots represent the K^+ and Cl^- ions respectively, the water molecule was neglected for clarify. Note that due to the high surface charge density on graphene sheet, the number of cation is much larger than that of the anion, however the strong external E-field (orange arrow) still induce a considerable separation of cation and anion in the nanoslit region.

Every graphene atom was imposed with a partial charge of $-0.0197e$ and the number of cations and anions was modified to keep the electro-neutrality of system. The details of simulation setup were tabulated in Table 7.1. In the initially state, the concentration of KCl electrolyte in the reservoir was still about 1M, and pure water is filled within the charged graphene hydrogel membrane similar to the initial configuration in the previous Chapter.

However the surface charge density in MD simulation ($\sigma = -60.33\text{ mC/m}^2$) was considerably exaggerated to emphasize the influence of surface on electrophoresis. And limited by the low computational efficiency of MD simulation, the high ionic strength electrolyte was required to obtain a reasonable statistical result within the acceptable computational time. Thus the surface charge density in MD simulation is 26 times higher than that in experiment (about -2.3 mC/m^2)[199]. But our MD simulation could still provide a qualitative insight into the influence of the surface charge on the electrophoresis in the

charged graphene hydrogel membrane, especially with the comparison with the MD simulations for the neutral graphene membrane.

Table 7.1 Particle number of KCl solution in simulation box for different channel height

h (Å)	Reservoir Length (Å)	K+	Cl-	Water #	Graphene #
6.99	100	932	828	50726	5280
8.12	100	932	828	51126	5280
12.8	100	932	828	53526	5280
17.50	100	932	828	55926	5280
22.11	100	932	828	58326	5280
30.66	150	1500	1396	87180	5280

7.2.2 Post analysis

The method of post analysis in this Chapter is the same as the previous one. The structure and transport property of ions and water could be derived from the ionic trajectory file and full trajectory file respectively.

Besides the previous focus on nanoslit region, the scaling law of the whole charged graphene hydrogel membrane was discussed in this Chapter and the result with the neutral one would be compared with the experimental one. As the definition of S_m :

$$S_m = \frac{D_0}{D_m} \frac{\kappa_0}{\kappa_m} \quad (7.1)$$

The κ_m and D_m of graphene membrane in MD simulation need to be known. κ_m could be calculated from the equation for resistance of the modelling system in the series circuits:

$$\frac{L_{sys}}{\kappa_{sys}} A_{sys} = \frac{h_G}{\kappa_{sys}} A_{sys} + \frac{L_{sys} - h_G}{\kappa_0} A_{sys} \quad (7.2)$$

Where κ_{sys} , L_{sys} and A_{sys} were the mobility, length and cross-section of the simulation system, respectively. h_G was the thickness of membrane and $L_{sys} - h_G$ was the thickness of two reservoirs. Thus Eq.(7.2) could be derived as:

$$\frac{\kappa_0}{\kappa_m} = \left(\frac{\kappa_0}{\kappa_{sys}} - 1 \right) \frac{L_{sys}}{h} + 1 \quad (7.3)$$

The unknown of κ_{sys} could be calculated as

$$\kappa_{sys} = \frac{E}{I_{sys}} A_{sys} \quad (7.4)$$

Where E is the strength of the external E-field and I_{sys} was the total electro-kinetic current through the system.

In order to calculate the scaling law of the graphene membrane in the MD simulation, the diffusivity drop of the membrane should be known. Thus, the extra COMSOL modelling rather than the MD simulation was taken. Because, the significantly long computational time is required to achieve the good statistic average for the diffusion of the MD simulation.

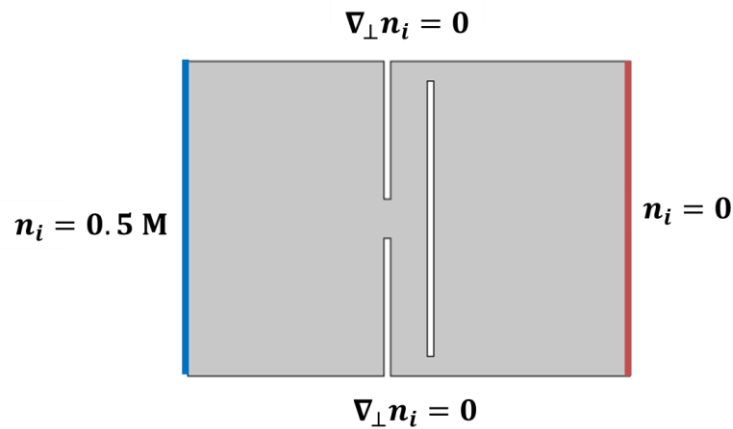


Figure 7.2 is the schematic of extra COMSOL modelling setup for diffusivity drop.

Figure 7.2 is the schematic of COMSOL modelling setup. Both the boundary condition and the governing equation are similar to these in Chapter 4. A constant concentration different ($\Delta n = 0.5 \text{ M}$) was maintained across the system. The geometry of the COMSOL

modelling was the same as that of the MD simulation. Thus, similar to Eq.(7.3), the diffusivity could be calculated as

$$\frac{D_0}{D_m} = \left(\frac{D_0}{D_{sys}} - 1 \right) \frac{L_{sys}}{h} + 1 \quad (7.5)$$

7.3 Results and Discussion for the charged graphene membrane

7.3.1 Binary Boundary Layers (BBLs) structure

As discussed in the introducing section, the surface charge would be introduced into the MD simulation system. Thus the structure of BLs depended on not only the external E-field but also the surface charge. Figure 7.3 was an example of the concentration distributions of ions on charged graphene sheets with $h = 22.11 \text{ \AA}$ under the external E-field ($E = 0.01 \text{ V/\AA}$). For comparison, the BLs structure in the equilibrium state was presented in Figure 7.4. As demonstrated in Chapter 3, the surface charge attracted the extra counter-ions and repelled the co-ions. Similar to the discovery in the Chapter 3, a symmetric EDLs structure was induced by the surface charge, with the concentration increase of K^+ and the decrease of Cl^- . Beyond the graphene membrane, the bulk-like solution was obtained in the reservoirs.

With the introducing of the external E-field, the asymmetric BLs structure was presented in Figure 7.3. Similar to the discovery in the Chapter 6, the cation accumulated on the left of graphene sheet while the anion on the right. As mentioned in Chapter 5, the concentration distribution in the charged membrane under the external E-field would be a combination of two terms: 1) EDLs and 2)BBLs.

In the MD simulation, the strength of external E-field was significantly higher than that in the continuum modelling. Thus, the BBLs structure, comparable with EDLs was established. The symmetric EDLs of K^+ was broken with the decrease of the concentration on the left side of the graphene sheet surface.

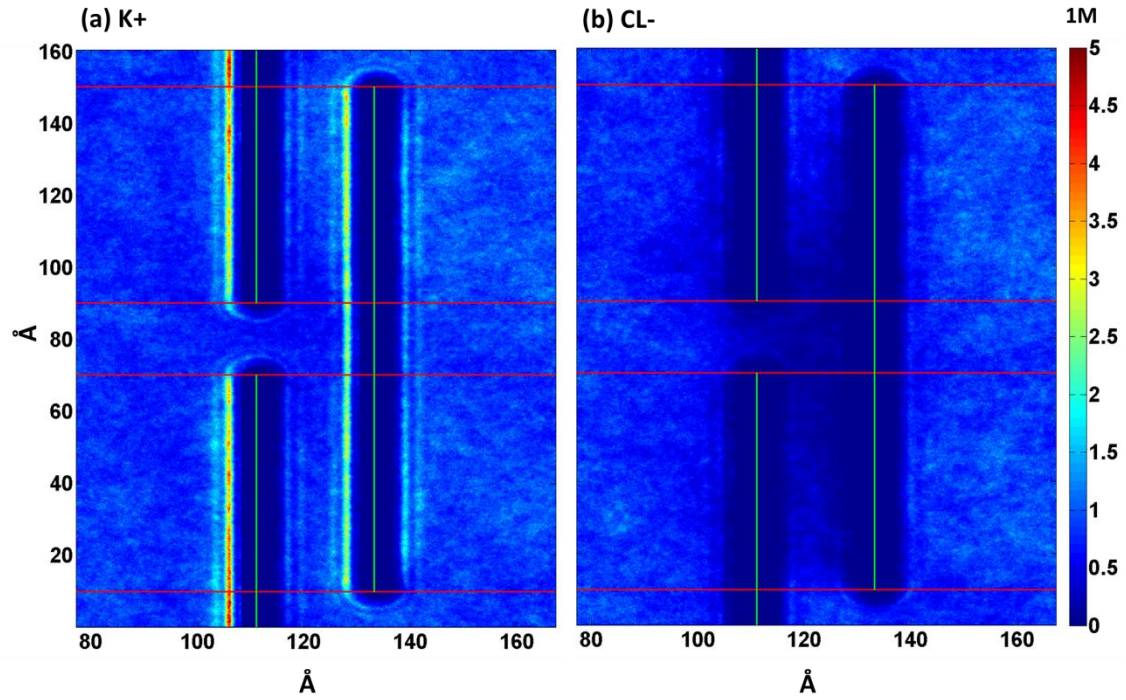


Figure 7.3 The concentration profile (1M) for K⁺ cation (a) and Cl⁻ anion (b) where $h = 22.11\text{\AA}$, $E = 0.01\text{V/\AA}$, $\sigma = -60.33\text{mC/m}^2$. The solid green lines represented the position of graphene sheet and the solid red lines are just guideline line. Thus the rectangular regions surrounded by red and the green lines indicate the nanoslit regions in the discussion. Note that the high surface charge density on graphene has repelled the co-ions from the nanoslit region.

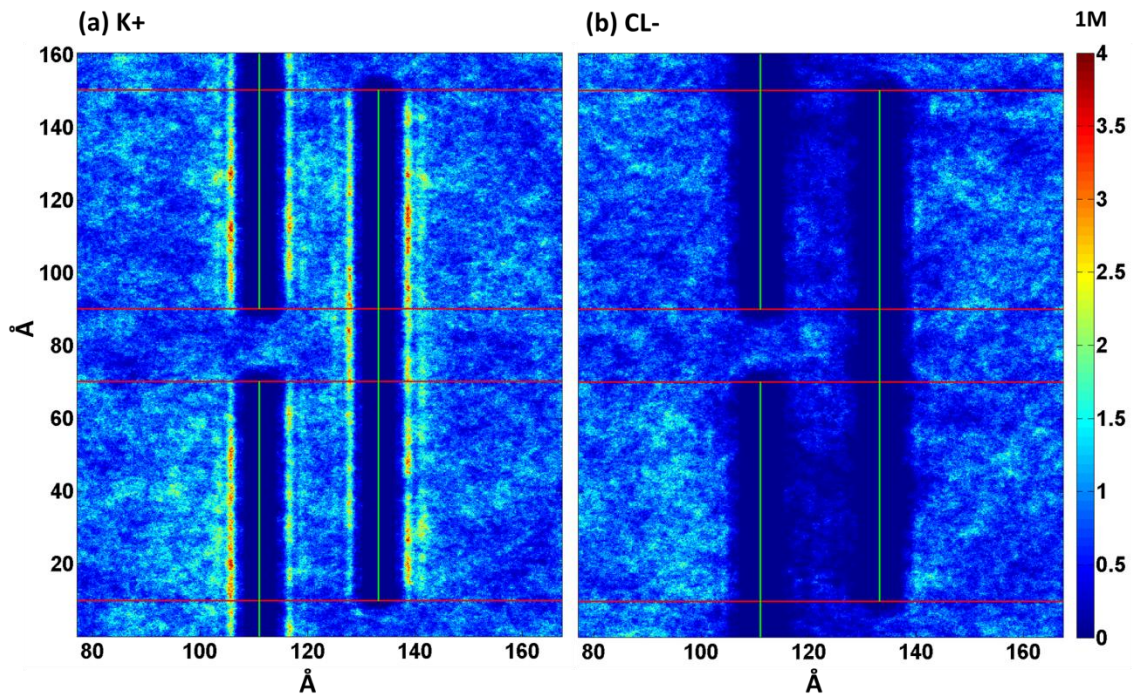


Figure 7.4 The concentration profile (1M) for K⁺ cation (a) and Cl⁻ anion (b) where $h = 22.11\text{\AA}$, $E = 0.0\text{V/\AA}$, $\sigma = -60.33\text{mC/m}^2$. Note that the EDLs formed on the graphene surface.

However, the anions were repelled by the surface charge, giving a nearly zero concentration on aperture region. And the triangular BLs distributions of anion were found in the nanoslit channel, which is similar to the exotic triangular BBLs structure in Chapter 5. Because, the extensions of exotic triangular BBLs structure in the continuum model depends on the reservoir concentration (Debye length). The decrease of concentration of anions brought out the BLs structure of anion. Reversely, the high concentration of cation in the membrane cannot form the triangular shape of BLs structure.

Besides the electrolyte ions, the relative density profile for water molecule, namely the oxygen and hydrogen atoms the under the same E-field was plotted in Figure 7.5. As discussed in the previous Chapter, the external E-field owned a negligible influence on the distribution of water molecule. Thus the density profile of water molecule under the external E-field is omitted.

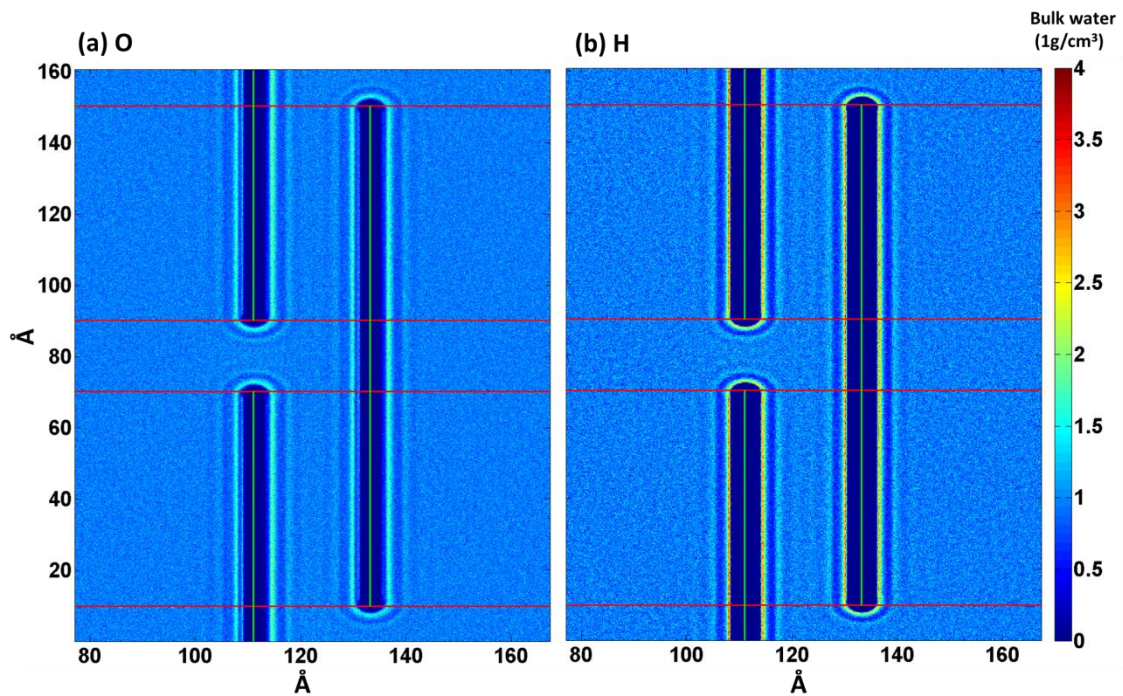


Figure 7.5 The relative density profile for water molecule vs bulk water (1g/cm³): (a) Oxygen atom and (b) Hydrogen atom, where $h = 22.11\text{\AA}$, $E = 0.0\text{V/\AA}$ and $\sigma = -60.33\text{mC/m}^2$. Note that the point charge hydrogen atoms have been significantly absorbed onto the graphene surface that shift the orientation of water molecule in the first water layer and considerably increase the concentration on graphene surface.

The structure of water molecule was similar to that on the neutral graphene membrane in the previous Chapter, except for the significantly accumulation of hydrogen atom on the graphene surface (3~4x). It is due to the strong Columbic attraction between hydrogen and surface charge and the tilt of water molecule on the first water layer (as described in Chapter 3).

As discussed in the previous Chapter, the nanoslit region inside the graphene membrane played the dominant role in the electro-kinetic flow. Thus, the similar concentration average profile in nanoslit region was plotted in Figure 7.6 with (top) and without (bottom) the external E-field.

As presented in Figure 7.4, the symmetric EDLs emerged on the graphene sheet surface. Thus in the equilibrium state, the oscillated EDLs formed on the both side of graphene sheet as the description in Chapter 3. In the middle of nanoslit channel, the bulk-like solution was obtained ($n = 1M$) at $h = 30.66 \text{ \AA}$. The EDLs structure of cation was similar to that on the neutral graphene membrane except for the higher concentration peaks (+0.5~1M) on graphene sheet surface. For anions, the concentration on the graphene sheet surface was significantly reduced by Columbic repulsion.

With reducing the channel height, the influence of the surface charge, (σ/h) [89] would be increased that considerably enhanced the concentration changes in nanoslit region and the EDLs from opposite walls started to overlap with each other.

At $h = 12.80 \text{ \AA}$, the two peaks concentration profile of cation formed and the magnitudes of the peaks was greatly increased (~3M). However the Columbic repulsion enforced the single layer of anion with the maximum concentration (~0.5 M) in the centre of nanoslit region and minimum (nearly zero) on the sheet surface.

Actually in neutral graphene membrane, the overlap of EDLs by van der Waal absorption gave the single peak profile for both cation and anion. However Owing to the strong Columbic attraction between the cation and graphene sheet, the single layer of cation in neutral graphene membrane was spited into double layers.

With the further reducing the channel height ($h < 10 \text{ \AA}$), the anion was completely excluded from the nanoslit region and the EDLs of cation collapsed into the single peak profile with the increase of concentration. The splitting of double layers by Columbic attraction at larger channel height ($h = 12.80 \text{ \AA}$) was strongly confined by the graphene walls

Besides the distribution of electrolyte ions, the average concentration profiles of water molecule were also plotted in Figure 7.6. In equilibrium, the symmetric and oscillated EDLs structure of water molecule was similar to that in the neutral graphene membrane except for the titling of water molecule on graphene surface. Thus, a small hydrogen peak formed beyond the first water layer, similar to the EDLs structure on charge graphene sheet in Chapter 3.

With the decrease of channel height, the EDLs of water also started to overlap with each other with the vanishing of bulk-like solution in the middle. At very small channel height ($h < 10 \text{ \AA}$), the single peak profile of oxygen atoms also formed like that in the neutral membrane.

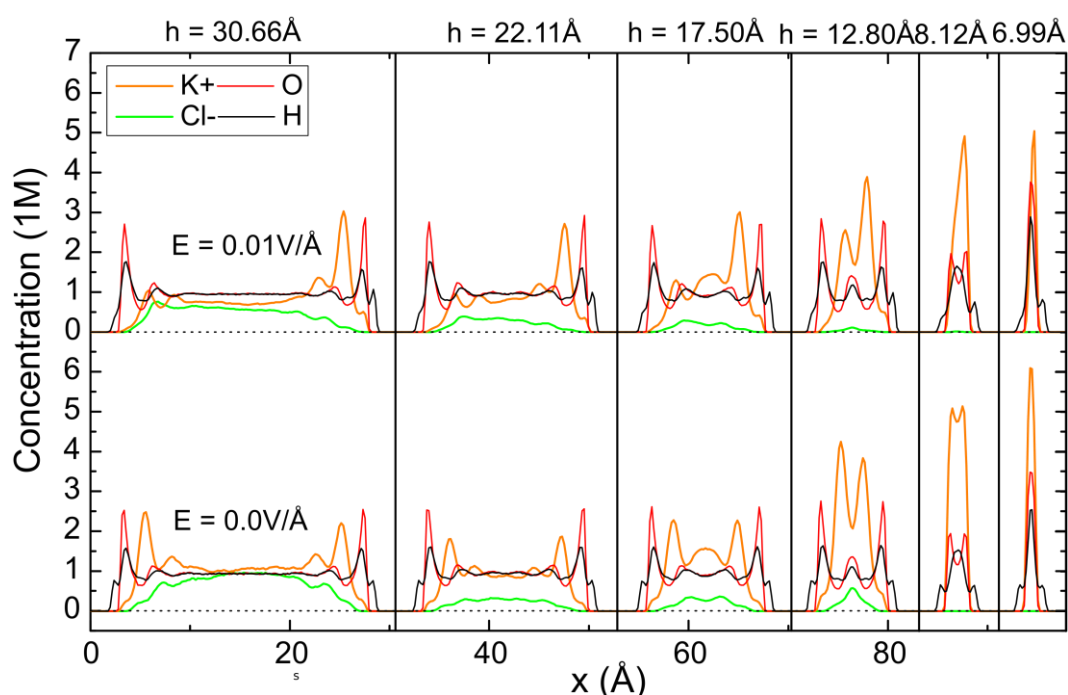


Figure 7.6 The 1D concentration profile for KCl solution in nanoslit region with different channel height from 30.66 Å to 6.99 Å with (top) and without (bottom) the external E-field. The orange and green lines represent the concentration distribution of K⁺ and Cl⁻, while red and black lines represented the relative density (1M bulk solution) of oxygen and hydrogen atoms. Note that the concentration profile of ion at $h = 6.99 \text{ \AA}$ was rescaled by 0.5 to present the result clearly.

With the introducing of the external E-field, the EDLs structure of both the ions and water molecule responded. At large channel height ($h = 30.66 \text{ \AA}$), the external E-field significantly increased the concentration of cation (n_{K+}) on the right side of nanoslit region. Even with the repulsion from the graphene sheet, the anion could still accumulated on the left of nanoslit region. It formed the polarized concentration distribution, namely the BBLs structure.

As describe in the Chapter 5, the concentration profile in the charged membrane would be a combination of EDLs and BBLs. Thus, the asymmetric BBLs structure was induced. Compared with the symmetric BBLs in neutral membrane with the similar concentration accumulation on each side, the concentration of cation on one side was much higher than that on the other side.

With the reduction of channel height, BBLs structure started to overlap with each other. And the influence of surface charge was also enhanced. Thus the magnitude of anion concentration was significantly reduced with the increase of concentration of cation on the right side of nanoslit region. But the concentration polarization (BBLs structure) still remained in nanoslit region.

However for cation, the overlap of BBLs and strong Columbic attraction changed the original double peaks EDLs structure. The external E-field increased the magnitude of concentration peaks on the right side of nanoslit. Compared with the polarized single peak in neutral graphene membrane, the external E-field didn't change the original (equilibrium) EDLs structure, only modifying the magnitudes of concentration peaks.

With the further decreasing the channel height ($h < 10 \text{ \AA}$), the anion was completely repelled from the nanoslit region by the Columbic repulsion. While the BBLs structure of cation has been enforced to collapse into the single peak profile (single layer) by the steric confinement. Like the result in the neutral graphene membrane, the asymmetric peaks of cation still indicated the influence of the external E-field. It is worth noting that depletion of anion at the small channel height formed a unipolar nanochannel which has been widely adopted in the nanofluidics field to reveal the novel property in nanoscale [18, 89, 119].

Beyond the electrolyte ion, the water molecule also responded with the external E-field. However the structure of BBLs of water molecule was similar to that in the equilibrium state for all different channel height. The external E-field only changed the orientation of water molecule in the first water layer.

The attraction between graphene sheet and the hydrogen atoms on the left side of nanoslit was cancelled by the external E-field. Thus the hydrogen peaks on the left side of the nanoslit region was removed.

However, the hydrogen peaks on the other side were merely raised by the external E-field. Because the high surface charge density on graphene sheet has “saturated” the first water layer, namely the dielectric saturation in Chapter 3. Thus the further increase the E-field strength by the external E-field cannot considerably increase the hydrogen peaks on graphene surface.

In general, the BBLs structure of KCl solution in charged graphene membrane depended on both the surface charge and the external E-field. The surface charge would drop the concentration of anion and enlarge the concentration peaks of cations on graphene surface. However the external E-field could still induce the concentration polarization and forms the BBLs structure. At small channel height, the unipolar nanochannel formed with only cations resided inside, which would significantly change the transport property of electro-kinetic flow.

As mentioned in the Chapter 6, the entrance of the aperture region may play some critical role in the electro-kinetic flow especially for small channel height. Figure 7.7 summarized the concentration profile of K^+ at the aperture region for different channel height ($h = 17.50, 12.80, 8.12 \text{ \AA}$). And due to the strong Columbic repulsion, the concentration of anion was nearly zero at these channel height. Thus, the result of Cl^- was neglected in the discussion.

For equilibrium state (top part), the Columbic interaction between the surface charge and cation induced a continuous bright ribbon (concentration peak) on both sides of the graphene

sheet surface. With reducing the channel height ($h = 12.80 \text{ \AA}$), the EDLs structure of cation collapsed into the double layers structure as indicated in Figure 7.6.

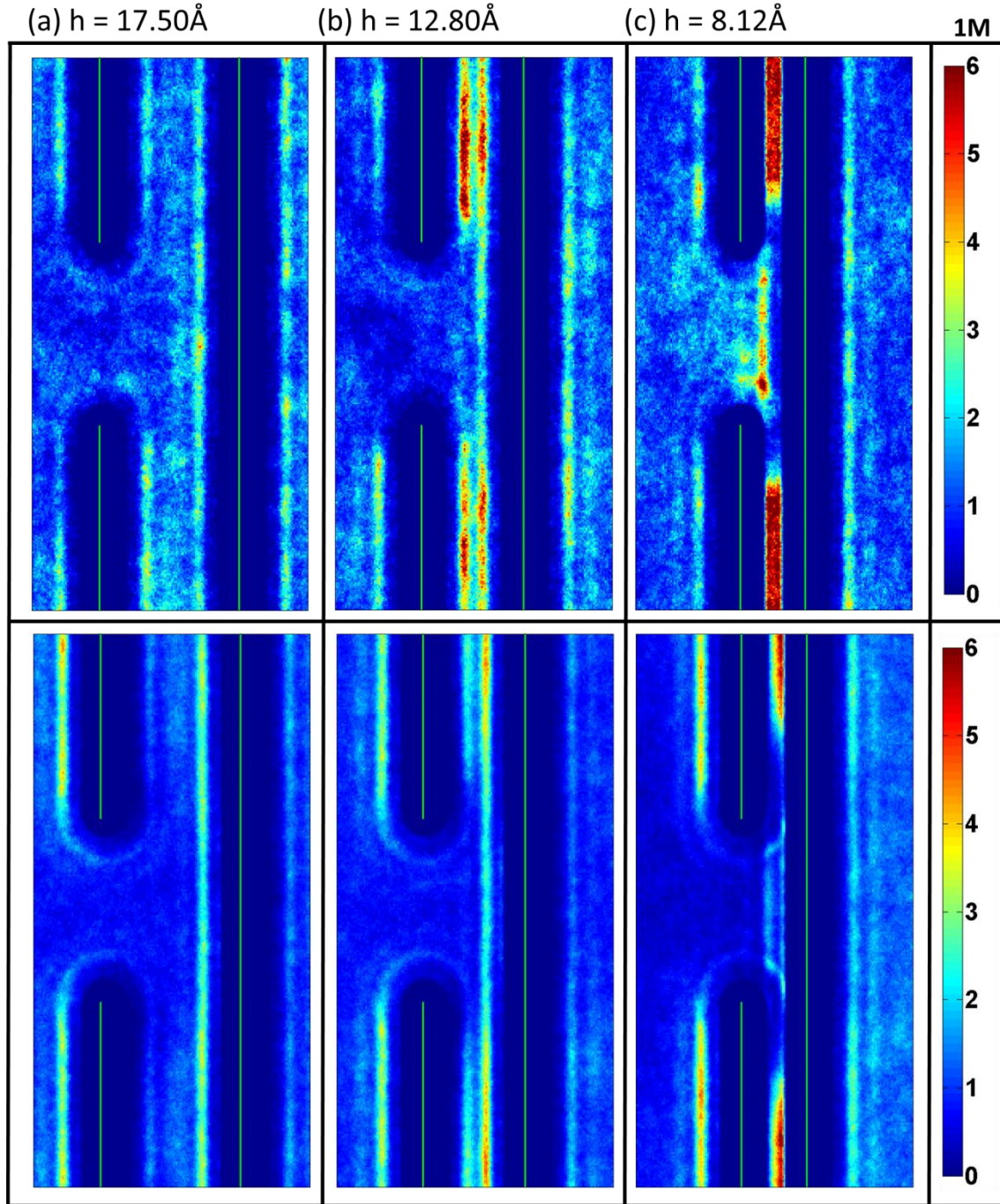


Figure 7.7 The K⁺ concentration profile in aperture region for different channel height (h) with (bottom) and without (top) the external E-field: (a) $h = 17.50 \text{ \AA}$; (b) $h = 12.80 \text{ \AA}$; (c) $h = 8.12 \text{ \AA}$. Note that owing to the high surface charge density on graphene sheet, the co-ions (Cl⁻) has been considerably excluded from the membrane at small channel height. Thus only the concentration of K⁺ was plotted.

It is worth noting that there was no ribbon mismatch in aperture region at $h = 12.80 \text{ \AA}$. From Figure 7.6 we could also confirmed that most of the ions located behind the dense first water layer for $h > 10 \text{ \AA}$. Namely the external E-field was not strong enough to overcome the barrier of first water layer. The ions were still in hydrated state. Thus the position of the continuous bright ribbon (concentration peak) is determined by the hydration shell radius of K^+ .

However the mismatch of the bright ribbon emerged at $h = 8.12 \text{ \AA}$, which is similar to the previous discovery in neutral membrane with the external E-field. Figure 7.6 alternatively confirm the dehydration process at small channel. The cation was absorbed into the graphene sheets surface of the aperture region with its hydration shell. The entrance of ions into the very small nanochannel required a dehydration process that changed the position of bright ribbon (concentration peaks)

As mentioned before, EDLs structure would respond with the external E-field. Thus we could clearly observe the vanishing of bright ribbon (concentration peaks) on the right side of graphene sheet at $h > 10 \text{ \AA}$.

At $h = 8.12 \text{ \AA}$, the bright ribbons inside the nanoslit region was polarized by the external E-field. The strong E-field along the Y axis inside the nanoslit region would shift position of cation absorbed by the surface charge. Thus on the entrance of the nanoslit region, the concentration of the cation would be decreased. Reversely, the bright ribbons expanded outside the nanoslit region on the exit.

Besides the polarization of bright ribbon, the EDLs structure in the aperture region also changed under the external E-field. It decreased the concentration of cation in the aperture region and pushed the cation forward into the graphene sheet surface. We recognised the formation of a double layers structure in the aperture region. The first layer of cation, overcoming the barrier of first water layer would be partial dehydrated which was similar to the discovery of partially dehydration under the strong E-field in Chapter 3.

However the origin of exotic double layers BBLs structure still remained unknown and would be really complicated. The influence of the Electro-Osmosis Flows (EOFs) induced by the unipolar nanochannel should also be taken into account. Furthermore, the partial dehydration on the entrance of the nanoslit would also play a critical role in the electro-kinetic flow. It might also modify the BBLs structure on the aperture region.

Generally speaking, the concentration profile in the charged membrane was rather complicated than the neutral membrane. Especially for strong nanoconfinement and high surface charge density, the various issues were focused on the nanoscale aperture region. Thus exotic BBLs structure was found and really hard to be explained.

7.3.2 Electric potential and Nernst potential

Besides the stationary concentration distribution, the driving force, electric and Nernst potential profile should also be reviewed in this Chapter. Figure 7.8a was the counter plot of net electric potential on oxygen atom in system with $h = 22.11 \text{ \AA}$. Figure 7.8b was the electric potential profile by the electrolyte itself without the influence of the external E-field.

Actually there was no obvious difference for electric potential profile between the neutral and the charged graphene membrane. Both of them formed a funnel like potential drop on the entrance of the aperture opening and nearly constant potential drop along the graphene sheet in nanoslit region.

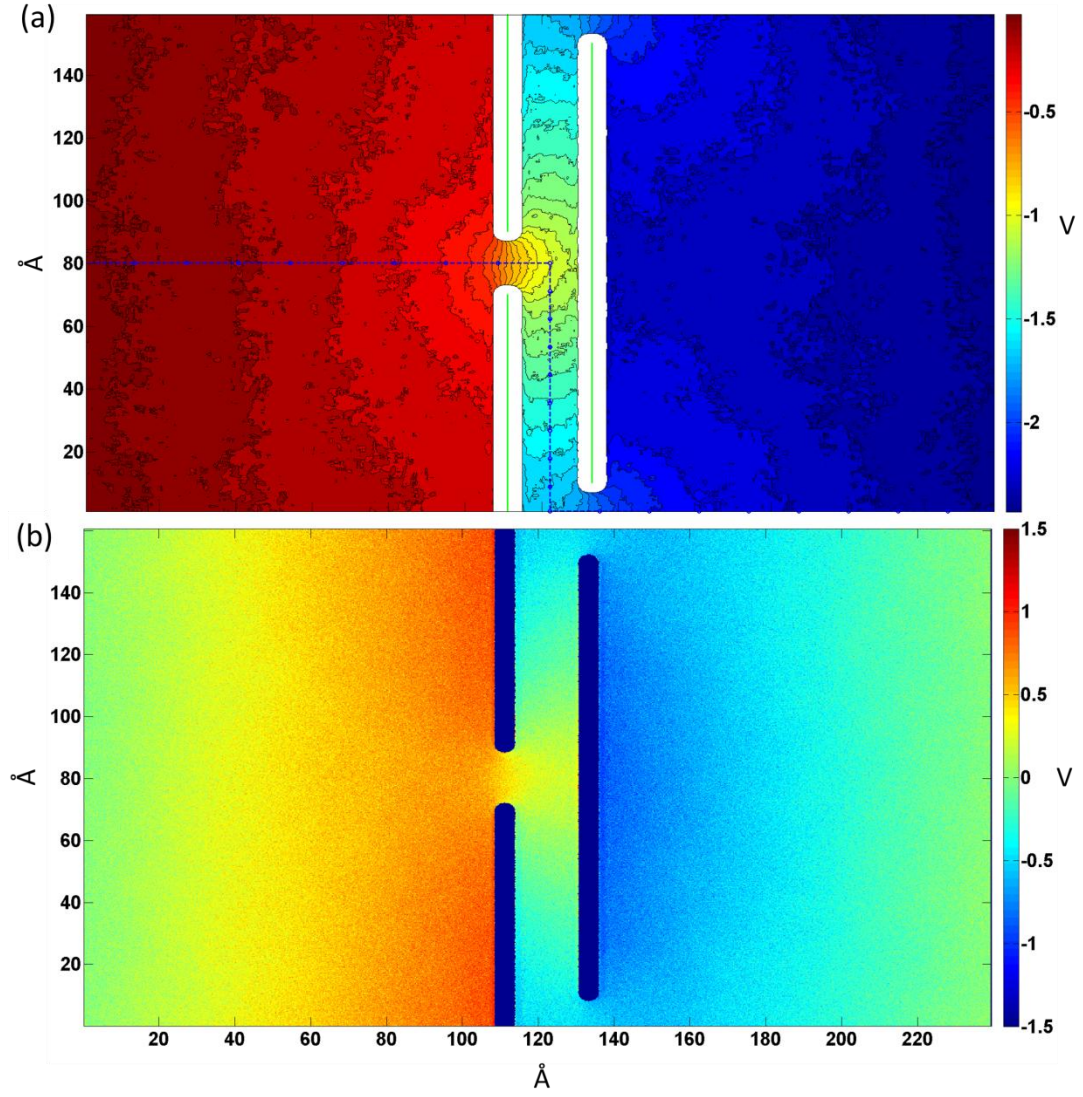


Figure 7.8 The electric potential of oxygen atom where $h = 22.11\text{\AA}$, $E = 0.01\text{V}/\text{\AA}$ and $\sigma = -60.33\text{mC}/\text{m}^2$: (a) the contour plot of net electric potential after smooth; (b) The inner electric potential by electrolyte itself. The green line represents the position of graphene wall and the cycle dashed lines indicate the “transport path” to evaluate the potential drop in the cascading electro-kinetic flow.

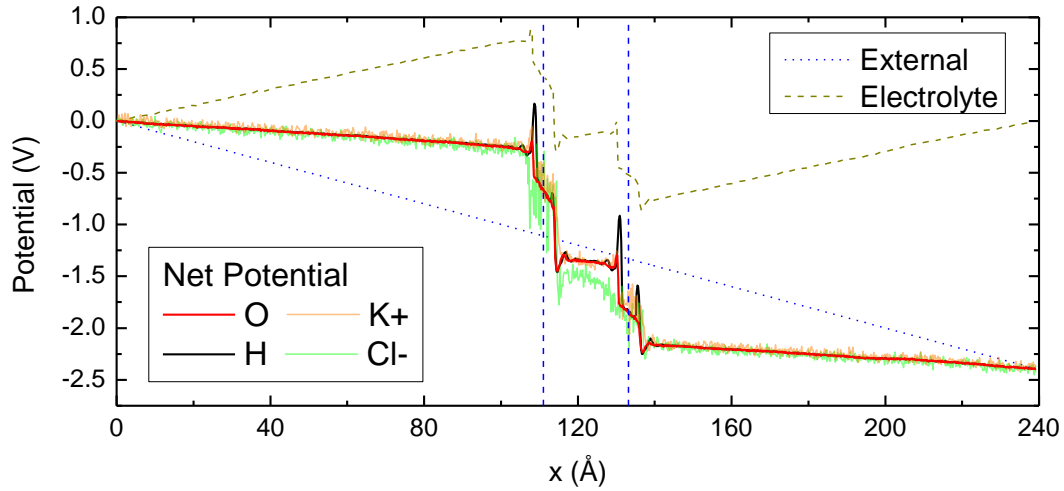


Figure 7.9 The average electric potential of different ions along the X-direction with $h = 20.11\text{\AA}$ and $E = 0.01\text{V/\AA}$ and $\sigma = -60.33\text{mC/m}^2$. The dashed orange line indicated the distribution of inner electric potential by solution itself with zero potential on each end. The blue dot line indicates the potential by external electric field and the solid green curves with different colour were net electric potential on different type of atoms. The vertical dashed blue lines marked the position of graphene wall.

Then, the average electric potential of electrolyte along the X-direction was also drawn in Figure 7.9 where the solid lines with the different colors indicated the net electric potential on different types of atoms. The potential curves from the oxygen, hydrogen and K^+ overlapped with each other except for the anion inside the graphene membrane where the decreased concentration of anion cannot provide a good statistic average. To be consistency with the Chapter 6, the electric potential on oxygen atoms was used to evaluate the driving force in the MD system.

The shapes of oxygen potential curve in Figure 7.9 was similar to that in the neutral graphene membrane with small and linear potential drop on the two side reservoirs and abrupt oscillated electric potential change on BBLs.

However, the 1D average electric potential profiles along the X-direction were not an intuitive method to present the driving force of the graphene membrane. The potential drop along the “transport path” (cycle dashed line in Figure 7.8) was proposed to study the potential drop for the cascading electro-kinetic flow.

Figure 7.10 was the potential drop along the transport path for different channel height. The solid lines with different colour indicated the Φ_E profile at different h . The black dot

curves overlapped with the solid lines was $\Phi_E + \Phi_N$ curve. Unlike the considerable contribution of diffusion flow in the continuum modelling, the Nernst potential in the MD simulation owned a negligible contribution to the overall ion transport. But the strength of electric field in MD simulation was significantly higher than that in the continuum modelling. Thus, the electrophoresis flow in the MD simulation was dominant.

The shapes of the electric potential drop in Figure 7.10 were also similar to that in the neutral graphene membrane where there were a constant electric potential drops in the reservoirs and the center of nanoslit region (along the graphene sheet, Y-axis).

At large channel height ($h = 30.66 \text{ \AA}$), there was an obviously abrupt potential drop on the aperture opening. As reported in Chapter 5&6, the size of the aperture opening (d) was much smaller than the channel of electro-kinetic flow ($2h$). Thus the extra driving force was required to overcome the bottleneck of the aperture opening.

With the decrease of the channel height, the bottleneck of the aperture opening would be gradually removed. At $h = 12.80 \text{ \AA}$, the slope of potential drop at the aperture opening was almost the same as that in the nanoslit region.

However at the very small channel height ($h < 10 \text{ \AA}$), there was a significant potential drop at the entrance of the nanoslit region but no other counterpart on the exit. As mentioned in the previous Chapter, both the cation and anion would partially dehydrate on each end of the nanoslit region, giving a double abrupt potential drops on each end. For charged membrane with the unipolar nanoslit the partially dehydration of cation only occurred on the one end of nanoslit region (entrance).

Moreover, the magnitude of the potential drop in the entrance ($\sim 1 \text{ V}$) seemed to be double times higher than that in the neutral graphene membrane ($\sim 0.5 \text{ V}$). The origin of the extra electric potential cost was still undiscovered. It must closely relate with exotic BBLs structure (Figure 7.7) and the strong EOF flow in the modelling system. Due to the complexity of various effects, the extra study should be taken to identify the exotic concentration and potential distribution in the graphene membrane.

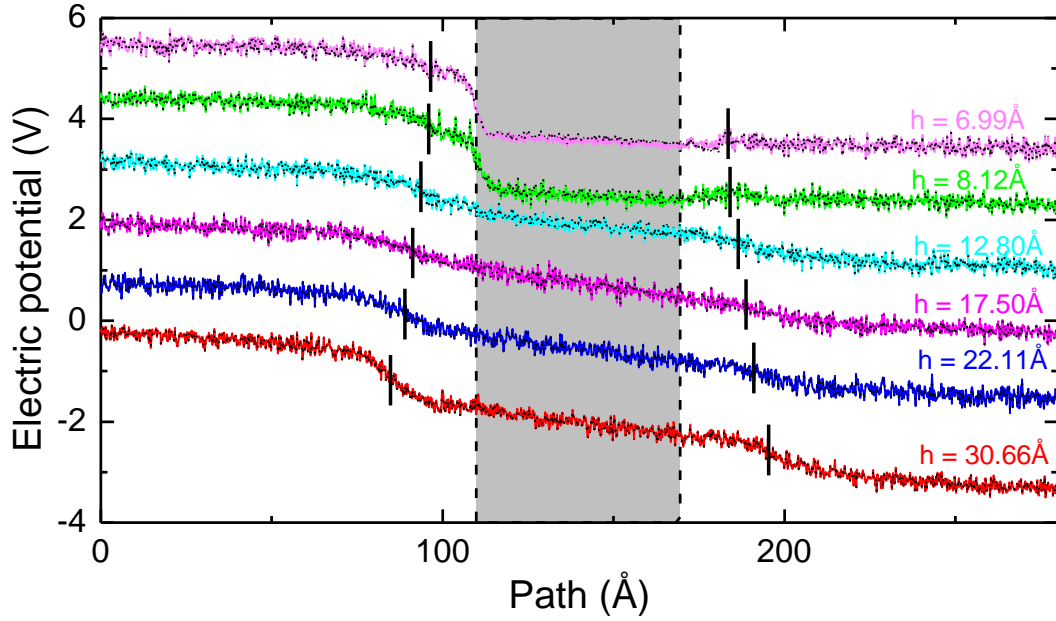


Figure 7.10 The potential distribution along the “transport path”: the solid curves with different colour were Φ_E for different h , while the overlapped black dotted curves were the potential of $\Phi_E + \Phi_N$ for the same h . The labels on the right shown the corresponding h for each curved. The shadowed region marked the positions of the nanoslit region. The short vertical lines in each curves indicated the location of the aperture opening

Taken together, the electric potential distribution in the charged graphene membrane was similar to that in the neutral one. And the Nernst potential played a negligible role in the ion transport. At $h < 10$ Å, the partial dehydration of cations induced an abrupt electric potential drop on the entrance of nanoslit region but no extra potential drop on the exit of the nanoslit, due to the single dehydration of cations on the entrance.

7.3.3 Velocity profile and ion mobility

Besides the stationary concentration and driving force distribution, the velocity profile for ions and water molecule was directly related with the property of the electro-kinetic flow. Thus, Figure 7.11 was the mean mobility of ions and water in the nanoslit region along the graphene sheet. It takes the same post-analysis methods in the previous Chapter and the velocity was rescaled by the E-field strength in nanoslit region along the Y-axis \bar{E}_{slit} , namely the mobility

At large channel height ($h = 30.66$ Å), we could still observed the polarized velocity profile for ions with the maximum velocity of cation on the right side of nanoslit and that of

anion on the other side. And the corresponding polarized EOF was also induced by the BBLs structure as described in the Chapter 6. Unlike the symmetric EOF in the neutral graphene membrane with equal but opposite directions of velocity on each side, the average velocity of the EOF in the charged membrane was positive (along the movement of cation). Thus the overall EOF in the charged graphene membrane would be a combination of two terms:

- 1) The polarized EOF by the BBLs structure (polarized ion concentration distribution)
- 2) The general EOF by extra cation in the nanoslit region absorbed by the surface charge

Thus we could observe the later terms accelerated the polarized EOF on right side of nanoslit and decreased that on left side. The changes of EOF also varied the velocity profile of the ions. It further increased the maximum velocity of cations ($\sim 250 \text{ nm}^2/(\text{V} \cdot \text{ns})$) which was much higher than that in the neutral graphene membrane ($\sim 170 \text{ nm}^2/(\text{V} \cdot \text{ns})$). The velocity of anions on the right side has been considerably reduced by the EOF in the opposite direction, giving the positive velocity value. It seemed that the strong EOF has dragged the anion moving with the same direction as that of the cation on that side.

As described in the previous Chapter, the polarized EOF would be weakened with the decrease of channel height. In contrast, the general EOF would be enhanced by the concentration increased of cation in nanochannel. Thus with the shrinkage of the channel height, the velocity of water flow would be enhanced that further increased the velocity of cation. But the polarized EOF structure could still observed until $h = 12.80 \text{ \AA}$.

At $h = 12.80 \text{ \AA}$, the anion was considerably excluded from the nanoslit region and the unipolar nanochannel of the cations significantly increased the velocity of EOF. Although the anions still moved along the opposite direction under the E-field, the strong EOF in nanoslit region has force the all the anion in the nanoslit region moving along the same direction as that of cation.

With the further decreasing of channel height ($h < 10 \text{ \AA}$), the anion was completely repelled from the nanoslit region and there were only the cation and water molecule moving

along the positive direction. Thus the EOF in the charged membrane could be significantly higher than that in the neutral one (nearly zero). But the velocities of both were reduced with the decrease of the channel height. Similar to the description in the previous Chapter, the partially dehydration on the entrance and friction between the wall and electrolyte decelerated the electro-kinetic flow in the graphene membrane.

For the velocity profile, we could conclude that the electro-kinetic flow of ions was still a polarized structure in nanoslit region and influenced by both the general and polarized EOF. However for the larger channel height, the polarized EOF was dominant, while at the small h , it would be the general EOF. At very small channel height ($h < 10 \text{ \AA}$), the strong confinement effect will considerably decelerate the electro-kinetic flow in the nanoslit region.

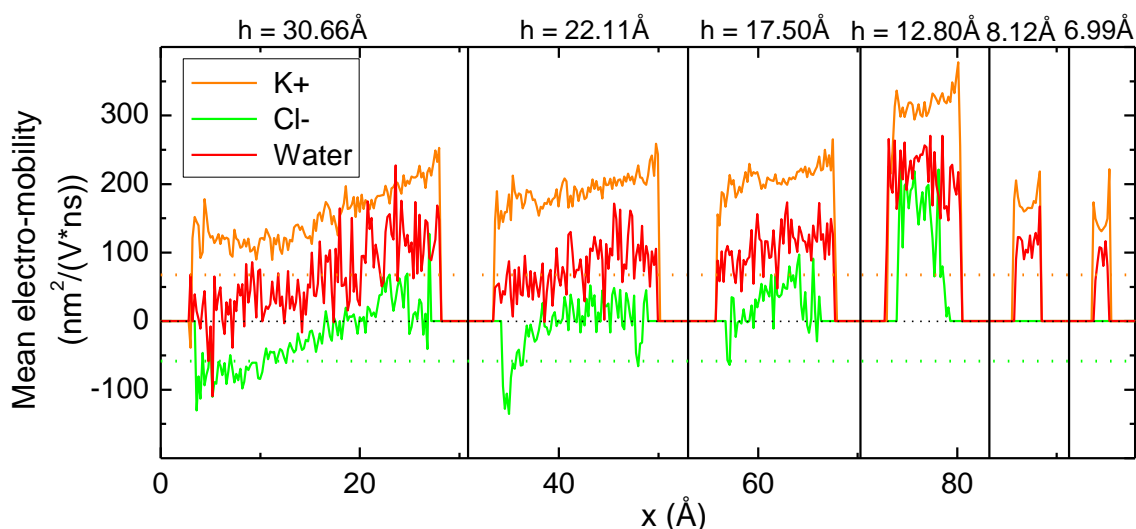


Figure 7.11 The mobility profile of electrolyte along the graphene sheet in the nanoslit region. The solid orange, green and red lines represent the distribution of mean velocity for K+, Cl- and water respectively. The horizontal orange and blue dotted lines represent the mobility of K+ and Cl- in bulk solution.

In order to better understanding the novel electro-kinetic flow in the charged graphene membrane, the mean mobility of ions and water molecules in nanoslit region was plotted in Figure 7.12. The calculation method of mean mobility was the same as the previous Chapter. But the influence of the EOF (“mobility” of water in Figure 7.13) was removed from the result. Thus the result of ions presented was the relative mobility with the moving EOF background. For comparison, the electro-motilities of ions in the bulk solutions (horizontal

dotted line) and the nanoslit region of the neutral graphene membrane were also added into Figure 7.12.

As mentioned before, overall EOF would be a combination of two terms, polarized EOF by BBLs and the general EOF by EDLs. Only the latter contributed to the “mobility” of water in the nanoslit region. Thus the mobility of ions in Figure 7.12 included the influence of the polarize EOF by the BBL structure.

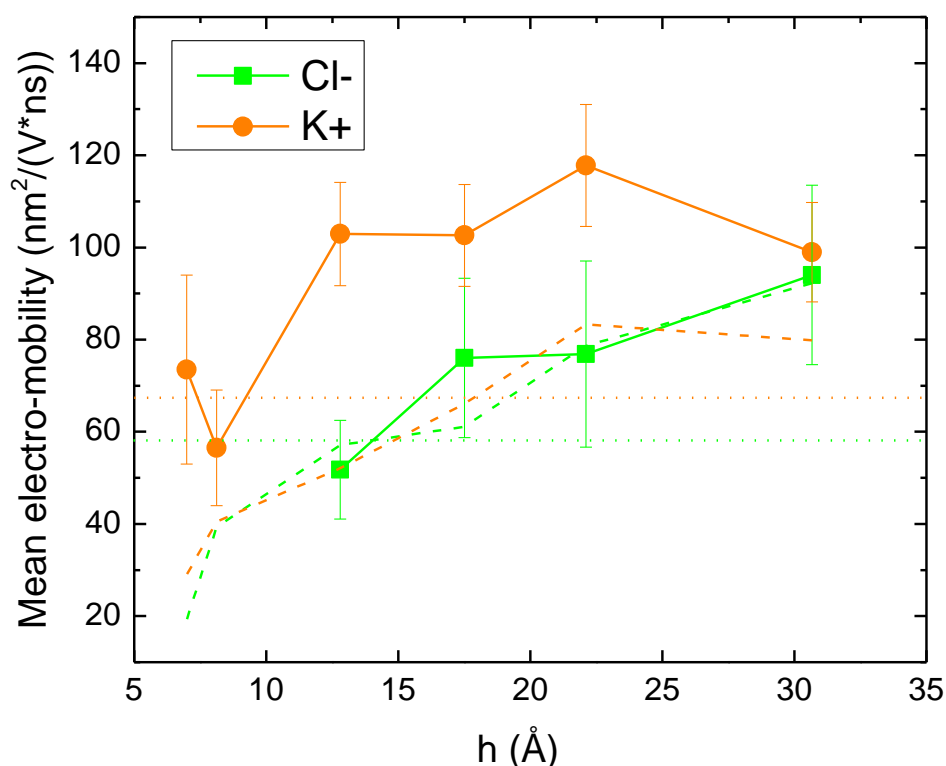


Figure 7.12 The mean mobility nanoslit region as a function of different channel height: The cycle orange and square green lines indicated the calculated mobility of K+ and Cl- respectively. The dashed lines with the same colours were the results for K+ and Cl- in the neutral graphene membrane.

For anion, the result mobility curves were similar to that in the neutral graphene membrane. At the large channel height, the mobility of anion was higher than that in the bulk solution. With the decrease of channel height, the mobility of anion dropped with the overlap of the BBLs structure. From the overlap of the anion curves between the neutral and charged membrane, the effect of the BBLs structure induced by the external E-field would be similar for both membrane, even the significant different concentration profile.

However for cation, the result mobility curve was considerably different from that in the neutral membrane. Besides the conventional EOF by the extra cations, the high concentration of cation and special BBLs structure has further accelerated the transport of cation. It seemed that at large channel height ($h > 10 \text{ \AA}$), the result mobility would be about $100 \text{ nm}^2/(\text{V} \cdot \text{ns})$ that was essentially higher than that in the neutral graphene membrane.

At very small channel height ($h < 10 \text{ \AA}$), the mobility of cation was reduced by the strong nanoconfinement. But the results were still similar to that in the bulk solution and greatly higher than that in the neutral graphene membrane. The acceleration of cation in the charge nanoslit region would be induced by two terms:

- 1) The exclusion of the anions by the surface charge reduced the friction between cation and anions, that increased the mobility of the cation
- 2) The special BBLs structure. At the position of maximum EOF (the right side of nanoslit), the concentration of cation was increased by the surface charge adoption that increased the mean mobility.

As mentioned before both the EDLs and BBLs structures were presented in the charged graphene membrane. However the cooperation of EDLs and BBLs seemed further accelerated the major transport of cations, but not much influence on the minor anions.

Besides the mobility of ions, the “mobility” of water was plotted in Figure 7.13, which was dominantly contributed from the general EOF by the extra cations. Obviously, there was a maximum mobility of water molecule ($\sim 200 \text{ nm}^2/(\text{V} \cdot \text{ns})$) at $h = 12.80 \text{ \AA}$.

For $h > 12.80 \text{ \AA}$, the decrease of the channel height increased the influence of the surface charge and the concentration of extra cation, namely the driving force of the general EOF. However for $h < 12.80 \text{ \AA}$, the further decreased of the channel height would enhance the confinement effect that decrease the “mobility” of both ions and water in the very small nanochannel.

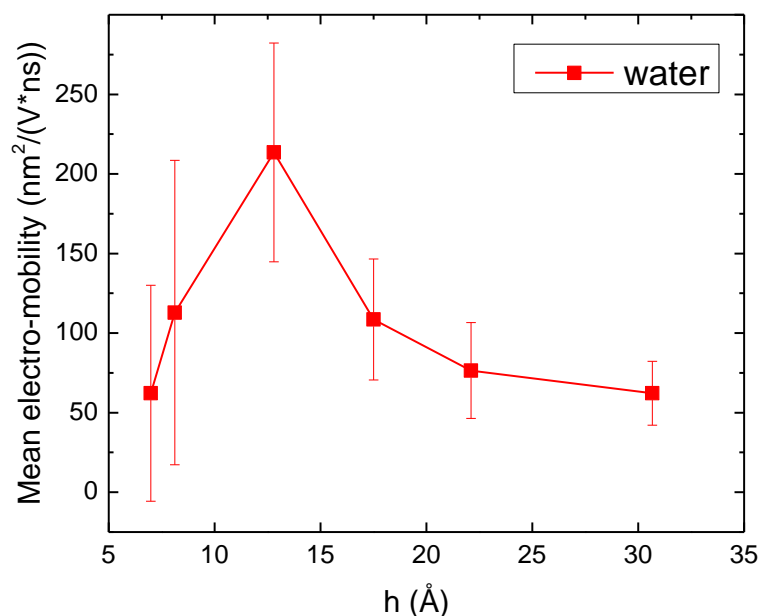


Figure 7.13 The mean “mobility” of water molecule by EOF in the nanoslit region in the charged graphene membrane.

Generally speaking, EOF was also induced in the charged graphene membrane and could be decomposed into two terms: the polarized EOF by BBLs and General EOF by EDLs and. Similar to that in the neutral graphene, the former would accelerate both cations and anions but was weakened with the nanoconfinement. Reversely the latter only accelerated the cations and slowed the transport of cation. Furthermore, the general EOF would be enhanced with the reduced of h . However at very small channel height ($h < 10$ Å), both ions and water would be impeded by the friction with nanoslit wall.

7.3.4 Nanoslit electro-kinetic flux and Scaling law

Although the electro-kinetic flow in nanoslit region (both the structure and velocity profile) was discussed in this and previous Chapter, the overall electro-kinetic flows through the membrane have not be mentioned in this thesis. Thus the electro-kinetic flux of ions (the produce of concentration and velocity) in the nanoslit region was plotted in Figure 7.14.

The top and bottom part in Figure 7.14 was the flux profile in charged and neutral graphene membrane respectively. While the dashed curves were the results in the 1-D nanochannel. And the integral of flux curves gave the corresponding electro-kinetic current in each case.

Obviously, the polarized BBLs structure in the graphene membrane also induced a polarized electro-kinetic flow with the maximum flux density of ions in each side. Reversely, there was no polarized flux density distribution in the neutral 1-D nanochannel. Moreover, the significantly increase of the concentration of cation on the right side of the charged graphene membrane also induced a significant increase of the density flux at the same position.

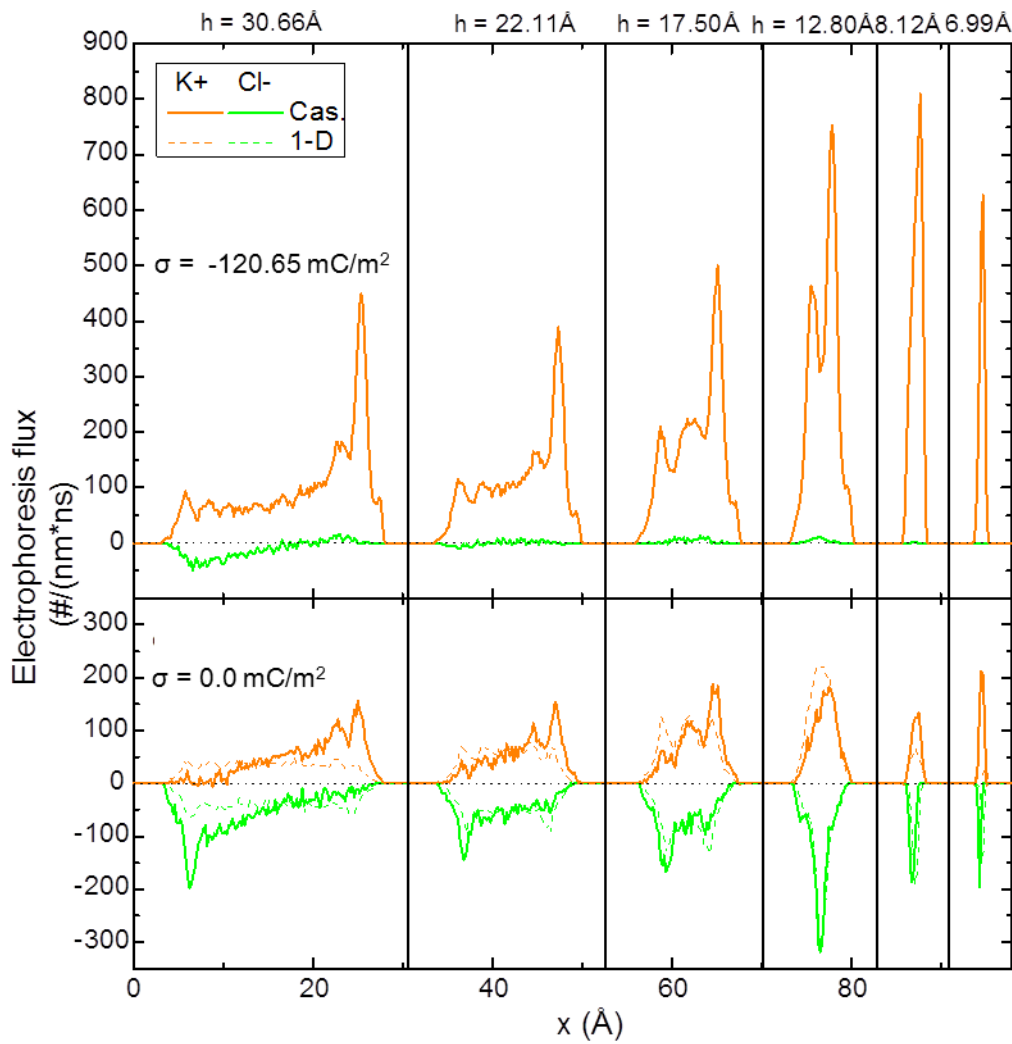


Figure 7.14 The electro-kinetic flux of ions in nanoslit region for different channel height: (top) in charge graphene hydrogel membrane; (bottom) in neutral graphene hydrogel membrane and 1-D nanochannel (dashed line). The results of K⁺ and Cl⁻ were coloured as orange and green lines respectively. Note that the result in the charge membrane with $h = 6.99\text{\AA}$ have been scaled by 0.5 to present the result clearly.

Besides the polarized flux density, the contributions of the electro-kinetic current were also different. For the charged graphene membrane, the cation was the dominant contribution

to the electro-kinetic current. Because both the concentration and velocity of the cation was significantly reduced, giving a negligible influence to the overall current. However, for the neutral nanochannel, both the cation and anions contributed equally to the electro-kinetic current.

Comparing the area surrounded by the flux density curves, namely the overall electro-kinetic current (I_{sys}), the strength of current in the charged graphene membrane was considerably higher than that in the neutral membrane or 1-D nanochannel, it would be attributed to the general EOF by EDLs structure.

Once the overall electro-kinetic current of system was obtained (I_{sys}), the scaling law of the graphene membrane was calculated as the description in Post-analysis section and was plotted in Figure 7.15.

For neutral graphene membrane, the scaling law was similar to experiment result with $n_{res} = 1M$ that the negligible changes of S_m with the decrease of h at large channel height. Because, the surface charge of the graphene sheet owned a negligible influence on the high ionic strength electrolyte. At large channel height ($h > 10 \sim 15 \text{ \AA}$), the scaling law of both seemed to maintain a constant value. However at $h < 10 \sim 15 \text{ \AA}$, the strong nanoconfinement and partial dehydration on the entrance of nanochannel would considerably decreased the conductivity of ion inside the membrane, namely the decrease of S_m .

As mentioned in Chapter 6, the polarized EOF at large channel height ($h = 30.66 \text{ \AA}$) could accelerate the ion transport inside the nanoslit. However the bottleneck of the small aperture opening would cancel the acceleration by the polarized EOF. Thus the similar S_m was obtained for $h > 10 \text{ \AA}$.

For the charged graphene membrane, the higher surface charge density ($\sigma = -60.33mC/m^2$) owned a considerable influence on the higher ionic strength (1M), which was similar to the experimental case with low surface charge density ($\sigma = -60.33mC/m^2$) to that of low ionic strength (0.01~0.001 M). Thus the experimental result at ($n_{res} = 0.001M$) was added into as the inset of the Figure 7.15 for comparison.

We found that the surface charge would induce the EOF in the nanoslit that increased the conductivity of ions (S_m). At $h = 12.80 \text{ \AA}$, the maximum S_m was achieved with the maximum velocity of EOF. At $h < 12.80 \text{ \AA}$, the S_m was reduced with the weakening of EOF.

The similar S_m with the maximum value (~ 7) at $h = 8 \text{ \AA}$ for $n_{res} = 0.001 \text{ M}$ were also shown in the inset of the Figure 7.15. But the increase of experimental S_m would be attributed to the increase of charge carrier density (the description in Chapter 5) rather than the EOF. Because, the E-field strength in experiment was significantly weak that cannot induce the meaningful EOF in the membrane. But the decrease of S_m at very small channel would be the same, owing to the nanoconfinement effect and the partially dehydration cost.

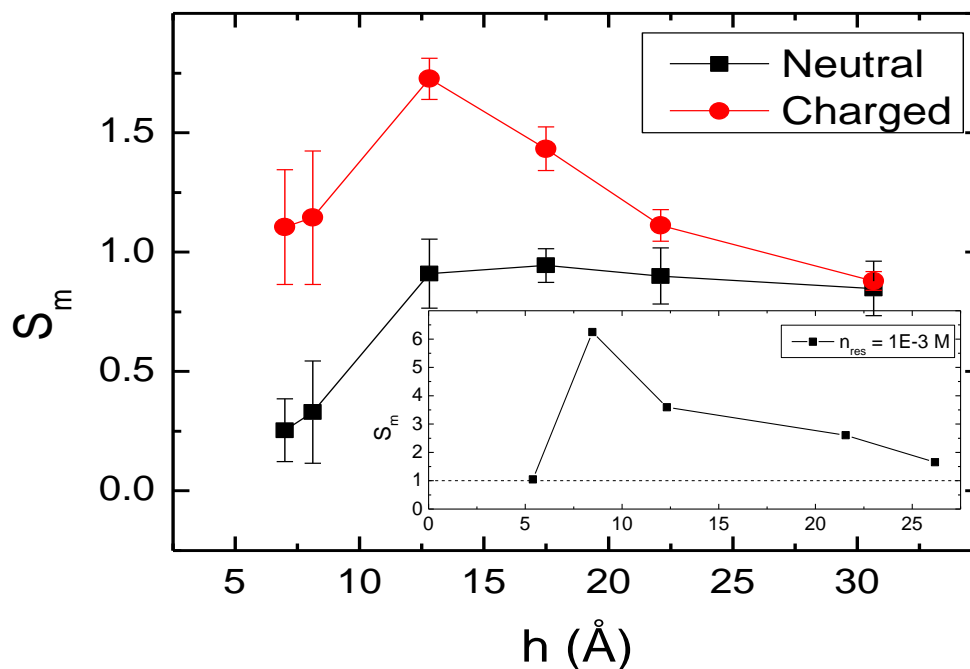


Figure 7.15 The Scaling law for the cascading electro-kinetic flow in the neutral (red) and charged (black) membrane. The inset: the experiment S_m for $n_{res} = 1\text{E-}3 \text{ M}$

Generally speaking, MD simulations have successfully reproduced the electro-kinetic flow inside the staggered graphene membrane. Especially the drops of S_m at very small channel height ($h < 10 \text{ \AA}$) was identified which cannot be predicted by the continuum modelling in the classic thermodynamics framework. The surface charge on graphene sheet would induce the general EOF in nanoslit that was the major contribution to the increase of S_m . However that discovery would be different from the experiment.

7.4 Conclusion

The electro-kinetic flow through the charged graphene membrane was investigated via the MD simulation and the result was compared with that in the neutral graphene membrane in the previous Chapter. Although the BBLs structure could still be observed in both neutral and charged graphene membrane, the surface charge on the charged graphene wall induced an EDLs that gave an asymmetric BBLs structure with a higher maximum concentration of cation in nanoslit region.

With the reducing of channel height, the overlap of BBLs structure would significantly reduce the concentration of anion and increase that of cation. At very small channel height ($h < 10 \text{ \AA}$), the partially dehydration occurred again in the charge graphene membrane. However, with the combination of strong EOF, partial dehydration and high surface charge density, the abnormal BBLs structure formed on the aperture region at $h < 10 \text{ \AA}$, which cannot be explained in the present Thesis.

For electric potential drops, we found the electric potential distribution in the charged case was similar to that in the neutral one. The electric potential drop along the nanoslit region could also be regarded to be constant. At very small channel height, the abrupt potential drop at the entrance of nanoslit region was also generated by the partially dehydration process. Due to the completely exclusion of anion, it only occurred on the one side of the charged nanoslit (entrance), rather than the two sides of the neutral nanoslit.

In the charged nanoslit, the similar polarized velocity profile of ions was obtained. And the transport of ions was essentially modified by the EOF. While the two types of EOF, the general EOF by EDLs and the polarized EOF by BBLs was prompted. At $h = 12.80 \text{ \AA}$, the maximum general EOF was obtained, which was the majorly attributed to the increase of conductivity in the membrane. The further decrease of the channel height ($h < 10 \text{ \AA}$) enhanced the nanoconfinement effect that weakened the EOF.

Finally, we compared the scaling law between the MD simulation and experimental data. We found the result of neutral MD simulation was similar to the experiment with high ionic

strength electrolyte, the conductivity of both curves dropped at very small channel height ($h < 10 \text{ \AA}$). For the charged graphene membrane, S_m was enhanced by the general EOF and also dropped at $h < 10 \text{ \AA}$. However the increase of S_m in the charged graphene membrane was majorly prompted by the EOF rather than the increase of charge carrier density in experiment. But, the simulation results revealed the conductivity drops at very small channel height by the partial dehydration which cannot be predicted in the continuum modelling.

The validation of the continuum model in the MD simulation is in a great debate. Generally, for the electrolyte solution, the mismatch property of ions and water molecules required an atomistic decryption of BBLs structure. Thus, when h is smaller than the tenth of the ionic radius, the continuum model was thought to be breakdown [87, 88]. In our study we could discover that in the high ionic strength, most of the ions located within the Helmholtz Layers (HL) which is consistent with the discovery in the continuum model. However at $h \leq 12.80 \text{ \AA}$, the BBLs collapsed into the single layer structure and the result started to deviate from the continuum model and the corresponding different transport property would be obtained. The transition of the continuum model into the atomistic description would occur between the double and single layer model.

Chapter 8: Conclusion

Inspired by the great of advance of the nanofluidics and the abnormal discovery by my colleagues for the electrophoresis enhancement, the present thesis started the investigation for the mass transport through the staggered graphene membrane by combining two theoretical methods, 1) continuum modelling and 2) MD simulation.

Initially, EDLs on the graphene surface was investigated for the different ionic types in Chapter 3. We found that that the larger ions, such as Rb^+ , Cs^+ , Cl^- and I^- , will be dehydrated subject to the external electric field and penetrate the first water layer to form the impact Helmholtz layer (IHL). In contrast, the small ions, such as Na^+ , K^+ , and F^- , no IHL will be formed. However, because of the low dielectric constants for the electrolyte with large size ions, the overall potential drop U_{tot} is almost the same, rendering a similar capacitance. It is worth noting in the Helmholtz layer there is a lower dielectric constant than the average value of whole EDL. This can be partly understood in terms of high density in HL.

Subject to higher electrical field, the ionic density peaks tend to get closer to the electrode surface, leading to a reduced IHL/OHL layers thickness. Thus U_{ion} is less proportional to the increase of the surface charges, suggesting an increasing trend of capacitance. However, due to the observed dielectric saturation effect (i.e., reduced dielectric constant under a high electric field), the calculated capacitance of cathode is reduced and the capacitance of anodes almost remains unchanged. This provides clear explanations to our experimental results.

Secondly, to investigate the mass transport process, the microstructure of the graphene membrane should be determined in prior. By combing the experimental data and the continuum modelling, we successfully simplified the complex 3D nanoporous network into an order 2D staggered CG mod via the classic thermodynamics framework.

The geometrical parameters of 2D model were determined via a reverse Monte Carlo Calculation, giving the similar result D_0/D_m as the experimental membrane. The prediction (linear interpolation) with $L = 50\text{nm}$ and $d = 1.6\text{nm}$ has been verified via the extra 2D modelling. There is a little deviation between two methods, except for the very small channel

height ($h < 1$ nm) where the corrugation of CCG flakes and the strong solution/wall interactions were not accounted into the classic thermodynamics framework. The small lateral size indicates the invisible pin-hole which was usually ignored in the graphene membrane study.

We also further simplified the 2D staggered model into an effective 1-D nanochannel with L_{eff} and A_{eff} . The relationship between the key geometric parameters and the effective 1-D nanochannel were presented and discussed. A_{eff} in the modelling study at $h < 1$ nm was found to be considerably underestimated.

Thirdly, once the microstructure of graphene (2D model) was obtained, the continuum electrophoresis modelling could be taken with the almost the same setup as the experiment. In the neutral graphene membrane, the novel BBLs structure was discovered inside the membrane, which is dependent on the strength of the external E-field, Debye length and nanochannel size.

The formations of BBLs structure in the neutral membrane would modify the potential distribution in the membrane, giving torturous electric potential drop that drives the ions to bypass the graphene sheet. We also found not only the electrophoresis flow, but also the diffusion flow contributed the total ion transport. However for the neutral membrane, the unity scaling law was obtained, which was different from the experiment discovery.

With the introducing the surface charge, the EDLs formed on the surface of the graphene sheet. The shapes of EDLs depended on the surface charge density, Debye length and the size of nanoconfinement. Although the magnitude of EDLs was much higher than that of BBLs, the BBLs structure was still generated by the external E-field. The behavior of BBLs structure was similar to the discovery in the neutral membrane and the weak BBLs structure played a crucial role in generating the tortuous electrophoresis flow.

The electric (Φ_E) and Nernst (Φ_N) potential profile in the charged membrane was similar as that in the neutral membrane. But the surface charge induced a “background” distribution

of Φ_E and Φ_N with $\Phi_E + \Phi_N = 0$. To discuss the influence of the external electric potential different ($\Delta\Phi_E = 0.01$ V), the background should be removed.

Even for the similar BBLs structure and the potential profile, the induced EDLs gave an increase of S_m with the decrease of h which is similar to the experiment result. It was attributed to the increase of ion concentration (charge carrier density) by the EDLs. But there was still a large deviation between the modelling and the experiment.

Fourthly, to elucidate the discrepancy in the continuum modelling, especially for the drop of S_m at $h < 1$ nm, the MD simulation was proposed to study the ion transport through the staggered graphene membrane with small channel height ($h < 3$ nm). And the result was compared with the MD simulation of the 1-D neutral graphene nanochannel and bulk solution. The similar BBLs, as predicted in the continuum modelling were also induced by the strong external E-field. The reducing of channel height introduced the overlap of BBLs structure that diminishes the polarization of boundary layers structure into a single peak profile. And the density profile visually indicated the partial dehydration process at the entrance of nanoslit region. E-field in nanoslit region was almost constant along the graphene sheet (in Y-direction). The potential drop normal to the graphene sheet is consumed to maintain the BBLs.

The novel polarized EOF was discovered in nanoslit region with opposite direction on both sides. The separation of ions in large channel is benefit for the enhancement of the sheared laminar EOF. With the reduction of channel height, the diminishing of polarization will reduce the EOFs and at $h = 12.8 \text{ \AA}$, a nearly symmetric velocity profile in slit region. With the further reduction of channel height, the strong friction interaction between the wall and ions will significantly hinder the transport of ions in very small nanochannel.

Finally, the electro-kinetic flow through the charged graphene membrane, more similar to the experimental CCG flakes, was investigated via the MD simulation. Although the BBLs structure could still be observed in both neutral and charged graphene membrane, the surface

charge on the charged graphene wall has induced intrinsic EDLs that gave an asymmetric BBLs structure with a higher maximum concentration of cation in the nanoslit region.

With the reducing of channel height, the overlap of BBLs structure would significantly reduce the concentration of anion and increase that of cation. At $h < 10 \text{ \AA}$, the partial dehydration occurred again in the charged graphene membrane and the co-ions (anions) were completely excluded from the nanoslit region. Thus, only the abrupt electric potential drop of the partial dehydration only occurred on the entrance of counter-ion into the nanoslit region rather than the two sides in the neutral graphene membrane

In the charged nanoslit, the similar polarized velocity profile of ions was obtained. And the transport of ions was essentially modified by the EOF. While the two types of EOF, the general EOF by EDLs and the polarized EOF by BBLs was prompted. At $h = 12.80 \text{ \AA}$, the maximum general EOF was obtained, which was the major contribution to the increase of conductivity in the membrane. The further decrease of the channel height ($h < 10 \text{ \AA}$) enhanced the nanoconfinement effect that weakened the EOF.

We found the result of neutral MD simulation was similar to the experiment with low ionic strength electrolyte, the conductivity of both curves dropped at very small channel height ($h < 10 \text{ \AA}$). For the charged graphene membrane, S_m was enhanced by the general EOF and also dropped at $h < 10 \text{ \AA}$. However the increase of S_m in the charged graphene membrane was prompted by the EOF the increase of charge carrier density in experiment. But, the simulation results revealed the conductivity drops at very small channel height by the partial dehydration which cannot be predicted in the continuum modelling.

Reference

- [1] Bocquet, L.; Charlaix, E. Nanofluidics, from bulk to interfaces. *Chemical Society Reviews* **2010**, 39, 1073-1095.
- [2] Bocquet, L.; Tabeling, P. Physics and technological aspects of nanofluidics. *Lab on a Chip* **2014**, 14, 3143-3158.
- [3] Eijkel, J. T.; Berg, A. Nanofluidics: what is it and what can we expect from it? *Microfluid Nanofluid* **2005**, 1, 249-267.
- [4] Eijkel, J. C. T.; van den Berg, A. Nanofluidics and the chemical potential applied to solvent and solute transport. *Chemical Society Reviews* **2010**, 39, 957-973.
- [5] Gravelle, S.; Joly, L.; Detcheverry, F.; Ybert, C.; Cottin-Bizonne, C.; Bocquet, L. Optimizing water permeability through the hourglass shape of aquaporins. *Proceedings of the National Academy of Sciences* **2013**, 110, 16367-16372.
- [6] Greger, R. *Cellular membrane transport mechanisms*; Springer, 1996.
- [7] Murata, K.; Mitsuoka, K.; Hirai, T.; Walz, T.; Agre, P.; Heymann, J. B.; Engel, A.; Fujiyoshi, Y. Structural determinants of water permeation through aquaporin-1. *Nature* **2000**, 407, 599-605.
- [8] Stein, D.; Kruithof, M.; Dekker, C. Surface-Charge-Governed Ion Transport in Nanofluidic Channels. *Physical Review Letters* **2004**, 93, 035901.
- [9] Duan, C.; Majumdar, A. Anomalous ion transport in 2-nm hydrophilic nanochannels. *Nat Nano* **2010**, 5, 848-852.
- [10] Coleman, M.; Tang, X. Diffusive transport of two charge equivalent and structurally similar ruthenium complex ions through graphene oxide membranes. *Nano Res.* **2015**, 8, 1128-1138.
- [11] Duan, C.; Wang, W.; Xie, Q. Review article: Fabrication of nanofluidic devices. *Biomicrofluidics* **2013**, 7, 026501.
- [12] Nair, R. R.; Wu, H. A.; Jayaram, P. N.; Grigorieva, I. V.; Geim, A. K. Unimpeded Permeation of Water Through Helium-Leak-Tight Graphene-Based Membranes. *Science* **2012**, 335, 442-444.
- [13] Joshi, R. K.; Carbone, P.; Wang, F. C.; Kravets, V. G.; Su, Y.; Grigorieva, I. V.; Wu, H. A.; Geim, A. K.; Nair, R. R. Precise and Ultrafast Molecular Sieving Through Graphene Oxide Membranes. *Science* **2014**, 343, 752-754.
- [14] Li, H.; Song, Z.; Zhang, X.; Huang, Y.; Li, S.; Mao, Y.; Ploehn, H. J.; Bao, Y.; Yu, M. Ultrathin, Molecular-Sieving Graphene Oxide Membranes for Selective Hydrogen Separation. *Science* **2013**, 342, 95-98.
- [15] Huang, K.; Liu, G.; Lou, Y.; Dong, Z.; Shen, J.; Jin, W. A Graphene Oxide Membrane with Highly Selective Molecular Separation of Aqueous Organic Solution. *Angewandte Chemie International Edition* **2014**, 53, 6929-6932.
- [16] Mi, B. Graphene Oxide Membranes for Ionic and Molecular Sieving. *Science* **2014**, 343, 740-742.
- [17] Sparreboom, W.; Berg, A. v. d.; Eijkel, J. C. T. Transport in nanofluidic systems: a review of theory and applications. *New Journal of Physics* **2010**, 12, 015004.
- [18] Daiguji, H. Ion transport in nanofluidic channels. *Chemical Society Reviews* **2010**, 39, 901-911.

- [19] Gad-el-Hak, M. The fluid mechanics of microdevices-the freeman scholar lecture. *Transactions-American Society of Mechanical Engineers Journal of FLUIDS Engineering* **1999**, *121*, 5-33.
- [20] Napoli, M.;Eijkel, J. C. T.; Pennathur, S. Nanofluidic technology for biomolecule applications: a critical review. *Lab on a Chip* **2010**, *10*, 957-985.
- [21] Dutta P, M. J. A review of nanofluidic patents. *Recent Pat Nanotechnol* **2008**, *2*, 150.
- [22] Abgrall, P.; Nguyen, N. T. Nanofluidic Devices and Their Applications. *Analytical Chemistry* **2008**, *80*, 2326-2341.
- [23] Eijkel, J. C. T.;Bomer, J. G.; van den Berg, A. Osmosis and pervaporation in polyimide submicron microfluidic channel structures. *Applied Physics Letters* **2005**, *87*, 114103.
- [24] Wu, J.;Gerstandt, K.;Zhang, H.;Liu, J.; Hinds, B. J. Electrophoretically induced aqueous flow through single-walled carbon nanotube membranes. *Nat Nano* **2012**, *7*, 133-139.
- [25] Derjaguin, B.;Dukhin, S.; Korotkova, A. Diffusiophoresis in electrolyte solutions and its role in the Mechanism of the formation of films from caoutchouc latexes by the ionic deposition method. *Progress in Surface Science* **1993**, *43*, 153-158.
- [26] Abecassis, B.;Cottin-Bizonne, C.;Ybert, C.;Ajdari, A.; Bocquet, L. Boosting migration of large particles by solute contrasts. *Nature materials* **2008**, *7*, 785-789.
- [27] Eijkel, J. C. T.; van den Berg, A. Water in micro- and nanofluidics systems described using the water potential. *Lab on a Chip* **2005**, *5*, 1202-1209.
- [28] Helmholtz, H. Ueber einige Gesetze der Vertheilung elektrischer Ströme in körperlichen Leitern mit Anwendung auf die thierisch-elektrischen Versuche. *Annalen der Physik* **1853**, *165*, 211-233.
- [29] Zhang, L. L.; Zhao, X. S. Carbon-based materials as supercapacitor electrodes. *Chemical Society Reviews* **2009**, *38*, 2520-2531.
- [30] Kötz, R.; Carlen, M. Principles and applications of electrochemical capacitors. *Electrochimica Acta* **2000**, *45*, 2483-2498.
- [31] Conway, B. *Electrochemical supercapacitors: scientific fundamentals and technological applications (POD)*; Kluwer Academic/Plenum: New York, 1999.
- [32] El-Kady, M. F.;Strong, V.;Dubin, S.; Kaner, R. B. Laser Scribing of High-Performance and Flexible Graphene-Based Electrochemical Capacitors. *Science* **2012**, *335*, 1326-1330.
- [33] Liu, C.;Yu, Z.;Neff, D.;Zhamu, A.; Jang, B. Z. Graphene-Based Supercapacitor with an Ultrahigh Energy Density. *Nano Letters* **2010**, *10*, 4863-4868.
- [34] Zhu, Y.;Murali, S.;Stoller, M. D.;Ganesh, K. J.;Cai, W.;Ferreira, P. J.;Pirkle, A.;Wallace, R. M.;Cychoz, K. A.;Thommes, M.;Su, D.;Stach, E. A.; Ruoff, R. S. Carbon-Based Supercapacitors Produced by Activation of Graphene. *Science* **2011**, *332*, 1537-1541.
- [35] Yang, X.;Zhu, J.;Qiu, L.; Li, D. Bioinspired Effective Prevention of Restacking in Multilayered Graphene Films: Towards the Next Generation of High-Performance Supercapacitors. *Advanced Materials* **2011**, *23*, 2833-2838.
- [36] Yang, X.;Cheng, C.;Wang, Y.;Qiu, L.; Li, D. Liquid-Mediated Dense Integration of Graphene Materials for Compact Capacitive Energy Storage. *Science* **2013**, *341*, 534-537.
- [37] Gouy, G. Constitution of the electric charge at the surface of an electrolyte. *J. phys* **1910**, *9*, 457-467.

- [38] Schoch, R. B.; Han, J.; Renaud, P. Transport phenomena in nanofluidics. *Reviews of Modern Physics* **2008**, *80*, 839-883.
- [39] Hückel, E.; Debye, P. The theory of electrolytes. I. Lowering of freezing point and related phenomena. *Phys. Zeitschrift* **1923**, *24*, 185-206.
- [40] Hunter, R. J. *Zeta potential in colloid science: principles and applications*; Academic press, 2013.
- [41] Chapman, D. L. LI. A contribution to the theory of electrocapillarity. *The London, Edinburgh, and Dublin Philosophical Magazine and Journal of Science* **1913**, *25*, 475-481.
- [42] Stern-Hamburg, H. O. ZUR THEORIE DER ELEKTROLYTISCHEN DOPPELSCHICHT. *S. f. Electrochemie* **1924**, *30*, 508-516.
- [43] Qu, W.; Li, D. A Model for Overlapped EDL Fields. *Journal of Colloid and Interface Science* **2000**, *224*, 397-407.
- [44] Baldessari, F. Electrokinetics in nanochannels: Part I. Electric double layer overlap and channel-to-well equilibrium. *Journal of Colloid and Interface Science* **2008**, *325*, 526-538.
- [45] Chen, Y.; Ni, Z.; Wang, G.; Xu, D.; Li Electroosmotic Flow in Nanotubes with High Surface Charge Densities. *Nano Letters* **2008**, *8*, 42-48.
- [46] Chmiola, J.; Yushin, G.; Gogotsi, Y.; Portet, C.; Simon, P.; Taberna, P. L. Anomalous Increase in Carbon Capacitance at Pore Sizes Less Than 1 Nanometer. *Science* **2006**, *313*, 1760-1763.
- [47] Largeot, C.; Portet, C.; Chmiola, J.; Taberna, P.-L.; Gogotsi, Y.; Simon, P. Relation between the ion size and pore size for an electric double-layer capacitor. *Journal of the American Chemical Society* **2008**, *130*, 2730-2731.
- [48] Huang, J.; Sumpter, B. G.; Meunier, V. A Universal Model for Nanoporous Carbon Supercapacitors Applicable to Diverse Pore Regimes, Carbon Materials, and Electrolytes. *Chemistry – A European Journal* **2008**, *14*, 6614-6626.
- [49] Dan, B.-Y.; David, A.; Daniel, H.; Rudi, P. Beyond standard Poisson–Boltzmann theory: ion-specific interactions in aqueous solutions. *Journal of Physics: Condensed Matter* **2009**, *21*, 424106.
- [50] Spohr, E. Ion adsorption on metal surfaces. The role of water-metal interactions. *Journal of Molecular Liquids* **1995**, *64*, 91-100.
- [51] Hautman, J.; Halley, J. W.; Rhee, Y. J. Molecular dynamics simulation of water between two ideal classical metal walls. *The Journal of Chemical Physics* **1989**, *91*, 467-472.
- [52] Cui, S. T.; Cochran, H. D. Molecular dynamics simulation of interfacial electrolyte behaviors in nanoscale cylindrical pores. *The Journal of Chemical Physics* **2002**, *117*, 5850-5854.
- [53] Glosli, J. N.; Philpott, M. R. Molecular dynamics study of interfacial electric fields. *Electrochimica Acta* **1996**, *41*, 2145-2158.
- [54] Spohr, E. Computer simulation of the structure of the electrochemical double layer. *Journal of Electroanalytical Chemistry* **1998**, *450*, 327-334.
- [55] Spohr, E. Molecular simulation of the electrochemical double layer. *Electrochimica Acta* **1999**, *44*, 1697-1705.
- [56] Philpott, M. R.; Glosli, J. N.; Zhu, S.-B. Molecular dynamics simulation of adsorption in electric double layers. *Surface Science* **1995**, *335*, 422-431.
- [57] Cagle, C.; Feng, G.; Qiao, R.; Huang, J.; Sumpter, B.; Meunier, V. Structure and charging kinetics of electrical double layers at large electrode voltages. *Microfluid Nanofluid* **2010**, *8*, 703-708.

- [58] DeYoung, A. D.; Park, S.-W.; Dhumal, N. R.; Shim, Y.; Jung, Y.; Kim, H. J. Graphene Oxide Supercapacitors: A Computer Simulation Study. *The Journal of Physical Chemistry C* **2014**, *118*, 18472-18480.
- [59] Feng, G.; Li, S.; Presser, V.; Cummings, P. T. Molecular Insights into Carbon Supercapacitors Based on Room-Temperature Ionic Liquids. *The Journal of Physical Chemistry Letters* **2013**, *4*, 3367-3376.
- [60] Kondrat, S.; Georgi, N.; Fedorov, M. V.; Kornyshev, A. A. A superionic state in nano-porous double-layer capacitors: insights from Monte Carlo simulations. *Physical Chemistry Chemical Physics* **2011**, *13*, 11359-11366.
- [61] Kondrat, S.; Kornyshev, A. Superionic state in double-layer capacitors with nanoporous electrodes. *Journal of Physics: Condensed Matter* **2011**, *23*, 022201.
- [62] Shim, Y.; Jung, Y.; Kim, H. J. Graphene-Based Supercapacitors: A Computer Simulation Study. *The Journal of Physical Chemistry C* **2011**, *115*, 23574-23583.
- [63] Vatamanu, J.; Borodin, O.; Smith, G. D. Molecular Insights into the Potential and Temperature Dependences of the Differential Capacitance of a Room-Temperature Ionic Liquid at Graphite Electrodes. *Journal of the American Chemical Society* **2010**, *132*, 14825-14833.
- [64] Vatamanu, J.; Borodin, O.; Smith, G. D. Molecular Dynamics Simulation Studies of the Structure of a Mixed Carbonate/LiPF₆ Electrolyte near Graphite Surface as a Function of Electrode Potential. *The Journal of Physical Chemistry C* **2011**, *116*, 1114-1121.
- [65] Vatamanu, J.; Cao, L.; Borodin, O.; Bedrov, D.; Smith, G. D. On the Influence of Surface Topography on the Electric Double Layer Structure and Differential Capacitance of Graphite/Ionic Liquid Interfaces. *The Journal of Physical Chemistry Letters* **2011**, *2*, 2267-2272.
- [66] Singh, R.; Rajput, N. N.; He, X.; Monk, J.; Hung, F. R. Molecular dynamics simulations of the ionic liquid [EMIM+][TFMSI-] confined inside rutile (110) slit nanopores. *Physical Chemistry Chemical Physics* **2013**, *15*, 16090-16103.
- [67] Vatamanu, J.; Borodin, O.; Smith, G. D. Molecular Simulations of the Electric Double Layer Structure, Differential Capacitance, and Charging Kinetics for N-Methyl-N-propylpyrrolidinium Bis(fluorosulfonyl)imide at Graphite Electrodes. *The Journal of Physical Chemistry B* **2011**, *115*, 3073-3084.
- [68] Feng, G.; Huang, J.; Sumpter, B. G.; Meunier, V.; Qiao, R. Structure and dynamics of electrical double layers in organic electrolytes. *Physical Chemistry Chemical Physics* **2010**, *12*, 5468-5479.
- [69] Yang, L.; Fishbine, B. H.; Migliori, A.; Pratt, L. R. Molecular Simulation of Electric Double-Layer Capacitors Based on Carbon Nanotube Forests. *Journal of the American Chemical Society* **2009**, *131*, 12373-12376.
- [70] Fedorov, M. V.; Kornyshev, A. A. Ionic Liquid Near a Charged Wall: Structure and Capacitance of Electrical Double Layer. *The Journal of Physical Chemistry B* **2008**, *112*, 11868-11872.
- [71] Merlet, C.; Limmer, D. T.; Salanne, M.; van Roij, R.; Madden, P. A.; Chandler, D.; Rotenberg, B. The Electric Double Layer Has a Life of Its Own. *The Journal of Physical Chemistry C* **2014**, *118*, 18291-18298.
- [72] Merlet, C.; Rotenberg, B.; Madden, P. A.; Salanne, M. Computer simulations of ionic liquids at electrochemical interfaces. *Physical Chemistry Chemical Physics* **2013**, *15*, 15781-15792.

- [73] Frolov, A. I.;Kirchner, K.;Kirchner, T.; Fedorov, M. V. Molecular-scale insights into the mechanisms of ionic liquids interactions with carbon nanotubes. *Faraday Discussions* **2012**, *154*, 235-247.
- [74] Shim, Y.; Kim, H. J. Nanoporous Carbon Supercapacitors in an Ionic Liquid: A Computer Simulation Study. *ACS Nano* **2010**, *4*, 2345-2355.
- [75] Feng, G.;Jiang, D.-e.; Cummings, P. T. Curvature Effect on the Capacitance of Electric Double Layers at Ionic Liquid/Onion-Like Carbon Interfaces. *Journal of Chemical Theory and Computation* **2012**, *8*, 1058-1063.
- [76] Li, S.;Feng, G.;Fulvio, P. F.;Hillesheim, P. C.;Liao, C.;Dai, S.; Cummings, P. T. Molecular Dynamics Simulation Study of the Capacitive Performance of a Binary Mixture of Ionic Liquids near an Onion-like Carbon Electrode. *The Journal of Physical Chemistry Letters* **2012**, *3*, 2465-2469.
- [77] Li, S.;Van Aken, K. L.;McDonough, J. K.;Feng, G.;Gogotsi, Y.; Cummings, P. T. The Electrical Double Layer of Dicationic Ionic Liquids at Onion-like Carbon Surface. *The Journal of Physical Chemistry C* **2014**, *118*, 3901-3909.
- [78] Merlet, C.;Rotenberg, B.;Madden, P. A.;Taberna, P.-L.;Simon, P.;Gogotsi, Y.; Salanne, M. On the molecular origin of supercapacitance in nanoporous carbon electrodes. *Nat Mater* **2012**, *11*, 306-310.
- [79] Merlet, C.;Péan, C.;Rotenberg, B.;Madden, P. A.;Daffos, B.;Taberna, P. L.;Simon, P.; Salanne, M. Highly confined ions store charge more efficiently in supercapacitors. *Nat Commun* **2013**, *4*, 2701.
- [80] Feng, G.;Li, S.;Atchison, J. S.;Presser, V.; Cummings, P. T. Molecular Insights into Carbon Nanotube Supercapacitors: Capacitance Independent of Voltage and Temperature. *The Journal of Physical Chemistry C* **2013**, *117*, 9178-9186.
- [81] Yang, L.;Fishbine, B. H.;Migliori, A.; Pratt, L. R. Dielectric saturation of liquid propylene carbonate in electrical energy storage applications. *The Journal of Chemical Physics* **2010**, *132*, 044701.
- [82] Wu, P.;Huang, J.;Meunier, V.;Sumpter, B. G.; Qiao, R. Voltage Dependent Charge Storage Modes and Capacity in Subnanometer Pores. *The Journal of Physical Chemistry Letters* **2012**, *3*, 1732-1737.
- [83] Wu, P.;Huang, J.;Meunier, V.;Sumpter, B. G.; Qiao, R. Complex Capacitance Scaling in Ionic Liquids-Filled Nanopores. *ACS Nano* **2011**, *5*, 9044-9051.
- [84] Jiang, D.-e.;Jin, Z.; Wu, J. Oscillation of Capacitance inside Nanopores. *Nano Letters* **2011**, *11*, 5373-5377.
- [85] Hu, G.; Li, D. Multiscale phenomena in microfluidics and nanofluidics. *Chemical Engineering Science* **2007**, *62*, 3443-3454.
- [86] Huang, D. M.;Sendner, C.;Horinek, D.;Netz, R. R.; Bocquet, L. Water Slippage versus Contact Angle: A Quasiuniversal Relationship. *Physical Review Letters* **2008**, *101*, 226101.
- [87] Qiao, R.; Aluru, N. R. Ion concentrations and velocity profiles in nanochannel electroosmotic flows. *The Journal of Chemical Physics* **2003**, *118*, 4692-4701.
- [88] Qiao, R.; Aluru, N. R. Scaling of Electrokinetic Transport in Nanometer Channels. *Langmuir* **2005**, *21*, 8972-8977.
- [89] Daiguji, H.;Yang, P.; Majumdar, A. Ion Transport in Nanofluidic Channels. *Nano Letters* **2004**, *4*, 137-142.

- [90] Schoch, R. B.; Renaud, P. Ion transport through nanoslits dominated by the effective surface charge. *Applied Physics Letters* **2005**, *86*, 253111.
- [91] Vlassiounk, I.; Smirnov, S.; Siwy, Z. Ionic Selectivity of Single Nanochannels. *Nano Letters* **2008**, *8*, 1978-1985.
- [92] Huang, D. M.; Cottin-Bizonne, C.; Ybert, C.; Bocquet, L. Ion-Specific Anomalous Electrokinetic Effects in Hydrophobic Nanochannels. *Physical Review Letters* **2007**, *98*, 177801.
- [93] Xu, Z.; Miao, J.; Wang, N.; Wen, W.; Sheng, P. Maximum efficiency of the electro-osmotic pump. *Physical Review E* **2011**, *83*, 066303.
- [94] Vajandar, S. K.; Xu, D.; Jiashu, S.; Markov, D. A.; Hofmeister, W. H.; Li, D. Field-Effect Control of Electroosmotic Pumping Using Porous Silicon/Silicon Nitride Membranes. *Microelectromechanical Systems, Journal of* **2009**, *18*, 1173-1183.
- [95] Schasfoort, R. B. M.; Schlautmann, S.; Hendrikse, J.; van den Berg, A. Field-Effect Flow Control for Microfabricated Fluidic Networks. *Science* **1999**, *286*, 942-945.
- [96] Karnik, R.; Castelino, K.; Fan, R.; Yang, P.; Majumdar, A. Effects of Biological Reactions and Modifications on Conductance of Nanofluidic Channels. *Nano Letters* **2005**, *5*, 1638-1642.
- [97] Taghipoor, M.; Bertsch, A.; Renaud, P. An improved model for predicting electrical conductance in nanochannels. *Physical Chemistry Chemical Physics* **2015**, *17*, 4160-4167.
- [98] Daiguji, H.; Oka, Y.; Shirono, K. Nanofluidic Diode and Bipolar Transistor. *Nano Letters* **2005**, *5*, 2274-2280.
- [99] Karnik, R.; Castelino, K.; Duan, C.; Majumdar, A. Diffusion-Limited Patterning of Molecules in Nanofluidic Channels. *Nano Letters* **2006**, *6*, 1735-1740.
- [100] Karnik, R.; Duan, C.; Castelino, K.; Daiguji, H.; Majumdar, A. Rectification of Ionic Current in a Nanofluidic Diode. *Nano Letters* **2007**, *7*, 547-551.
- [101] Cheng, L.-J.; Guo, L. J. Nanofluidic diodes. *Chemical Society Reviews* **2010**, *39*, 923-938.
- [102] Cheng, L.-J.; Guo, L. J. Rectified Ion Transport through Concentration Gradient in Homogeneous Silica Nanochannels. *Nano Letters* **2007**, *7*, 3165-3171.
- [103] Cao, L.; Guo, W.; Wang, Y.; Jiang, L. Concentration-Gradient-Dependent Ion Current Rectification in Charged Conical Nanopores. *Langmuir* **2012**, *28*, 2194-2199.
- [104] Siwy, Z.; Apel, P.; Baur, D.; Dobrev, D. D.; Korchev, Y. E.; Neumann, R.; Spohr, R.; Trautmann, C.; Voss, K.-O. Preparation of synthetic nanopores with transport properties analogous to biological channels. *Surface Science* **2003**, 532-535, 1061-1066.
- [105] Siwy, Z.; Heins, E.; Harrell, C. C.; Kohli, P.; Martin, C. R. Conical-Nanotube Ion-Current Rectifiers: The Role of Surface Charge. *Journal of the American Chemical Society* **2004**, *126*, 10850-10851.
- [106] Siwy, Z. S. Ion-Current Rectification in Nanopores and Nanotubes with Broken Symmetry. *Advanced Functional Materials* **2006**, *16*, 735-746.
- [107] Karnik, R.; Fan, R.; Yue, M.; Li, D.; Yang, P.; Majumdar, A. Electrostatic Control of Ions and Molecules in Nanofluidic Transistors. *Nano Letters* **2005**, *5*, 943-948.
- [108] Xiong, W.; Liu, J. Z.; Ma, M.; Xu, Z.; Sheridan, J.; Zheng, Q. Strain engineering water transport in graphene nanochannels. *Physical Review E* **2011**, *84*, 056329.
- [109] Beckstein, O.; Biggin, P. C.; Sansom, M. S. P. A Hydrophobic Gating Mechanism for Nanopores. *The Journal of Physical Chemistry B* **2001**, *105*, 12902-12905.

- [110] Shirono, K.; Tatsumi, N.; Daiguji, H. Molecular Simulation of Ion Transport in Silica Nanopores. *The Journal of Physical Chemistry B* **2009**, *113*, 1041-1047.
- [111] Ash, W. L.; Zlomislí, M. R.; Oloo, E. O.; Tieleman, D. P. Computer simulations of membrane proteins. *Biochimica et Biophysica Acta (BBA) - Biomembranes* **2004**, *1666*, 158-189.
- [112] Zhang, Z.; Zhang, H.; Ye, H. Pressure-driven flow in parallel-plate nanochannels. *Applied Physics Letters* **2009**, *95*, 154101.
- [113] Lynden - Bell, R. M.; Rasaiah, J. C. Mobility and solvation of ions in channels. *The Journal of Chemical Physics* **1996**, *105*, 9266-9280.
- [114] Kalra, A.; Garde, S.; Hummer, G. Osmotic water transport through carbon nanotube membranes. *Proceedings of the National Academy of Sciences* **2003**, *100*, 10175-10180.
- [115] Kim, D.; Darve, E. High-ionic-strength electroosmotic flows in uncharged hydrophobic nanochannels. *Journal of Colloid and Interface Science* **2009**, *330*, 194-200.
- [116] Huang, D. M.; Cottin-Bizonne, C.; Ybert, C.; Bocquet, L. Aqueous Electrolytes near Hydrophobic Surfaces: Dynamic Effects of Ion Specificity and Hydrodynamic Slip[†]. *Langmuir* **2007**, *24*, 1442-1450.
- [117] Vuković, L.; Vokac, E.; Král, P. Molecular Friction-Induced Electroosmotic Phenomena in Thin Neutral Nanotubes. *The Journal of Physical Chemistry Letters* **2014**, *5*, 2131-2137.
- [118] Král, P.; Wang, B. Material Drag Phenomena in Nanotubes. *Chemical Reviews* **2013**, *113*, 3372-3390.
- [119] Picallo, C. B.; Gravelle, S.; Joly, L.; Charlaix, E.; Bocquet, L. Nanofluidic Osmotic Diodes: Theory and Molecular Dynamics Simulations. *Physical Review Letters* **2013**, *111*, 244501.
- [120] Freund, J. B. Electro-osmosis in a nanometer-scale channel studied by atomistic simulation. *The Journal of Chemical Physics* **2002**, *116*, 2194-2200.
- [121] Joseph, S.; Aluru, N. R. Hierarchical Multiscale Simulation of Electrokinetic Transport in Silica Nanochannels at the Point of Zero Charge. *Langmuir* **2006**, *22*, 9041-9051.
- [122] Wang, M.; Liu, J.; Chen, S. Similarity of electroosmotic flows in nanochannels. *Molecular Simulation* **2007**, *33*, 239-244.
- [123] Qiao, R.; Aluru, N. R. Charge Inversion and Flow Reversal in a Nanochannel Electro-osmotic Flow. *Physical Review Letters* **2004**, *92*, 198301.
- [124] Lorenz, C. D.; Crozier, P. S.; Anderson, J. A.; Travesset, A. Molecular Dynamics of Ionic Transport and Electrokinetic Effects in Realistic Silica Channels. *The Journal of Physical Chemistry C* **2008**, *112*, 10222-10232.
- [125] Qiao, R.; Aluru, N. R. Atomistic simulation of KCl transport in charged silicon nanochannels: Interfacial effects. *Colloids and Surfaces A: Physicochemical and Engineering Aspects* **2005**, *267*, 103-109.
- [126] Gross, R.; Leach, M.; Bauen, A. Progress in renewable energy. *Environment International* **2003**, *29*, 105-122.
- [127] Lewis, N. S.; Nocera, D. G. Powering the planet: Chemical challenges in solar energy utilization. *Proceedings of the National Academy of Sciences* **2006**, *103*, 15729-15735.
- [128] Lewis, N. S.; Crabtree, G. Basic research needs for solar energy utilization: Report of the basic energy sciences workshop on solar energy utilization, April 18-21, 2005. **2005**.

- [129] Davies, A.; Yu, A. Material advancements in supercapacitors: From activated carbon to carbon nanotube and graphene. *The Canadian Journal of Chemical Engineering* **2011**, *89*, 1342-1357.
- [130] Goodenough, J. B.; Abruna, H.; Buchanan, M. Basic research needs for electrical energy storage. In *Report of the basic energy sciences workshop for electrical energy storage*, 2007.
- [131] Wang, G.; Zhang, L.; Zhang, J. A review of electrode materials for electrochemical supercapacitors. *Chemical Society Reviews* **2012**, *41*, 797-828.
- [132] Conway, B. E.; Birss, V.; Wojtowicz, J. The role and utilization of pseudocapacitance for energy storage by supercapacitors. *Journal of Power Sources* **1997**, *66*, 1-14.
- [133] Rogers, G. W.; Liu, J. Z. High-Performance Graphene Oxide Electromechanical Actuators. *Journal of the American Chemical Society* **2012**, *134*, 1250-1255.
- [134] Zhang, Y.; Feng, H.; Wu, X.; Wang, L.; Zhang, A.; Xia, T.; Dong, H.; Li, X.; Zhang, L. Progress of electrochemical capacitor electrode materials: A review. *International Journal of Hydrogen Energy* **2009**, *34*, 4889-4899.
- [135] Stoller, M. D.; Park, S.; Zhu, Y.; An, J.; Ruoff, R. S. Graphene-Based Ultracapacitors. *Nano Letters* **2008**, *8*, 3498-3502.
- [136] Vivekchand, S.; Rout, C.; Subrahmanyam, K.; Govindaraj, A.; Rao, C. Graphene-based electrochemical supercapacitors. *Journal of Chemical Sciences* **2008**, *120*, 9-13.
- [137] Xia, J.; Chen, F.; Li, J.; Tao, N. Measurement of the quantum capacitance of graphene. *Nat Nano* **2009**, *4*, 505-509.
- [138] Feng, G.; Cummings, P. T. Supercapacitor Capacitance Exhibits Oscillatory Behavior as a Function of Nanopore Size. *The Journal of Physical Chemistry Letters* **2011**, *2*, 2859-2864.
- [139] Kalluri, R. K.; Ho, T. A.; Biener, J.; Biener, M. M.; Striolo, A. Partition and Structure of Aqueous NaCl and CaCl₂ Electrolytes in Carbon-Slit Electrodes. *The Journal of Physical Chemistry C* **2013**, *117*, 13609-13619.
- [140] Wander, M. C. F.; Shuford, K. L. Molecular Dynamics Study of Interfacial Confinement Effects of Aqueous NaCl Brines in Nanoporous Carbon[†]. *The Journal of Physical Chemistry C* **2010**, *114*, 20539-20546.
- [141] Wander, M. C. F.; Shuford, K. L. Electrolyte Effects in a Model System for Mesoporous Carbon Electrodes. *The Journal of Physical Chemistry C* **2011**, *115*, 4904-4908.
- [142] Wander, M. C. F.; Shuford, K. L. Alkali Halide Interfacial Behavior in a Sequence of Charged Slit Pores. *The Journal of Physical Chemistry C* **2011**, *115*, 23610-23619.
- [143] Reed, S. K.; Lanning, O. J.; Madden, P. A. Electrochemical interface between an ionic liquid and a model metallic electrode. *The Journal of Chemical Physics* **2007**, *126*, 84704-84716.
- [144] Péan, C.; Merlet, C.; Rotenberg, B.; Madden, P. A.; Taberna, P.-L.; Daffos, B.; Salanne, M.; Simon, P. On the Dynamics of Charging in Nanoporous Carbon-Based Supercapacitors. *ACS Nano* **2014**, *8*, 1576-1583.
- [145] Merlet, C.; Péan, C.; Rotenberg, B.; Madden, P. A.; Simon, P.; Salanne, M. Simulating Supercapacitors: Can We Model Electrodes As Constant Charge Surfaces? *The Journal of Physical Chemistry Letters* **2012**, *4*, 264-268.
- [146] Wang, Z.; Yang, Y.; Olmsted, D. L.; Asta, M.; Laird, B. B. Evaluation of the constant potential method in simulating electric double-layer capacitors. *The Journal of Chemical Physics* **2014**, *141*, 184102-184107.

- [147] Fasolino, A.; Los, J. H.; Katsnelson, M. I. Intrinsic ripples in graphene. *Nat Mater* **2007**, *6*, 858-861.
- [148] Ma, M. D.; Shen, L.; Sheridan, J.; Liu, J. Z.; Chen, C.; Zheng, Q. Friction of water slipping in carbon nanotubes. *Physical Review E* **2011**, *83*, 036316.
- [149] Chen, C.; Ma, M.; Jin, K.; Liu, J. Z.; Shen, L.; Zheng, Q.; Xu, Z. Nanoscale fluid-structure interaction: Flow resistance and energy transfer between water and carbon nanotubes. *Physical Review E* **2011**, *84*, 046314.
- [150] Jorgensen, W. L. Quantum and statistical mechanical studies of liquids. 10. Transferable intermolecular potential functions for water, alcohols, and ethers. Application to liquid water. *Journal of the American Chemical Society* **1981**, *103*, 335-340.
- [151] Ryckaert, J.-P.; Ciccotti, G.; Berendsen, H. J. C. Numerical integration of the cartesian equations of motion of a system with constraints: molecular dynamics of n-alkanes. *Journal of Computational Physics* **1977**, *23*, 327-341.
- [152] Alexiadis, A.; Kassinos, S. Molecular Simulation of Water in Carbon Nanotubes. *Chemical Reviews* **2008**, *108*, 5014-5034.
- [153] Foloppe, N.; MacKerell, J. A. D. All-atom empirical force field for nucleic acids: I. Parameter optimization based on small molecule and condensed phase macromolecular target data. *Journal of Computational Chemistry* **2000**, *21*, 86-104.
- [154] MacKerell, A. D.; Bashford, D.; Bellott, D.; Dunbrack, R. L.; Evanseck, J. D.; Field, M. J.; Fischer, S.; Gao, J.; Guo, H.; Ha, S.; Joseph-McCarthy, D.; Kuchnir, L.; Kuczera, K.; Lau, F. T. K.; Mattos, C.; Michnick, S.; Ngo, T.; Nguyen, D. T.; Prodhom, B.; Reiher, W. E.; Roux, B.; Schlenkrich, M.; Smith, J. C.; Stote, R.; Straub, J.; Watanabe, M.; Wiórkiewicz-Kuczera, J.; Yin, D.; Karplus, M. All-Atom Empirical Potential for Molecular Modeling and Dynamics Studies of Proteins†. *The Journal of Physical Chemistry B* **1998**, *102*, 3586-3616.
- [155] Górniak, R.; Lamperski, S. Investigation of the Electrical Double Layer with a Graphene Electrode by the Grand Canonical Monte Carlo Simulation. *The Journal of Physical Chemistry C* **2014**, *118*, 3156-3161.
- [156] Dang, L. X.; Garrett, B. C. Photoelectron spectra of the hydrated iodine anion from molecular dynamics simulations. *The Journal of Chemical Physics* **1993**, *99*, 2972-2977.
- [157] Dang, L. X. Fluoride—fluoride association in water from molecular dynamics simulations. *Chemical Physics Letters* **1992**, *200*, 21-25.
- [158] Morishita, T. Fluctuation formulas in molecular-dynamics simulations with the weak coupling heat bath. *The Journal of Chemical Physics* **2000**, *113*, 2976-2982.
- [159] Lemak, A. S.; Balabaev, N. K. On The Berendsen Thermostat. *Molecular Simulation* **1994**, *13*, 177-187.
- [160] Mudi, A.; Chakravarty, C. Effect of the Berendsen thermostat on the dynamical properties of water. *Molecular Physics* **2004**, *102*, 681-685.
- [161] Behrens, S. H.; Borkovec, M. Exact Poisson-Boltzmann solution for the interaction of dissimilar charge-regulating surfaces. *Physical Review E* **1999**, *60*, 7040-7048.
- [162] Wang, S.; Li, S.; Cao, Z.; Yan, T. Molecular Dynamic Simulations of Ionic Liquids at Graphite Surface. *The Journal of Physical Chemistry C* **2009**, *114*, 990-995.
- [163] Crozier, P. S.; Rowley, R. L.; Henderson, D. Molecular dynamics calculations of the electrochemical properties of electrolyte systems between charged electrodes. *The Journal of Chemical Physics* **2000**, *113*, 9202-9207.

- [164] Bazant, M. Z.; Storey, B. D.; Kornyshev, A. A. Double Layer in Ionic Liquids: Overscreening versus Crowding. *Physical Review Letters* **2011**, *106*, 046102.
- [165] Fedorov, M. V.; Kornyshev, A. A. Towards understanding the structure and capacitance of electrical double layer in ionic liquids. *Electrochimica Acta* **2008**, *53*, 6835-6840.
- [166] Feng, G.; Huang, J.; Sumpter, B. G.; Meunier, V.; Qiao, R. A "counter-charge layer in generalized solvents" framework for electrical double layers in neat and hybrid ionic liquid electrolytes. *Physical Chemistry Chemical Physics* **2011**, *13*, 14723-14734.
- [167] Falk, K.; Sedlmeier, F.; Joly, L.; Netz, R. R.; Bocquet, L. r. Molecular Origin of Fast Water Transport in Carbon Nanotube Membranes: Superlubricity versus Curvature Dependent Friction. *Nano Letters* **2010**, *10*, 4067-4073.
- [168] Yang, K.-L.; Yiacoumi, S.; Tsouris, C. Monte Carlo simulations of electrical double-layer formation in nanopores. *The Journal of Chemical Physics* **2002**, *117*, 8499-8507.
- [169] Marti, J.; Nagy, G.; Gordillo, M. C.; Guàrdia, E. Molecular simulation of liquid water confined inside graphite channels: Thermodynamics and structural properties. *The Journal of Chemical Physics* **2006**, *124*, 094703.
- [170] Hunter, R. J. *Zeta Potential in Colloid Science: Principles and Applications*; Academic Press, 1988.
- [171] Mähler, J.; Persson, I. A Study of the Hydration of the Alkali Metal Ions in Aqueous Solution. *Inorganic Chemistry* **2011**, *51*, 425-438.
- [172] Richens, D. T. *The Chemistry of Aqua Ions: Synthesis, Structure and Reactivity: A Tour Through the Periodic Table of the Elements*; Wiley, 1997.
- [173] Aqvist, J. Ion-water interaction potentials derived from free energy perturbation simulations. *The Journal of Physical Chemistry* **1990**, *94*, 8021-8024.
- [174] Kalluri, R. K.; Biener, M. M.; Suss, M. E.; Merrill, M. D.; Stadermann, M.; Santiago, J. G.; Baumann, T. F.; Biener, J.; Striolo, A. Unraveling the potential and pore-size dependent capacitance of slit-shaped graphitic carbon pores in aqueous electrolytes. *Physical Chemistry Chemical Physics* **2013**, *15*, 2309-2320.
- [175] Schoch, R. B.; van Lintel, H.; Renaud, P. Effect of the surface charge on ion transport through nanoslits. *Physics of Fluids* **2005**, *17*, 100604.
- [176] Rajamani, S.; Ghosh, T.; Garde, S. Size dependent ion hydration, its asymmetry, and convergence to macroscopic behavior. *The Journal of Chemical Physics* **2004**, *120*, 4457-4466.
- [177] Cheng, C. Unpublished Data.
- [178] Dimitrov, D. I.; Raev, N. D.; Semerdzhiev, K. I. Molecular dynamics simulations of the electrical double layer at 1 M potassium halide solution/Hg electrode interfaces. *Physical Chemistry Chemical Physics* **2001**, *3*, 448-452.
- [179] Feng, G.; Qiao, R.; Huang, J.; Sumpter, B. G.; Meunier, V. Ion Distribution in Electrified Micropores and Its Role in the Anomalous Enhancement of Capacitance. *ACS Nano* **2010**, *4*, 2382-2390.
- [180] Levy, A.; Andelman, D.; Orland, H. Dielectric Constant of Ionic Solutions: A Field-Theory Approach. *Physical Review Letters* **2012**, *108*, 227801.
- [181] Wei, Y. Z.; Chiang, P.; Sridhar, S. Ion size effects on the dynamic and static dielectric properties of aqueous alkali solutions. *The Journal of Chemical Physics* **1992**, *96*, 4569-4573.

- [182] Fulton, R. L. The nonlinear dielectric behavior of water: Comparisons of various approaches to the nonlinear dielectric increment. *The Journal of Chemical Physics* **2009**, *130*, 204503-204512.
- [183] Qiu, L.;Zhang, X.;Yang, W.;Wang, Y.;Simon, G. P.; Li, D. Controllable corrugation of chemically converted graphene sheets in water and potential application for nanofiltration. *Chemical Communications* **2011**, *47*, 5810-5812.
- [184] Chua, C. K.; Pumera, M. Chemical reduction of graphene oxide: a synthetic chemistry viewpoint. *Chemical Society Reviews* **2014**, *43*, 291-312.
- [185] Paton, K. R.;Varrla, E.;Backes, C.;Smith, R. J.;Khan, U.;O'Neill, A.;Boland, C.;Lotya, M.;Istrate, O. M.;King, P.;Higgins, T.;Barwich, S.;May, P.;Puczkarski, P.;Ahmed, I.;Moebius, M.;Pettersson, H.;Long, E.;Coelho, J.;O'Brien, S. E.;McGuire, E. K.;Sanchez, B. M.;Duesberg, G. S.;McEvoy, N.;Pennycook, T. J.;Downing, C.;Crossley, A.;Nicolosi, V.; Coleman, J. N. Scalable production of large quantities of defect-free few-layer graphene by shear exfoliation in liquids. *Nat Mater* **2014**, *13*, 624-630.
- [186] Dimiev, A.;Kosynkin, D. V.;Alemany, L. B.;Chaguine, P.; Tour, J. M. Pristine Graphite Oxide. *Journal of the American Chemical Society* **2012**, *134*, 2815-2822.
- [187] Kim, T.;Jung, G.;Yoo, S.;Suh, K. S.; Ruoff, R. S. Activated Graphene-Based Carbons as Supercapacitor Electrodes with Macro- and Mesopores. *ACS Nano* **2013**, *7*, 6899-6905.
- [188] Rouquerol, J.;Rouquerol, F.;Llewellyn, P.;Maurin, G.; Sing, K. S. *Adsorption by powders and porous solids: principles, methodology and applications*; Academic press, 2013.
- [189] Zhang, J.;Yang, H.;Shen, G.;Cheng, P.;Zhang, J.; Guo, S. Reduction of graphene oxide vial-ascorbic acid. *Chemical Communications* **2010**, *46*, 1112-1114.
- [190] Erickson, K.;Erni, R.;Lee, Z.;Alem, N.;Gannett, W.; Zettl, A. Determination of the Local Chemical Structure of Graphene Oxide and Reduced Graphene Oxide. *Advanced Materials* **2010**, *22*, 4467-4472.
- [191] Bagri, A.;Mattevi, C.;Acik, M.;Chabal, Y. J.;Chhowalla, M.; Shenoy, V. B. Structural evolution during the reduction of chemically derived graphene oxide. *Nat Chem* **2010**, *2*, 581-587.
- [192] Li, D.;Muller, M. B.;Gilje, S.;Kaner, R. B.; Wallace, G. G. Processable aqueous dispersions of graphene nanosheets. *Nat Nano* **2008**, *3*, 101-105.
- [193] Yang, X.;Qiu, L.;Cheng, C.;Wu, Y.;Ma, Z.-F.; Li, D. Ordered Gelation of Chemically Converted Graphene for Next-Generation Electroconductive Hydrogel Films. *Angewandte Chemie International Edition* **2011**, *50*, 7325-7328.
- [194] Shih, C.-J.;Lin, S.;Strano, M. S.; Blankschtein, D. Understanding the Stabilization of Liquid-Phase-Exfoliated Graphene in Polar Solvents: Molecular Dynamics Simulations and Kinetic Theory of Colloid Aggregation. *Journal of the American Chemical Society* **2010**, *132*, 14638-14648.
- [195] Ying, Y.;Sun, L.;Wang, Q.;Fan, Z.; Peng, X. In-plane mesoporous graphene oxide nanosheet assembled membranes for molecular separation. *RSC Advances* **2014**, *4*, 21425-21428.
- [196] Kim, H.;Park, K.-Y.;Hong, J.; Kang, K. All-graphene-battery: bridging the gap between supercapacitors and lithium ion batteries. *Sci. Rep.* **2014**, *4*, 5278.
- [197] Chang, Y. C.; Myerson, A. S. The diffusivity of potassium chloride and sodium chloride in concentrated, saturated, and supersaturated aqueous solutions. *AIChE Journal* **1985**, *31*, 890-894.

- [198] Araújo, A. D.;Andrade, J. S.; Herrmann, H. J. Critical Role of Gravity in Filters. *Physical Review Letters* **2006**, 97, 138001.
- [199] Konkana, B.; Vasudevan, S. Understanding Aqueous Dispersibility of Graphene Oxide and Reduced Graphene Oxide through pKa Measurements. *The Journal of Physical Chemistry Letters* **2012**, 3, 867-872.
- [200] Elias, D. C.;Gorbachev, R. V.;Mayorov, A. S.;Morozov, S. V.;Zhukov, A. A.;Blake, P.;Ponomarenko, L. A.;Grigorieva, I. V.;Novoselov, K. S.;Guinea, F.; Geim, A. K. Dirac cones reshaped by interaction effects in suspended graphene. *Nat Phys* **2011**, 7, 701-704.
- [201] Sanchez-Yamagishi, J. D.;Taychatanapat, T.;Watanabe, K.;Taniguchi, T.;Yacoby, A.; Jarillo-Herrero, P. Quantum Hall Effect, Screening, and Layer-Polarized Insulating States in Twisted Bilayer Graphene. *Physical Review Letters* **2012**, 108, 076601.
- [202] Bostwick, A.;Speck, F.;Seyller, T.;Horn, K.;Polini, M.;Asgari, R.;MacDonald, A. H.; Rotenberg, E. Observation of Plasmarons in Quasi-Freestanding Doped Graphene. *Science* **2010**, 328, 999-1002.
- [203] Hu, W.;R. Haddad, P.;Hasebe, K.; Tanaka, K. Electrostatic ion chromatography using hydroxide solutions as mobile phase with suppressed conductivity detection. *Analytical Communications* **1999**, 36, 309-312.
- [204] Hu, W.;Haddad, P. R.;Tanakar, K.; Hasebe, K. Modulation of the separation selectivity of inorganic anions in electrostatic ion chromatography using acidic eluents. *Analyst* **2000**, 125, 241-244.
- [205] Stock, J. T.; Orna, M. V. *Electrochemistry, past and present*; ACS Publications, 1989.
- [206] Holt, J. K.;Park, H. G.;Wang, Y.;Stadermann, M.;Artyukhin, A. B.;Grigoropoulos, C. P.;Noy, A.; Bakajin, O. Fast Mass Transport Through Sub-2-Nanometer Carbon Nanotubes. *Science* **2006**, 312, 1034-1037.
- [207] Kannam, S. K.;Todd, B. D.;Hansen, J. S.; Davis, P. J. How fast does water flow in carbon nanotubes? *The Journal of Chemical Physics* **2013**, 138, 094701.
- [208] Barany, S. Electrophoresis in strong electric fields. *Advances in Colloid and Interface Science* **2009**, 147–148, 36-43.
- [209] Rathore, A. S.; Horváth, C. Capillary electrochromatography: theories on electroosmotic flow in porous media. *Journal of Chromatography A* **1997**, 781, 185-195.
- [210] Mishchuk, N. A. Concentration polarization of interface and non-linear electrokinetic phenomena. *Advances in Colloid and Interface Science* **2010**, 160, 16-39.
- [211] Feng, G.;Qiao, R.;Huang, J.;Sumpter, B. G.; Meunier, V. Atomistic Insight on the Charging Energetics in Subnanometer Pore Supercapacitors. *The Journal of Physical Chemistry C* **2010**, 114, 18012-18016.
- [212] Carrillo-Tripp, M.;Saint-Martin, H.; Ortega-Blake, I. A comparative study of the hydration of Na⁺ and K⁺ with refined polarizable model potentials. *The Journal of Chemical Physics* **2003**, 118, 7062-7073.
- [213] Mähler, J.; Persson, I. A study of the hydration of the alkali metal ions in aqueous solution. *Inorganic chemistry* **2011**, 51, 425-438.
- [214] Calero, C.;Faraudo, J.; Aguilera-Arzo, M. Molecular dynamics simulations of concentrated aqueous electrolyte solutions. *Molecular Simulation* **2011**, 37, 123-134.
- [215] Dukhin, S. S.; Mishchuk, N. A. Intensification of electrodialysis based on electroosmosis of the second kind. *Journal of Membrane Science* **1993**, 79, 199-210.

